Academic Press is an imprint of Elsevier
Linacre House, Jordan Hill, Oxford OX2 8DP, UK
32 Jamestown Road, London NW1 7BY, UK
Radarweg 29, PO Box 211, 1000 AE Amsterdam, The Netherlands
225 Wyman Street, Waltham, MA 02451, USA
525 B Street, Suite 1900, San Diego, CA 92101-4495, USA

First edition 2012

British Library Cataloguing in Publication Data
A catalogue record for this book is available from the British Library

Library of Congress Cataloging-in-Publication Data
A catalog record for this book is available from the Library of Congress

ISBN: 978-0-12-397018-3
ISSN: 0066-4103

Printed and bound in Great Britain
12 13 14 10 9 8 7 6 5 4 3 2 1

CONTRIBUTORS

Wen-Jang Chu
Department of Psychiatry and Behavioral Neuroscience; and Center for Imaging Research, University of Cincinnati, Cincinnati, Ohio, USA

Jonathan A. Dudley
School of Energy, Environmental, Biological, and Medical Engineering; and Center for Imaging Research, University of Cincinnati, Cincinnati, Ohio, USA

Thomas Echelmeyer
Institut für Physikalische Chemie, University of Münster, Corrensstr. 28–30, Münster, Germany

Jair C.C. Freitas
Department of Physics, Federal University of Espírito Santo, Vitória, Brazil

Richard A. Komoroski
Department of Psychiatry and Behavioral Neuroscience; and Center for Imaging Research, University of Cincinnati, Cincinnati, Ohio, USA

Jing-Huei Lee
School of Energy, Environmental, Biological, and Medical Engineering; Department of Psychiatry and Behavioral Neuroscience; and Center for Imaging Research, University of Cincinnati, Cincinnati, Ohio, USA

Mark E. Smith
Department of Physics, University of Warwick, Coventry, United Kingdom

Quang M. Tieng
Centre for Advanced Imaging, University of Queensland, Brisbane, Australia

Leo van Wüllen[1]
Institut für Physikalische Chemie, University of Münster, Corrensstr. 28–30, Münster, Germany

[1] Current address: Institut für Physik, Augsburg University, Universitätsstr. 1. 86159 Augsburg, Germany

Viktor Vegh
Centre for Advanced Imaging, University of Queensland, Brisbane, Australia

Sebastian Wegner
Bruker Biospin GmbH, Silberstreifen 4, Rheinstetten, Germany

PREFACE

Volume 75 of *Annual Reports on NMR Spectroscopy* consists of a collection of interesting accounts relating to recent progress in various areas of science where NMR is the tool of choice. Chapter 1 is a report on 'Constant Time REDOR NMR Spectroscopy' by T. Echelmeyer, S. Wegner and L. van Wüllen; following this is an account of 'Recent Advances in Solid-State ^{25}Mg NMR Spectroscopy' by J. C. C. Freitas and M.E. Smith. 'Methods and Applications of Phosphorus NMR Spectroscopy in vivo' are covered by J.-H. Lee, R. A. Komoroski, W.-J. Chu and J. A. Dudley. The volume concludes with an account of 'Compact Superconducting Magnet Design for Nuclear Magnetic Resonance: The Minimum Stored Energy Approach' by Q. M. Tieng and V. Vegh.

My grateful thanks go to all of these reporters for their interesting and timely contributions.

G. A. Webb
Royal Society of Chemistry
Burlington House
Piccadilly, London, UK

CHAPTER 1

Constant Time REDOR NMR Spectroscopy

Thomas Echelmeyer,* **Sebastian Wegner,†** and **Leo van Wüllen*,[1]**

Contents

Abstract

The constant time version of rotational echo double resonance (CT-REDOR) may be applied as an expedient alternative to the existing REDOR versions in cases in which strong heteronuclear dipolar couplings severely complicate the data analysis and render an accurate determination of the second moments impossible. The various facets of CT-REDOR are outlined and the applicability of the presented approaches exemplified on model compounds. For short dipolar evolution times, accurate values for the second moments can be obtained without the need to incorporate the full information about the detailed spin geometry of the multiple-spin systems into the simulation protocol.

* Institut für Physikalische Chemie, University of Münster, Corrensstr. 28–30, Münster, Germany
† Bruker Biospin GmbH, Silberstreifen 4, Rheinstetten, Germany
[1] Current address: Institut für Physik, Augsburg University, Universitätsstr. 1. 86159 Augsburg, Germany

Annual Reports on NMR Spectroscopy, Volume 75
ISSN 0066-4103, DOI: 10.1016/B978-0-12-397018-3.00001-6

Key Words: Heteronuclear dipolar couplings, REDOR spectroscopy, Structure, Second moments, Constant time, SIMPSON

1. INTRODUCTION

Solid state nuclear magnetic resonance spectroscopy has long been established as the routine spectroscopic tool for the structural characterization of solid materials.[1–14] The application of magic angle spinning (MAS), averaging all interactions which scale with the second Legendrian $(3\cos^2\theta - 1)$, provides highly resolved spectra, from which the quadrupole interaction and the chemical shift interaction can be evaluated. From this, a detailed knowledge about the immediate local environment (1–2 Å) of the nucleus under study may be obtained, elucidating the bonding situation and local symmetry. Information about structural details on an intermediate length scale (2–10 Å)—this influences the chemical shift and quadrupole interaction only to a marginal extent—becomes accessible analysing the homo- and heteronuclear magnetic dipole interactions which—due to the r^{-3} distance dependence—principally allow the determination of internuclear distances. During the past two decades, an impressive number of pulsed NMR methods has been developed which measure the homo- or heteronuclear dipolar couplings under the conditions of fast MAS. In most of the developed methods, the recoupling of the dipolar Hamiltionian is achieved by rotor-synchronised radio frequency pulses. Methods such as rotational resonance (R^2),[15] dipolar recovery at the magic angle (DRAMA),[16] radiofrequency driven recoupling (RFDR),[17] dipolar recovery with a windowless sequence (DRAWS)[18] and the C7-sequences and their variants[19,20] for the evaluation of the homonuclear dipolar couplings and rotational echo double resonance (REDOR),[21–29] transfer of populations in double resonance (TRAPDOR)[30–35], rotational echo adiabatic passage double resonance (REAPDOR)[31,36–41] or transferred echo double resonance (TEDOR)[42–48] for heteronuclear interactions have contributed enormously to an enhanced understanding of structural details on an intermediate length scale in a variety of materials such as biopolymers,[49–55] ceramics and glasses,[34,37,56–67] and solid state catalysts.[68–73] Among the various methods available for the quantification of heteronuclear dipolar couplings, the archetypical REDOR approach, introduced in 1989 by Schaefer and Gullion,[21] has evolved as the working horse. In REDOR (cf. Figure 1), the results from a rotor-synchronised spin-echo experiment for the observed (S) nuclei, defining the full echo intensity S_0, are compared to spectra resulting from an experiment in which the

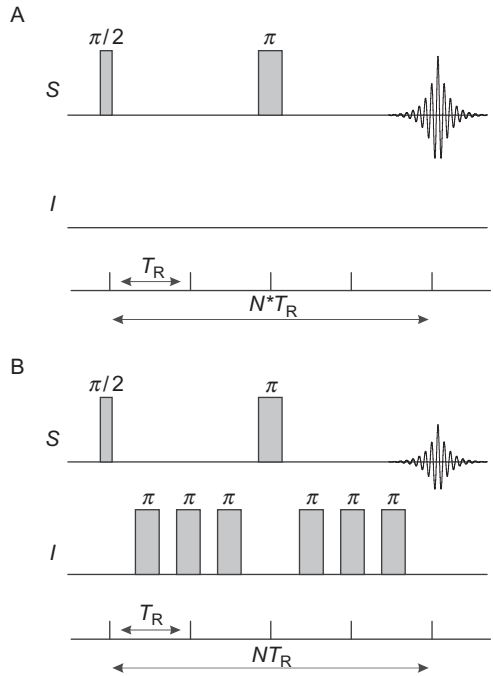

Figure 1 The archetypical REDOR pulse sequence.[21] (A) rotor-synchronised *S*-spin-echo experiment defining the reference echo amplitude S_0; the REDOR pulse sequence in (B) with the additional rotor-synchronised *I*-channel π-pulses provides the signal intensity *S*.

heteronuclear dipolar coupling between nuclei *S* and *I* has been reintroduced by the action of rotor-synchronised π-pulses (*I*-channel) in addition to the *S*-spin spin-echo pulses. The difference of the spectra from the two experiments then only contains contributions from *S* nuclei experiencing a dipolar coupling to *I* nuclei. In the case of an isolated I=½, S=½ spin pair, the resulting REDOR evolution data—in which the normalised signal intensity $(S_0-S)/S_0$ (cf. Figure 1)—is plotted as function of the dipolar evolution time $N\tau_R$ (N=number of rotor cycles; τ_R=rotor period)—exhibit a universal curve from which the heteronuclear dipolar coupling constant d (in Hz)

$$d = \frac{\hbar \mu_0 \gamma_I \gamma_S}{8\pi^2 r^3}. \quad (1)$$

and hence the internuclear distance can be readily obtained.[22] Such a situation can often be realised in biopolymers by a specific introduction of nuclear labels, for example, ^{13}C and ^{15}N. As a consequence, the major fraction of REDOR-related work has been devoted to the study of the

three-dimensional structure of biologically relevant systems, as has been recently reviewed by Grage and Watts[52] and by Gullion[53] in this book series.

Any departure from the isolated two-spin $I=½–S=½$ system entails severe complications in the data analysis. In the case of a quadrupolar nucleus, the dephasing efficiency strongly depends on the magnitude of the quadrupolar coupling; in case of multiple-spin interactions, the relative orientation of the internuclear vectors becomes an important parameter governing the shape of the REDOR evolution curves. In these cases, therefore, usually no universal REDOR curve can be applied to evaluate the dipolar couplings and internuclear distances. Principally, the evolution curves for multiple-spin systems can be calculated by a numerical evaluation of the Liouville–von Neumann equation; however, since the dimension of the spin matrix for an $S–I_n$ spin system is given by $(2S+1)\times(2I+1)^n$, the computation times with increasing n become quite large, especially with quadrupolar I nuclei involved. Thus, although in favourable cases a selective excitation of a single I nucleus in an $S–I_n$ spin system has been successfully demonstrated (θ-REDOR,[74,75] frequency-selective REDOR[76]), the case of multiple-spin interactions still poses some serious challenges.

An elegant solution to analyse the REDOR response in the presence of multiple-spin interactions was introduced by Eckert and co-workers.[77] As shown by the authors, the initial part of the REDOR evolution curves proves to be virtually independent on the exact spin geometry and distribution effects. Thus, when restricting the data analysis to $\Delta S/S_0$ values <0.3, the data can be analysed in terms of the second moment[78] defined by

$$M_2 = \frac{4}{15}\gamma_I^2\gamma_S^2\left(\frac{\mu_0}{4\pi}\right)^2\hbar^2 I(I+1)\sum_j r_{ij}^{-6}. \qquad (2)$$

Due to the independence on the spin geometry, this approach is found to be especially useful for the analysis of amorphous materials.[67,79–81] However, in the presence of strong heteronuclear dipolar couplings or limited MAS frequency, it is sometimes not possible to obtain enough REDOR data points needed for the second moment analysis. In these cases, the constant time version of REDOR, CT-REDOR, can be successfully applied, providing a calibration-free second moment analysis in the presence of multiple-spin interactions.[82] Apart from the possibility to obtain reliable second moments under these conditions, CT-REDOR offers the advantage of a roughly 50% time-saving over the conventional REDOR approach, since the reference intensity S_0 only has to be measured once. In the following section, we briefly recapitulate the theory of REDOR NMR spectroscopy and discuss the various facets of CT-REDOR; in the

third chapter, the various versions of CT-REDOR are validated employing a set of model compounds.

2. THEORY

2.1. REDOR spectroscopy

The dipolar interaction Hamiltonian under the conditions of MAS NMR is given as

$$\hat{H}_{\mathrm{DD,hetero}(t)} = -2C_{IS(\alpha,\beta,t)}\hat{I}_Z\hat{S}_Z, \tag{3}$$

with

$$C_{IS(\alpha,\beta,t)} = d\left(\frac{1}{2}\sin^2\beta\cos(2\alpha + 2\omega_R t) - \frac{1}{\sqrt{2}}\sin 2\beta\cos(\alpha + \omega_R t)\right). \tag{4}$$

The angles α and β define the orientation of the sample relative to the B_0-field; ω_R denotes the rotation frequency. For the REDOR reference experiment, the rotor-synchronised spin-echo experiment for the S nuclei (cf. Figure 1A), the dipolar Hamiltonian integrated over one rotor period T_R averages to zero

$$\left\langle \hat{H}_{\mathrm{DD,hetero}} \right\rangle = \frac{1}{T_R}\int_0^{T_R} \hat{H}_{\mathrm{DD,hetero}(t)}\mathrm{d}t = 0. \tag{5}$$

The acquired signal intensity then is only attenuated by transverse relaxation and therefore

$$S_0 = S_i \exp\left[-\frac{NT_R}{t}\right], \tag{6}$$

with S_i denoting the initial magnetization at $t=0$. If an additional train of rotor-synchronised π-pulses (every half rotor period) is applied to the I nuclei, then—in the case of perfect π-pulses and $I=½$—all I-spin states are inverted (i.e. a sign change in the dipolar Hamiltonian), resulting in a non-vanishing dipolar interaction.

$$\left\langle \hat{H}_{\mathrm{DD,hetero}} \right\rangle = \frac{1}{T_R}\left(\int_0^{T_R/2} \hat{H}_{\mathrm{DD,hetero}(t)}\,\mathrm{d}t - \int_{T_R/2}^{T_R} \hat{H}_{\mathrm{DD,hetero}(t)}\mathrm{d}t\right) \tag{7}$$

Thus, the heteronuclear dipolar information has been reintroduced into the MAS spin-echo experiment. The signal intensity follows from

$$S = S_i \exp\left[-\frac{NT_R}{t}\right]\cos(\Delta\varphi) \tag{8}$$

with the dipolar dephasing $\Delta\varphi$ defined as (for I-channel π-pulses at $T_R/2$)

$$\Delta\varphi = \int_0^{T_R/2} \omega_{DD(t)} dt - \int_{T_R/2}^{T_R} \omega_{DD(t)} dt, \tag{9}$$

with $\omega_{DD(t)} = \pm C_{IS(\alpha,\beta,t)}$. With this, summing over all possible orientations for a powdered sample, the following equation is obtained for the normalised difference intensity $(S_0 - S)/S_0 = \Delta S/S_0$:

$$\frac{\Delta S}{S_0} = 1 - \frac{1}{4\pi} \int_0^{2\pi} \int_0^{\pi} \cos\left(\frac{NT_R d}{\pi} \sqrt{2} \sin\alpha \sin 2\beta\right) \sin\beta d\alpha d\beta. \tag{10}$$

Since in the case of an isolated pair of spin ½ nuclei the dipolar dephasing, and hence the REDOR evolution curve, is exclusively governed by the dipolar Hamiltonian, the data analysis proves to be straightforward employing a universal REDOR curve, in which the normalised difference intensity $\Delta S/S_0$ is plotted as a function of the dimensionless product $NT_R \times d$.[23]

Approximate solutions derive from a series expansion of the cos-term in Equation (10), producing

$$\frac{\Delta S}{S_0} = \frac{15}{16} (NT_R)^2 d^2. \tag{11}$$

In the case of multiple-spin interactions, the second moment defined in Equation (2) may be approximated to first order by

$$M_2 = \frac{4}{15} 4\pi^2 I(I+1) \sum_j D_j^2, \tag{12}$$

and hence[77]

$$\frac{\Delta S}{S_0} = \frac{4}{3\pi^2} (NT_R)^2 M_2. \tag{13}$$

Thus, from a parabolic fit to the REDOR evolution data, the second moment can be evaluated. As mentioned in Section 1, this analysis has to be restricted to the initial part of the evolution curves $\Delta S/S_0 < 0.3$, as exemplified in Figure 2. However, the first order approximation entails a systematic underestimation of M_2, as shown by Bertmer and Eckert.[77]

Numerous variations of the original REDOR pulse sequence have been established to adapt the technique to specific needs. To account for pulse imperfections and other experimental errors, Chan and Eckert introduced compensated REDOR.[84] In this approach, an I-channel π-pulse in the centre of the pulse sequence cancels the reintroduction of the I–S dipolar couplings; hence the echo amplitudes are solely attenuated by the

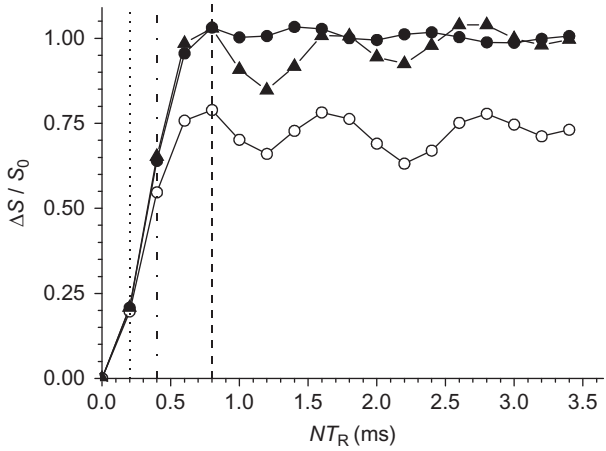

Figure 2 Simulated REDOR evolution curves for an $S–I_4$ five-spin system exhibiting tetrahedral geometry (filled circles), quadratic planar geometry (open circles) and an $S–I$ two-spin system (triangles). The dipolar coupling constant was chosen as 1150 Hz for a single $S–I$ interaction in the five-spin systems and 2299 Hz in the $S–I$ two-spin system, leading to M_2 values of $4.17 \times 10^7\,\mathrm{rad^2 s^{-2}}$ in all cases. All calculations were performed employing the SIMPSON simulation package.[83]

experimental imperfections. The $(S_0 - S)/S_0$ values are then corrected by the addition of a term $a \times (S_0 - S_D)/S_0$ (S_D denotes the echo intensity from the compensated REDOR experiment). The factor constitutes an empirical scaling factor which has been determined simulating the effect of pulse imperfections on the REDOR and compensated REDOR curves. For the data presented in [84] this parameter was always found to be close to unity but is unclear whether or not this proves to be a universal behaviour. Further modifications of REDOR, especially well suited for the analysis of three-spin interactions, are frequency-selective REDOR and q-REDOR, both introduced by Gullion.[74,76] Whereas in θ-REDOR only a fraction of the I spins is inverted employing I spin pulses with pulse lengths $<\pi$, in frequency-selective REDOR, a pair of $\pi/2$ pulses on the I-channel, separated by a time τ effectively, cancels the reintroduction of the dipolar coupling of a selected $S–I$ interaction simply by adjusting τ according to the offset of the selected I nucleus.[76]

2.2. Constant-time REDOR spectroscopy

Irrespective of the specific version of REDOR, as long as π-pulses every half rotor period constitute the pulse trains, the fast REDOR dephasing in the presence of very strong dipolar couplings entails severe problems in the data analysis. If the rotation frequency is limited by the NMR

hardware or by a CP step, then only rather few data points may be accessible in the important initial part of the REDOR curve. For these cases, CT-REDOR offers the possibility to evaluate the second moments in strongly coupled multiple-spin systems with an accuracy which proves to be distinctively higher as with the conventional REDOR approach.

In CT-REDOR, the dipolar evolution time is kept at a (small) constant value. [82,85] Then, either the position of the dephasing π-pulses (at $T_R/2$ in conventional REDOR, cf. Figure 1) is stepped through the rotation period (Variable Pulse Position, VPP) or the pulse lengths of these pulses are increased in steps from 0 to 2π (variable pulse duration, VPD). A combination of both approaches is possible as well. We note that the VPP scheme has already been mentioned in one of the first REDOR papers by Schaefer and Gullion,[21] without having been utilised for the evaluation of strong multiple couplings. As an additional benefit of CT-REDOR, the experimental time may be decreased roughly by 50%, since the reference intensity S_0 only needs to be measured once. The various versions of CT-REDOR will be presented in the following, together with results from numerical simulations. In the next section, the applicability of the various facets of CT-REDOR is exemplified on model compounds.

2.2.1. Variable pulse number (VPN)

This experiment was developed by Middleton et al.[85] and is quite similar to the original REDOR. Starting with a rotor-synchronised *S*-spin echo with an evolution time of several rotor periods, a successively increasing number of *I*-channel π-pulses are applied on the dephasing channel. As a consequence, the $\Delta S/S_0$ values increase from a value near zero to the value resulting from a conventional REDOR experiment with the same evolution time. This approach has been predominantly designed and utilised to benefit from the mentioned time-savings. Since the evolution time has to be set to several rotor periods, this variant seems less suitable for application in case of strong dipolar couplings.

2.2.2. Variable Pulse Position

In the CT-VPP-REDOR experiment (cf. Figure 3), the positions of the π-pulses on the *I*-channel which are applied at $T_R/2$ in conventional REDOR are changed stepwise over the complete rotor period, leading to but a partial reintroduction of the heteronuclear dipolar coupling. The resulting $\Delta S/S_0$ curve depends on the pulse position t_{PP} according to

$$\frac{\Delta S}{S_0} = 1 - \frac{1}{4\pi}\int_0^{2\pi}\int_0^{\pi} \cos\left(\frac{\pi d}{2\omega_R}\sin 2\alpha \sin^2\beta(\cos 2\omega_R t_{PP} - 1)\right.$$
$$\left. - \frac{\sqrt{2}\pi d}{\omega_R}\sin\alpha \sin 2\beta(\cos\omega_R t_{PP} - 1)\right) \sin\beta \mathrm{d}\alpha \mathrm{d}\beta. \qquad (14)$$

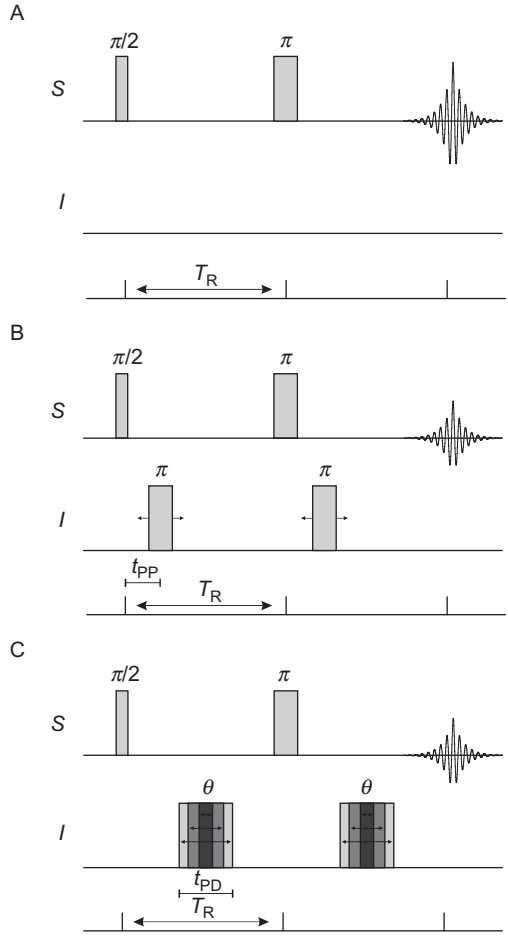

Figure 3 Pulse sequences for the different CT-REDOR versions for two rotor cycles (A) MAS spin-echo reference experiment; (B) CT-VPP-REDOR with the pulse position t_{PP} of the *I*-spin dephasing pulses stepped from 0 to T_R and (C) CT-VPD-REDOR with the pulse width t_{PD} of the *I*-spin dephasing pulses stepped from 0 to 2π.

A plot of the resulting $\Delta S/S_0$ values versus t_{PP}/T_R produces symmetric evolution curves with a maximum at $t_{PP}/T_R=0.5$.

Figure 4 shows the results of a simulation of CT-VPP-REDOR evolution curves calculated for the two different S–I_4 five-spin systems and the S–I two-spin system from Figure 2. Again the distances were chosen so that the resulting second moments as calculated employing Equation (12) are identical for the five-spin and the two-spin systems. As expected, the $\Delta S/S_0$ values at $t_{PP}/T_R=0.5$ match the data points of the REDOR curves (cf. Figures 2 and 4).

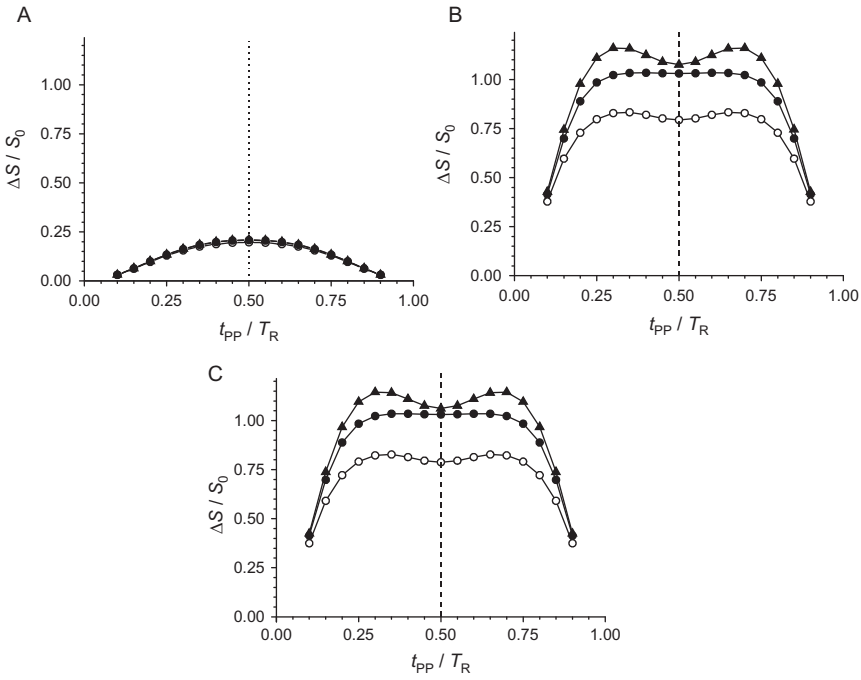

Figure 4 Simulated CT-VPP-REDOR evolution curves for a fictive $S–I_4$ five-spin system exhibiting tetrahedral geometry (filled circles), quadratic planar geometry (open circles) and a fictive $S–I$ two-spin system (triangles; $S=^{13}C$; $I=^{31}P$). The dipolar coupling constants were chosen as 1150 Hz for a single $S–I$ interaction in the five-spin systems and 2299 Hz in the $S–I$ two-spin system, leading to M_2 values of 4.17×10^7 rad^{2}s^{-2} in all cases. (A): $\nu_R=10{,}000$ Hz, $N=2$; (B) $\nu_R=10000$ Hz, $N=8$ and (C) $\nu_R=2500$ Hz, $N=2$.

As with conventional REDOR, the shape of the CT-VPP-REDOR evolution curves proves to be independent of the spin geometry for $\Delta S/S_0 \leq 0.3$ (cf. Figure 4A). At longer evolution times, however, the characteristic geometry-dependent oscillations can be clearly observed, in analogy to the REDOR experiment. Comparing Figure 4B and C, it is clear that the resulting $\Delta S/S_0$ values are exclusively dependent on the total evolution time and independent on the spinning speed.

2.2.3. Variable pulse duration

In this variant of CT-REDOR (cf. Figure 3C), the duration of the I-channel dephasing pulses t_{PD} is stepped from 0 to 2π while keeping the evolution time constant. This concept is quite similar to the θ-REDOR approach developed by Gullion and Pennington[74] but serves a different purpose. While the latter experiment aims at the determination of individual coupling constants in multiple-spin systems, the CT-VPD-REDOR enables

the facile measurements of second moments in systems with strong dipolar couplings. Due to the application of θ-pulses instead of π-pulses to the I nuclei, only a fraction $(1-\cos\theta)/2$ of the I spins is found to undergo a change of the spin state.

Upon a systematic variation of the pulse length between 0 and 2π with constant evolution time and pulse position, the fraction of I spins contributing to the actual dephasing increases up to a pulse length of π. With this pulse length, all S-spins change their spin states and the same dephasing as in conventional REDOR is achieved. For pulse lengths between π and 2π, the dephasing curve can be obtained by $(\Delta S/S_0)(\theta) = (\Delta S/S_0)(\pi-\theta)$. The responses of the three model spin systems, quadratic S–I_4, tetrahedral S–I_4 and S–I two spin, plotted as a function of the pulse length $t_{PD}/2\pi$, are compiled in Figure 5. The maxima of these curves at $t_{PD}/2\pi = 0.5$ correspond to the data points of the respective REDOR curve (cf. Figures 2 and 5).

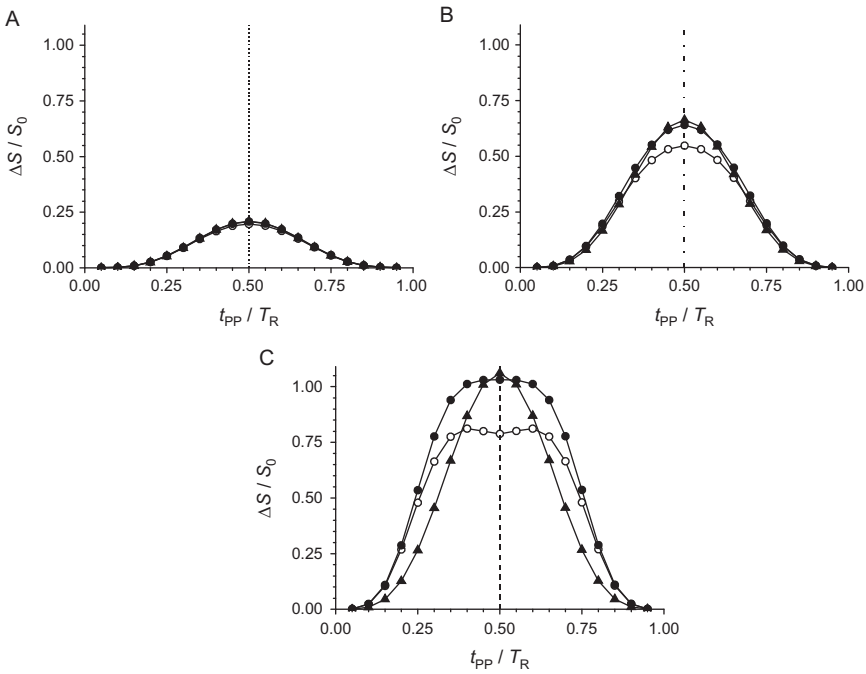

Figure 5 Simulated CT-VPD-REDOR evolution curves for a fictive S–I_4 five-spin system exhibiting tetrahedral geometry (filled circles), quadratic planar geometry (open circles) and a fictive S–I two-spin system (triangles; $S = {}^{13}C$; $I = {}^{31}P$). The dipolar coupling constants were chosen as 1150 Hz for a single S–I interaction in the five-spin systems and 2299 Hz in the S–I two-spin system, leading to M_2 values of 4.17×10^7 rad^2 s^{-2} in all cases. (A): $\nu_R = 10{,}000$ Hz, $N = 2$; (B) $\nu_R = 5000$ Hz, $N = 2$ and (C) $\nu_R = 2500$ Hz, $N = 2$.

As for CT-VPP-REDOR, for dipolar evolution times with a maximum DS/S_0 value < 0.3, the shape of the CT-VPD-REDOR curves only depends on the M_2-values and proves to be independent of the spin geometry. For longer evolution times, corresponding to the plateau region of the conventional REDOR curve, however, the evolution curves for the *S*–*I* two spin and the *S*–I_4 five spin exhibit clear differences even at low $\Delta S/S_0$ values. While all curves are symmetric, the response of the two-spin system is found to exhibit a much narrower plateau (cf. Figure 5C). As obvious from this figure, in this case the two-spin approximation does not constitute a suitable model to evaluate the second moments for the multiple-spin interactions. This peculiar behaviour can be traced back to the contribution of spin configurations to the dephasing, which in the case of *I*-spin π-pulses would not contribute due to the mutual cancellation of the dipolar effects within this spin configuration.

This can be best illustrated on a linear three-spin configuration. The two individual dipolar *S*–*I* couplings cancel each other in one half of all the spin combinations, entailing a REDOR curve (applying π-pulses for the *I* spins) levelling at a $\Delta S/S_0$ value of 0.5. These ''silent'' specific spin configurations will contribute to the dephasing, if only a fraction of the *I* spins changes its spin state. This is illustrated in Figure 6, in which the dipolar evolution curves for θ-REDOR for an *S*–*I* two-spin and a linear *S*–I_2 three-spin system (with identical M_2 values) for different pulse angles are compared.

In case of the two-spin system, the $\Delta S/S_0$ values for a given evolution time decrease in synchrony with an increasing deviation of the applied pulse length from π. However, for the linear three-spin system, the $\Delta S/S_0$ values for pulse lengths between 90° and 150° surpass those obtained for applied *I*-spin π-pulses, exemplifying the stronger dephasing upon incomplete inversion of spin states in the three-spin system. We note a variation of the pulse lengths from 0 to 2π—in essence a CT-VPD-REDOR experiment—has been performed by Gullion [24] to illustrate the effect of pulse length missets on the dephasing behaviour.

2.2.4. Variable pulse duration and position (VPDP)

For the sake of completeness, we note that the two approaches described above, VPD and VPP, may be combined, which may be useful for spin systems with extremely strong dipolar interactions. The $\Delta S/S_0$ values as a function of pulse position t_{PP} and duration t_{PD} are plotted in Figure 7 for the *S*–*I* two-spin system (Figure 7A and B) and for the tetrahedral *S*–I_4 five-spin system (Figure7C). Here, the difference between the responses for the two-spin and multiple-spin system with identical M_2 value due to the contribution of the ''silent'' spin geometries for *I*-spin pulse lengths deviating from π and evolution times corresponding to the plateau region of the conventional REDOR curve is even more pronounced. This is

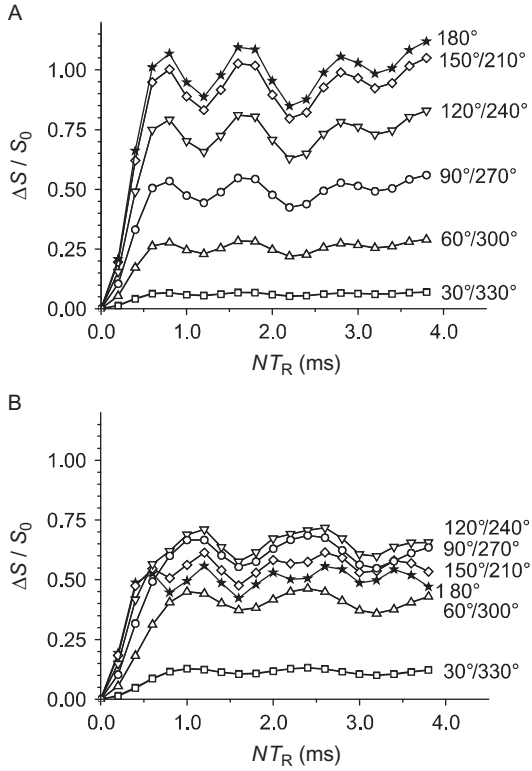

Figure 6 Simulated θ-REDOR evolution curves for a fictive *S–I* two-spin system (A) and linear $S–I_2$ three-spin system (B) for the indicated pulse lengths ($\nu_R = 10{,}000$ Hz, $S = {}^{13}C$; $I = {}^{31}P$). The dipolar coupling constants were chosen as 1626 Hz for a single *S–I* interaction in the three-spin systems and 2299 Hz in the *S–I* two-spin system, leading to M_2 values of 4.17×10^7 rad^2 s^{-2} in both cases. The θ-REDOR version with a single dephasing pulse of length θ was employed.[74]

illustrated in Figure 7D, in which the response at a constant *I*-spin pulse length of $0.15/2\pi$ is demonstrated for the *S–I* two- and $S–I_4$ five-spin system. Again, under these experimental conditions, the two-spin approximation cannot be employed for the evaluation of the second moments for multiple-spin interactions.

3. EXPERIMENTS ON MODEL COMPOUNDS

To validate the CT-REDOR concept, the experiments described above were performed on different model compounds with known structure. As an example for a two-spin system, doubly labelled glycine (^{15}N, $^{13}C_2$

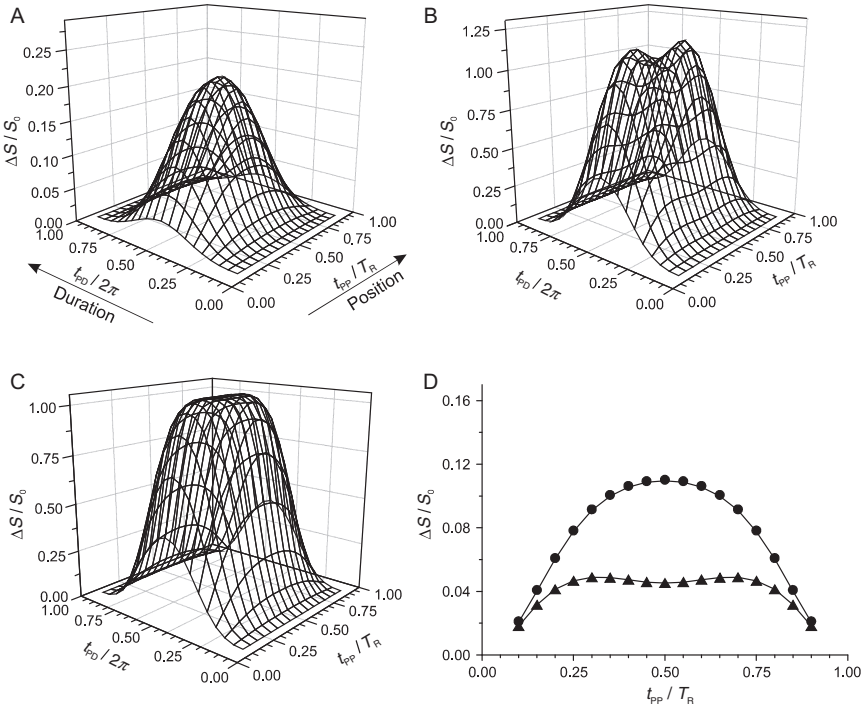

Figure 7 Simulated CT-VPDP-REDOR evolution surfaces for (A) a fictive *S–I* two-spin system: $N=2$; $\nu_R=10{,}000$ Hz; (B) a fictive *S–I* two-spin system: $N=2$; $\nu_R=2500$ Hz; (C) a tetahedral $S–I_4$ five-spin system: $N=2$; $\nu_R=2500$ Hz. $S={}^{13}C$; $I={}^{31}P$. In (D) the VPDP slices ($N=2$; $\nu_R=2500$ Hz at $t_{PD}/2\pi=0.15$) obtained from (B) and (C) are plotted for the two different spin systems (circles: $S–I_4$ five-spin system; triangles: *S–I* two-spin system). Again, the dipolar coupling constants were chosen as 1150 Hz for a single *S–I* interaction in the five-spin system and 2299 Hz in the *S–I* two-spin system, leading to M_2 values of $4.17\times10^7\,\mathrm{rad^2\,s^{-2}}$ in both cases.

glycine) was investigated. The C—N-bond length[86,87] of 1.49 Å translates into a dipolar coupling constant of 926 Hz and an M_2-value of $6.77\times10^6\,\mathrm{rad^2\,s^{-2}}$. $Al(PO_3)_3$[88] and BPO_4[89] constitute examples for multiple-spin systems. In $Al(PO_3)_3$, six phosphorous atoms are found in the second coordination sphere of aluminium in a distance of 3.13 Å (3×) and 3.42 Å (3×), respectively (cf. Figure 8A). In BPO_4, the second coordination sphere is composed of four phosphorous atoms each in a distance of 2.73 Å (cf. Figure 8B). The resulting heteronuclear second moments, taking into account the $^{27}Al–^{31}P$ ($^{11}B–^{31}P$) dipolar interactions within a 5 Å sphere, are 6.77×10^6 and $1.87\times10^7\,\mathrm{rad^2\,s^{-2}}$ for $Al(PO_3)_3$ and BPO_4, respectively.

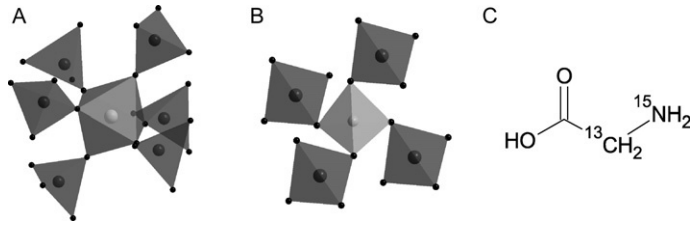

Figure 8 Samples used for the validation of the various CT-REDOR approaches. (A) and (B): second coordination sphere of Al in $Al(PO_3)_3$ (A) and B in BPO_4 (B) as examples for an $S–I_6$ and $S–I_4$ multiple-spin system with strong dipolar coupling; (C): doubly labelled glycine (in a 9:1 mixture unlabelled/labelled glycine) as an example for an isolated two-spin system.

3.1. $Al(PO_3)_3$

The CT-REDOR behaviour for $Al(PO_3)_3$ was studied as an example for a strong multiple-spin interaction. The REDOR evolution curves for conventional REDOR, compensated REDOR and for a REDOR experiment in which a CRAMPS rotor was used to improve the RF homogeneity are plotted in Figure 9A. As exemplified by the data, even for a rotation speed of 10 kHz, only a few data points are available for the second moment analysis. Employing the parabolic approximation, a second moment of $M_2 = 3.5 \times 10^6 \text{rad}^2\text{s}^{-2}$ is obtained for the REDOR experiment, whereas a value of $M_2 = 4.6 \times 10^6 \text{rad}^2\text{s}^{-2}$ is obtained employing the compensated REDOR approach.[84] As obvious from Figure 9, the improvement in the RF homogeneity indeed entails second moment values closer to the theoretical value ($M_2 = 5.3 \times 10^6 \text{rad}^2\text{s}^{-2}$), even better than the result obtained from the compensated REDOR approach. In Figures 9B and C, the results of a CT-VPP-REDOR (Figure 9B) and a CT-VPD-REDOR experiment on Al $(PO_3)_3$ are presented. Here, the evaluation of the second moment, employing the SIMPSON software[83] and applying the two-spin approximation as outlined in the previous section, results in M_2 values of $5.8 \times 10^6 \text{rad}^2\text{s}^{-2}$ (86% of the theoretical value), in considerably better agreement with the theoretical value than the values obtained from the analysis of the REDOR curves. Figure 9D finally presents the results of a combined CT-VPDP-REDOR experiment, varying the pulse position and the pulse length, together with a simulation assuming a second moment of $5.8 \times 10^6 \text{rad}^2\text{s}^{-2}$. The results convincingly illustrate the advantage of CT-REDOR over the conventional REDOR approach.

3.2. BPO_4

The CT-REDOR data for BPO_4 is collected in Figure 10. The data illustrates the influence of the dipolar evolution time chosen for the CT-VPP-REDOR experiment and demonstrates the effect of the compensation

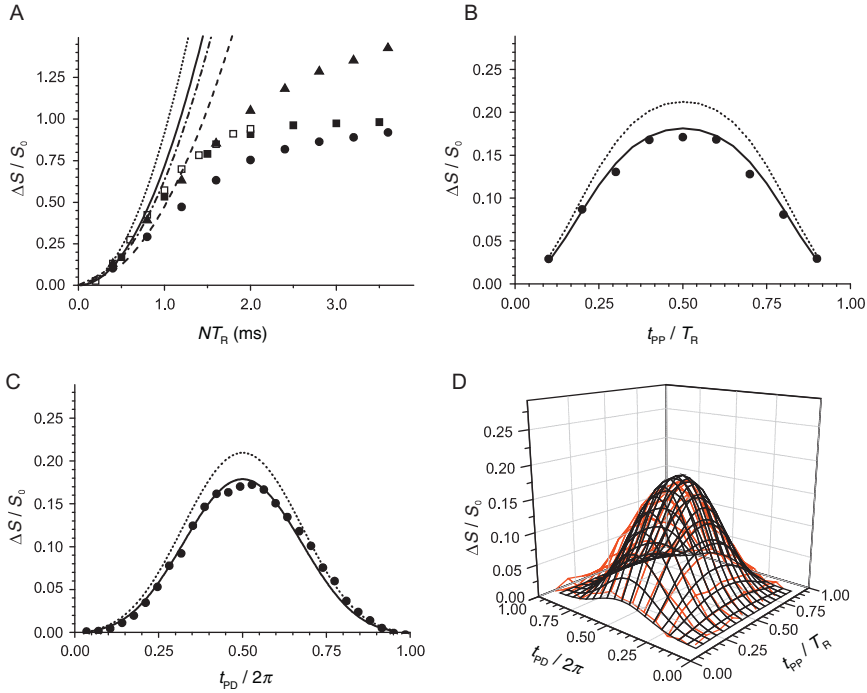

Figure 9 (A) $^{27}Al\{^{31}P\}$-REDOR evolution curves for $Al(PO_3)_3$: filled circles: conventional REDOR; filled triangles: compensated REDOR; squares: REDOR data obtained employing a CRAMPS rotor at 4000 Hz (filled) and at 10,000 Hz (open). The lines represent parabolic fits to the REDOR curves assuming second moments of $3.5 \times 10^6\,rad^2s^{-2}$ (dashed), $4.6 \times 10^6\,rad^2s^{-2}$ (dashed-dotted), $5.3 \times 10^6\,rad^2s^{-2}$ (solid). (B) and (C) VPP- (B) and VPD- (C) CT-REDOR data (filled circles) for $Al(PO_3)_3$: $N=2$; $\nu_R=4$ kHz. The solid lines represent a simulation of the data employing the two-spin approximation and assuming an M_2 value of $5.8 \times 10^6\,rad^2s^{-2}$. The dotted lines in (A)–(C) represent the result of simulations employing the theoretical M_2 value of $6.77 \times 10^6\,rad^2s^{-2}$. (D) CT-VPDP-REDOR together with the simulation assuming $M_2=5.8 \times 10^6\,rad^2s^{-2}$.

technique on the resulting M_2 values. As with the data on $Al(PO_3)_3$, the data on BPO_4 for small evolution times clearly shows that the CT-REDOR approach produces an M_2 value ($1.77 \times 10^7\,rad^2s^{-2}$; employing the two-spin approximation), which proves to be much closer to the theoretical value as the value ($1.4 \times 10^7\,rad^2s^{-2}$), resulting from a parabolic fit to the REDOR curves (cf. Figure 8A). With increasing dipolar evolution times, however, the accumulation of experimental imperfections in combination with the effect of the first order approximation of M_2 entails a successive underestimation of the second moment (cf. Table 1).

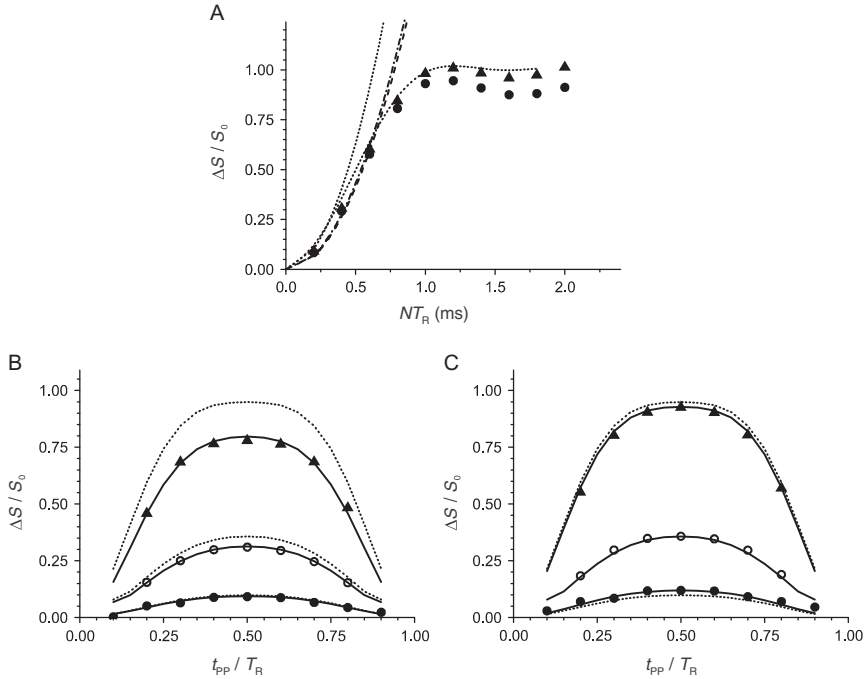

Figure 10 (A) $^{11}B\{^{31}P\}$-REDOR evolution curves for BPO_4. Filled circles: conventional REDOR; filled triangles: compensated REDOR. The lines represent parabolic fits to the REDOR curves assuming second moments of 1.4×10^7 rad^{2}s^{-2} (dashed) and 1.6×10^7 rad^2 s^{-2} (dashed-dotted). (B) Results of VPP-CT-REDOR for $N=2$ (full circles), $N=4$ (open circles) and $N=8$ (triangles) together with simulations applying the two-spin approximation. The solid lines correspond to M_2 values of $M_2=1.77 \times 10^7$ rad^{2}s^{-2}($N=2$), 1.60×10^7 rad^{2}s^{-2} ($N=4$) and 1.34×10^7 rad^{2}s^{-2}($N=8$); (C) results of compensated VPP-CT-REDOR for $N=2$ (full circles), $N=4$ (open circles) and $N=8$ (triangles) together with simulations applying the two-spin approximation. The solid lines correspond to M_2 values of $M_2=2.02 \times 10^7$ rad^{2}s^{-2}($N=2$), 1.87×10^7 rad^{2}s^{-2} ($N=4$) and 1.77×10^7 rad^{2}s^{-2} ($N=8$). In (B) and (C), the dashed lines correspond to a two-spin calculation employing the theoretical M_2 value of 1.87×10^7 rad^{2}s^{-2}.

The data for the compensated CT-VPP-REDOR curves exhibits a similar trend, a decrease of the M_2 values with increasing value for the dipolar evolution time (cf. Table 1). For the compensated CT-VPP-REDOR approach, however, the data for short evolution times ($N=2$) produces an M_2 value slightly higher than the theoretical value, whereas the data for $N=8$ entails an M_2 value smaller than the theoretical value. Thus, the compensation technique tends to overcompensate the experimental imperfections at low evolution times, whereas it leads to an undercompensation at longer evolution times. This behaviour may be the

TABLE 1 Second moments (in $rad^2 s^{-2}$) as calculated from simulations of the CT-VPP-REDOR data in Figure 10B and C employing the two-spin approximation and the full five-spin calculation

	Two-spin approximation		Full five-spin calculation	
	CT-VPP-REDOR	Compensated CT-VPP-REDOR	CT-VPP-REDOR	Compensated CT-VPP-REDOR
$N=2$	1.77×10^7	2.02×10^7	1.77×10^7	2.26×10^7
$N=4$	1.60×10^7	1.87×10^7	1.64×10^7	1.95×10^7
$N=8$	1.34×10^7	1.77×10^7	1.46×10^7	2.08×10^7

consequence of the uncertainty in the evaluation of the scaling factor a as outlined in Ref. 84. Considering this uncertainty and the inability to predict the dipolar evolution times for which the compensation technique works best, the uncompensated CT-REDOR approach can be identified as the best strategy for an accurate evaluation of second moments. Of course, it is possible to obtain M_2 values in even better harmony with the theoretical values when analysing the data employing the exact geometry of the spin geometry. The improvement, most prominent at longer dipolar evolution times (cf. Table 1), however, proves to be only marginal in the case of short dipolar evolution times.

The data for the doubly labeled glycine sample serves the purpose to validate the oscillatory behavior found in the CT-REDOR responses at longer evolution times (cf. e.g. Figs. 4b and 7b). For the experiments a diluted sample 9 glycine : 1 ^{13}C,^{15}N glycine was used. As a consequence, the REDOR data has to be corrected for the signal response of the ^{13}C nuclei from the unlabelled glycine.[90] All REDOR data presented here was obtained employing SW TPPM ^1H decoupling,[91] one of the most efficient proton decoupling techniques available to date. However, as obvious from Fig. 11, the REDOR data is still biased by residual ^1H ^{13}C dipolar coupling within the $^{13}CH^2$ group. This bias increases with decreasing MAS frequency (see, e.g., the REDOR data at an evolution time of 2ms, for which the $\Delta S/S_0$ value for $\nu_R=15$kHz adopts a value of 0.9, whereas for $\nu_R=1$kHz $\Delta S/S_0$ is found as 0.8). This bias complicates the data analysis: optimising the simulation to fit the oscillations at longer evolution times produces dipolar coupling constants in synchrony with the theoretical value; an optimization with respect to the data points $0\leq\Delta S/S_0\leq0.7$—as is usually done—entails an underestimation of the dipolar couplings, especially at slow MAS speeds. Since the experimental validation of the CT-VPDP-REDOR surface in Figure 7B necessitates very slow spinning speeds, the simulation results in Figure 11D and E were scaled by the ratio $\Delta S/S_0(\nu_R=15\text{kHz})/\Delta S/S_0(\nu_R=1\text{kHz})$. The CT-VPP and VPD

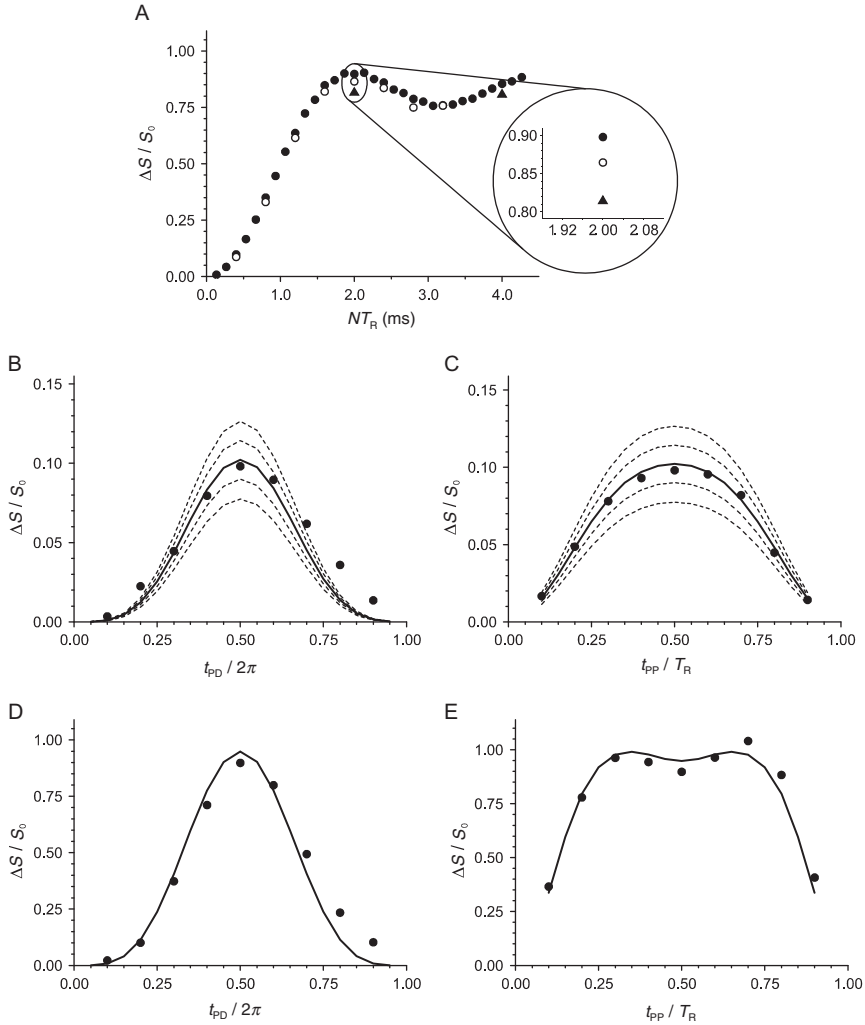

Figure 11 $^{13}C\{^{15}N\}$-REDOR data for a 9:1 mixture of unlabelled glycine $^{15}N,^{13}C_2$-glycine; (A) conventional REDOR employing spinning speeds of 15 kHz (filled circles); 5 kHz (open circles) and 1 kHz (triangles), respectively. (B) CT-VPD-REDOR data (filled circles) at $\nu_R = 5$ kHz together with simulations assuming (from top to bottom) $M_2 = 6.77 \times 10^6\,\mathrm{rad^2\,s^{-2}}$ (100%), 90%, 80%, 70% and 60%, that is, the solid line corresponds to an M_2 of $5.5 \times 10^6\,\mathrm{rad^2\,s^{-2}}$; (C) CT-VPP-REDOR data employing the same arrangement as in (B); (D) CT-VPD-REDOR data (filled circles) at $\nu_R = 1$ kHz together with a simulation assuming $M_2 = 5.8 \times 10^6\,\mathrm{rad^2\,s^{-2}}$; (E) CT-VPP-REDOR data (filled circles) at $\nu_R = 1$ kHz together with a simulation assuming $M_2 = 5.8 \times 10^6\,\mathrm{rad^2\,s^{-2}}$.

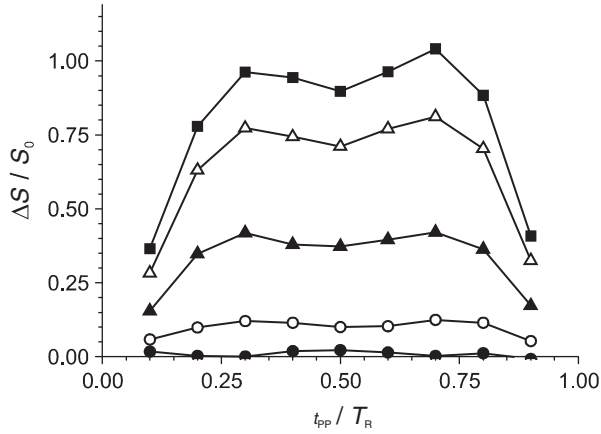

Figure 12 $^{13}C\{^{15}N\}$ VPDP-CT-REDOR data ($N=2$, $\nu_R=1000$ Hz) for a 9:1 mixture of unlabelled glycine $^{15}N,^{13}C_2$-glycine. Data points correspond to slices along $t_{PD}=0.2\pi$ (filled circles), 0.4π (open circles), 0.6π (filled triangles), 0.8π (open triangles) and π (filled squares).

data presented in Figure 11B (VPD) and C (VPP) produce an $M_2=5.5\times10^6$ rad^{2}s^{-2}, which translates into an internuclear distance of 1.55 Å. In Figure 11D and E, the CT-VPD- and CT-VPP-REDOR experiments are shown for $N=2$ and $\nu_R=1$ kHz.

The observed CT-VPP-REDOR data confirms the expected general behaviour and can be best simulated assuming a second moment of 5.8×10^6 rad^{2}s^{-2}. Interestingly, in CT-VPDP-REDOR, this oscillatory behaviour can be observed even at low maximum $\Delta S/S_0$ values, which can be adjusted via the θ-pulse length. This is shown in Figure 12, in which the slices taken from a CT-VPDP-REDOR experiment on the glycine sample for five different θ pulse lengths are collected.

4. CONCLUSION AND OUTLOOK

As shown in the preceding two sections, the constant time version of REDOR, CT-REDOR, may be applied as an expedient alternative to the existing REDOR versions in the presence of strong heteronuclear dipolar couplings. In these cases, only few data points are available for the data analysis, which especially in the case of multiple-spin systems renders an evaluation of the second moments impossible. The efficiency of the dipolar recoupling may be intentionally reduced either via a dislocation of the dephasing π-pulses from the centre of the rotor period or via an application of non-π-dephasing pulses. A variation of the pulse position t_{PP}

(CT-VPP-REDOR) or the pulse duration t_{PD} (CT-VPD-REDOR) then produces CT-REDOR curves, from which the second moment may be evaluated with distinctively superior accuracy as compared to the values obtained from a parabolic fit to the conventional REDOR data. When restricting the experiment to short dipolar evolution times, the two-spin approximation may be applied for the data analysis, which proves to be especially attractive for amorphous solids, for which the exact spin geometry is unknown. The data presented on the model compounds illustrate the various facets of CT-REDOR NMR spectroscopy. First application examples, namely, the evaluation of the heteronuclear ^{6}Li–^{7}Li dipolar couplings within the garnet structure of $Li_5La_3Nb_2O_{12}$,[82,92] the determination of the internuclear ^{11}B–^{31}P distance in frustrated Lewis pairs,[93,94] the analysis of ^{23}Na–^{19}F dipolar interaction in fluormica[95] or ^{23}Na–^{31}P or ^{27}Al–^{31}P connectivity in sodium(alumino)phosphate glasses[96] illustrate the usefulness of this extension of REDOR spectroscopy.

REFERENCES

1. M. J. Duer, Solid-state NMR studies of molecular motion, *in*: Annual Reports on NMR Spectroscopy, G. A. Webb (ed.), 2006, Vol. 59, Academic Press, London, pp. 41–116.
2. D. D. Laws, H. M. L. Bitter and A. Jerschow, *Angew. Chem. Int. Ed.*, 2002, **41,** 3096–3129.
3. S. P. Brown and H. W. Spiess, *Chem. Rev.*, 2001, **101,** 4125–4155.
4. A. McDermott and T. Polenova, *Curr. Opin. Struct. Biol.*, 2007, **17,** 617–622.
5. F. Bertocchi and M. Paci, *J. Agric. Food Chem.*, 2008, **56,** 9317–9327.
6. M. Edgar, *Annu. Rep. Prog. Chem., Sect. B*, 2009, **105,** 340–362.
7. C. Gröger, K. Lutz and E. Brunner, *Prog. Nucl. Magn. Reson. Spectrosc.*, 2009, **54,** 54–68.
8. M. Kaupp and F. H. Köhler, *Coord. Chem. Rev.*, 2009, **253,** 2376–2386.
9. U. Scheler, *Curr. Opin. Colloid Interface Sci.*, 2009, **14,** 212–215.
10. M. Attila, S. Zsófia and D. Adam, *Acta Pharm. Hung.*, 2010, **80,** 18–45.
11. T. Blasco, *Chem. Soc. Rev.*, 2010, **39,** 4685–4702.
12. A. S. Borisov, P. Hazendonk and P. G. Hayes, *J. Inorg. Organomet. Polymer. Mater.*, 2010, **20,** 183–212.
13. S. Paasch and E. Brunner, *Anal. Bioanal. Chem.*, 2010, **398,** 2351–2362.
14. M. Renault, A. Cukkemane and M. Baldus, *Angew. Chem. Int. Ed.*, 2010, **49,** 8346–8357.
15. D. P. Raleigh, M. H. Levitt and R. G. Griffin, *Chem. Phys. Lett.*, 1988, **146,** 71–76.
16. R. Tycko and G. Dabbagh, *Chem. Phys. Lett.*, 1990, **173,** 461–465.
17. A. E. Bennett, J. H. Ok, R. G. Griffin and S. Vega, *J. Chem. Phys.*, 1992, **96,** 8624–8627.
18. D. M. Gregory, D. J. Mitchell, J. A. Stringer, S. Kiihne, J. C. Shiels, J. Callahan, M. A. Mehta and G. P. Drobny, *Chem. Phys. Lett.*, 1995, **246,** 654–663.
19. M. Carravetta, M. Edén, X. Zhao, A. Brinkmann and M. H. Levitt, *Chem. Phys. Lett.*, 2000, **321,** 205–215.
20. A. Brinkmann, M. Edén and M. H. Levitt, *J. Chem. Phys.*, 2000, **112,** 8539–8554.
21. T. Gullion and J. Schaefer, *J. Magn. Reson.*, 1989, **81,** 196–200.
22. T. Gullion and M. S. Conradi, *J. Magn. Reson.*, 1990, **86,** 39–45.
23. Y. Pan, T. Gullion and J. Schaefer, *J. Magn. Reson.*, 1990, **90,** 330–340.
24. T. Gullion, *Concepts Magn. Reson.*, 1998, **10,** 277–289.
25. E. R. H. van Eck and W. S. Veeman, *Solid State Nucl. Magn. Reson.*, 1993, **2,** 307–315.
26. K. T. Mueller, *J. Magn. Reson. A*, 1995, **113,** 81–93.

27. L. Van Wüllen, L. Züchner, W. Müller-Warmuth and H. Eckert, *Solid State Nucl. Magn. Reson.*, 1996, **6,** 203–212.
28. T. Gullion, *Magn. Reson. Rev.*, 1997, **17,** 83–131.
29. T. Gullion and J. Schaefer, *J. Magn. Reson.*, 1991, **92,** 439–442.
30. C. P. Grey and W. S. Veeman, *Chem. Phys. Lett.*, 1992, **192,** 379–385.
31. M. Kalwei and H. Koller, *Solid State Nucl. Magn. Reson.*, 2002, **21,** 145–157.
32. C. P. Grey and A. J. Vega, *J. Am. Chem. Soc.*, 1995, **117,** 8232–8242.
33. H. M. Kao and C. P. Grey, *J. Phys. Chem.*, 1996, **100,** 5105–5117.
34. T. Schaller, C. Rong, M. J. Toplis and H. Cho, *J. Non-Cryst. Solids*, 1999, **248,** 19–27.
35. L. Van Wüllen and M. Kalwei, *J. Magn. Reson.*, 1999, **139,** 250–257.
36. T. Gullion, *Chem. Phys. Lett.*, 1995, **246,** 325–330.
37. L. Van Wüllen, U. Müller and M. Jansen, *Chem. Mater.*, 2000, **12,** 2347–2352.
38. E. Hughes, T. Gullion, A. Goldbourt, S. Vega and A. J. Vega, *J. Magn. Reson.*, 2002, **156,** 230–241.
39. L. Van Wüllen and G. Schwering, *Solid State Nucl. Magn. Reson.*, 2002, **21,** 134–144.
40. E. Nimerovsky and A. Goldbourt, *J. Magn. Reson.*, 2010, **206,** 52–58.
41. T. Gullion, K. Yamauchi, M. Okonogi and T. Asakura, *Macromolecules*, 2007, **40,** 1363–1365.
42. C. A. Fyfe, K. T. Mueller, H. Grondey and K. C. Wong-Moon, *Chem. Phys. Lett.*, 1992, **199,** 198–204.
43. A. W. Hing, S. Vega and J. Schaefer, *J. Magn. Reson. A*, 1993, **103,** 151–162.
44. C. A. Klug and J. Schaefer, *J. Magn. Reson. B*, 1996, **110,** 176–181.
45. C. A. Fyfe, A. R. Lewis and J. M. Chézeau, *Can. J. Chem.*, 1999, **77,** 1984–1993.
46. C. P. Jaroniec, C. Filip and R. G. Griffin, *J. Am. Chem. Soc.*, 2002, **124,** 10728–10742.
47. K. Riedel, J. Leppert, O. Ohlenschläger, M. Görlach and R. Ramachandran, *J. Biomol. NMR*, 2005, **31,** 49–57.
48. J. P. Amoureux, J. Trébosc and G. Tricot, *Magn. Reson. Chem.*, 2007, **45,** S187–S191.
49. S. M. Holl, G. R. Marshall, D. D. Beusen, K. Kociolek, A. S. Redlinski, M. T. Leplawy, R. A. McKay, S. Vega and J. Schaefer, *J. Am. Chem. Soc.*, 1992, **114,** 4830–4833.
50. D. D. Mueller, A. Schmidt, K. L. Pappan, R. A. McKay and J. Schaefer, *Biochemistry*, 1995, **34,** 5597–5603.
51. S. Jehle, M. Falb, J. P. Kirkpatrick, H. Oschkinat, B. J. Van Rossum, G. Althoff and T. Carlomagno, *J. Am. Chem. Soc.*, 2010, **132,** 3842–3846.
52. S. L. Grage and A. Watts, *in*: Annual Reports on NMR Spectroscopy, G. A. Webb (ed.), 2006, Vol. 60, Academic Press, London, pp. 191–228.
53. T. Gullion, *in*: Annual Reports on NMR Spectroscopy, A. W. Graham (ed.), 2009, Vol. 65, Academic Press, London, pp. 111–137.
54. S. Macholl, I. Sack, H. H. Limbach, J. Pauli, M. Kelly and G. Buntkowsky, *Magn. Reson. Chem.*, 2000, **38,** 596–603.
55. S. Matsuoka and M. Inoue, *Chem. Commun.*, 5664–5675.
56. M. Zeyer-Düsterer, L. Montagne, G. Palavit and C. Jäger, *Solid State Nucl. Magn. Reson.*, 2005, **27,** 50–64.
57. D. Franke, R. Maxwell, D. Lathrop and H. Eckert, *J. Am. Chem. Soc.*, 1991, **113,** 4822–4830.
58. L. Van Wüllen and M. Jansen, *J. Mater. Chem.*, 2001, **11,** 223–229.
59. C. Bischoff, H. Eckert, E. Apel, V. M. Rheinberger and W. Höland, *Phys. Chem. Chem. Phys.*, 2011, **13,** 4540–4551.
60. L. Van Wüllen and M. Jansen, *Solid State Nucl. Magn. Reson.*, 2005, **27,** 90–98.
61. L. Zhang, J. C. C. Chan, H. Eckert, G. Helsch, L. P. Hoyer and G. H. Frischat, *Chem. Mater.*, 2003, **15,** 2702–2710.
62. S. Wegner, L. van Wüllen and G. Tricot, *Solid State Sci.*, 2010, **12,** 428–439.
63. L. van Wüllen, G. Tricot and S. Wegner, *Solid State Nucl. Magn. Reson.*, 2007, **32,** 44–52.
64. L. Van Wüllen, S. Wegner and G. Tricot, *J. Phys. Chem. B*, 2007, **111,** 7529–7534.

65. T. Emmler, O. Tsetsgee, G. Buntkowsky, M. Weinmann, F. Aldinger and K. Müller, *Soft Mater.*, 2006, **4,** 207–225.
66. B. Chen, W. Z. Ulrike, M. L. F. Nascimento, L. Ghussn, E. D. Zanotto and J. W. Zwanziger, *J. Phys. Chem. C*, 2009, **113,** 20725–20732.
67. H. Eckert, S. Elbers, J. Epping, M. Janssen, M. Kalwei, W. Strojek and U. Voigt, *in*: New Techniques in Solid-State NMR, J. Klinowski (ed.), 2005, Vol. 246, Springer, Berlin/ Heidelberg, pp. 195–233.
68. D. R. Studelska, L. M. McDowell, M. P. Espe, C. A. Klug and J. Schaefer, *Biochemistry*, 1997, **36,** 15555–15560.
69. J. M. Goetz, B. Poliks, D. R. Studelska, M. Fischer, K. Kugelbrey, A. Bacher, M. Cushman and J. Schaefer, *J. Am. Chem. Soc.*, 1999, **121,** 7500–7508.
70. S. Ganapathy, M. Fournier, J. F. Paul, L. Delevoye, M. Guelton and J. P. Amoureux, *J. Am. Chem. Soc.*, 2002, **124,** 7821–7828.
71. A. Naito, M. Kamihira, R. Inoue and H. Saitô, *Magn. Reson. Chem.*, 2004, **42,** 247–257.
72. J. Schaefer, H. Jiang, A. E. Ransome and T. J. Kappock, *Biochemistry*, 2007, **46,** 9507–9512.
73. T. Y. Yu, R. D. O'Connor, A. C. Sivertsen, C. Chiauzzi, B. Poliks, M. Fischer, A. Bacher, I. Haase, M. Cushman and J. Schaefer, *Biochemistry*, 2008, **47,** 13942–13951.
74. T. Gullion and C. H. Pennington, *Chem. Phys. Lett.*, 1998, **290,** 88–93.
75. T. Gullion, *J. Magn. Reson.*, 1999, **139,** 402–407.
76. E. Mihaliuk and T. Gullion, *J. Magn. Reson.*, 2008, **193,** 308–310.
77. M. Bertmer and H. Eckert, *Solid State Nucl. Magn. Reson.*, 1999, **15,** 139–152.
78. J. H. Van Vleck, *Phys. Rev.*, 1948, **74,** 1168.
79. J. C. C. Chan, M. Bertmer and H. Eckert, *J. Am. Chem. Soc.*, 1999, **121,** 5238–5248.
80. J. D. Epping, W. Strojek and H. Eckert, *Phys. Chem. Chem. Phys.*, 2005, **7,** 2384–2389.
81. R. R. Deshpande, L. Zhang and H. Eckert, *J. Mater. Chem.*, 2009, **19,** 1151–1159.
82. T. Echelmeyer, L. van Wüllen and S. Wegner, *Solid State Nucl. Magn. Reson.*, 2008, **34,** 14–19.
83. M. Bak, J. T. Rasmussen and N. C. Nielsen, *J. Magn. Reson.*, 2000, **147,** 296–330.
84. J. C. C. Chan and H. Eckert, *J. Magn. Reson.*, 2000, **147,** 170–178.
85. D. A. Middleton, X. Peng, D. Saunders, K. Shankland, W. I. F. David and A. J. Markvardsen, *Chem. Commun.*, 2002, **8,** 1976–1977.
86. R. A. Haberkorn, R. E. Stark, H. Van Willigen and R. G. Griffin, *J. Am. Chem. Soc.*, 1981, **103,** 2534–2539.
87. P.-G. Jonsson and A. Kvick, *Acta Crystallogr. B*, 1972, **28,** 1827–1833.
88. L. Pauling and J. Sherman, *Z. Kristallogr.*, 1937, **96,** 481.
89. G. E. R. Schulze, *Zeitschrift fur Physikalische Chemie B*, 1934, **24,** 215.
90. C. P. Jaroniec, B. A. Tounge, C. M. Rienstra, J. Herzfeld and R. G. Griffin, *Journal of Magnetic Resonance*, 2000, **146,** 132–139.
91. R. S. Thakur, N. D. Kurur and P. K. Madhu, *Chemical Physics Letters*, 2006, **426,** 459–463.
92. L. Van Wüllen, T. Echelmeyer, H. W. Meyer and D. Wilmer, *Phys. Chem. Chem. Phys.*, 2007, **9,** 3298–3303.
93. O. Ekkert, G. Kehr, R. Fröhlich and G. Erker, *J. Am. Chem. Soc.*, 2011, **133,** 4610–4616.
94. T. Wiegand, H. Eckert, G. Erker, submitted to *J. Am. Chem. Soc.*, 2012.
95. A. S. Cattaneo, S. Bracco, A. Comotti, M. Galimberti, P. Sozzani and H. Eckert, *J. Phys. Chem. C*, 2011, **115,** 12517–12529.
96. F. Behrends, H. Eckert, *J. Phys. Chem. C*, 2011, **115,** 17175.

CHAPTER 2

Recent Advances in Solid-State ^{25}Mg NMR Spectroscopy

Jair C. C. Freitas* and **Mark E. Smith†**

Contents

* Department of Physics, Federal University of Espírito Santo, Vitória, Brazil
† Department of Physics, University of Warwick, Coventry, United Kingdom

Annual Reports on NMR Spectroscopy, Volume 75
ISSN 0066-4103, DOI: 10.1016/B978-0-12-397018-3.00002-8

Abstract In spite of the relatively unfavourable characteristics of the ^{25}Mg nuclide for NMR experiments—such as low natural abundance, small magnetogyric ratio and sizeable quadrupolar broadening—there is increasing evidence that solid-state ^{25}Mg NMR is a powerful tool for studies involving many different materials. Much of the recent boost in this field has been driven by instrumental improvements, such as the availability of high magnetic fields and fast-spinning speeds, as well as by the use of signal-enhancement methods developed in the past decade for half-integer spin quadrupolar nuclei. The most relevant advances in solid-state ^{25}Mg NMR spectroscopy are reviewed here, including a detailed account of the use of signal-enhancement methods and of the more recent applications of first-principles calculations of ^{25}Mg NMR parameters. Examples of the application of ^{25}Mg solid-state NMR are given for different classes of materials, including organic compounds, oxide-based materials, glasses, alloys and intermetallic compounds.

Key Words: ^{25}Mg NMR, Solid state NMR, Signal enhancement, First-principles calculations, Materials characterisation

ABBREVIATIONS

1D	one-dimensional
2D	two-dimensional
3Q	triple quantum
5Q	quintuple quantum
Ac	acetate
Acac	acetylacetonate
APE1	apurinic/apyrimidinic endonuclease 1
ATP	adenosine-5′-triphosphate
BChl	bacteriochlorophyll
BPA	bis(2-pyridyl)amine
CP	cross-polarisation
Cp	cyclopentadienyl
CSA	chemical shielding anisotropy
CT	central transition
DFS	double frequency sweeps
DFT	density functional theory
DNA	deoxyribonucleic acid
DNP	dynamic nuclear polarisation
EDTA	ethylenediaminetetraacetate
EFG	electric field gradient
FAM	fast amplitude modulation

FID	free induction decay
FPLAPW	full-potential linearized augmented plane wave
FSG	frequency switched Gaussian
FT	Fourier transform
FWHM	full width at half maximum
GGA	generalized gradient approximation
GIAO	gauge-including atomic orbital
GIPAW	gauge-including projector augmented wave
HS	hyperbolic secant
KSA	Knight shift anisotropy
LDA	local density approximation
MAS	magic angle spinning
MQ	multiple quantum
MQMAS	multiple quantum magic angle spinning
NMR	nuclear magnetic resonance
NQR	nuclear quadrupole resonance
PAS	principal axis system
PAW	projector augmented wave
Pc	phthalocyanine
PI	polyimide
Py	pyridine
QCPMG	quadrupolar Carr–Purcell–Meiboom–Gill
QCPMG–MAS	combination of QCPMG and MAS experiments
RAPT	rotor-assisted population transfer
REDOR	rotational echo double resonance
RF	radiofrequency
RHF	restricted Hartree–Fock
S/N	signal to noise
ST	satellite transition
STMAS	satellite transition magic angle spinning
TTP	tetraphenylporphyrin
VOCS	variable offset cumulative spectra
WURST	wideband, uniform rate, smooth truncation

1. INTRODUCTION

1.1. Overview of review

This review sets out to present a comprehensive overview of the current development of ^{25}Mg solid-state NMR as at mid-2011. Magnesium is a highly significant critical element in the solid-state chemistry of technologically important ceramics, minerals and glasses, as well as being important in the structure and function of many biomolecular systems.[1–4]

To date, the spectroscopic probes that provide real insight into the local structure around magnesium are very limited. Given the almost unique sensitivity of solid-state NMR to provide structural information about the local coordination of magnesium, there is a strong driving force to develop this spectroscopic approach. Given the potentially high significance of ^{25}Mg NMR, the background to the NMR characteristics of the ^{25}Mg nuclide is introduced, which places it firmly in the category of nuclei which have been termed low-γ.[5,6] These are nuclei with a Larmor frequency below that of ^{15}N. Some perspective is provided as to how changes in available experimental methodology, which include high magnetic fields as well as the development of signal-enhancement approaches that manipulate satellite transition (ST) intensity to increase that of the central transition (CT) (see Section 2 for more details), have made ^{25}Mg NMR more accessible. ^{25}Mg provides a good example of how a nucleus which had only limited accessibility a decade ago, and while it is still moderately challenging, is observable with care in most materials. The experimental approaches including referencing and more advanced techniques are examined. A brief background to the rapidly burgeoning utility of first-principles calculations of NMR parameters is given with emphasis on application to ^{25}Mg. The application of ^{25}Mg NMR to a range of metals, inorganic and organic materials is described, showing the real benefits of observing ^{25}Mg via solid-state NMR to provide new atomic scale perspectives on problems of scientific and technological significance.

1.2. Nuclear characteristics of ^{25}Mg and their influence on its NMR study

Magnesium has one NMR-active isotope, ^{25}Mg, which is only 10.0% naturally abundant. This is a spin 5/2 nucleus with a magnetogyric ratio of $-1.639 \times 10^7 \,\mathrm{rad\,s^{-1}\,T^{-1}}$, which means it has a Larmor frequency that is 6% of that of protons in the same magnetic field and a receptivity of 72.9% of that of ^{29}Si.[7] The relatively low Larmor frequency was one of the key factors that limited the early study of ^{25}Mg when only relatively modest magnetic fields were available. Along with the intrinsic reduction in sensitivity both from the reduction in the Boltzmann factor and the size of the induced signal, there were other problems such as the increased effects of ringing (e.g. acoustic) at lower frequencies, which makes the recording of broad lines using Fourier transform (FT) techniques difficult.[8] The quadrupole interaction comes about from a nuclear electric quadrupole moment of 199.4 mb.[7] This produces a quadrupolar broadening factor of the CT of 8.60 compared to ^{27}Al.[9] Hence in Hertz at the same magnetic field, the CT spectrum is roughly a factor of 10 broader than for ^{27}Al for the nuclei in a site of the same structural distortion if both the second-order quadrupolar broadening and Sternheimer antishielding factor are taken into account (see Ref. 9

and references therein). The broadening, low intrinsic sensitivity and low Larmor frequency combine to explain why solid-state ^{25}Mg NMR is so much less common than ^{27}Al NMR.

1.3. NMR interactions

The simplest NMR experiment is to place a static sample in a solenoidal coil within the static magnetic field. For a solid, the sample is usually presented as a finely ground powder such that a static powder pattern is observed. The nucleus experiences a series of interactions with the main ones being the Zeeman interaction with the main magnetic field, and in the high-field limit, this essentially defines the energy level spacing and hence the Larmor frequency (ν_0) at which the nucleus is observed.[10] The other interactions of the nucleus with its surroundings are then normally regarded as perturbations of the Zeeman levels. These local interactions include dipolar (with other spins through space) and the chemical shielding due to the electronic surroundings of the nucleus modifying the magnetic field at the nucleus. All these interactions are three-dimensional (3D) tensor interactions. The principal axis system (PAS) is the system in which only the diagonal elements are non-zero. These interactions both have the same spatial dependence of $(3\cos^2\theta - 1)$, with θ being the angle between the external magnetic field and one of the axes (named Z-axis) of the PAS of the corresponding tensor (when the tensor is axially symmetric, the symmetry axis is chosen as the Z-axis). This term corresponds to the angular part of the second-order Legendre polynomial, which produces the powder patterns usually observed in static polycrystalline materials. The tensor is typically redescribed in combinations of the PAS elements that are more directly related to the features of the observed spectral lineshape. In the case of the chemical shielding anisotropy (CSA) tensor, a number of different conventions are in common use.[11–14] In one of the currently most used notations,[13] the principal components of the CSA tensor are labelled and ordered as $\delta_{11} \geq \delta_{22} \geq \delta_{33}$; the isotropic chemical shift (δ_{iso}) is then given by:

$$\delta_{iso} = \frac{1}{3}(\delta_{11} + \delta_{22} + \delta_{33}). \quad (1)$$

The CSA tensor is characterised by δ_{iso} (proportional to its trace) and by the parameter span (Ω) and skew (κ), defined as:[13]

$$\Omega = \delta_{11} - \delta_{33}, \quad (2)$$

$$\kappa = \frac{3(\delta_{22} - \delta_{iso})}{\Omega}. \quad (3)$$

Alternatively, in the so-called Haeberlen notation,[11,14] the convention is $|\delta_{ZZ}-\delta_{iso}| \geq |\delta_{XX}-\delta_{iso}| \geq |\delta_{YY}-\delta_{iso}|$, where the capital letters refer to the principal components and the isotropic chemical shift has a definition similar to Equation 1. The anisotropy ($\Delta\delta$) and asymmetry (η) are then defined as:

$$\Delta\delta = \delta_{ZZ} - \frac{\delta_{XX} + \delta_{YY}}{2}, \tag{4}$$

$$\eta_{CSA} = \frac{\delta_{YY} - \delta_{XX}}{\delta_{ZZ} - \delta_{iso}}. \tag{5}$$

For metals, the analogous shielding interaction is the Knight shift (K) caused by the conduction electrons in the system; the components of the Knight shift tensor have definitions similar to the ones given above for the chemical shift. For a nucleus with $I>1/2$, there is an additional interaction because the nucleus possesses an electric quadrupole moment (eQ) which interacts with the gradient in the electric field at the nucleus. The electric field gradient (EFG) is again a tensor quantity; it is symmetric and traceless,[15,16] with the largest component defined as eq_{ZZ} (although often q alone is used to designate the largest component). The quadrupole interaction is characterised by two parameters: the quadrupolar coupling constant (C_q)* and the asymmetry parameter (η_q), which are defined as:

$$C_q = \frac{e^2 q_{ZZ} Q}{h}, \tag{6}$$

$$\eta_q = \frac{V_{XX} - V_{YY}}{V_{ZZ}}, \tag{7}$$

where $V_{\alpha\beta} = \frac{\partial^2 V}{\partial x_\alpha \partial x_\beta}$ is the second derivative of the electric potential with respect to Cartesian coordinates, evaluated at the nuclear position, and the axes in the PAS of the EFG tensor are ordered so that $|V_{ZZ}| \geq |V_{YY}| \geq |V_{XX}|$.[16] In this way, the asymmetry parameter is always in the range $0 \leq \eta_q \leq 1$.

The quadrupole interaction will perturb all energy levels to first order ($\propto 3\cos^2\theta - 1$, where θ is the angle between the external magnetic field and the Z-axis of the PAS of the EFG tensor), apart from the CT.[15,16] If C_q is significant, it tends to broaden the non-central transition or ST over a range of frequencies $\sim\nu_q$, which for an $I=5/2$, nucleus is $\nu_q = 3C_q/20$. This can vary from hundreds of kilohertz to a few megahertz, which makes these low intensity broad transitions somewhat difficult to observe by conventional pulsed techniques and usually requires an echo of some description to minimise the distortion to the lineshape. The quadrupole

* In the literature, there are typically three symbols used for the quadrupolar interaction, C_q, C_Q or χ_Q, with the latter IUPAC recommendation.[17]

interaction can become so large that second-order effects become important and this is particularly noticeable for the CT where first-order effects are absent. Two key features of the second-order effects are their dependence (in ppm) on $(C_q/\nu_0)^2$, which then makes the spectra dependent on the magnetic field, and the much more complex angular dependence proportional to the fourth-order Legendre polynomial.[6,18] In a powder, again a distinct pattern is observed from which the parameters associated with the quadrupole interaction (C_q and η_q, besides the isotropic chemical shift) can be deduced. This field dependence makes immediate comparison of results at different fields somewhat more difficult, but it turns out to be a highly useful feature, since it constrains simulations of multiple-field spectra, especially because this field dependence differs from the other interactions present such as the chemical shielding. This means that for a static powder pattern where both the chemical shielding and quadrupole interactions are present, these interactions can be separated by taking data at several magnetic fields.

^{25}Mg being a light nuclide with relatively low Larmor frequency and a moderate nuclear electric quadrupolar moment, means that the quadrupole interaction tends to be dominant. However, as magnetic fields increase, the chemical shielding increases ($\propto B_0$, in Hz) and the second-order quadrupole effects decrease ($\propto B_0^{-1}$), so that the shielding can start to have a real influence on the static lineshape at the very highest magnetic fields.

Some typical CT-only spectra simulated for static samples considering solely the quadrupole interaction are shown in Figure 1A, for sites with different values of the asymmetry parameter η_q. The widths of these lineshapes depend on the η_q value and are proportional to the parameter A, defined for a nucleus with $I=5/2$ as[6,20]:

$$A = \frac{9}{800}\frac{{C_q}^2}{\nu_0}, \tag{8}$$

where A, C_q and ν_0 are all given in the same frequency units (e.g. MHz). For a site with an axially symmetric EFG tensor, for example, the total breadth of the CT spectrum is $\sim(25/9)A$. It is important to observe that all these lineshapes are asymmetrically broadened around the isotropic chemical shift position (δ_{iso}). Only for $\eta_q=1.0$, the strongest singularity (peak) coincides with δ_{iso} (but even in this case, the line is asymmetrical).

To improve the spectral resolution from powders, the most common approach is to apply magic angle spinning (MAS). MAS involves bodily rotating a sample at typically 5–65 kHz at an axis inclined at 54.7° to the main magnetic field. This will remove the broadening proportional to $3\cos^2\theta - 1$, greatly improving the resolution of the spectrum. The presence of second-order quadrupolar broadening with its more complex angular

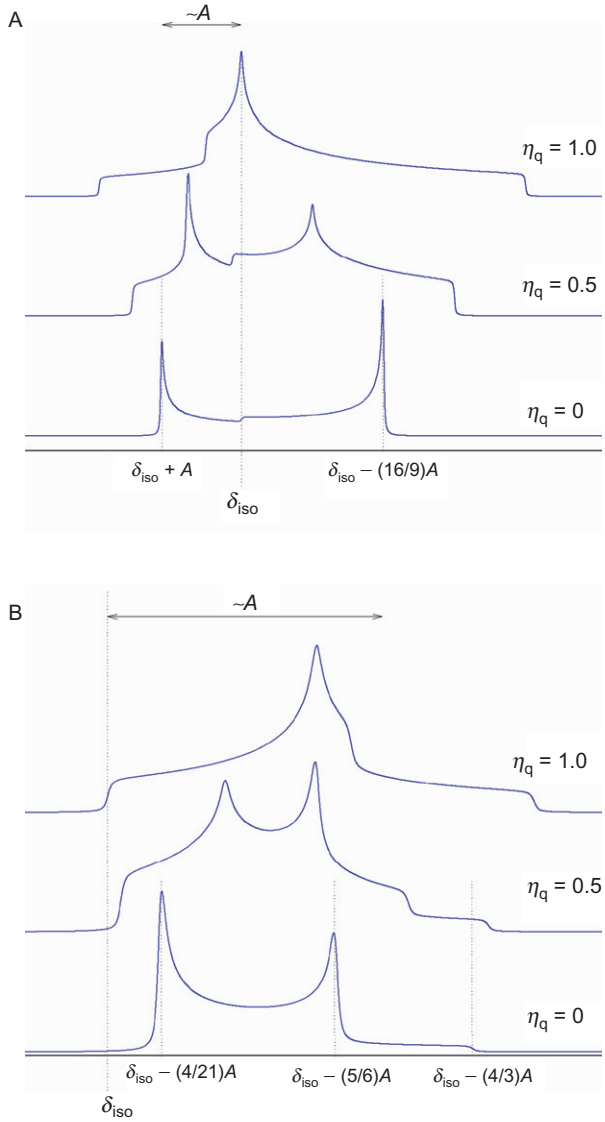

Figure 1 Simulations of CT lineshapes corresponding to (A) static and (B) MAS experiments, for different values of the asymmetry parameter η_q. The positions of the isotropic chemical shift (δ_{iso}) and some well-defined singularities are shown, in terms of the parameter A, defined in Equation 8. All simulations were done with the DMFIT software.[19]

dependence can only be partially averaged by MAS and there is still broadening which can be noticeable if C_q is significant.[6,18] A residual powder pattern lineshape is observed, again with distinct features from which the quadrupole parameters can be deduced, which is a factor 3–4 narrower than the static lineshape. The spectrum is simplified as compared to the static case as there is no CSA under MAS. Some typical simulated CT-only MAS spectra are shown in Figure 1B, again for different η_q values. The widths of these lineshapes are scaled by the same parameter A defined above for the static case. When powder patterns like these ones are available, the NMR parameters C_q, η_q and δ_{iso} can be readily obtained by fitting the experimental spectra to theoretical lineshapes or by numerical simulation of the complete experiment, using one of the many currently available simulation softwares.[19,21–23]

As it can be seen in these simulations, all MAS spectra are shifted towards low frequencies with respect to the true isotropic chemical shift—an effect known as the second-order quadrupole-induced shift. The centre of gravity (δ_{cg}) of these lineshapes is given by[9,20]:

$$\delta_{cg} = \delta_{iso} - 6000\left(\frac{C_q}{\nu_0}\right)^2\left(1 + \frac{\eta_q^2}{3}\right), \tag{9}$$

where the shifts (δ_{iso} and δ_{cg}) are given in ppm and C_q and ν_0 are given in the same frequency units (e.g. MHz).

However, commonly due to a spread of quadrupole parameters caused by structural variation, with the extreme case being glassy or amorphous materials, the distinct features of the lineshape can be lost. This is particularly true if C_q is small. Then an approach which records spectra at several magnetic fields will allow both the second-order quadrupole effect parameter P_q, defined as

$$P_q = C_q\sqrt{1 + \frac{\eta_q^2}{3}}, \tag{10}$$

and δ_{iso} to be deduced from the gradient and the y-intercept of a plot of the position of δ_{cg} against $(B_0)^{-2}$ or $(\nu_0)^{-2}$.[6,9]

For samples that have multiple magnesium sites, the residual broadening even under MAS can cause severe overlap between different sites. More advanced narrowing techniques can be applied, one of the most widely used and successful of these approaches is the two-dimensional (2D) multiple quantum (MQ) MAS experiment developed by Frydman.[24] In this experiment, a higher order coherence is correlated with the single quantum coherence. In the 2D data set, there exist times when the second-order effects of the two coherences cancel one another, giving ridges of intensity where only isotropic shifts are refocussed

and hence better resolved information exists.[6] The data is usually presented in a sheared format so that the isotropic, resolved spectrum is parallel to the x-axis. For an $I=5/2$ nucleus, two possibilities exist, either a 3Q (triple quantum) or a 5Q (quintuple quantum) resonance experiment, with a number of different approaches for excitation of MQ coherence and its conversion to single quantum coherence.[25–27] There are examples of MQMAS experiments from ^{25}Mg, as described below. However, with the various factors that determine the MQ intensity, it is clear why MQ of low-γ nuclei has found limited application. There is a natural low sensitivity which limits any 2D experiment since this varies approximately as γ^3. Another key factor in determining the sensitivity of the MQMAS method is the strength of the RF field ($\nu_1=\gamma B_1$), which needs to be as high as possible, especially for the multiple to single quantum reconversion. It is of course much more difficult to generate high RF fields because γ is small. It has also been shown that MQ coherences are most efficiently excited when the MAS spinning (ν_r) speed is low,[28] but this then limits the value of C_q which can be narrowed, which demands higher ν_r. Hence these two factors work against each other when choosing the optimum ν_r.

An alternative approach to MQ is that of ST MAS, which was proposed in 2000 by Gan.[29] Two commonly used pulse sequences used for MQMAS and STMAS are shown in Figure 2 where the coherence pathway diagram illustrates the difference in the experiments very clearly. The STMAS experiment is based on the fact that both the CT and the ST (non-central) are second-order quadrupolar broadened by an orientation-dependent factor.[29,31] Hence, as in the MQ approach, correlation of the two transitions in a 2D experiment results in echo formation at certain times and then in the doubly FT dataset certain directions where this anisotropic broadening will be removed, providing much better resolution and separation on the basis of the isotropic shift. STs are excited with a single pulse which evolves for a time t_1, before a second pulse converts them into CT coherence where the magnetisation is detected. The coherence pathway diagram shows that the MQ experiment proceeds via a higher order coherence, which is a key source of the poorer sensitivity of the MQ experiment. However, in comparison, the ST approach only involves single quantum transitions, which are much more efficiently excited by RF pulses.

These differences and hence the advantages are more pronounced for low-γ nuclei.[30,32] A plot of the relative sensitivity of the ST approach to the MQ approach was evaluated by numerical simulation as a function of the parameter (ν_1/ν_q); the ST experiment shows a factor of at least three better sensitivity, which is a significant advantage (Figure 2C). Although more use of STMAS has developed, it has not yet become as popular as the MQ approach, probably as a result of its reputation as an experiment

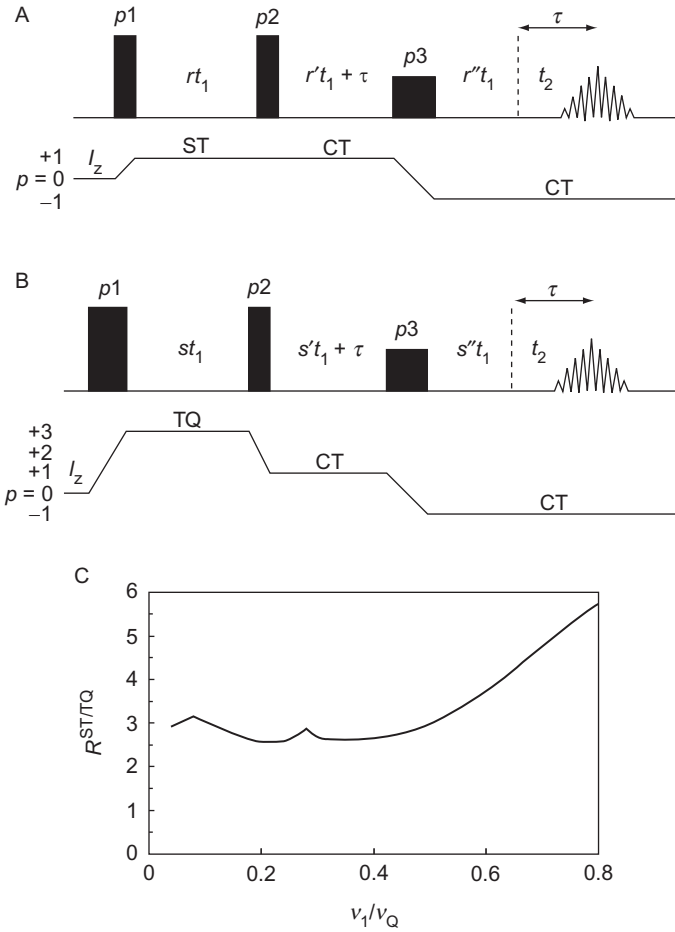

Figure 2 Pulse sequences and coherence pathway diagrams for the phase-modulated split-t_1 (A) STMAS and (B) triple-quantum MAS NMR, showing the generic sequences with the specific values for ^{25}Mg being r=24/31, r'=0, r''=7/31 and s=12/31, s'=0, s''=19/3 and (C) numerical simulations of the relative sensitivity of the ST and MQ experiments as a function of the ratio between the RF field strength and the quadrupolar coupling frequency. Reprinted with permission from Dowell et al.,[30] Copyright 2004 American Chemical Society.

that has highly stringent magic angle setting and rotor synchronisation requirements—points dealt with by Ashbrook and Wimperis.[31] However, the sensitivity advantage of ST experiment has been applied to the observation of ^{25}Mg NMR, with examples of brucite, diopside and talc, where for various mixtures, the isotropic peaks could be separated in the ST experiment.[30]

1.4. Overview of practical considerations of experimental approaches for solid-state ^{25}Mg NMR

The recommended primary chemical shift reference for ^{25}Mg NMR experiments is an 11M solution of $MgCl_2$ in deuterated water.[7] However, a number of other aqueous solutions of Mg^{2+} salts such as $MgSO_4$, $MgCl_2$ and $Mg(NO_3)_2$ in different concentrations have been mentioned in the literature.[33–39] There is no reported significant effect of cation concentration on the chemical shift determined with these solutions, at least within experimental uncertainty. MacKenzie and Meinhold[35] stated that shifts referenced to 1M $MgSO_4$, saturated $MgSO_4$, 1M $Mg(NO_3)_2$ and 1M $MgCl_2$ (all aqueous solutions) were comparable within 0.2ppm. Accordingly, Cahill et al.[40] reported that aqueous solutions of 1M $MgSO_4$, 3M $MgSO_4$, 1M $Mg(NO_3)_2$ and saturated $MgCl_2$ all exhibited chemical shifts at 0 ± 0.5ppm. In the solid state, it is quite common to use secondary references, with MgO being by far the most frequent choice. The ^{25}Mg NMR spectrum of this compound shows a single and relatively narrow peak, with zero quadrupole coupling (due to the cubic symmetry of the Mg site) and $\delta_{iso} = 26$ppm relative to 11M $MgCl_2$ aqueous solution (see Section 4.2 for more details). Unfortunately, the ^{25}Mg spin–lattice relaxation time is quite long in MgO, $T_1 \cong 16$s,[34] so experiments with MgO are a bit time-consuming. An alternative is to use a material with a well-defined set of quadrupole parameters and having fast spin–lattice relaxation. Obviously, in this case, the shifts corresponding to the observed singularities will be dependent on the strength of the static magnetic field (B_0). Freitas et al.[41] proposed the use of the compound magnesium disodium ethylenediaminetetraacetate tetrahydrate ($Na_2MgEDTA \cdot 4H_2O$), which gives a relatively narrow second-order MAS CT lineshape with $C_q = 1.675(5)$MHz, $\eta_q = 015(1)$ and $\delta_{iso} = 0.25(10)$ppm. This spectrum is easily observed in short experimental time due to a fast spin–lattice relaxation of ^{25}Mg in the compound. In that work, a set of numerical relationships, graphical plots and tabulated data were provided to help using $Na_2MgEDTA \cdot 4H_2O$ as a reference for chemical shifts in ^{25}Mg NMR experiments performed at various magnetic fields. Table 1 below gives the calculated relative shifts (with respect to an 11M $MgCl_2$ aqueous solution) of the most intense peak (δ_0) in the ^{25}Mg MAS NMR spectra of the $Na_2MgEDTA \cdot 4H_2O$ compound for some typical external magnetic field values (and spectrometer frequencies), as well as the total frequency range (Δf) spanned by this spectrum (see Figure 3 for a graphical definition of these parameters).

Due to the reasons discussed in the previous section, only the CT is usually observed in ^{25}Mg MAS NMR spectra. In the regime of low RF power ($\nu_1 \ll \nu_q$), the excitation of the CT is provided by a selective $\pi/2$ pulse, with duration reduced by the factor $I + 1/2 = 3$ in comparison with the value determined using a solution or a material with zero quadrupole

TABLE 1 Calculated values of δ_0 (shift of the most intense peak) and Δf (total breadth) in the ^{25}Mg MAS NMR spectrum of the $Na_2MgEDTA{\cdot}4H_2O$ compound[41]

Magnetic field (T)	^{1}H NMR frequency (MHz)	^{25}Mg NMR frequency[a] (MHz)	δ_0[b] (ppm)	Δf[b] (kHz)
7.05	300	18.38	−23.1	2.1
9.4	400	24.51	−13.1	1.6
11.7	500	30.63	−8.3	1.3
14.1	600	36.76	−5.6	1.1
16.4	700	42.89	−4.1	0.90
18.8	800	49.01	−3.1	0.79
20.0	850	52.07	−2.6	0.74
21.1	900	55.13	−2.4	0.70

[a] Calculated for each magnetic field using $|^{25}\gamma|=1.639\times10^7\,\mathrm{rad\,s^{-1}T^{-1}}$.[7]
[b] See Figure 3. Shift relative to an 11M $MgCl_2$ aqueous solution.

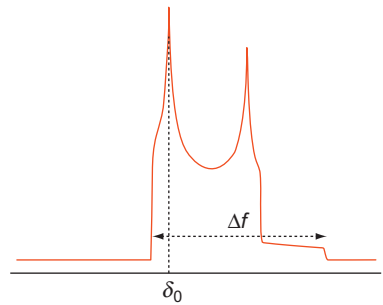

Figure 3 Definition of the parameters δ_0 (shift of the most intense peak) and Δf (total breadth), in the ^{25}Mg MAS NMR spectrum of the $Na_2MgEDTA{\cdot}4H_2O$ compound. Reproduced from Freitas et al.[41] Copyright 2008 John Wiley and Sons, Ltd.

coupling.[9,18] The condition $\nu_1 \ll \nu_q$ is satisfied for most usual probes, since the RF strength ν_1 is typically well below ν_q value for a low-γ nucleus such as ^{25}Mg. In the cases where more RF power is required, as it is typically the case of MQMAS and related experiments, the use of probes especially designed to attain high RF power levels and appropriate tuning at the low ^{25}Mg NMR frequency has been reported.[37,42–44]

Typical commercial probes used for MAS experiments are equipped with rotors having diameters in the range 2.5–7mm, which allows spinning speeds up to 45kHz. This value is sufficient in many cases for attaining the maximum possible narrowing of the second-order quadrupolar broadened CT in ^{25}Mg NMR spectra recorded at strong magnetic

fields. When the quadrupole coupling is so small that lower speeds can be used or, in the other extreme, when it is so large that MAS is not a viable approach, sample holders with larger diameters (such as 9.5 and 14mm) can be useful, with the obvious advantage of accommodating a large amount of material.

Besides the use of large volume samples, there are also other ''brute force'' approaches frequently used since the earlier reports of solid-state ^{25}Mg NMR, including isotopic enrichment and the use of magnetic fields as strong as possible.[6,37,39,42,43,45–52] There is no doubt that the increase in the number of reports involving solid-state ^{25}Mg NMR has been driven by the wider availability of high-field magnets (e.g. $\geq$14.1T). Another key driver has been the development of signal-enhancement techniques which are described in detail in Section 2, including multiple-pulse spin-echo methods and techniques based on population transfer from the STs to increase the population difference across the CT. Another approach was an early use of dynamic nuclear polarisation (DNP) in solid-state NMR, for ^{25}Mg NMR study of Cr^{3+}-doped forsterite (Mg_2SiO_4).[53] Improvements in the electronic characteristics of the excitation/detection systems have also been proposed, as in the reports by Ellis and collaborators,[54–57] who used low-temperature double-resonance probes for studies of biological materials. Some related work recently published involved the design of an electrically balanced probe capable of generating a high RF field strength to enhance the sensitivity of ^{25}Mg MQMAS NMR experiments in Mg/Al layered double hydroxides (LDHs).[44]

1.5. Development of ^{25}Mg solid-state NMR

The historical development of ^{25}Mg NMR is interesting in that there have been sporadic, almost one off attempts, which were then followed by more concerted streams of work as the quality of the data gradually improved, until the present day position of well-reproduced lineshapes across a wide range of compounds, has been achieved. The first reported solid-state ^{25}Mg NMR data is probably the 1970 observation of the Knight shift in magnesium metal.[58] The 1980s saw some one off studies which included a study of MgO and the paramagnetic solid solution $Ni_xMg_{1-x}O$ where the cubic symmetry allowed static NMR to be employed.[59] The intermetallic Cu_2Mg was studied in 1981 as part of a series of cubic Laves phases.[60] Single-crystal work was reported for forsterite (Mg_2SiO_4) which allowed the tensor parameters to be determined from a rotation pattern.[53,61] MAS was first applied to ^{25}Mg in 1988 when a limited series of magnesium-containing compounds, mostly in relatively symmetric environments, was reported.[33] This illustrated the potential sensitivity of ^{25}Mg and that MAS could narrow the lineshape, with the clear hint that things would improve at higher magnetic fields.

MacKenzie recognised the potential of this early ^{25}Mg work and started a systematic ^{25}Mg NMR investigation of geominerals, with one of his major studies involving 16 minerals and closely related inorganic compounds.[34] This study was carried out at 11.7T using MAS of 20kHz and really tested the limits of what could be done at that time for ^{25}Mg. Subsequently, studies at much higher magnetic fields and faster MAS resulted in some of the parameters obtained in the MacKenzie and Meinhold paper being refined, but nevertheless this initial study revealed the trends and correlations of the ^{25}Mg NMR parameters to structural distortion (see Section 4.2), illustrating the structural sensitivity of ^{25}Mg and strongly suggesting the utility it is now finding. MacKenzie and co-workers then embarked on an extensive series of studies using ^{25}Mg NMR to probe the thermal decomposition of a range minerals, as discussed in Section 4.2.[62–68] Another area where ^{25}Mg NMR began to find utility was the work of Bastow looking at magnesium-based alloys and intermetallics (see Section 4.1).[69–73] The availability of higher magnetic fields and signal-enhancement schemes has subsequently resulted in the very significant increase in reports of solid-state NMR of ^{25}Mg from around 2008 onwards.

2. SENSITIVITY ENHANCEMENT METHODS

2.1. Introduction

Many techniques have been proposed in recent years to enhance the sensitivity and signal-to-noise (S/N) ratio of NMR spectra of low-γ, half-integer spin quadrupolar nuclei. The most commonly used are the quadrupolar Carr–Purcell–Meiboom–Gill (QCPMG) pulse sequence (based on multiple-pulse spin-echo methods)[36,74–76] and population transfer techniques such as rotor-assisted population transfer (RAPT), [77–80] double frequency sweeps (DFS)[81,82] and use of adiabatic inversion pulses, such as hyperbolic secant (HS) and WURST pulses.[83–87] There are several reviews and original papers about the theoretical and practical aspects involved in these methods.[74,76,84,86,88–95] In this section, the principles underlying these approaches to signal enhancement are briefly revisited with reports of their applications to solid-state ^{25}Mg NMR experiments highlighted.

2.2. Methods based on population transfer

Figure 4A shows schematically the thermal equilibrium population distribution over the nuclear energy levels for an ensemble of nuclei with spin 5/2 (such as ^{25}Mg) in a strong applied magnetic field and in the high-temperature regime.[10] Under this scenario, the fractional population p_m of each energy level (labelled with the magnetic quantum number m) is given by

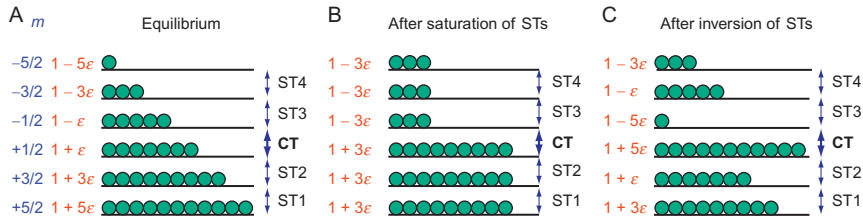

Figure 4 Schematic representation of the populations of the nuclear spin energy levels of a quadrupolar nucleus with spin 5/2 (such as ^{25}Mg) under a strong magnetic field and a perturbative quadrupole coupling showing (A) populations at thermal equilibrium, (B) populations after complete saturation of the satellite transitions, and (C) populations after complete inversion of the satellite transitions, following the order: first, inversion of ST1 and ST4 and then inversion of ST2 and ST3. The numbers at left of each level (named p_m' in the text) are proportional to the population of that level, with $\varepsilon = h\nu_L/2k_BT \cong 10^{-5}$.

$$p_m = \frac{e^{mh\nu_L/k_BT}}{2I+1} \cong \frac{1}{2I+1}(1+2m\varepsilon) = \frac{1}{2I+1}p_m', \tag{11}$$

where T is the absolute temperature, ν_L is the Larmor frequency, I is the nuclear spin quantum number (5/2 for ^{25}Mg), h Planck's constant, k_B is Boltzmann's constant and $\varepsilon = h\nu_L/2k_BT \cong 10^{-5}$. In the high-temperature approximation, ε is then a number measuring the excess or deficit population of each level with respect to a common background, as illustrated in Figure 4A. The parameter p_m', which is equal to $1+2m\varepsilon$ in thermal equilibrium, is a convenient measure of the unnormalized population of each level. The population difference between the levels $m = \pm 1/2$ (which is proportional to 2ε at thermal equilibrium) defines the intensity recorded for the CT. If, by whatever means, both ST1 and ST2 are saturated, as indicated in Figure 4B, then the population difference between the levels $m = \pm 1/2$ becomes proportional to 6ε. This means the CT will have an intensity three times larger compared to the thermal equilibrium case (this factor is $I+1/2$ in the general case). However, if the STs are inverted in a specific order, first the outer ones (ST1 and ST4), followed by the inner ones (ST2 and ST3), as illustrated in 4c, then the population difference between the levels $m = \pm 1/2$ becomes proportional to 10ε, which means an enhancement factor of 5 for the CT intensity (this factor is $2I$ in the general case).

For single crystals with STs well separated from the CT line, saturating or inverting STs without disturbing the CT is in principle straightforward, with use of frequency-selective pulses; this is illustrated in Figure 5. For powders, on the other hand, the quadrupolar first-order broadened ST

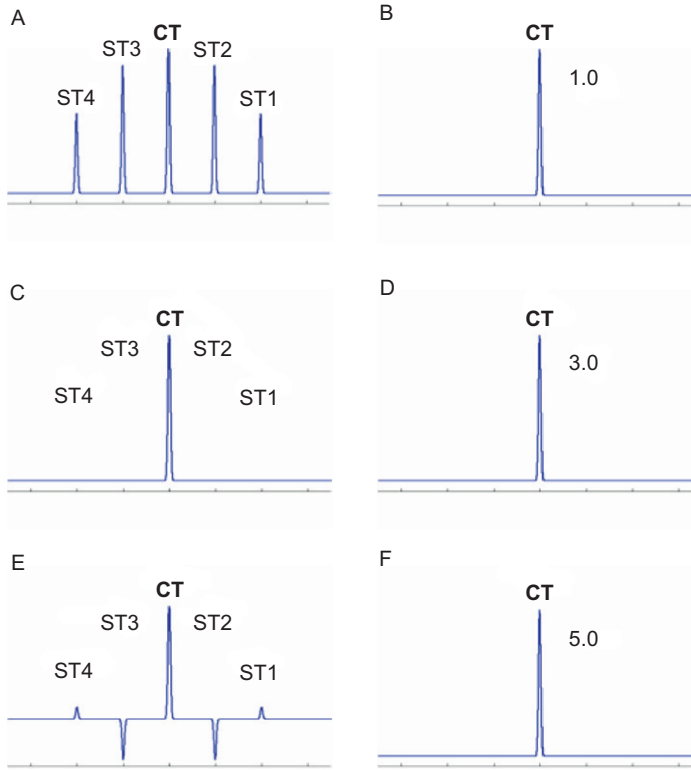

Figure 5 Simulated NMR spectra for a nucleus with spin 5/2 (such as ^{25}Mg) in a single crystal, in the case of: (A) and (B) populations corresponding to thermal equilibrium, with non-selective excitation ("hard" pulse) in (A) and CT-selective excitation ("soft" pulse) in (B). For (C) and (D) populations achieved after saturation of STs, with non-selective excitation (C) and CT-selective excitation (D). For (E) and (F) Populations achieved after complete inversion of the satellite transitions (in the order: first, inversion of ST1 and ST4 and then inversion of ST2 and ST3), with non-selective excitation (E) and CT-selective excitation (F). The numbers at the right-hand side of the spectra in (B), (D) and (F) indicate the corresponding enhancement factors of the CT resonance.

lines are spread over a wide frequency range around the CT line. Thus, hitting the STs requires a means of sweeping the frequency or using a pulse with a large bandwidth.

In DFS, this is accomplished by applying an RF pulse with amplitude modulation so that, in the frequency domain, the RF frequency changes linearly and adiabatically as a function of time on both sides of the CT.[82,88] This ''DFS pulse'' is applied at the beginning of the pulse sequence, being followed by a selective pulse applied solely to excite and detect the CT (or by a conventional spin-echo pulse sequence, also with CT-selective

pulses) (see Figure 6). With well-optimised DFS, enhancements close to the ideal value (2*I*) have been observed in single crystals for different nuclides, such as ^{23}Na (I=3/2) and ^{27}Al (I=5/2).[81,82,84] In powdered samples submitted to MAS experiments, the situation is complicated by the combined effects of frequency sweeping and spinning (which generates a set of spinning sidebands, instead of the well-defined frequency of the ST peaks in static single crystals). The enhancement factors obtained in MAS experiments change a lot from sample to sample and depend strongly on the experimental parameters of the DFS pulse (such as RF strength, sweeping range and duration); enhancement factors intermediate between the ideal cases of complete ST saturation and complete inversion of the STs (in the right order) are usually found.[84]

RAPT involves the use of a train of pulse pairs during MAS experiments, with 180° change in phase within each pair. This method is closely related to the fast amplitude modulation (FAM) technique, which was originally proposed as a means of enhancing the sensitivity of MQMAS experiments.[77] After that proposal, many reports appeared involving the use of RAPT for the enhancement of the signal due to the CT of half-integer spin quadrupolar nuclei in one-dimensional experiments.[78–80] Another interesting use of RAPT involves the separation of components having different quadrupole parameters based on their response to RAPT-based enhancement schemes.[96] In RAPT experiments, the pulse train with alternating phases is applied before the selective excitation of the CT under MAS (see Figure 6). The effect of the pulse train is the creation of sidebands separated from the carrier frequency by a frequency interval (known as modulation frequency) inversely proportional to the pulse separation.[84] The rotor motion under MAS acts then to provide a sweep of the ST resonance frequencies corresponding to the randomly oriented crystallites. As a consequence, a partial or complete saturation occurs for the STs, causing an enhanced CT population difference.[78] Some modifications in the RAPT method involve the use of off-resonance pulses with Gaussian shape—named frequency switched Gaussian (FSG) pulses—and the repetition of the RAPT transfer for a number of times

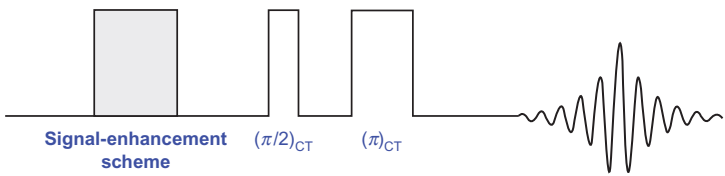

Figure 6 Typical pulse sequence used in experiments with a signal-enhancement scheme (which can involve DFS, RAPT or application of adiabatic pulses) placed before the CT excitation and detection, with formation of a spin-echo.

before the recycle delay needed to re-establish thermal equilibrium (known as multiple RAPT).[79,86,96] The maximum enhancement factors obtained with RAPT or FSG-RAPT are usually close to the ideal value corresponding to ST saturation ($I+1/2$). The most important parameters to be considered in a RAPT experiment are the modulation frequency and the RF strength used for the selective excitation of the CT coherence.[84,86]

Whereas DFS- and RAPT-based excitation schemes mostly cause saturation of the STs, a proper inversion of the population difference across these transitions can be, in principle, achieved with good efficiency using adiabatic inversion pulses. This type of pulse is largely employed in magnetic resonance imaging applications and broadband decoupling, aimed at achieving uniform broadband magnetisation inversion.[97,98] Adiabatic pulses are commonly constructed by amplitude and phase modulation of the pulse waveform. HS pulses, for example, are constructed using amplitude modulation (with the shape of a HS function, Equation 12) combined with phase modulation (Equation 13), which leads to an effective frequency sweep during the pulse (Equation 14).

$$\omega_1(t) = \gamma B_1{}^{\mathrm{amp}}(t) = \omega_1{}^{\max}\mathrm{sech}\left[\beta\left(1-\frac{2t}{T_\mathrm{p}}\right)\right], \tag{12}$$

$$\phi(t) = \Delta\omega_0 t + \left(\frac{\lambda}{\beta}\right)\frac{T_\mathrm{p}}{2}\ln\left\{\mathrm{sech}\left[\beta\left(1-\frac{2t}{T_\mathrm{p}}\right)\right]\right\}, \tag{13}$$

$$\Delta\omega(t) = \frac{\mathrm{d}\phi}{\mathrm{d}t} = \Delta\omega_0 + \lambda\tanh\left[\beta\left(1-\frac{2t}{T_\mathrm{p}}\right)\right]. \tag{14}$$

In these equations, T_p is the pulse duration; β is a truncation factor that determines the starting and ending values of the pulse amplitude (for a typical value $\beta=5.3$, these edge amplitude values are 1% of the maximum amplitude); λ is one-half of the inversion sweep width (SW), that is, SW$=2(\lambda/2\pi)$ and $\Delta\omega_0$ is the frequency offset of the pulse. The typical profiles of these functions are shown in Figure 7. As can be seen, the effective frequency of the pulse varies across the pulse between two limits symmetrically placed around the offset frequency, following a hyperbolic tangent form.[84,98]

A double HS pulse with symmetrically placed offsets about the transmitter frequency ($\Delta\omega_0=0$) can be created by cosine modulation of the pulse amplitude:

$$\omega_1{}^{\max} = \omega_1^0|\cos(\Delta\omega_{\mathrm{off}}t)|. \tag{15}$$

In this expression, $\omega_1^{\max}$ is the maximum amplitude of the HS shape (given in Equation 12) and $\Delta\omega_{\mathrm{off}}$ represents the absolute value of the offsets (which are therefore located at $\pm\Delta\omega_{\mathrm{off}}$). A similar expression applies to

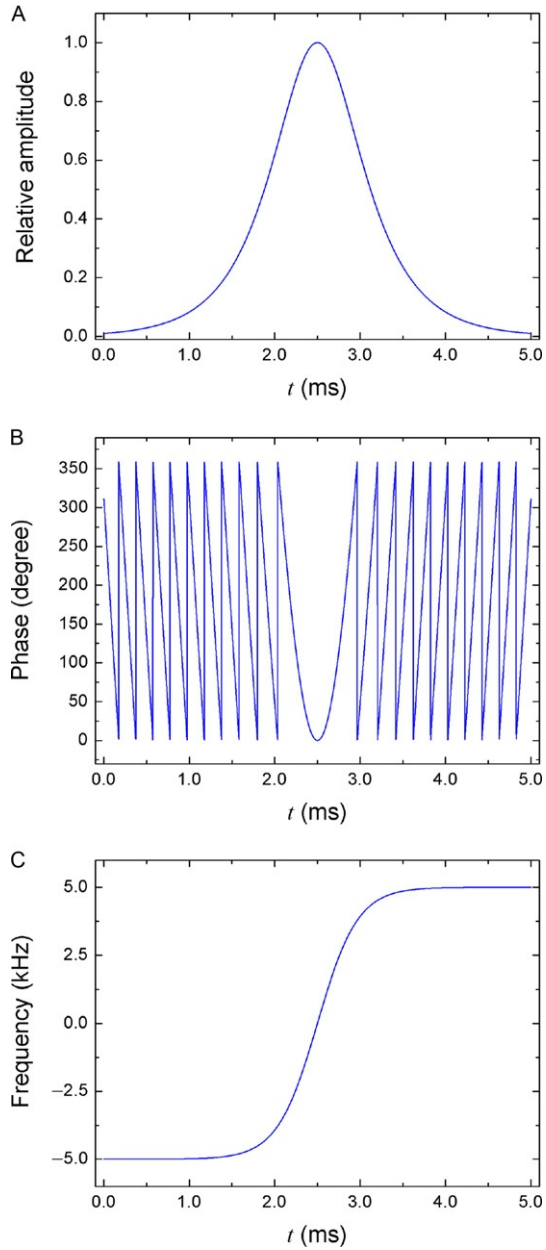

Figure 7 Amplitude (A) and phase (B) modulation of an HS pulse, with the corresponding frequency sweep (C). These simulations were calculated for T_p=5.0ms, $\lambda/2\pi$=5.0kHz (SW=10.0kHz), β=5.3 and $\Delta\omega_0$=0.

the phase modulation with a cosine function. The frequency spectra of a single and a double HS pulse are shown in Figure 8. These spectra do not correspond exactly to the excitation profile of the pulses[99] but are useful for qualitative frequency domain analysis. The inversion profiles of HS pulses in the frequency domain are characterised by a flat plateau between the limits defined by phase and/or amplitude modulation, with remarkably little sensitivity to RF strength inhomogeneity.[83] Besides HS pulses, there are many waveforms used to produce adiabatic pulses.[98] Among these, WURST pulses, which are also produced with amplitude and phase modulation and exhibit flat inversion profiles, have the advantage of requiring lower RF strength.[97] Both HS and WURST pulses (among some other adiabatic pulses) have been extensively employed for the ST inversion and consequent CT enhancement in NMR experiments involving half-integer spin quadrupolar nuclei.[41,83–86,91,100]

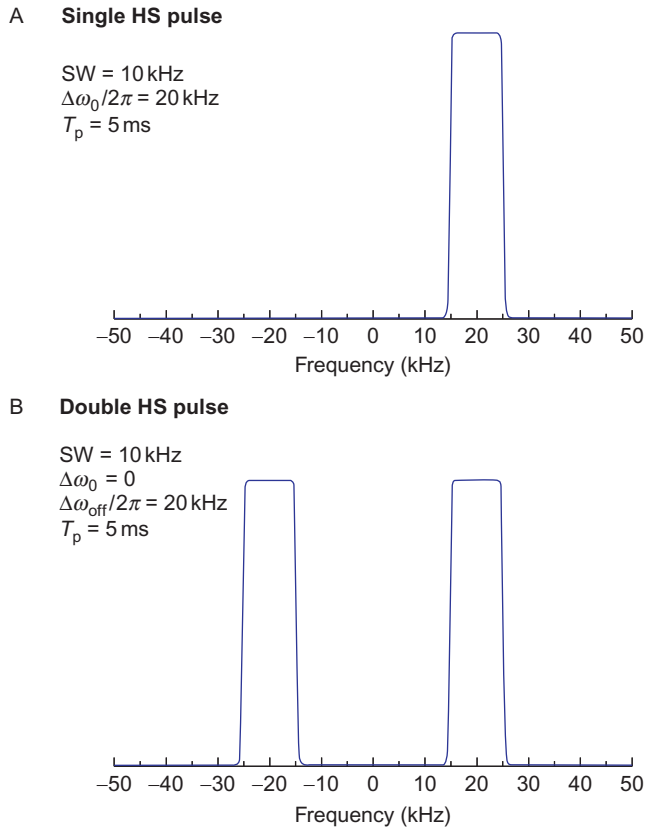

Figure 8 Frequency spectra of (A) single and (B) double HS pulses, calculated with the indicated parameters and taking β=5.3.

There are several parameters which need to be optimised for the achievement of the highest possible CT enhancement with minimal lineshape distortion. With optimal settings, HS and other adiabatic pulses usually give the highest enhancements (close to the theoretical limits of 2*I* for perfect ST inversion), when compared to other methods such as DFS and RAPT.[84,85,100] Even without detailed optimisation, it is usually found that *some* CT enhancement (although with possible lineshape distortion) is easily obtained with HS or WURST pulses, as long as the offsets are high enough in order to avoid hitting the CT itself (but not too high so as to miss the ST powder pattern). Therefore, the use of these pulses is particularly good for initial tests where the most important question is to observe any possible signal.

For proper optimisation of the parameters characteristic of the adiabatic inversion pulses, some general rules have been given in the literature.[84,85,100] For static samples, the SW should be high enough to cover most of the ST powder pattern, but not reach the CT resonance frequency range. In the case of spinning samples, Siegel et al. reported optimum CT enhancements with the use of a double HS pulse with offsets located around the peaks of the static powder pattern[100] so that the HS pulse is expected to hit an intense ST spinning sideband (an illustrative example of this will be presented in Section 2.4). The SW must be set close to the spinning rate so that only one spinning sideband is ideally inverted. Recently, the theoretical basis for understanding the adiabatic inversion process in MAS experiments was developed.[95] In this work, the authors showed that low-power adiabatic pulses applied with a width covering a single spinning sideband (named single-sideband selective pulses) can produce an efficient inversion of the entire sideband manifold independent on the RF strength (above a minimum threshold). Thus, high CT signal enhancements can be achieved with use of low-power adiabatic pulses applied to a single sideband.[85] For nuclei with spin $>3/2$, the sweep direction should be chosen so as to first invert the outer STs and then the inner ones, as depicted in Figure 4C. It is usually found that the CT enhancements increase with the HS pulse duration, but a stable value is reached for T_p values above a certain minimum.

Special care must be taken regarding the RF strength used for the CT-selective excitation following the adiabatic inversion pulses. It has been demonstrated that the conditions for optimum CT excitation depend on the distribution of population across the energy levels. Typically, the enhancement decreases with increasing the RF power used for the CT excitation, but too low RF powers are also undesirable, since an insufficient bandwidth will not provide proper excitation of the CT resonance.[86] The nutation behaviour following population distributions deviating from thermal equilibrium can be calculated numerically using the density operator formalism.[87,101] Thus, it is necessary to optimise the pulse length

and the RF power for the CT excitation pulse(s) already with the populations changed by the adiabatic pulses.

Even if the optimisation of the use of DFS, RAPT or adiabatic inversion pulses is not straightforward for nuclei with low sensitivity, it is nonetheless worth applying one of these methods to improve sensitivity. As long as there is no influence on the CT resonance, these techniques are likely to produce an enhanced CT signal compared to standard spin-echo experiments. Therefore, for ^{25}Mg (as well as for other insensitive half-integer spin quadrupolar nuclei such as ^{33}S, ^{39}K and ^{43}Ca), it is always advisable to apply some population transfer technique before the excitation of the CT signal.

2.3. The QCPMG experiment

The S/N ratio of NMR spectra of nuclei exposed to inhomogeneous interactions can be improved with use of multiple-pulse sequences involving a train of uniformly spaced refocusing π pulses applied after a $\pi/2$ excitation pulse. This method was formerly proposed in the early days of NMR—and it is still used nowadays for the same goal—as a means of measuring the intrinsic transverse relaxation time (T_2) of nuclei in liquids when in the presence of severe magnetic field inhomogeneity, being known as the Carr–Purcell–Meiboom–Gill (CPMG) pulse sequence.[102,103] The method was revisited later to separate inhomogeneous and homogeneous contributions to the line broadening in NMR studies of organic solids,[104] including the synchronisation of the multiple-pulse train with the rotor period in MAS experiments.[105] These authors noted that the FT of the whole echo train gives rise to a spectrum made of ''spikelets'' placed symmetrically around the carrier frequency, whose separation in the frequency domain is equal to the inverse of the time spacing between the echoes. The linewidth of each individual spikelet is dictated by homogeneous interactions, whereas the envelope of the spikelet spectrum is dominated by inhomogeneous interactions.[90] This is similar to the case of the envelope of the spinning sidebands in NMR spectra obtained in MAS experiments (performed with a relatively slow spinning rate), which yields a powder pattern corresponding to that of the static sample.[106]

In 1997, Larsen et al. proposed the use of a ''quadrupolar version'' of the CPMG experiment, named QCPMG, showing that a substantial gain in S/N ratio could be achieved for half-integer spin quadrupolar nuclei by recording quadrupolar echo spectra and using CT-selective $\pi/2$ and π pulses.[74] The method was used to obtain the magnitudes and relative orientation of EFG and CSA tensors for nuclei exhibiting very large quadrupole couplings. The gain in S/N is clearly associated with the concentration of the spectral intensity into a set of narrow sidebands, as compared to the broad spectrum corresponding to a standard quadrupolar echo

experiment. One year later, the same group used a combination of MAS and QCPMG, synchronising the rotor period with the timing for application of the refocusing pulses (i.e. making the rotational echoes coincide with the quadrupolar echoes). The so-called QCPMG–MAS experiments were used to achieve S/N ratio enhancements of about one order of magnitude for the CT spectrum of half-integer spin quadrupolar nuclei.[75] The dominant inhomogeneous interaction in this case (associated with the envelope of the spikelets spectra) was the second-order quadrupolar broadening of the CT, which is only partially removed by MAS.[6,9]

The pulse sequence used in this QCPMG–MAS experiment is illustrated in Figure 9.[75] Part A is a conventional quadrupolar echo experiment, with CT-selective $\pi/2$ and π pulses and the τ_1 delay adjusted so that the acquisition starts at the echo top. In MAS experiments, this echo detection must be rotor synchronised, that is, $\tau_1 = \tau_r - \tau_{\pi/2}$, where τ_r is the rotor period and $\tau_{\pi/2}$ is the duration of the $\pi/2$ pulse. Part B is the repeating unit, consisting of CT-selective refocusing π pulses (with pre- and post-pulse delays of τ_2 to protect the receiver) followed by sampling of the echo for a period τ_a; this unit is repeated a number of times (M), typically as long as there is any remaining intensity in the decaying echoes to be refocused. Again, in MAS experiments, it is essential to keep the cycle in part B rotor synchronised, that is, the duration of part B must be an even multiple of the rotor period.[75] Part C is an extension of the last recorded echo for a period τ_d, allowing full signal decay and detection with a number of points according to the desired acquisition time.

The spectrum obtained by FT of the whole train of decaying echoes consists of a series of spikelets separated by the frequency $\nu_{CPMG} = 1/\tau_a$. The envelope of these sidebands is defined by the second-order quadrupolar CT lineshape under MAS. The linewidth of each spikelet is determined by the true transverse relaxation time (T_2) of the material, which is a measure of the decay time of the amplitude of the echoes in the

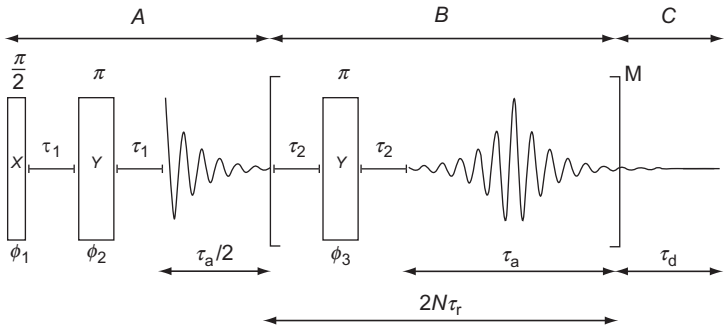

Figure 9 Pulse sequence used in QCPMG–MAS experiments. Reprinted from Larsen et al.,[75] Copyright 1998, with permission from Elsevier.

train. This intrinsic transverse relaxation is normally associated with the presence of homogeneous interactions (not refocused by spin-echo pulse sequences), including effects of molecular dynamics.[74,90,105]

The gain in S/N ratio in QCPMG experiments depends on a number of factors. First, it is clear that the higher the number of detected echoes, the higher the overall intensity in the QCPMG spectrum; this is to be compared with the intensity of a single echo detected in a conventional two-pulse (Hahn-echo) experiment. Thus, in order to obtain a reasonable S/N ratio gain, it is necessary that the decay time of the whole echo train be much larger than the decay time of the initial FID or of any individual echo (named T_2*). In the case of strong homogeneous interactions, T_2 will be comparable or even equal to T_2*, which means just a single echo will be effectively detected in the QCPMG experiment; in such a case, there is obviously no S/N ratio gain. When $T_2 \gg T_2$*, a large number of echoes will be recorded; the S/N ratio gain now depends on the echo spacing. For large separation frequencies of the spikelets (ν_{CPMG}), the whole spectral intensity is concentrated into a few narrow sidebands, leading to a high S/N ratio gain. However, with few spikelets, it is difficult to define the envelope lineshape associated with the inhomogeneous interactions (mostly the second-order quadrupolar broadening of the CT in the case of half-integer spin quadrupolar nuclei in MAS experiments) and to extract the corresponding tensor parameters, which is evidently a goal of the experiment. Thus, a judicious choice of the inter-pulse spacing (which defines ν_{CPMG}) is necessary, in order to get a reasonable S/N gain whilst at the same time keeping the desired information about the inhomogeneous interactions.[90]

Lefort et al. studied the details of the CPMG experiment with special emphasis on the achievable S/N ratio gain in MAS and MQMAS experiments involving half-integer spin quadrupolar nuclei.[76] They showed that the S/N ratio gain can be approximately calculated by the expression $G_{S/N} \cong 2\sqrt{T_2 T_{off}}\nu_{CPMG}$. In practice, T_2 is determined from the inverse linewidth of the individual spikelets, whereas T_{off} is the time required for the signal to become comparable with the noise level in a standard two-pulse experiment (which is normally the same for the initial FID or for any individual echo in the CPMG echo train). Several methods of data processing were also discussed for improving the analysis of CPMG-derived spectra, including the reconstruction of the ''conventional'' spectrum by superimposing all echoes, the shifting of echoes in order to modify the effective echo spacing (and thus ν_{CPMG}) and the use of optimised filtering.[76]

QCPMG experiments, both for static and for spinning samples, have been extensively used for S/N ratio enhancement in experiments involving many half-integer spin quadrupolar nuclei, including ^{25}Mg (as exemplified in the next section), ^{33}S, ^{35}Cl, ^{39}K, ^{67}Zn and ^{87}Sr. In many of these

cases, QCPMG was combined with other enhancement schemes based on polarisation or population transfer, such as cross-polarisation (CP), DFS, RAPT and the use of adiabatic pulses.[36,54,90,91]

2.4. Examples in ^{25}Mg NMR

^{25}Mg is an obvious natural case for the application of signal-enhancement schemes such as those described in the previous sections. The pioneering report of the use of QCPMG in studies of half-integer, low-γ nuclei, including ^{25}Mg, was presented by the same authors who proposed QCPMG as a sensitivity-enhancement method.[36] $Mg(VO_3)_3$ was used as a model compound in this study. Shortly after, Ellis and collaborators reported the first of a series of papers devoted to the study of Mg^{2+} and Zn^{2+} sites in proteins and protein complexes.[54–57] For such purposes, they developed a special probe for low-temperature experiments (down to 10 K) at magnetic fields up to 18.8 T and employed ^{1}H—^{25}Mg CP combined with QCPMG. After testing this approach with a number of model compounds, these authors applied the method to characterise the binding sites for Mg^{2+} in a DNA repair protein. They demonstrated the presence of a single specific binding site, but with disorder in the Mg^{2+} environment leading to more than one set of quadrupole parameters.[57]

As mentioned in the previous section, the QCPMG method is especially helpful for recording spectra with large inhomogeneous broadening, as is commonly the case of the quadrupolar-affected CT resonance in ^{25}Mg NMR spectra. As an example, we show in Figure 10 the QCPMG time domain signal and the corresponding spikelets spectrum recorded for magnesium acetylacetonate dihydrate ($Mg(Acac)_2 \cdot 2H_2O$) in a static experiment. This spectrum spans a total range of ca. 80 kHz (inhomogeneous broadening), whereas each spikelet has about 60 Hz linewidth (homogeneous broadening). QCPMG spectra can be numerically simulated to yield the quadrupole and chemical shift parameters, using programmes such as SIMPSON, for example.[21] It is common practice, however, to simulate the complete inhomogeneously broadened spectrum, obtained in a conventional Hahn-echo experiment or from the envelope of the spikelets in the QCPMG spectrum, which can be done using packages especially developed for fitting purposes, such as DMFIT[19] or WSolids1.[23] In the case of $Mg(Acac)_2 \cdot 2H_2O$, whose QCPMG spectrum is shown in Figure 10, a simulation of a conventional Hahn-echo spectrum by Cahill et al. yielded the values $\delta_{iso} = -1(1)$ ppm, $C_q = 7.1(2)$ MHz and $\eta_q = 1.00(1)$,[40] in reasonable agreement with the values $\delta_{iso} = 2.7(4.0)$ ppm, $C_q = 7.2(1)$ MHz and $\eta_q = 0.96(2)$ reported by Pallister et al.,[39] who used a combination of static QCPMG, QCPMG–MAS and static Hahn-echo experiments.

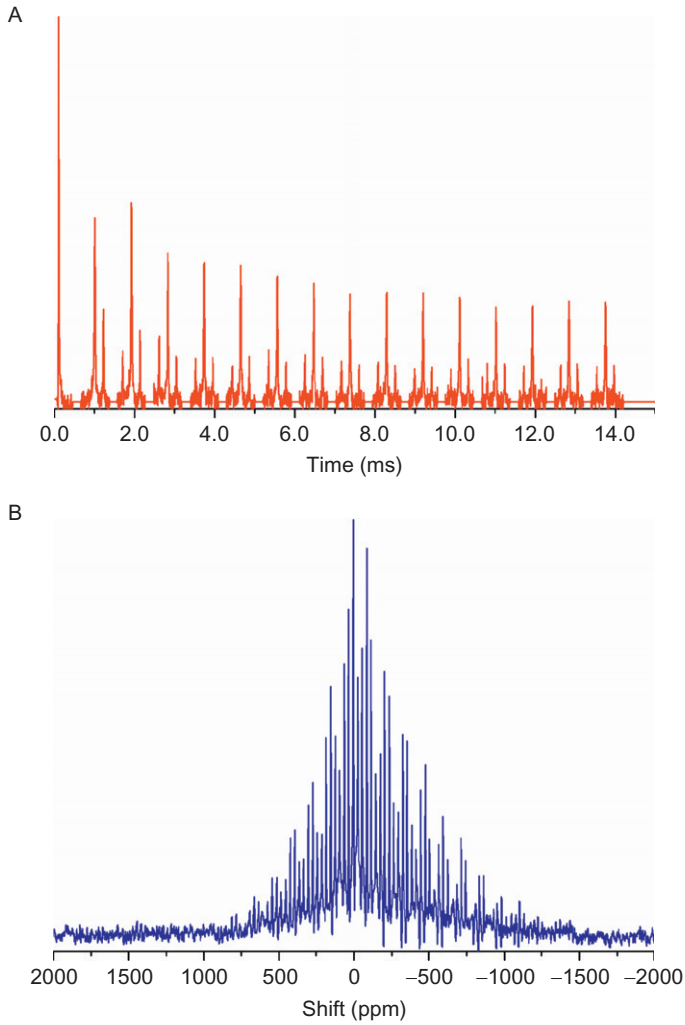

Figure 10 ^{25}Mg QCPMG NMR time domain signal (A) and the corresponding spectrum (B) recorded for $Mg(Acac)_2 \cdot 2H_2O$. A static powder packed into a 14 mm diameter sample holder was used in this experiment, which was performed at 14.1T, with ν_{CPMG}=1.1kHz. Shifts are given relative to 1 1M $MgCl_2$ aqueous solution.

^{25}Mg QCPMG spectra with good S/N ratio were recorded also for other Mg-containing organic complexes, including bis(cyclopentadienyl) magnesium ($MgCp_2$)[107] and monopyridinated aqua(magnesium) phthalocyanine,[51] with quite large C_q values of 5.80 and 13.0MHz, respectively. More recently, many other studies involving ^{25}Mg QCPMG NMR

appeared, including investigations about the Mg environment in microporous Mg-containing aluminophosphates with varying Al/Mg ratios[38] and in layered Mg phosphates.[108] ^{25}Mg QCPMG NMR was also used to probe the Mg environments in the Mg silicate forsterite (Mg_2SiO_4)[109] and to study its dissolution mechanism—in this case, using information provided by ^{1}H—^{25}Mg CP QCPMG NMR spectra as well.[110] Moreover, Pallister et al.[39] made wide use of QCPMG (in static and in MAS-synchronised experiments) for the analysis of a series of organic and inorganic Mg compounds presenting large C_q values (typically above 5MHz). The compounds with reported QCPMG spectra included Mg_3N_2, $Mg(VO_3)_2$, $Mg_3(VO_4)_2$, α-$MgSO_4$, β-$MgSO_4$ and $Mg(Acac)_2{\cdot}2H_2O$. The example of β-$MgSO_4$ is illustrated in Figure 11. This was the compound with the largest quadrupole coupling among the oxygen-coordinating Mg anhydrous salts studied in that work. The very broad CT static spectrum (total breadth ~120kHz) was recorded with QCPMG; the use of rotor-synchronised QCPMG–MAS (at a speed of 16kHz, which is close to the maximum value attained with the used 4mm rotor) led to the achievement of a

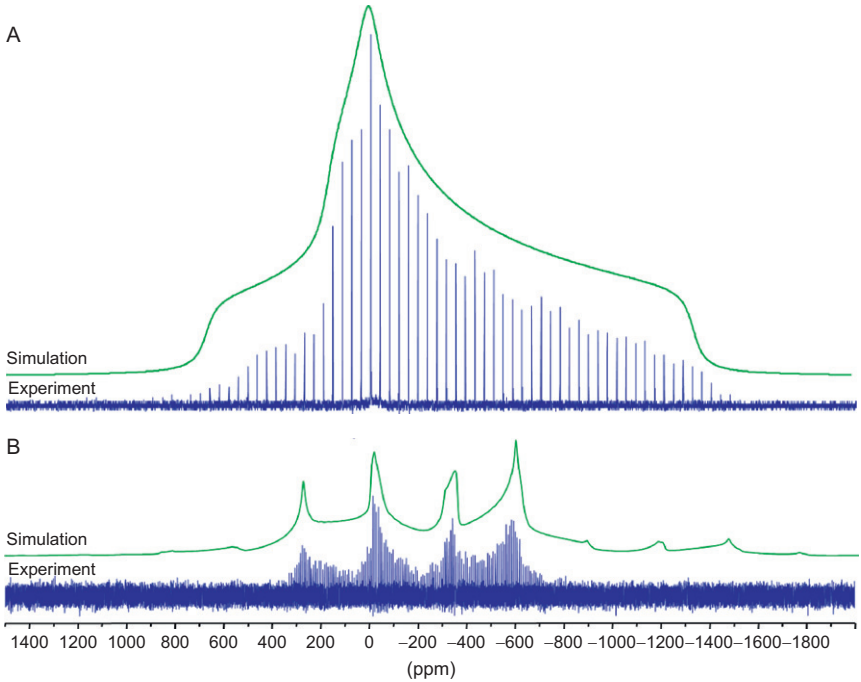

Figure 11 ^{25}Mg QCPMG NMR spectra of β-$MgSO_4$ recorded in static (A) and in MAS (B) experiments at 21.1T, compared with the respective simulated spectra. Reproduced from Pallister et al.,[39] Copyright 2009, by permission of the PCCP Owner Societies.

spectrum with a complex shape, containing intense spinning sidebands. The simulation of the envelope of both QCPMG spectra (also shown in Figure 11) allowed the extraction of the quadrupole parameters with good accuracy: $C_q = 10.4(1)$ MHz, $\eta_q = 1.00(2)$.

Regarding the use of methods based on population transfers, DFS was used in combination with QCPMG in the studies referred to above involving Mg-containing aluminophosphates[38] and phosphates.[108] In 2008, Freitas et al.[41] reported for the first time the use of adiabatic inversion pulses with the purpose of enhancing the CT signal in ^{25}Mg NMR spectroscopy. The model compound used in that work was magnesium disodium ethylenediaminetetraacetate tetrahydrate ($Na_2MgEDTA \cdot 4H_2O$). As mentioned in Section 1.4, this compound showed a moderate quadrupole coupling ($C_q = 1.675$ MHz) and fast spin–lattice relaxation, allowing the achievement of spectra with high S/N ratio in short time: a recycle delay of 50 ms combined with an acquisition time of 40 ms was sufficient for the complete recovery of the thermal equilibrium populations of the $\pm 1/2$ energy levels in MAS experiments. Due to these facts, this compound was extensively used as a ''test sample'' for the implementation of signal-enhancement methods, using the experimental set-up tuned at the ^{25}Mg NMR frequency.[41] In that work, the authors compared the performance of WURST and HS pulses with DFS, achieving enhancement factors of 2.2 for the adiabatic pulses and 2.6 for DFS (as compared to the CT intensity recorded in a standard Hahn-echo experiment). These somewhat low enhancement factors (compared with the ideal values of 3.0 and 5.0 in the cases of complete saturation and perfect inversion in the right order of all STs, respectively, as described before) were attributed to the fast spin–lattice relaxation found for ^{25}Mg nuclei in $Na_2MgEDTA \cdot 4H_2O$, which causes a rapid re-establishment of thermal equilibrium populations after the disturbing DFS or adiabatic pulses. This relaxation leads to a partial destruction of the effects of these signal-enhancement methods during the execution of the pulse sequence. Also, this explains why the DFS method gave a higher enhancement factor, since the used adiabatic pulses were longer than the DFS pulse.

As described in Section 2.2, the performance of adiabatic pulses is especially sensitive to the values of the frequency offsets of the pulses and this aspect is also affected by the probe response to the large offsets eventually used for the pulses. The offset dependence of the enhancement factors obtained with use of HS pulses was also investigated, taking advantage of the ease to obtain ^{25}Mg NMR spectra with good S/N ratio in $Na_2MgEDTA \cdot 4H_2O$.[41] Some illustrative results are shown in Figure 12, where the enhancement factors obtained in ^{25}Mg MAS NMR spectra are plotted against the offsets of the HS pulses used to disturb the populations of the energy levels. The same plot also includes the theoretical first-order quadrupole static powder pattern, calculated using the parameters

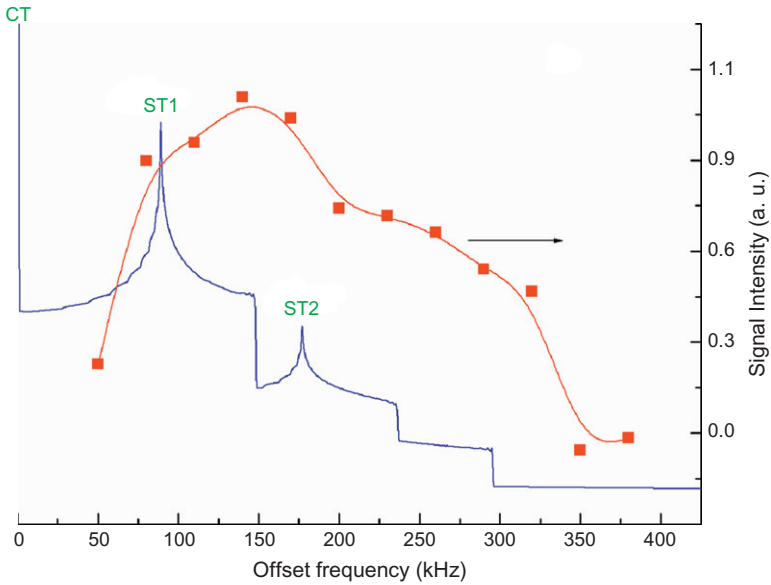

Figure 12 Offset dependence of the intensity of the CT resonance in ^{25}Mg MAS NMR spectra of $Na_2MgEDTA{\cdot}4H_2O$, recorded with a single HS pulse placed before the spin-echo sequence. The experimental data (square points) were recorded using a 7 mm probe (with 7 kHz MAS rate); the solid red line is just a guide for the eyes. Also shown (blue line) is the simulated first-order quadrupole static powder pattern for the single Mg site in this compound.

experimentally determined from ^{25}Mg MAS NMR spectra in $Na_2MgEDTA{\cdot}4H_2O$: $C_q = 1.675(5)$ MHz, $\eta_q = 0.15(1)$, $\delta_{iso} = 0.25(10)$ ppm.[41] This plot illustrates a feature already discussed in Section 2.2 and frequently reported for other half-integer spin quadrupolar nuclei[85,100]: the enhancement factor curve has a broad maximum for offsets in the region around the most intense singularities of the static powder pattern, which correspond to the most intense spinning sidebands in MAS experiments. Further, the signal-enhancement factors decrease for very short or very large offsets but this depends also on the frequency response of the RF probe.[41] This type of analysis of the effects of the large offsets typically used for adiabatic inversion pulses is very useful for proper optmisation of signal-enhancement methods based on population transfer; it is clearly advantageous to perform these tests at the ^{25}Mg NMR frequency with a sample with good sensitivity such as the $Na_2MgEDTA{\cdot}4H_2O$ compound.

Other examples of use of methods based on population transfers in ^{25}Mg NMR were provided in the comprehensive work by Cahill et al.[40] These authors used FSG-RAPT as a routine signal-enhancement technique

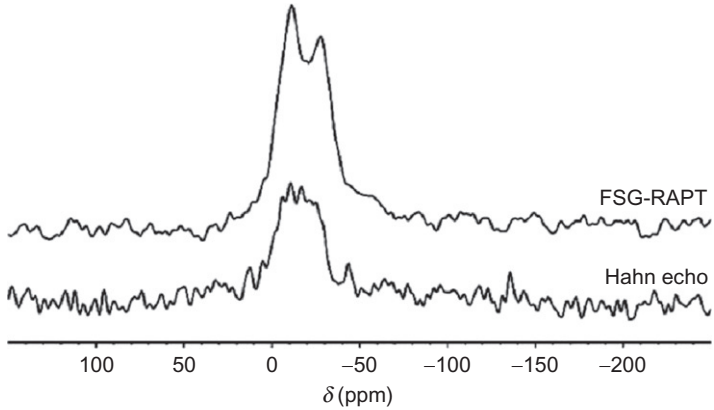

Figure 13 ^{25}Mg MAS NMR spectra of $MgCO_3 \cdot Mg(OH)_2 \cdot 3H_2O$, recorded using the FSG-RAPT signal-enhancement method (top) and a simple two-pulse Hahn-echo experiment (bottom). Both spectra were acquired at 11.75T, with the same experimental conditions. Reproduced from Cahill et al.,[40] Copyright 2009, with permission from Wiley.

executed before the recording of a two-pulse Hahn-echo experiment. A fixed offset (200kHz) was used for the FSG pulses at 11.75T, leading to moderate sensitivity enhancement for a variety of different organic and inorganic compounds. As an example, Figure 13 shows a comparison of the ^{25}Mg MAS NMR spectra of the compound $MgCO_3 \cdot Mg(OH)_2 \cdot 3H_2O$, obtained with and without use of the FSG-RAPT pulse train. Both spectra were recorded using the same experimental conditions so that the difference in the observed intensities is a direct measure of the enhancement provided by FSG-RAPT. In this case, the enhancement factor was ca. 1.8, significantly below the theoretical limits. This was attributed to the limited bandwidth of the RF probe, which precluded the use of large offsets. However, the increase in S/N ratio compared to a simple two-pulse experiment is evident, showing how useful these techniques based on population transfers are, even without detailed optmisation.

3. FIRST-PRINCIPLES CALCULATIONS IN SOLID-STATE ^{25}MG NMR

Calculations of chemical shielding and EFG parameters for crystalline materials have become a valuable tool for the interpretation of solid-state NMR data. With the advent of powerful computational resources and methods that allow calculations to be performed within a reasonable time, quantum chemical first-principles approaches are nowadays feasible and of very great applicability to NMR.[111–113] Former studies dealt with the prediction of chemical shifts and other NMR parameters from

first principles in isolated molecules and clusters, with use of computational packages well known in quantum chemistry, such as Gaussian.[114–116] Whereas these methods showed some success in solid-state NMR spectroscopy, the need to take into account long-range interactions demanded the development of techniques appropriate for extended systems. In crystalline materials, the translational symmetry can be exploited to allow calculations of parameters depending on long-range effects, such as the electrostatic interactions responsible for EFGs in crystal lattices. Approaches including the full-potential linearized augmented plane wave (FPLAPW) and the projector augmented wave (PAW) methods were applied with success for EFG calculations and interpretation of quadrupole parameters derived from NMR or NQR data in many solids.[117–121] An ''all-electron'' scheme using density functional theory (DFT) approach combined with FPLAPW and related methods was implemented into the Wien code, which has been used for many years for calculating several electronic and magnetic properties of crystalline materials.[122,123] This scheme is recognised for its high accuracy but suffers from the limitation of significant computational cost.

To calculate chemical shielding in the solid state, it is necessary to consider the electronic response of crystalline systems to an applied magnetic field. Former studies employed molecular cluster models for these calculations, with the gauge-including atomic orbital (GIAO) method[124] and by testing different basis sets implemented in packages such as Gaussian, for example.[116] More recently, an alternative approach appeared, allowing first-principles calculations of EFG and chemical shielding parameters (among other properties) in extended systems, as implemented in the CASTEP code.[125,126] This DFT-based code employs the gauge-including projector augmented wave (GIPAW) formalism, combined with plane-wave basis sets and pseudopotentials to distinguish between core and valence states.[111,113,127] CASTEP is currently the most commonly used code to perform calculations of parameters in solid-state NMR of crystalline systems.

There are several examples of successful calculations of shielding and EFG parameters for many quadrupolar nuclides in solid-state NMR (see, e.g., Ref. 128 and references therein). In the case of ^{25}Mg nuclide, earlier reports involving computation of NMR parameters were generally concerned with EFG tensor calculations, either using point-charge models or the FPLAPW approach.[53,72,117,129,130] The first quantum-chemical-based predictions of ^{25}Mg chemical shielding parameters (together with EFG data as well) were carried out using Gaussian, in systems restricted to a single molecule or to small molecular clusters.[50,51,107] CASTEP calculations for ^{25}Mg started to be reported in the mid-2000s[45,131] and, in 2009, two extensive independent accounts appeared almost simultaneously, comparing CASTEP predictions to ^{25}Mg NMR experimental data in a

series of organic and inorganic compounds.[39,40] More recently, CASTEP calculations have been used to support experimental solid-state ^{25}Mg NMR results in various materials, such as the ferroelectric compound $BaMgF_4$,[132] the polymorphs of enstatite ($MgSiO_3$)[133] and some layered Mg phosphates (in this latter case with comparison to results of Gaussian calculations obtained using molecular clusters).[108]

One of the pioneering reports of calculations of ^{25}Mg NMR parameters was a paper co-authored by the creators of Wien code.[117] In this work, EFG tensor calculations for both ^{25}Mg and ^{17}O nuclei were performed for forsterite (Mg_2SiO_4) with the FPLAPW method, with use of either the generalized gradient approximation (GGA) or the local density approximation (LDA) for computing the charge density.[112] After comparing the EFG parameters (V_{ZZ} and η_q) with previously reported experimental values,[53] the conclusion was that the GGA performed better. It is interesting to observe that such former Wien calculations gave better results when compared to experimental data—reported independently and in reasonable agreement by Derighetti et al.,[53] Pallister et al.[39] and Davis et al.[109]—than recently reported CASTEP calculations.[39,40] A similar situation occurred also in the case of magnesite ($MgCO_3$), for which Wien calculations reproduced quite well the experimental C_q value[129]; on the other hand, the values obtained with CASTEP (even after geometry optimisation) were significantly discrepant, which led the authors to describe this observation as ''a mystery''.[39] Wien calculations were also used to interpret the ^{25}Mg EFG parameters in the intermetallic superconductor compound MgB_2, in excellent agreement with experimental results.[72,130]

The molecular cluster approach was used to calculate EFG and shielding tensors in a number of Mg-containing organic complexes, including metalloporphyrins and chlorophyll, using the Gaussian package.[50,51,107] Special care was taken in these reports regarding the choice of the basis sets, which was evaluated by considering the agreement between predicted and experimental results. This approach was reasonably successful especially for EFG calculations in these materials, which are, in general, simpler and less demanding of computational capacity than chemical shielding calculations. The largest ^{25}Mg C_q values ever reported were found in nitrogen-containing compounds presenting Mg—N bonds, as in bis(pyridine)-(5,10,15,20-tetraphenylporphyrinato)magnesium(II) (15.32 MHz), monopyridinated aqua(magnesium) phthalocyanine (13.0 MHz) and chlorophyll *a* (12.9 MHz); these values agreed reasonably well with Gaussian-predicted results[50,51] and also with CASTEP calculations.[40] Information on chemical shielding was difficult to obtain experimentally in most of these samples due to the strong quadrupolar broadening of the resonance lines. A remarkable case was that of the compound bis(cyclopentadienyl)magnesium ($MgCp_2$), for which ^{25}Mg QCPMG NMR spectra revealed the largest shielding ever reported for ^{25}Mg ($\delta_{iso} = -91$ ppm).

This result was correctly predicted by Gaussian calculations, which also predicted a small CSA effect, difficult to observe at the magnetic field strength used in that study.[107] As for EFG data, the best results were obtained with the restricted Hartree–Fock (RHF) method, but the agreement with the experimental values was marginal: the calculated values closest to the experimental data [$C_q^{exp} = 5.80(5)$ MHz and $\eta_q^{exp} = 0.01(1)$] were $C_q^{calc} = 5.13$ MHz and $\eta_q^{calc} = 0.23$. This discrepancy was attributed to the inability of the single-molecular approach used to represent the long-range electrostatic interactions responsible for the EFG. In fact, more recent CASTEP calculations using the PAW approach predicted $C_q^{calc} \cong 6.0$ MHz and $\eta_q^{calc} \cong 0.1$, in better agreement with the experimental data.[39,40]

CASTEP calculations have also been performed in many crystalline inorganic Mg compounds. MgO is probably the simplest Mg compound to be studied, with a cubic environment around the Mg^{2+} ion and thus zero EFG at the ^{25}Mg nucleus. Rossano et al.[131] studied the effect of temperature increase in the range of 25–1000 °C on the calculated ^{17}O and ^{25}Mg chemical shifts, using the GIPAW method. They showed that the experimentally observed increase of the isotropic chemical shift as a function of temperature[134] could not be accounted for solely by thermal expansion of the crystalline lattice; instead, it was necessary to consider the vibrational corrections associated with thermal fluctuations of atoms around their equilibrium positions.[131] $MgBr_2$ was also investigated in a study involving ^{25}Mg as well as ^{79}Br and ^{81}Br NMR experiments plus first-principles calculations. CASTEP-derived ^{25}Mg C_q values were three to four times bigger than the experimental result (0.85 MHz), with the best agreement obtained after full geometry optimisation of the crystalline structure of the compound.[45] However, it is intriguing that excellent agreement has been obtained between experimental and calculated EFG parameters for ^{79}Br/^{81}Br nuclei after structure optmisation, whereas the agreement achieved for ^{25}Mg data was quite poor.

Comprehensive ^{25}Mg NMR investigations of a series of different Mg-containing compounds—including organic and inorganic compounds, both in oxygen as well as in non-oxygen local environments—were reported by Pallister et al.[39] and by Cahill et al.,[40] with comparisons between experimental data and CASTEP calculations of EFG and shielding parameters. EFG calculations were performed following three different strategies: directly employing crystallographic data from the literature, with full geometry optimisation of the crystal structure (i.e. allowing all atomic positions to relax) or with geometry optimisation of only the proton positions. The calculated ^{25}Mg NMR parameters were extremely sensitive to the details of the crystal structure, and the best method of geometry optimisation was somewhat different from sample to sample. In most cases, best agreement was obtained using unoptimised structures, but some exceptions were observed especially for materials where crystallographic information was

based on early X-ray diffraction data (which were not appropriate for determining atomic positions of light atoms such as hydrogen) instead of neutron diffraction. In these cases, the use of proton optimised structures was preferable. Full structure optimisation gave the best results in the case of compounds with nitrogen atoms in the first coordination sphere around Mg, which is an indication of the sensitivity of the calculations to the positions of soft ligands.[40] During geometry optimisation, it was observed that even small changes in Mg—O and Mg—H bond lengths (~0.001 Å) resulted in large changes in C_q values (up to ~0.2 MHz in some cases), which is an indication of the high accuracy required for the crystal structure in order that the predicted NMR results can be reliably compared to experimental data.

Parenthetically, it is worth noting that this difficulty is not just for ^{25}Mg NMR calculations, but it is a general feature found in many modern computational methods applied to NMR analysis, both for spin 1/2 and for quadrupolar nuclei. It seems that many former (and in some cases well established) crystallographic data need to be revised in light of the new information brought about by ''NMR crystallography'' methods.[128,135,136] Strategies for structure determination based on first-principles methods have been proposed as a means of complementing/correcting previous diffraction results or to address new structures not accessible to conventional diffraction experiments (see Ref. 137 and references therein).

^{25}Mg NMR spectra recorded for both organic and inorganic salts showed that EFG and shielding parameters are extremely sensitive to hydration effects,[33] a behaviour that was correctly reproduced by CASTEP calculations.[39,40] The hydrated Mg sulphates provide a good example of this. The ^{25}Mg NMR spectra of $MgSO_4 \cdot H_2O$ (one site with large disorder in Mg environment), $MgSO_4 \cdot 6H_2O$ (two sites) and $MgSO_4 \cdot 7H_2O$ (one site) are very different.[40] CASTEP calculations of C_q, η_q and δ_{iso} gave acceptable results in the case of $MgSO_4 \cdot H_2O$[40] and $MgSO_4 \cdot 7H_2O$.[39,40] As for $MgSO_4 \cdot 6H_2O$, although similar MAS spectra were presented by Pallister et al.[39] and by Cahill et al.,[40] different fitting models were used in these reports, giving discrepant EFG and shielding parameters. Pallister et al.[39] used spectra recorded with MAS and in static experiments, obtaining $C_q = 0$ and 2.147 MHz for sites 1 and 2, respectively. These values did not compare well with the CASTEP predictions of 3.460 and 1.904 MHz, respectively. A better agreement with CASTEP-predicted values was obtained by Cahill et al.,[40] who used experimental spectra recorded at multiple magnetic field strengths (11.7, 14.1 and 18.8 T) to constrain the spectral simulation. It is interesting to mention that, in the case of one of the crystalline sites (named site 1), the best agreement between experimental (1.65 MHz) and the calculated (1.40 MHz) C_q value was obtained without any structure relaxation (i.e. using an unoptimised structure from the literature). However, for site 2, with an experimental

C_q of 2.40MHz, the unoptimised structure calculation gave C_q=1.86MHz, whereas full geometry optimisation led to a much better calculated value of C_q=2.36MHz. These facts illustrate that the choice of the best structure to be used in calculations of ^{25}Mg NMR parameters is still an open issue that needs to be addressed case by case.

Besides being useful for interpretation of ^{25}Mg NMR data, first-principles calculations of EFG parameters are also valuable when experimental data are not available or are difficult to obtain for some specific sites. A nice example of this is provided by the ^{25}Mg NMR studies of enstatite ($MgSiO_3$). Although the crystal structure of the room temperature polymorphs of enstatite contains two Mg sites, only one site was detected in early ^{25}Mg MAS NMR experiments, with C_q estimated at ~2.4MHz.[34] However, CASTEP calculations predicted very different C_q values for the two sites (2.54 and 14.0MHz).[40] The site with larger C_q is quite difficult to be observed using standard MAS or static experiments, due to excessive quadrupolar broadening; so in this case, the results of first-principles calculations were useful to guide the experiments aiming the observation of the previously missing Mg site. The two sites were unambiguously detected in a recent study[133] of two enstatite polymorphs (clinoenstatite and orthoenstatite), using QCPMG and the variable offset cumulative spectroscopy (VOCS) method to allow the detection of the severely broadened spectrum associated with the site with larger C_q. The experimental values were C_q=2.6 and 2.8MHz for the first site and C_q=12.6 and 12.8 MHz for the second site in clinoenstatite and orthoenstatite, respectively. In this study, new CASTEP calculations were presented, with good agreement between experimental and calculated values of C_q, η_q and δ_{iso}. Calculations were performed also for a metastable polymorph (protoenstatite), predicting a large difference between C_q values for the two sites in this case, as well.[133]

The calculation of isotropic chemical shifts is also possible, but it should be noted that first-principles methods allow the calculation of the absolute shielding tensor associated with each site, whereas experimentally one measures the chemical shift with respect to a reference substance.[6] Thus, in order to make direct comparisons of isotropic chemical shifts, it is necessary to calculate beforehand the absolute isotropic shielding corresponding to the reference (σ_{ref}). This has been done before with Gaussian calculations, taking the fully hydrated Mg^{2+} ion in $[Mg(H_2O)_6]^{2+}$ as the shielding reference (since, as mentioned in Section 1.4, the commonly used experimental reference is a saturated aqueous solution of a Mg^{2+} salt such as $MgCl_2$).[50,107] To avoid the possible introduction of errors associated with this extra calculation, an alternative procedure is to take the y-intercept (i.e. at δ_{iso}=0) of the linear regression obtained from the plot of the calculated isotropic shieldings as a function of the experimental isotropic chemical shifts. This procedure was followed in several

recent reports dealing with CASTEP calculations, with quite consistent values obtained independently (and using different sets of experimental and calculated values) for σ_{ref}: 566.1(1.0),[39] 565(3),[40] and 565.7 ppm.[133]

In the case of materials with multiple Mg sites, the results of DFT calculations of isotropic chemical shifts help in the assignment of the different NMR peaks. This is the case of $MgSO_4 \cdot 6H_2O$, for which the calculated δ_{iso} values of 7 and 4 ppm allowed (together with the C_q values mentioned above) the assignment of sites 1 and 2, with experimental δ_{iso} values of 6 and 5 ppm, respectively.[40] Mg formate dihydrate is another example of this: the existence of two crystallographically distinct sites (but with close values of Mg—O bond lengths and O—Mg—O bond angles) in ^{25}Mg NMR spectra was demonstrated using MQMAS by Sham and Wu,[49] but no assignment of the NMR parameters to each site was possible. Cahill et al.[40] studied this compound again, recording spectra at multiple magnetic field strengths and obtaining quadrupolar and shielding parameters different from those of Sham and Wu.[49] This discrepancy—which was also noted by Pallister et al.[39] in other organic compounds—was attributed to possible problems with purity and/or hydration degree of the samples used in the Sham and Wu study. Using CASTEP calculations of isotropic chemical shifts and EFG parameters, Cahill et al.[40] were able to unambiguously assign the distinct resonances to each crystallographic site of Mg formate dihydrate.

DFT calculations also help to study the contribution of CSA to the spectral lineshape, which is generally difficult to assess in ^{25}Mg NMR spectra due to the dominance of quadrupole effects. An example of this was provided by Hung and Schurko,[107] as mentioned above, who used Gaussian calculations in $MgCp_2$ to predict a small CSA contribution to the ^{25}Mg NMR powder pattern, with a span of $\Omega \sim 40$ ppm. This could not be verified by comparison with experimental results, since the quadrupole effects were far more important at the modest (compared to today's state-of-art) magnetic field strength of 9.4 T. The good agreement between the calculated and measured isotropic chemical shifts lent, however, good confidence on the reliability of the CSA tensor predictions. CSA tensor parameters were calculated using CASTEP by Pallister et al.,[39] and observable effects at high magnetic field (21.1 T) were reported for $Mg(OH)_2$ (brucite), Mg_3N_2 and α-$MgSO_4$. The largest observed anisotropy value ($\Delta\delta$) was obtained for Mg_3N_2, with an experimental value of 42(6) ppm and a calculated value of 40.84 ppm. This compound showed the most deshielded Mg environment, with experimental and calculated δ_{iso} values of 101(2) and 100.9 ppm, respectively. A calculation was also performed for $MgCp_2$ (although no new experimental result at a magnetic field higher than the one used by Hung and Schurko[107] was presented), with an anisotropy of $\Delta\delta = 53.74$ ppm. In most cases, however, the calculated CSA effects were minutely compared to the quadrupolar ones.[39]

To conclude this section, we present in Figure 14 a plot of calculated versus experimental values of δ_{iso} and C_q, constructed mostly from the results of the two comprehensive CASTEP-based reports mentioned above,[39,40] but also including a number of other results.[38,45,50,51,72,107–109,117,129,132,133] It is interesting to note that a good correlation is observed for a quite wide range of chemical shifts (Figure 14A), effectively from 100 to −100 ppm. Apart from some extreme cases—high deshielding for Mg_3N_2 and Mg_2Si, the largest shielding for $MgCp_2$—most δ_{iso} values are clustered around 0 ppm, especially for compounds with Mg in octahedral O-coordinating environments.[39]

As for C_q calculations (Figure 14B), good agreement between measured and calculated values is generally obtained, including the cases of very large quadrupole couplings referred to above (organic compounds with Mg—N bonds and one of the Mg sites in enstatite), but a number of failures and drawbacks are also noted. Similar plots for the asymmetry parameter (η_q) show considerably higher scatter and less agreement between calculated and measured values.[40] Distinct from the chemical shift case (where the points are more or less symmetrically distributed around the line corresponding to a slope of 1), there is a trend for overestimation of C_q in all classes of compounds. EFG calculations in forsterite ($Mg_2Si_2O_4$), magnesite ($MgCO_3$) and $MgBr_2$ are among these cases, as mentioned above, and other compounds with poor agreement between theoretical and experimental data include $Mg(VO_3)_2$ and $Mg(NO_3)_2 \cdot 6H_2O$. Apart from inaccuracies in the crystal structures used, there are other effects that can contribute to lack of agreement between experimental and calculated values. First, a precise knowledge of the degree of hydration in the case of Mg salts (which can be sensitive to ambient moisture) is necessary. Elemental analysis and thermogravimetry help to assure that one is dealing with the same compound (and hopefully with the same structure) both in the experiments and in the calculations. Another important point to be considered is the effect of thermal motion of the atoms/ions. All calculations are usually based on rigid crystal structures, corresponding to 0 K (an exception to this is the already-mentioned theoretical work by Rossano et al.[131] on MgO). On the other hand, all NMR experiments reported above were performed at room temperature, where atomic motion is certainly present. This can be particularly problematic for soft ligands and water molecules. The averaging effect associated with thermal motion can be one of the reasons for the generally observed fact that calculated C_q values were mostly overestimated as compared to experimental data.[39,40] Finally, the existence of problems intrinsically related to the pseudopotentials used to represent the electronic wavefunctions for Mg and neighbouring atoms has also been considered as a possible source of disagreement between calculated and CASTEP-predicted NMR parameters.[39,132]

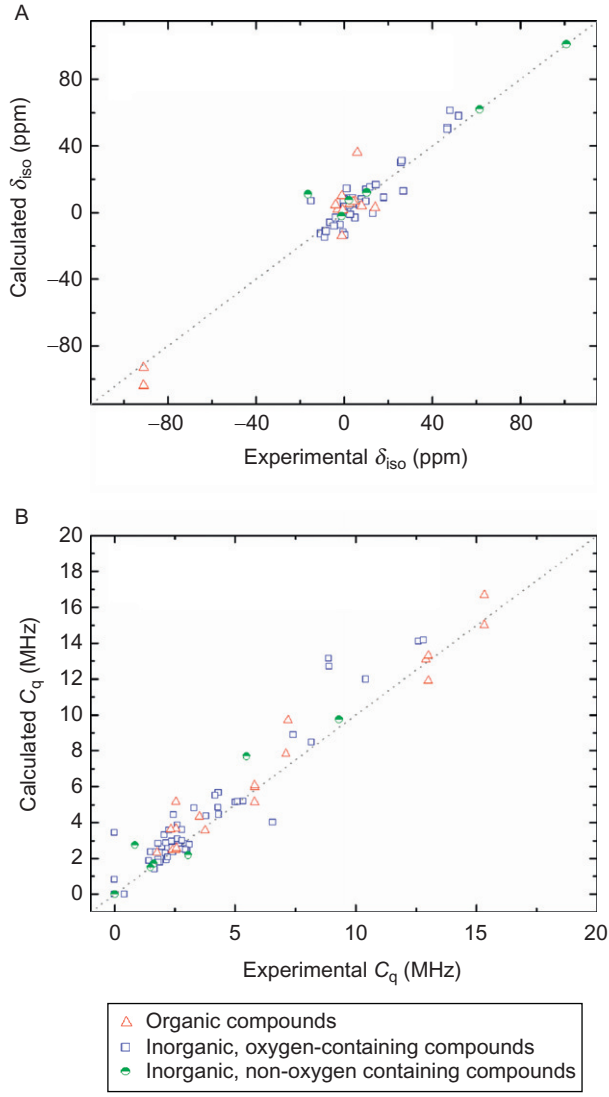

Figure 14 Comparison between calculated and experimental values of δ_{iso} (A) and C_q (B), for different Mg-containing compounds. Data taken from Refs. 38–40,45,50,51,72,107–109,117,129,132,133. The line corresponding to a slope of 1 is shown, to illustrate the deviation between the experimental and calculated values. In the case of different experimental and/or calculated values reported for the same compound, all available data are included. The calculated values in each case correspond to the best choice among the various available possibilities given in each independent report.

4. APPLICATIONS OF SOLID-STATE ^{25}MG NMR

4.1. Mg metal, alloys, MgB_2 and other intermetallics

The main experimental difficulties associated with ^{25}Mg NMR measurements in metallic samples come from the usually broad character of the spectra (affected by Knight shift and quadrupole coupling) and the skin depth problem related to the electrical conductivity of the material.[138] Due to these facts, spectra are typically recorded using fine powders (or files), with broadband probes and by employing echo pulse sequences.[6]

^{25}Mg NMR results for hcp Mg metal have been recently revisited by Bastow and Celotto,[73] using a moderate magnetic field strength (9.4T). They reported a well-defined spectrum dominated by first-order electric quadrupole coupling, with clearly visible ST features surrounding the sharp CT line. From this spectrum, values of $C_q = 0.260(5)$MHz and $\eta_q = 0$ (consistent with the axial symmetry imposed by the hcp crystal structure) were derived, along with the isotropic Knight shift (K_{iso}) of 1150(5) ppm. These values compare well with previously reported data.[58,69,71] The spectral lineshape was analysed in detail by Bastow and Smith.[70] The filing process was found to affect the quadrupole powder pattern, with the singularities associated with STs being severely smeared as consequence of the creation of a distribution of EFGs within the material; on the other hand, after annealing the sample, these singularities were clearly observed, allowing the accurate measurement of quadrupole coupling parameters. By comparing static and MAS spectra, the origin of the broadening of the CT resonance in the static case was attributed to a combination of Knight shift anisotropy (KSA), dispersion of isotropic Knight shifts, dipole–dipole coupling and second-order quadrupole effects, all these affected by residual structural defects not removed by annealing.[70] The temperature dependence of Knight shift and quadrupole parameters in Mg metal was also investigated. A reduced temperature coefficient was determined for K_{iso}, as compared to other hcp metals (such as Zn and Cd). In the range from room temperature up to the melting point of Mg metal (922K), K_{iso} was found to increase up to ca. 1220ppm.[71] At low temperatures, K_{iso} [58] and the Korringa product T_1T[69] were both reported to be nearly temperature independent. The quadrupole coupling showed a much stronger temperature dependence, with ca. 10% increase on decreasing the temperature from 400 to 150K.[69]

Mg–Al alloys and intermetallics have been the focus of many investigations motivated by the interest in these materials due to their industrial use in the manufacture of lightweight components. ^{25}Mg NMR spectra of Mg-rich alloys are similar to Mg metal. The alloy Mg–6wt% Al was studied by Bastow and Smith,[70] who reported a slight shift of the resonance compared to that found in pure Mg metal (~16ppm upfield) and a

strong increase in the CT linewidth (fivefold), this latter effect being attributed to a distribution of Knight (or chemical) shifts caused by Al substitution into Mg sites. At the same time, the ST singularities were smeared out, as a consequence of the existence of a distribution of EFGs also associated with substitutional disorder, and the C_q value showed a reduction of ~15% in comparison to Mg metal. The intermetallic compound $Mg_{17}Al_{12}$, which precipitates as a stable phase in Mg-rich Mg–Al alloys, was also investigated by ^{25}Mg NMR. The spectrum was composed of three separate resonances, associated with the three crystallographically distinct sites in the structure of the compound.[70,73] One of the sites (named 2a, with the lowest occupancy) had cubic symmetry, such that $C_q=0$. A second site (named 8c, with intermediate occupancy) showed axial symmetry ($\eta_q=0$) and moderate quadrupole coupling; the first-order inner STs (corresponding to $\pm1/2\leftrightarrow\pm3/2$ transitions) were not observed in a former investigation,[70] but they were clearly detected in a more recent spectrum recorded with improved S/N ratio,[73] which allowed the accurate determination of $C_q=0.87$ MHz. The third site (named 24g, with highest occupancy) showed the highest quadrupole coupling, giving rise to a CT resonance with second-order quadrupolar lineshape, from which accurate quadrupole parameters were determined: $C_q=2.2$ MHz and $\eta_q=0.90$.

In the Al-rich side of the Mg–Al phase diagram, ^{25}Mg NMR spectra of dilute Mg species entering as substitutional defects into the fcc Al lattice were composed of a single and sharp resonance with a shift quite distinct from pure Mg metal.[73] This resonance was also easily distinguished from that in the intermetallic Mg_2Al_3, which forms as a precipitate with ageing in Mg–Al solid solutions with Mg contents around 10 at.% and above. The latter resonance was also relatively narrow and showed no evidence of quadrupolar structure. Owing to the distinct shifts, growth of the Mg_2Al_3 phase was monitored as a function of ageing time in Al–10 at.% alloy, which was first quenched from the heat-treated solution at 550°C and then subjected to ageing at 150°C.[73]

Other intermetallic compounds involving Mg also studied by ^{25}Mg NMR include Mg_2Si,[33,39] Cu_2Mg,[60] Mg_2Sn, $MgZn_2$, $CuMg_2$, Y_2Cu_2Mg and Al_2CuMg.[73] Among these materials, C_q values are less than ca. 8 MHz, and Knight shifts typically lie in the range of 500–1700 ppm. The semiconducting compounds Mg_2Sn and Mg_2Si (both with cubic crystal structure) show much lower shifts, as expected, and zero quadrupole coupling. A very accurate measurement of the isotropic chemical shift in Mg_2Si was provided recently by Pallister et al.[39]: $\delta_{iso}=61.67(10)$ ppm; this value agreed well with CASTEP calculations of the shielding constant performed by the same authors.

Perhaps the Mg intermetallic compound which attracted most interest in the past 10 years is MgB_2. The reason for this lies in its superconductivity below 39 K, which is an unusually high value for a phonon-mediated

BCS superconductor.[139] Soon after the discovery of this phenomenon in March 2001, two independent ^{25}Mg NMR reports appeared (as well as many other ^{11}B NMR studies), with complementary and consistent results. The first one was by Mali et al.,[140] who performed variable-temperature static experiments on a powdered MgB_2 sample. The room temperature ^{25}Mg NMR spectrum of the CT is shown in Figure 15; the inset shows the spectrum recorded in a wider spectral range, from which the inner ST singularities can clearly be observed. These spectra were interpreted in terms of an axially symmetric Mg site in the MgB_2 hexagonal crystal structure, giving the quadrupole parameters C_q=1.480(10) MHz and η_q=0. The downfield shift of the CT with respect to the Larmor frequency of ^{25}Mg in an aqueous solution $MgCl_2$ is also apparent, allowing the calculation of the Knight shift. The authors took the point in the powder pattern corresponding to the crystallites oriented with c-axis parallel to the external magnetic field (indicated as θ=0° in the figure) to measure the component of the Knight shift tensor named K_c, since for this particular orientation, the second-order quadrupole-induced CT shift is zero.[6] The parameters K_c and C_q were measured for temperatures varying from 294K down to 19K (still in the normal conducting phase in the presence of the large magnetic field of 9.047T), remaining constant at 242(4)ppm and 1.480(10)MHz, respectively. From the deviation of the

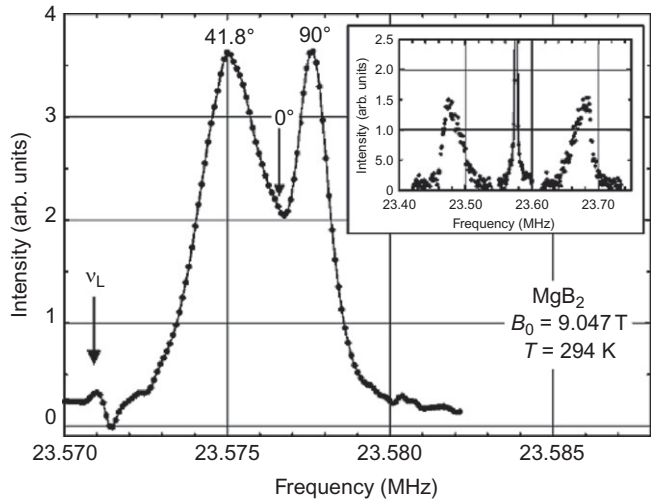

Figure 15 ^{25}Mg NMR CT spectrum of MgB_2, recorded at 294K under a magnetic field of 9.047T (corresponding to the ^{25}Mg Larmor frequency ν_L=23.571MHz). The spectral features corresponding to crystallites with c-axis oriented at three specific angles with respect to the magnetic field are indicated. Inset: The same spectrum is recorded with a higher spectral width, allowing the detection of the inner ST singularities. Reprinted with permission from Mali et al.,[140] Copyright 2002 by the American Physical Society.

observed powder pattern with respect to ideal second-order quadrupolar powder patterns, a small KSA was estimated as $K_{ab}-K_c\approx 10$ ppm. For temperatures below 19 K, the shape of the CT spectrum changed, which was interpreted as a signature of the onset of superconductivity for crystallites oriented perpendicular to the magnetic field.[140] Spin–lattice relaxation was also studied, evidencing a relaxation mechanism dominated by purely magnetic interactions. From the determined T_1 parameter, the Korringa product T_1T was calculated, which remained nearly constant in the temperature range studied (30–294 K).

The study by Bastow,[72] with commercial MgB_2 powder at room temperature, confirmed most of these findings. The quadrupole coupling constant was calculated from the separation of the inner ST singularities, giving $C_q=1.49$ MHz (and $\eta_q=0$), in good agreement with the results by Mali et al.[140] The isotropic Knight shift was determined by fitting the quadrupole perturbed CT lineshape, giving $K_{iso}=260(10)$ ppm. KSA was also estimated from this powder pattern, but the obtained value $K_{ax}=50(10)$ ppm was of relatively low accuracy and did not agree with the results by Mali et al.[140] or with theoretical predictions (see below). In fact, Bastow[72] reported that the incorporation of KSA did not improve the quality of the fitting of the CT lineshape and attributed the deviations from the expected second-order quadrupolar plus KSA powder pattern to be due to the existence of disorder in the material. Spin–lattice relaxation measurements indicated again a purely magnetic relaxation mechanism and T_1 values depending on the crystallite orientation.[72]

The experimental results of EFG, Knight shift and spin–lattice relaxation described above were in satisfactory agreement with *ab initio* calculations performed using LDA[141] or DFT-based FPLAPW methods.[72,130] Pavarini and Mazin[141] used LDA to calculate spin–lattice relaxation rates T_1^{-1} and Knight shifts for both ^{25}Mg and ^{11}B nuclei, which are related to the electronic spin susceptibility of electrons close to the Fermi level.[16] It was shown that both the Knight shift and the spin–lattice relaxation in ^{25}Mg NMR of MgB_2 are dominated by the Fermi-contact interaction. The calculated values of K_c, K_{ab} and of the Korringa product T_1T (all without any renormalization factor) showed good agreement with the experimental results reported later by Mali et al.[140] and also with the K_{iso} results of Bastow.[72] As for the EFG results, Tsvyashchenko et al. predicted the value $V_{ZZ}=-3.2\times 10^{20}$ V/m^2 for the principal component of the EFG tensor along the *c*-axis, using the FPLAPW method implemented in the Wien code[130]; a later calculation performed by Bastow using the same method agreed with this result.[72] The V_{ZZ} values derived from the experimental C_q data of Mali et al.[140] and Bastow,[72] both around 3.1×10^{20} V/m^2, were also in well accord with the absolute value of this calculation (since NMR-derived quadrupole parameters are insensitive to the sign of the EFG components). The success of the comparison between experimental data

and *ab initio* theoretical predictions in this case (which also occurred for ^{11}B NMR data) is testimony for the appropriateness of the LDA and FPLAPW methods when applied to the calculations of MgB_2 properties and parameters.

4.2. Oxide-based crystalline inorganic materials

Magnesium oxide is a good starting point to examine the use of ^{25}Mg NMR to probe inorganic materials since its rigorously cubic structure results in an EFG of zero and hence produces a narrow resonance. In series of reports, the isotropic chemical shift of MgO is given in the range of 25–26.5 ppm, which in such a narrow resonance does represent a fairly significant variation. As mentioned in Section 3, there have been two recent, extensive reports of solid-state ^{25}Mg NMR in a wide range of materials, combining experimental work with first-principles calculations.[39,40] Pallister et al.[39] suggested that the variation reported for the shift of MgO could be due to the uncertainty introduced from variations in the external reference (commonly a solution of a Mg^{2+} salt). Cahill et al.[40] looked at variations in the shift and found only a very small (~0.5 ppm) variation in the shift values for different solutions, but this could explain the differences in the MgO reported shifts. The value of the ^{25}Mg isotropic chemical shift of MgO should now be taken as 26.26 ± 0.05 ppm, from Pallister et al.[39] One of the first reports of ^{25}Mg NMR from a solid was from the paramagnetic solid solution $Ni_xMg_{1-x}O$ at 18.36 MHz.[59] MgO can exhibit a long spin–lattice relaxation time, but this is reduced by the addition of the paramagnetic ion, increasing observability. Addition of Li^+ although distorting the lattice did not cause any change in the linewidth or shift. However, addition of Ni^{2+} does cause a significant increase in the linewidth which is inversely proportional to temperature. There was also a change of intensity, as those Mg sites which are close to the Ni^{2+} centre are broadened beyond detection and the paramagnetically shifted Mg sites observed are due to more distant Ni^{2+} ions. The ^{25}Mg NMR spectrum of pure MgO has also been recorded from room temperature to 1300 °C, but there was little variation in δ_{iso} and T_1 over this temperature range.[134] The small change observed in δ_{iso} with temperature was in the opposite direction to that expected from simple bond length correlations, necessitating an explanation in terms of the orbital overlap being increased by the thermal vibration.[134] DFT calculations helped to elucidate this point,[131] as described in Section 3. A more recent study centred on ^{17}O NMR in nanocrystalline MgO with crystallite sizes in the range of 1.8–35 nm, where the ^{17}O NMR results revealed three sites, two from the bulk and one from a surface oxygen site.[142] ^{25}Mg NMR on the same samples showed that there was a progressive increase in the linewidth from 450 Hz to ~2 kHz and the corresponding isotropic shift

decreased from 25.3 to 18 ppm and could not be detected in samples with particles below 1.8 nm. To increase the stability of nanocrystalline MgO samples, SiO_2 and Al_2O_3 were added as pinning particles.[143] As samples were annealed, the nanocrystallites were preserved to higher temperatures due to the action of the pinning particles. However, there is some reaction with the pinning particle to form intermediate phases, which are spinel ($MgAl_2O_4$) and forsterite (Mg_2SiO_4). ^{25}Mg NMR on the silica-pinned sample showed the singularities of the second-order quadrupolar lineshape of one of the magnesium sites of forsterite, and the linewidth of the dominant MgO resonance decreased as the MgO particles grew.[143] ZnO shows the hexagonal wurtzite structure and magnesium has some solid solution behaviour substituting into the structure which means that in principle the magnesium should be in an MgO_4 coordination. A very ill-defined ^{25}Mg NMR lineshape was observed from $Zn_{0.85}Mg_{0.15}O$ from which it was difficult to extract any NMR parameters, but it did appear that the intensity was around −30 to −40 ppm.[144] The MgO_4 unit is expected to be quite distorted so significant second-order quadrupole effects could be shifting the resonance well away from the isotropic chemical shift. Also the 12 next nearest neighbours will be a range of combinations of zinc and magnesium, and these could also be having an effect on the electron density and hence the shielding of the nucleus. The fact that no sharp resonance was observed at the MgO position strongly indicates that the magnesium is not present as a separate oxide phase. ^{25}Mg MAS NMR was also used to study the occurrence of MgO nanoparticles in hybrid films of fluorinated polyimide (PI), prepared from Mg acetate tetrahydrate.[145] The insertion of MgO nanoparticles was investigated as a means of enhancing the thermal conductivity of the films. The ^{25}Mg NMR spectrum of the PI/MgO film cured at 380°C showed the expected resonance for MgO, clearly evidencing the conversion of the organic precursor to MgO upon thermal curing.

Magnesium hydroxide [brucite, $Mg(OH)_2$] has also been studied with reports using powders and single-crystal work.[30,34,146] Pallister et al.[39] recorded recently some high-field data on a deuterated sample (Figure 16) where it was shown that there was little difference between the MAS spectra of $Mg(OH)_2$ and $Mg(OD)_2$, indicating that the ^{1}H—^{25}Mg dipolar interaction has little effect. The parameters agreed well between the high-field value and the single-crystal work of Bastow[146] (see also Table 2). The relatively small dipolar interaction means that brucite provides one of the few examples of ^{25}Mg NMR where the CSA can be detected, with an anisotropy of $\Delta\delta = 15.75 \pm 3.00$ ppm and asymmetry of $\eta_{CSA} = 0.0 \pm 0.1$, using the definitions of Equations 4 and 5.[39] ^{25}Mg NMR has been used to investigate the role of $Mg(OH)_2$ as a fire retardant in ethylene-vinyl acetate copolymers.[147] The very significant change in the lineshape indicated that on combustion a glassy phase was formed that was the source of the

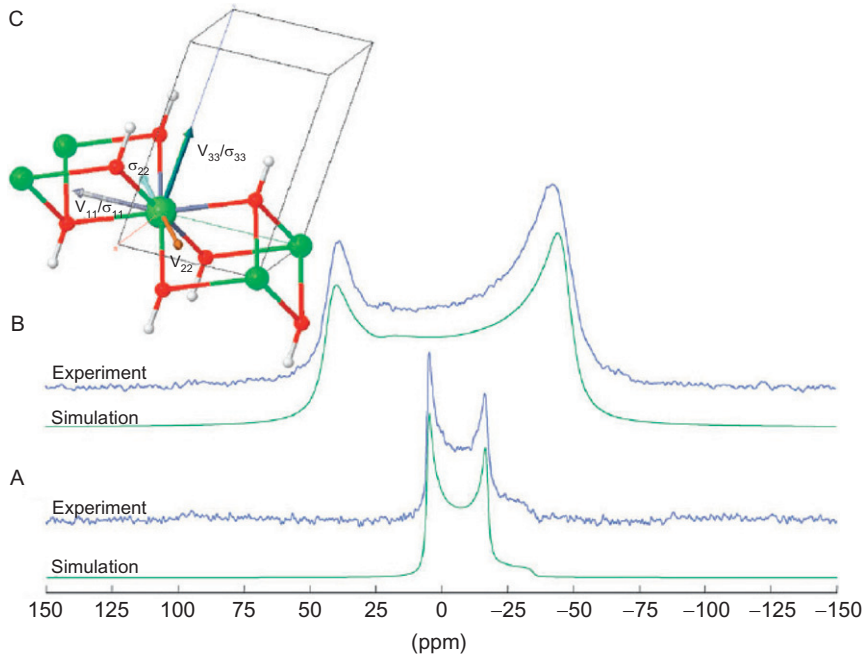

Figure 16 Experimental and simulated ^{25}Mg NMR spectra of $Mg(OD)_2$ recorded at 21.1T, for (A) MAS (10kHz) and (B) static conditions. (C) Representative portion of the brucite unit cell showing the one crystalline Mg site in the lattice. Calculated CSA and EFG tensor orientations are shown for one Mg atom. Reproduced from Pallister et al.,[39] Copyright 2009, by permission of the PCCP Owner Societies.

retarding action. ^{25}Mg NMR has been used to study the thermal decomposition of $Mg(OH)_2$ to MgO. There was definite evidence from this data of the coherent growth of small domains of MgO which then at higher temperature coalesce into larger crystallites.[64]

A range of other simple oxygen-containing compounds have been studied by ^{25}Mg NMR to determine if the NMR parameters can differentiate the oxygen coordination. $MgAl_2O_4$ made up of MgO_4 units showed a shift difference of +25ppm compared to MgO (with MgO_6 coordination).[33] Inorganic phases where the oxygen comes from water of hydration or silicate units are examined below. Recent high-field studies have compared experimentally derived parameters and those from DFT calculations in a series of anhydrous compounds.[39,40] In magnesite ($MgCO_3$), the calculations showed excellent agreement with the asymmetry parameter of $\eta_q = 0$, as expected from the C_3 symmetry for the unique magnesium site of the crystal structure.[39,129] Comparison of static and MAS data showed that there is no CSA present and accurate values of C_q were extracted

between studies, although this result could only be reproduced well by Wien calculations[129] (and not by more recent CASTEP results[39]). Five natural magnesites were compared[62] and spectra with broadly the same linewidths were observed, but with differing spectral resolution and definition of the second-order quadrupolar lineshape. Such effects are often observed in natural samples as a result of atomic substitutions, creating local structural disorder, but especially as a result of the presence of iron (and other paramagnetics) that causes paramagnetic broadening. The loss of resolution made accurate extraction of the NMR parameters difficult. The thermal decomposition of $MgCO_3$ to form MgO has also been followed by ^{25}Mg MAS NMR.[62] The much sharper MgO resonance at ~25 ppm is well separated from the second-order quadrupolar lineshape of the carbonate so the formation of MgO is readily detected. NMR reveals the presence of MgO before XRD, which can often be the case because of the differing length scale sensitivities of the two techniques. The much shorter length scale of NMR means only local MgO-like environments are necessary for its detection by ^{25}Mg NMR. The thermal decomposition of $MgCO_3$ was contrasted to that of dolomite [$MgCa(CO_3)_2$].[63] The ^{25}Mg MAS NMR spectrum of dolomite is considerably narrower than for magnesite, indicating a much more symmetric magnesium environment in the dolomite structure. As the dolomite sample is heated, again a well-separated MgO resonance is detected, although initially it is broader (65 Hz) than the eventual linewidth after heating above 800°C (35 Hz) (Figure 17). Again the presence of MgO is detected some 100°C prior to its being detected by XRD. Hence, initially some very small MgO-like domains must be formed that go undetected by XRD, which then grow to become sufficiently large that XRD can readily detect them.[63]

In the perovskite-like compound $MgTiO_3$, the NMR lineshape revealed a site with $\eta_q = 0.10 \pm 0.03$ which was accurately verified between two separate studies at different fields.[39,148] Although the crystal structure requires C_{3v} symmetry at the magnesium site, the very close agreement between the two studies must indicate that small local distortions give rise to a slightly different local geometry at the magnesium sites. Spectra from a range of oxygen-coordinated magnesium species in various inorganic compounds have been reported including various phosphates[39] and vanadates,[36,39] which are summarised in Table 2. ^{25}Mg NMR data combining static and MAS experiments at two magnetic fields (9.4, 21.1 T) along with DFS and QCPMG approaches have been reported for some layered magnesium phosphates which have a range of potential technological applications (e.g. ion exchangers, catalysts).[108] Three such phases with known structure were studied with the MgO_6 units showing only a very small shift variation, but with a much larger range of C_q values (see Table 2). Although there was a reasonable correlation using ideas of distortion of the local environment (vide infra), there are definite

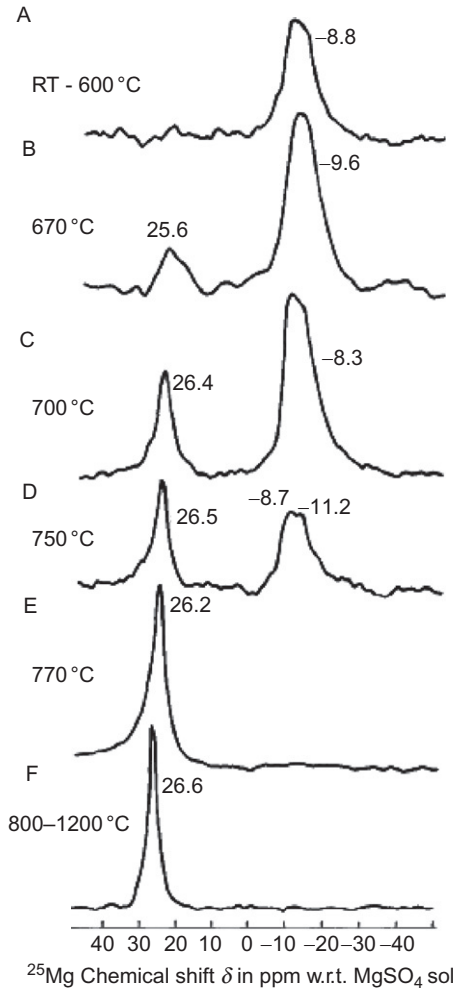

Figure 17 ^{25}Mg MAS NMR at 11.7T at 10kHz showing the decomposition of dolomite at ~−8ppm and the subsequent formation of MgO with various heat treatments (A–F). Reprinted from MacKenzie and Meinhold,[63] Copyright 1993, with permission from Elsevier.

contributions to the EFG from beyond the immediate local coordination. In a closely related layered material ($MgHPO_4 \cdot 1.2H_2O$) of unknown structure, the ^{25}Mg NMR data showed there was only one Mg site with MgO_6 coordination, which was slightly more distorted than in the other layered phosphates studied.[108] ^{25}Mg NMR has been reported from the microporous sodalite structured magnesium aluminophosphate MgAPO-20 combining data from 9.4 to 14.1T and using the DFS-QCPMG

approach.[38] As magnesium can substitute into the aluminophosphate framework, it produces a charge on the framework that can tailor the ion-exchange capability. The MgO_4 environment showed a small C_q of 3.8 MHz and a small CSA (with a span of $\Omega \leq 15$ppm), again indicating a relatively small distortion of the MgO_4 unit. The isotropic shift was in the range expected for this coordination at 50 ± 5ppm.[38] The overall summary from the oxygen-containing materials is that the dominant coordination for magnesium is octahedral, with the occasional observation of tetrahedral environments. The shift range with oxygen coordination for magnesium in this series of anhydrous compounds (excluding silicates) is from ca. 50ppm for $MgAl_2O_4$ and MgAPO-20 to -10.6ppm for one of the sites of $MgMoO_4$.

There are many hydrated magnesium salts and in these the oxygen coordinating the magnesium can come from water molecules alone or a mixture of water molecules and other oxygen within the structure. When water molecules are the exclusive local coordination, the shift range is very small and close to 0ppm, indicating its close similarity to the environment found in the reference solution. As other O^{2-} ions coordinate in addition to the water oxygen, small shift variations are detected. However, the small shift range gives a clear indication of how dominant the local, nearest neighbour coordination sphere is in determining the shielding in such systems. There is a much more significant variation in the quadrupole parameters, where C_q ranges from 0MHz in $MgCl_2 \cdot 6H_2O$ to 6.55MHz in one of the sites in $Mg_3(PO_4)_2 \cdot 8H_2O$.[39] There was on the whole quite good agreement with DFT calculations, although some cases where noticeable discrepancies occurred were noted, which could possibly be related to motion of the water molecules.[39] The strong variation of ^{25}Mg NMR parameters with hydration state was noted even in some of the early studies, with the ^{25}Mg linewidth increasing significantly as water is lost from the initially fully hydrated $MgCl_2 \cdot 6H_2O$ to the partially dehydrated $MgCl_2 \cdot xH_2O$ ($x < 6$).[33] A series of sulphates again showed a marked variation in the lineshape as the hydration state varied (Figure 18).[40] In $MgSO_4 \cdot H_2O$, a single magnesium site is obtained, but with a clear distribution of parameters indicated by the tail of the resonance to low frequency.[6,22] $MgSO_4 \cdot 6H_2O$ has two magnesium sites which were unambiguously simulated using data at three magnetic fields (11.75, 14.1, 18.8T). A single magnesium site is observed for the sulphate phase with seven water molecules. These latter two samples are much more highly ordered than for the monohydrated sulphate, suggesting that there is a small chemical shift to lower frequency with increased hydration.[40]

^{25}Mg NMR was used to investigate the cation ordering in Mg/Al LDHs.[46] These are compounds with the formula $Mg_{1-x}Al_x(OH)_2(NO_3)_x \cdot yH_2O$, which are of large current interest due to applications involving their anion-exchange capability. Studies combining fast-spinning ^{1}H

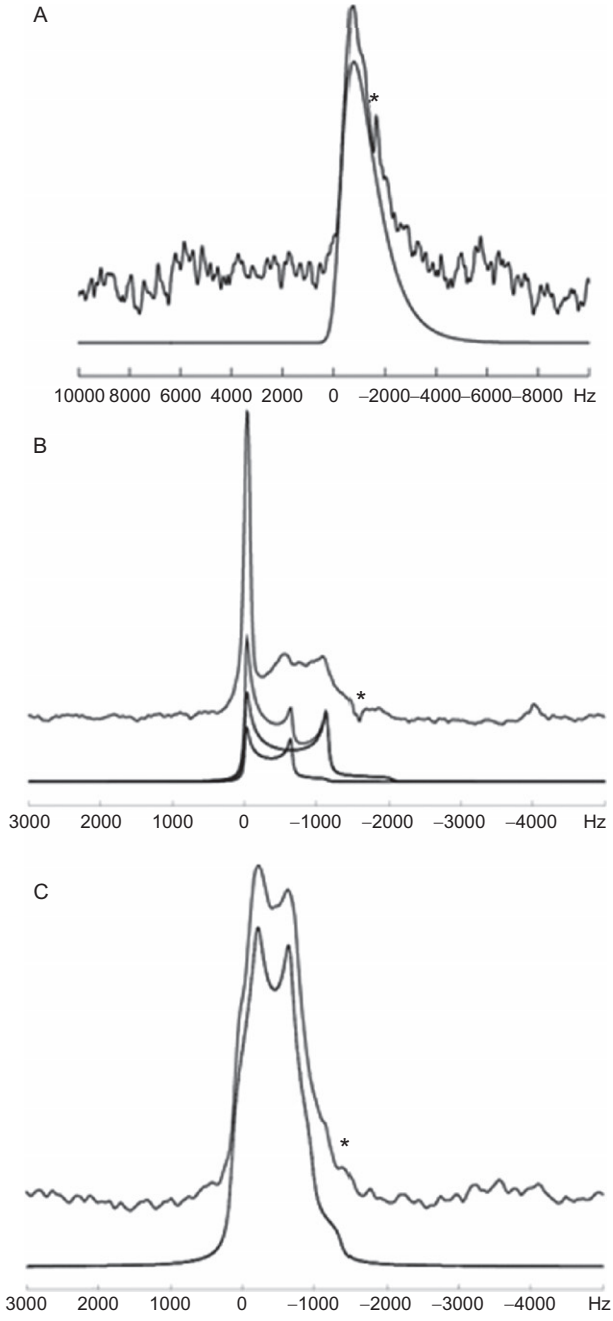

Figure 18 ^{25}Mg MAS NMR experimental (upper trace) and simulated (lower trace) spectra recorded at 14.1 T using 4 kHz MAS from (A) $MgSO_4 \cdot H_2O$, (B) $MgSO_4 \cdot 6H_2O$ and (C) $MgSO_4 \cdot 7H_2O$. The asterisk in each spectrum indicates a spurious background signal arising from the probe. Reproduced from Cahill et al.,[40] Copyright 2009, with permission from Wiley.

NMR and ^{25}Mg NMR performed with samples having different Al contents (MgAl-19, MgAl-25, MgAl-33, with 19%, 25% and 33% Al, respectively) evidenced the occurrence of cation ordering within the metal hydroxide layers of sample MgAl-33 (with Mg:Al ratio of 2:1). Partial ordering was observed in samples with lower Al content, with avoidance of direct contact Al^{3+}–Al^{3+}. ^{25}Mg MAS NMR spectra were recorded at high magnetic field (21.1 T) for the LDH samples and compared to brucite [$Mg(OH)_2$], all with ^{25}Mg at natural abundance. Samples MgAl-19 and MgAl-25 showed the superposition of a brucite-like lineshape with contributions from other sites. In sample MgAl-33, the spectrum was again dominated by a second-order quadrupolar CT MAS powder pattern for a single site, but with an increased C_q (4.6 MHz) and nearly unaltered η_q (0) and δ_{iso} (13 ppm) as compared to brucite. This new component was interpreted as due to an axially symmetric Mg environment of the type $Mg(OMg)_3(OAl)_3$, associated with a honeycomb-like ordering of Mg and Al.[46] A sample with the same Al content as in MgAl-33 but enriched in ^{25}Mg was also studied by MQMAS (3Q) at 19.5 T. The analysis of the resulting 2D spectrum (with a single peak in the isotropic dimension) evidenced the existence of only one Mg local environment in this material, in agreement with the 1D ^{25}Mg MAS NMR spectra.

Hydrotalcite, $Mg_6Al_2(OH)_{16}CO_3{\cdot}4H_2O$, is another LDH phase with the carbonate anion $(CO_3)^{2-}$. Thermal decomposition of this phase has uses including in catalyst supports, flame retardants, absorbents and anion exchangers. ^{25}Mg NMR of the thermal decomposition of hydrotalcite[65] showed the loss of a broader second-order quadrupolar lineshape to produce a much narrower line at the MgO position after heat treatment at 600 °C. It was expected that, after heating to higher temperature, the MgO_4 unit from $MgAl_2O_4$ should become visible as XRD clearly shows its presence, but this was not observed.[65]

Silicates and aluminosilicates form a large group of materials where the local coordination is also by oxygen. The ^{25}Mg NMR interaction parameters have been reported for a series of mineral-related samples which included the 2:1 magnesiosilicates talc, hectorite, saponite, montmorillonite and phlogopite, the 1:1 layer magnesiosilicates chrysotile, antigorite and other magnesium-containing minerals sepiolite, palygorskite, enstatite and forsterite.[34] The data were collected at 11.7 T with a spinning speed of 20 kHz using single-pulse excitation, which meant with the relatively low observation frequency (30.5 MHz) the first 100 μs of the time domain was missing and linear back prediction was used to recover the full data set. Forsterite (Mg_2SiO_4) has two inequivalent magnesium sites M1 and M2, and very accurate ^{25}Mg NMR single-crystal data have been obtained using DNP.[53] The quadrupole interaction at the two sites in this mineral has been calculated by superposition analysis of the structural distortion of the oxygen coordination octahedra.[61] A more recent study at 21.1 T on a powder sample[39] reproduced closely the single-crystal

values and was supported by DFT-derived values (Figure 19). The two sites can be well resolved and the sites can be differentiated on the basis of the C_q, η_q and δ_{iso} values. A shift difference of more than 12ppm does suggest that the shift could be a potentially useful discriminator alongside DFT calculations. A recent detailed study[109] used a combination of MAS, 3QMAS and static QCPMG experiments and previously reported first-principles calculations[117] to confirm the resonance assignment with the crystallographic sites. Forsterite is the pure magnesium end member of the olivine series which is an important mineral in Earth sciences and its dissolution behaviour was studied using ^{29}Si MAS, ^{1}H—^{29}Si CPMAS, ^{25}Mg QCPMG and ^{1}H—^{25}Mg CP QCPMG.[110] On dissolution, the changed magnesium environments were not readily observed probably due to a low concentration and increased quadrupolar broadening.

Another important mineral is enstatite ($MgSiO_3$), a member of the pyroxene family that has three polymorphs. The original report by MacKenzie and Meinhold[34] only showed one magnesium site, whereas the crystal structure is known to contain two inequivalent magnesium sites. The existence of distortion in the other site, leading to excessive broadening, was invoked to explain this result. The quadrupole parameters and isotropic chemical shift of the second site were calculated by Cahill et al.,[40] using CASTEP: C_q=14.0MHz, η_q=0.26 and δ_{iso}=13ppm. A very recent

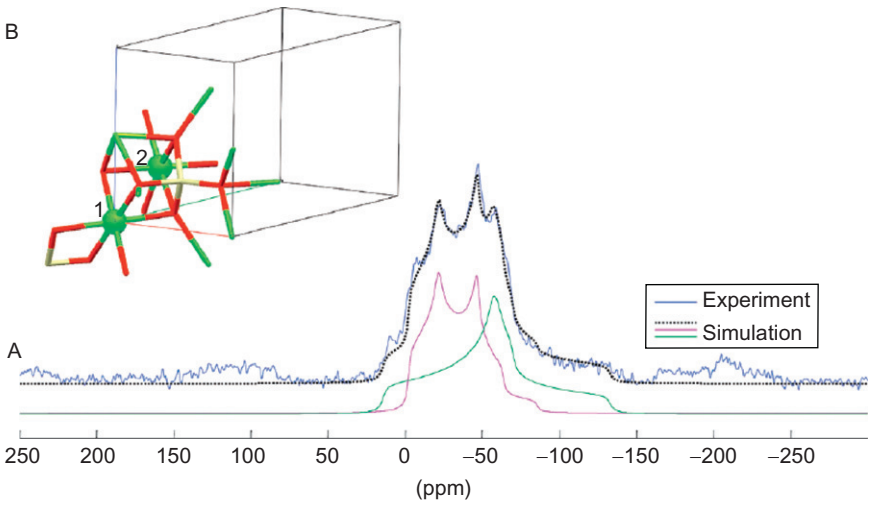

Figure 19 (A) ^{25}Mg MAS NMR spectrum at 21.1T using 8kHz MAS with a single-pulse experiment from natural forsterite (Mg_2SiO_4), showing both crystalline Mg sites clearly resolved along with (B) a representative portion of the forsterite unit cell showing the two crystallographically unique magnesium sites. Reproduced from Pallister et al.,[39] Copyright 2009, by permission of the PCCP Owner Societies.

study performed at strong magnetic fields (14.1 and 20.0T) using MAS and static QCPMG VOCS experiments helped to solve this inconsistency.[133] This was also backed up by DFT calculations, which showed, in agreement with the previous prediction,[40] that the two sites have very different quadrupole parameters, with the second site (Mg2) having a C_q some five times that of the more readily observed site (see Table 2). This was shown to be true for all three polymorphs, with the static VOCS spectrum clearly revealing the site with the larger C_q for the first time (Figure 20).

^{25}Mg-enriched silicate minerals diopside (MgO_6 coordination) and akermanite (MgO_4 coordination) show a large difference in the shift (ca. 40ppm).[149] This shift difference between units was confirmed in a later study of leucite ($K_2MgSi_5O_{12}$), which also contains magnesium in MgO_4 coordination and shows a much higher isotropic shift than the majority of shifts reported from minerals, although from the lineshape the value could not be precisely determined.[150] The dominant coordination in such materials is MgO_6, with some MgO_4 units seen, with the only report for an MgO_5 unit reported so far in the fascinating mineral grandidierite. From grandidierite, a fairly broad resonance was observed with some hint of quadrupolar features.[35] A δ_{iso} value for this MgO_5 bipyramidal unit was given as 55 ± 2ppm, which might be an underestimate of the likely error value, but looks to be more positive than the MgO_4 shifts reported, which could be related to boron and aluminium next nearest neighbours. Pyrope [$Mg_3Al_2(SiO_4)_3$] has magnesium in an MgO_8 coordination, but the width of the resonance at 8.45T meant that the isotropic chemical shift could not be determined with sufficient precision to make any comment on the ability of the shift to distinguish this coordination.[33] More data are still required to have a real view on the ^{25}Mg chemical shift ranges of coordinations in silicates, and the long-range structural effects that influence these ranges will need to be understood.

The high-temperature behaviour of silicates will provide some information about minerals under natural conditions, and ^{25}Mg NMR measurements at temperatures up to 1400°C have been used to investigate the mechanism of magnesium exchange between different sites in crystals and melts. High-temperature ^{25}Mg NMR spectra of a single crystal of forsterite (Mg_2SiO_4) have allowed the magnesium exchange between the different sites to be measured, giving results which are in agreement with estimates of the hopping frequency based on diffusion data.[151] Magnesium in molten silicates has also been studied by ^{25}Mg NMR which showed that melting is accompanied by an increase in the shielding of ~4ppm. This suggests an increase in the average coordination of the Mg, which again tends to have a preference for octahedral coordination in the melt.[152] Spin–lattice relaxation studies in molten magnesium silicate suggest that magnesium's motion is strongly coupled to motions of the

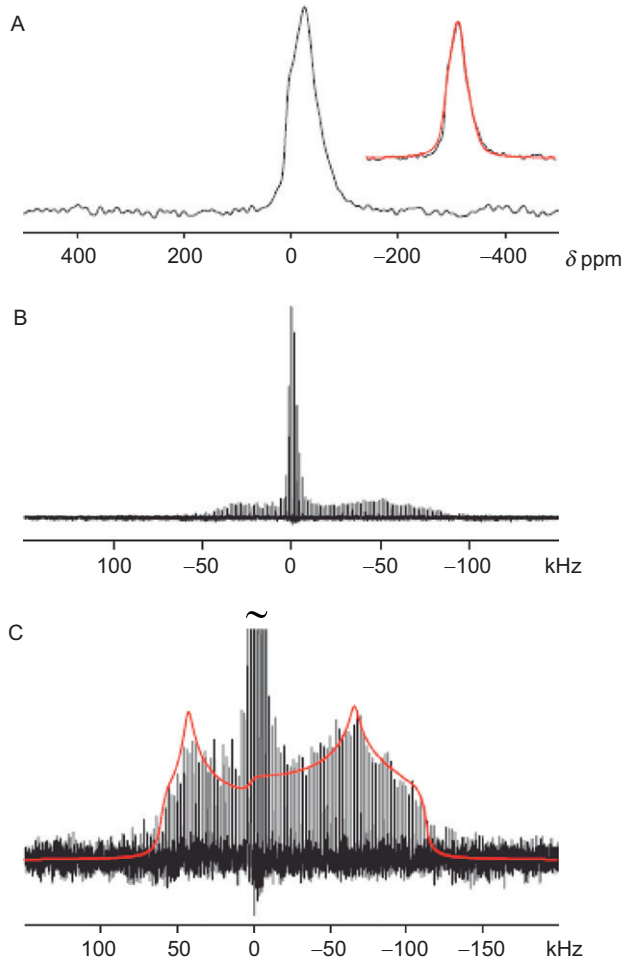

Figure 20 (A) A ^{25}Mg MAS NMR spectrum of orthoenstatite recorded at 14.1T. (B) A ^{25}Mg QCPMG VOCS spectrum of orthoenstatite recorded at 14.1T. The spectrum is the result of co-adding four subspectra recorded in steps of 50kHz across the Mg2 resonance, resulting in a total experimental time of 3.8 days. (C) An expanded view of the Mg2 resonance is shown in (B), together with a fit to the observed spikelet manifold (shown in red). Reprinted from Griffin et al.,[133] Copyright 2011, with permission from Elsevier.

network, since there was a correlation of the shear viscosity relaxation with the NMR correlation time related to T_1.[152]

^{25}Mg NMR can be used to provide information on the thermal decomposition of silicates and aluminosilicates such as for the asbestos mineral chrysotile [$Mg_3Si_2O_5(OH)_4$]. Combining ^{25}Mg and ^{29}Si NMR showed the

thermal decomposition to be quite a complex process. Loss of the hydroxyls was accompanied by the formation of a Mg-rich amorphous phase, which from the shift tended to suggest that the Mg is octahedrally coordinated, which then subsequently transforms to forsterite at 670–700 °C.[68] On occasions, very significant loss of signal intensity can occur as heat treatments progress. This observation parallels that from the early days of ^{27}Al (see Ref. 6 and references therein). For ^{27}Al, this became understood in terms of some signal not being recorded due to significant quadrupolar broadening at the magnetic fields and MAS rates available. The thermal decomposition of the related layer-lattice mineral talc, $Mg_6Si_8O_{20}(OH)_4$, was shown to form orthoenstatite, $MgSiO_3$, by a simple reaction in which the Mg remains in octahedral coordination throughout.[66] Very closely related to talc is the synthetic mineral hectorite [$(Mg_{5.3}Li_{0.6})Si_8O_{20}(OH)_4$-$Na_{0.9}\cdot nH_2O$], where some magnesium is substituted by lithium. The thermal decomposition of hectorite was followed by a combination of ^{25}Mg, ^{29}Si and ^{7}Li NMR.[67] Again the silicate structure becomes disrupted by the loss of hydroxyls from the layers such that the MgO_6 sites become progressively more distorted, as reflected by broadening and intensity loss of the ^{25}Mg signal, but again the Mg remains in octahedral coordination throughout.[67] The range of studies by MacKenzie and Meinhold in the mid-1990s showed how useful the addition of ^{25}Mg NMR was to the NMR methodology, as it shows directly the fate of the magnesium in the system. This early work pushed the limits and it would be very interesting indeed to use the very much higher magnetic fields and MAS rates now available to revisit some of these studies.

It is clear that the ability to calculate NMR parameters using DFT calculations is changing the methodology of relating experimental data to structural features. This approach does require some knowledge of the structure. Hence, correlations of NMR parameters to structural features provide a practical way to make initial estimates as to what is happening to the structure. This is especially useful when the phases formed are disordered and do not have a well-defined crystal structure. For local coordination with M—O bonds, Ghose and Tsang[153] defined longitudinal and shear strain parameters in terms of the deviations of the bond lengths and angles, respectively, from the ideal coordination polyhedron around the nucleus of interest. The initial ideas were developed for ^{27}Al, but given the similarity in the coordination chemistry with ^{25}Mg, the ideas can be transferred directly across. The longitudinal strain was defined as

$$|\alpha| = \sum_i \left| \ln\left(\frac{l_i}{l_o}\right) \right|, \tag{16}$$

where l_i and l_o are the actual and ideal Mg—O bond lengths, respectively, for all the direct bonds to the magnesium site of interest. The ideal bond

length is derived from a perfect octahedron with exactly the same volume as that in the structure, but with no distortion. The shear strain is defined in terms of the O—Mg—O bond angles and is given by

$$|\phi| = \sum_i |\tan(\theta_i - \theta_o)|, \tag{17}$$

where again the subscripts i and o designate the actual and ideal bond angles, respectively (for an octahedron, e.g., $\theta_o = 90°$). MacKenzie and Meinhold[34] also looked at the distortion index (DI) which was defined as

$$\mathrm{DI} = \sum_{i=1}^{12} \frac{|\theta_i - \theta_o|}{12\theta_o}. \tag{18}$$

A linear relationship was found between C_q and DI for a subset of 15 minerals such that the relationship

$$C_q \ (\text{in MHz}) = 41.1\mathrm{DI} + 1.05 \tag{19}$$

was observed.[34] Another suggested correlation was between C_q and the shear strain:

$$C_q \ (\text{in MHz}) = 2.18|\varphi| + 0.832. \tag{20}$$

There is no fundamental reason why these relationships should be linear. However, reasonably good linear correlations have been found in the study by Cahill et al.[40] between C_q and $|\alpha|$, where for the inorganic compounds studied with magnesium in octahedral coordination, a correlation coefficient (R^2) of 0.754 was found. This correlation would assign all the two site magnesium structures correctly (as confirmed by DFT) on the basis of the longitudinal strain. The correlation over a large number of Mg—O octahedral units showed a much poorer correlation with the shear strain, with a worse correlation coefficient suggesting that the point-charge model is not sufficient to capture all the structural features determining the NMR parameters from beyond the immediate coordination sphere. The reasonable correlation found by MacKenzie and Meinhold[34] on the more limited set of data was attributed to all the samples included (other than hydrotalcite) being anhydrous. When water is included in the coordination sphere, it can have a significant effect on C_q.

Oxide ion-conducting ceramics have also been recently studied using solid-state ^{25}Mg NMR. Buzlukov et al.[154] investigated the compounds $La_{1-x}Sr_xGa_{1-x}Mg_xO_{3-x}$, with x varying from 0.0 to 0.2, combining ^{25}Mg with ^{71}Ga NMR data to get information about oxygen environments of magnesium and gallium and also using ^{17}O NMR to study the thermally activated motion of oxygen ions in the material. The static ^{25}Mg NMR spectrum of the most doped compound ($x = 0.2$) showed a relatively

narrow resonance close to the Larmor frequency, with a small quadrupolar broadening (~0.2 MHz) attributed to effects of charge disorder in the outermost atomic shells. The conclusion was for the magnesium environment in the form of symmetric MgO_6 units, with no vacancy in the first coordination shell around Mg in these compounds.[154]

4.3. Crystalline non-oxide inorganic materials

The occurrence of magnesium in environments where it is coordinated by elements (X) other than oxygen is much less common. These compounds cover a wide range of covalency of the Mg—X bonds. The ionic end of such compounds includes anhydrous magnesium halides where for MgF_2 the ^{25}Mg C_q was reported from low temperature (77 K) NQR field-cycling double-resonance experiments, which revealed a moderate coupling constant of 3.438 MHz.[155] In $MgCl_2$, the magnesium is sited in an octahedral coordination, and although there is a relatively small shift from the octahedrally coordinated environment by water in the hexahydrate, there appears to be quite a large increase in C_q in the anhydrous material[39] from the value of zero in the highly symmetric environment of the hydrate. In $BaMgF_4$, which forms a ternary diamagnetic end member of some ferroelectric quaternary fluorides, magnesium appears in MgF_6 coordination. This material was recently studied by static ^{25}Mg NMR at 14.1 T.[132] A well-defined second-order quadrupolar lineshape was observed that did not require any CSA to obtain a good fit. There was some discrepancy between the experimentally determined NMR parameters and those obtained from GIPAW DFT calculations using the CASTEP code (see Table 2), which was attributed to limitations in the pseudopotentials used. Data recorded at 150 and 292 K showed no real variation in the NMR parameters, although subtle changes may have been masked by the broad static NMR lines observed. ^{25}Mg NMR parameters from MgH_2 [39] revealed one of the few cases where DFT calculations underestimated the magnitude of C_q. Both non-zero C_q and η_q are entirely in keeping with D_{2h} symmetry at the magnesium site. MgS has the same cubic structure as MgO and similarly exhibits a zero EFG and hence a very sharp resonance, but with a shift difference of ~27 ppm.[39]

In more covalently bonded inorganic compounds such as Mg_3N_2 in which the magnesium is in MgN_4 coordination, the single Mg site shows very strong deshielding, with an isotropic chemical shift determined of 101.0 ± 2.0 ppm.[39] The most recent study at high field (21.1 T) revealed a very large C_q of 9.300 ± 0.050 MHz which was in very good agreement with the CASTEP calculation.[39] This reflects the distorted local tetrahedral environment and points to why an earlier study at the much lower magnetic field of 8.45 T had trouble recording the lineshape accurately.[33] This material also has the largest CSA so far reported for ^{25}Mg at

$\Delta\delta \sim 42$ ppm.[39] An early study of related nitride phases $MgSiN_2$ and $MgAlSiN_3$ carried out with MAS at 10 kHz at an applied magnetic field of 11.7 T revealed several peaks.[156] If the C_q in these compounds approached that reported for Mg_3N_2, these experimental conditions would only cause partial narrowing of the resonance.

4.4. Glassy inorganic materials

The short-range, atomic length scale information provided by NMR means that materials which show structural disorder can be probed, with the structural disorder being reflected in a distribution of interactions. This causes, for example, broader lines and a blurring of sharp spectral features that allow the more precise determination of the NMR interaction parameters in crystalline materials. Nevertheless, one of the great advantages of NMR is that key structural information is still readily available even with the loss of spectral resolution, for example, estimates of the quadrupole coupling, changes of coordination number and connectivity of the network.[6] In aluminosilicate glasses, ^{27}Al NMR has been very widely used to probe the changes of aluminium coordination.[157] The coordination of magnesium in aluminosilicate glasses is potentially a very important question giving the possibility that magnesium, which in crystalline aluminosilicates is predominantly found in octahedral coordinations, could occur in tetrahedral coordination. This possibility would have profound consequences for the thermodynamics of aluminosilicate melts which are core to much geochemistry. For example, having a magnesium silicate melt as the pressure is increased with an element such as magnesium which can comparatively easily change its coordination compared to silicon offers different viscosity–pressure behaviour compared to other compositions. As magnesium is a relatively light element, there are relatively few probes that can provide unequivocal information about its coordination, hence this provides one of the drives to develop solid-state ^{25}Mg NMR.

The first ^{25}Mg NMR results from glasses were reported for two 96.75% ^{25}Mg-enriched glasses based on the diopside ($CaMgSi_2O_6$) and leucite ($K_2MgSi_5O_{12}$) compositions.[150,158] It was interesting to note that no signal could be obtained on these samples previously at 9.4 T[149] compared to the 14.1 T used in the more recent studies. As expected, the ^{25}Mg resonances from the glasses were considerably broader than from the corresponding crystalline materials and showed the expected ''tail'' to negative shift that is expected from a distribution of quadrupolar interactions for half-integer spin quadrupolar nuclei.[22] As the MAS rate increased, there was a shift in the peak maximum, and the linewidth increased as sites with larger quadrupole coupling constants became successively narrowed.[159,160] A larger range of structures are probably present in the

diopside glass compared to the leucite composition as there was a greater change in the spectrum observed in increasing the spinning speed from 10 to 20 kHz. A key observation from this initial work was that the most deshielded (positively shifted) edge of the spectra of glassy and corresponding crystalline materials did not change very much, indicating insignificant differences in δ_{iso} values and thus suggesting that the magnesium coordination in the glass was similar to that in the original crystal. In high-field data from diopside glass,[152] an isotropic chemical shift of 21 ppm was reported in the melt at 1400 °C, deshielded by some 13 ppm from the environment found in the mineral. The data from the diopside glass appeared to lie in the range defined by the crystal and the melt. In the work by Kroeker and Stebbins,[150] the shift parameters for diopside suggested that the magnesium coordination was octahedral, which apparently contradicted the X-ray absorption results. This discrepancy probably reflects the shortcomings in both techniques at definitively identifying the coordination number under the experimental conditions pertaining at that time. The change of magnesium coordination in a glass could be related to the cation field strength, defined as the ratio of the formal charge (Z) of the cation and the square of the average distance to oxygen for that cation in the coordination it finds itself in (d^2). As the field strength of the cation varies, magnesium ability to coordinate oxygen changes and hence the nature of the local coordination is likely to change, as observed between leucite and diopside glasses.[150]

More recently, there was extension of the study of glasses to still higher field of 21.8 T. A range of glasses prepared from 99%-enriched ^{25}MgO were investigated, separated into two groups: $MgSiO_3$, $CaMgSi_2O_6$, $Ca_2MgSi_2O_7$ and $Mg_3Al_2Si_3O_{12}$ (group A) and $Na_2MgSi_2O_6$ and $K_2MgSi_2O_6$ (group B); comparison to diopside and akermanite was also presented.[42,161] The two groups showed distinct spectra as can be seen by a comparison of the studies at two magnetic fields of 16.4 and 21.8 T (Figure 21).[42] The MAS spectra show a broader component that sits on potentially an even unnarrowed component for group A compared to B. The nature of the spectra shows just how crucial the combination of high field and moderate MAS of 18 kHz was since there is just separation of the sidebands from the centreband, even under these high-field conditions. This is almost certainly the reason why work at lower field did not produce any observable resonance.

The MAS experiments were then extended to 2D 3QMAS experiments. Comparison of the two groups showed the much broader peaks of group A (with width of 140–190 ppm at 21.8 T) peaked at −46.3 to −25.7 ppm, whereas the narrower peaks on group B with width of 90–100 ppm (at 21.8 T) peaked at −3.4 to −0.9 ppm. The 3QMAS NMR data from the groups differed as well, with the group A glasses suggesting multiple, but potentially distinct sites whereas group B showed effectively a single type

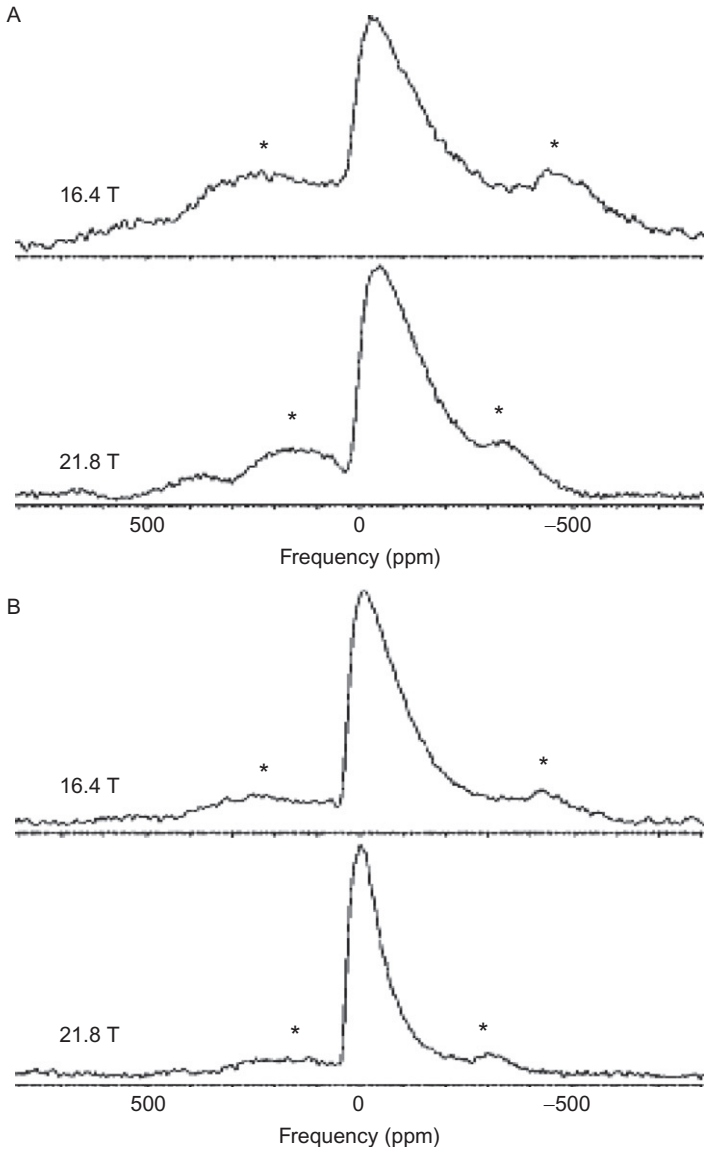

Figure 21 Comparison of ^{25}Mg MAS NMR spectra at 16.4 and 21.8 T for representative glasses from group A, $MgSiO_3$ (A), and group B, $K_2MgSi_2O_8$ (B). Asterisks indicate spinning sidebands. Reprinted with permission from Shimoda et al.,[42] Copyright 2008 American Chemical Society.

of site but with a distribution. In the $MgSiO_3$ glass, it was suggested that the magnesium coordination could be a mixture of MgO_6 and MgO_5 environments whereas in the $K_2MgSi_2O_6$ glass coordination was probably MgO_4,

agreeing with the previous conclusion of Kroeker and Stebbins.[150] ^{17}O MAS NMR provides an interesting alternative perspective in that it showed[162] that in K–Mg silicate glasses the Mg preferentially bonded to non-bridging oxygens, with the K^+ ions associated with bridging oxygens. In contrast, in Ca–Mg glass, there was no bonding preference detected by ^{17}O NMR. The cation bond strength argument advanced probably explains this as the magnesium changes from dominantly MgO_4 to MgO_6 in these glasses. Shimoda et al.[42] analysed all the data that was available at the time for ^{25}Mg NMR in such aluminosilicate systems and showed an interesting plot of δ_{iso} for ^{25}Mg against the cation field strength (Z/d^2), Figure 22. Clear clustering of the shifts around the tetrahedral and octahedral values was observed that showed a strong dependence on the cation field strength. There was a clear break in the data in the region of the cation field strength 0.30–0.33, suggesting magnesium's behaviour changes around here. This observation would also explain why on lithium-related glasses magnesium again shows octahedral coordination as opposed to tetrahedral in the sodium and potassium analogues, since lithium has a much stronger cation field strength compared to the other two alkali metals.[42]

Amorphous slags—which are by-products of iron- and steel-making processes—constitute another example of Mg-containing glassy materials studied using ^{25}Mg MQMAS NMR experiments at high magnetic

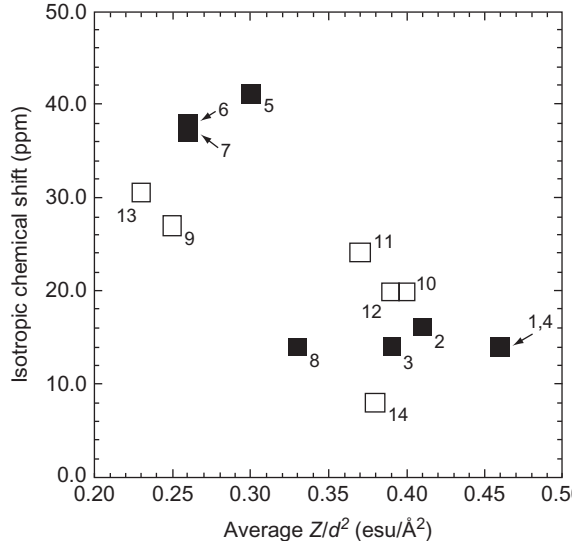

Figure 22 ^{25}Mg isotropic chemical shift as a function of the average modifier cation field strength (Z/d^2). Reprinted with permission from Shimoda et al.,[42] Copyright 2008 American Chemical Society, where the references to the numbered data points can be found.

fields.[37,43] In a first work, two slag samples containing ^{25}Mg at natural abundance were investigated at 16.4T in comparison to model compounds, showing the presence of Mg species other than MgO and Mg $(OH)_2$.[37] More recently, a multinuclear study combining ^{17}O, ^{25}Mg, ^{27}Al, ^{29}Si and ^{43}Ca NMR in a synthetic model slag enriched in ^{17}O, ^{25}Mg and ^{43}Ca was carried out.[43] The ^{25}Mg MAS NMR spectrum was quite similar to the one of $CaMgSi_2O_6$ glass.[150,161] ^{25}Mg 3QMAS NMR spectra revealed the presence of two sites with δ_{iso} of 10 and 17ppm, both associated with MgO_6 units. However, the occurrence of minor amounts of sites with MgO_4 or MgO_5 coordination could not be disregarded, considering the quite broad distribution of shifts observed in the 2D spectra.[43]

In a series of magnesium silicate glasses of composition $MgO_x(SiO_2)_{1-x}$ $(0.50 \leq x \leq 0.667)$, nine compositions were studied.[47] As MgO is added, ^{29}Si MAS NMR revealed a depolymerisation of the silicate network. The ^{29}Si NMR spectral intensity was used to determine the variation of the different Q^n species present and compared to the binary and random models for the potential distribution. The observed distribution was between the two extremes, with at some compositions the distribution being much closer to a statistical distribution. The ^{25}Mg MAS NMR spectra revealed the classical ''tail'' distribution as expected from a quadrupolar nucleus in a glass.[6] The average isotropic chemical shift was 17ppm and $C_q \sim 7.6$MHz, indicating that the sites are quite distorted. However, the majority of magnesium is of the MgO_6 type, although with the available S/N ratio on these natural abundance samples, the presence of a small fraction of lower coordinations could not be ruled out. It was clear from overlaying the spectra that there was very little change in the typical coordination of magnesium across the series.[47] In comparison with other structural probes, this provided clear evidence that any structural model for these glasses needs to have very little MgO_4 (and MgO_5) content.

Another situation where magnesium-containing glasses are important is in the production of densified non-oxide ceramics such as Si_3N_4 and sialon compounds. MgO is often added in small quantities to promote densification during sintering. ^{25}Mg NMR has been used to study the effect of 10wt% additions of MgO to Si_3N_4 sintered at 1500–1700°C. The ^{25}Mg MAS NMR spectra of these samples showed two broad resonance bands with no specific shape that had some similarity to what had been observed in $MgSiN_2$ and $MgAlSiN_3$, suggesting that the magnesium finds its way into a glassy intergranular phase.[156] The positions of the resonances at ~35 and ~−80ppm suggest that both 4- and 6-coordinated Mg sites are present, probably stabilised by nitrogen. Again some caution is necessary here, since under the conditions used in this study, there may be broader spectral components that are only partially being observed. The magnesium is most likely present in a Mg—Si—O—N glass formed by reaction of the MgO with the surface oxide and part of the nitride

component and this glass is not readily recrystallised.[156] Sintering of other oxynitride ceramics using MgO was also studied by ^{25}Mg NMR in the case of β′-sialon[163] and X-sialon.[164] All these results suggest multiple magnesium sites probably in both tetrahedral and octahedral coordination.

We conclude this survey of applications of solid-state ^{25}Mg NMR to studies of inorganic materials given in Table 2, a compilation of the experimentally derived solid-state ^{25}Mg NMR parameters (C_q, η_q and δ_{iso}) reported to date for a large number of non-metallic Mg-containing inorganic compounds. Also mentioned in the table are any points of note such as the special methods used to improve sensitivity or resolution in the performed experiments (e.g. isotopic enrichment, QCPMG, methods based on population transfers, MQMAS, STMAS, etc.) and the eventual discrepancies observed between results achieved by different researchers.

4.5. Mg-containing organic compounds

Most of the early work dealing with ^{25}Mg NMR in Mg-containing organic compounds involved the use of isotopically enriched compounds. More recent reports make use of intense magnetic fields and of signal-enhancement methods as those described in Section 2, allowing studies of samples containing ^{25}Mg at natural abundance. In one of the pioneering studies of Mg-containing organic compounds, Sham and Wu used ^{25}Mg-enriched samples (synthesised from MgO containing 99.1 at.% ^{25}Mg) and determined the quadrupole parameters of a set of Mg^{2+}-binding complexes taken as models for inner-sphere Mg^{2+} coordination.[49] A number of other reports dealing with solid-state ^{25}Mg NMR studies in related Mg-containing organic compounds appeared thereafter, including acetate, chlorophyll, EDTA complex, ATP, proteins and hydroxyapatite.[41,48,50–52,54,57,107,165] As mentioned before, two comprehensive and independent accounts were published recently, containing a large number of ^{25}Mg NMR experimental results in organic compounds (among others) and with detailed comparisons to DFT calculations.[39,40] In these studies, a combination of strategies including high magnetic fields, sensitivity-enhancement methods (such as QCPMG and FSG-RAPT) and large volume sample holders made possible the investigation of materials at natural abundance. Some previously studied compounds were re-analysed in these investigations, confirming and improving the accuracy of previous results; however, in many cases, important discrepancies were found, which were attributed to mistakes in previous interpretation of NMR data (usually acquired at lower magnetic fields) and/or erroneous sample structural identification in the former studies.[39,40]

The importance of Mg in biochemistry has been emphasised in many solid-state ^{25}Mg NMR studies. In one of the first reports in this field,

TABLE 2 Experimental ^{25}Mg NMR parameters for non-metallic Mg-containing inorganic compounds

Compound	C_q (MHz)	η_q	δ_{iso} (ppm)[a]	Comments	References
Periclase MgO	0	–	26(1)		33
Periclase MgO	0	–	25	Study of temperature variation of the isotropic chemical shift, from room temperature up to 1300°C.	134
Periclase MgO	0	–	26.54	Experimental data compared with first-principles calculations in Ref. 131.	
Periclase MgO	0	–	26.6	Experimental data compared with first-principles calculations in Ref. 40.	34
Periclase MgO	0.0	–	26.26(5)		37
				Experimental data supported by first-principles calculations.	39
Brucite $Mg(OH)_2$	2.9	0	10(50)	Experimental data compared with first-principles calculations in Ref. 40.	33
Brucite $Mg(OH)_2$	3.056(5)	0	13.5	Single-crystal rotation study.	146
Brucite $Mg(OH)_2$	3.15	0	14.1		34
Brucite $Mg(OH)_2$	3.1	0.05	10	Comparison of MQMAS and STMAS experiments, using both enriched and nonenriched materials.	30
Brucite $Mg(OH)_2$	6.9[b]	0	11.1	Use of MQMAS. See Refs. 30,33,34,39,146 for other C_q results not agreeing with this work.	37

Brucite $Mg(OH)_2$	3.091(10)	0.00(1)	11.8(2)	Experimental data supported by first-principles calculations. A small CSA contribution was calculated and detected using static experiments with the deuterated compound, $Mg(OD)_2$.	39
Forsterite Mg_2SiO_4				Use of DNP in single-crystal studies. Experimental data compared with first-principles calculations in Refs. 40,109,117.	53
Site 1	4.996	0.963	n.d.[c]		
Site 2	4.313	0.396	n.d.		
Forsterite Mg_2SiO_4				Forsterite was detected as a secondary phase in thermally annealed silica-pinned MgO. δ_{iso} value not in agreement with a more recent result given in Ref. 39.	143
Site 1	n.d.	n.d.	n.d.		
Site 2	4.3	0.40	51(2)[b,d]		
Forsterite Mg_2SiO_4				Experimental data supported by first-principles calculations.	39
Site 1	5.097(30)	0.97(2)	14.5(1.0)		
Site 2	4.169(40)	0.40(2)	2.4(1.0)		
Forsterite Mg_2SiO_4				Use of QCPMG and MQMAS experiments. Experimental data compared with first-principles calculations taken from Ref. 117.	109
Site 1	5.33(7)	0.99(1)	n.d.		
Site 2	4.31(5)	0.39(4)	n.d.		

(*continued*)

TABLE 2 (*continued*)

Compound	C_q (MHz)	η_q	δ_{iso} (ppm)[a]	Comments	References
Enstatite $MgSiO_3$[e]	2.4[f]	0.4[f]	27[b,f]	Sample prepared from talc by heat treatment at 1300°C, tentatively identified as orthoenstatite. Experimental data compared with first-principles calculations in Ref. 40. See Ref. 133 for more recent results comprising the two sites and with δ_{iso} value not agreeing with this work.	34
Clinoenstatite $MgSiO_3$				A high-field study at 14.1 and 20.0T using a static QCPMG VOCS approach to record the line due to the site with larger C_q. Experimental data supported by first-principles calculations.	133
Site 1	2.6(1)	0.45(10)			
Site 2	12.6(2)	0.25(10)			
Orthoenstatite $MgSiO_3$				A high-field study at 14.1 and 20.0T using a static QCPMG VOCS approach to record the line due to the site with larger C_q. Experimental data supported by first-principles calculations.	133
Site 1	2.8(1)	0.65(10)	18(4)		
Site 2	12.8(2)	0.25(10)	0(20)		
$Mg_2Si_3O_8$	n.d.	n.d.	0(50)[g]		33
Talc $Mg_3Si_4O_{10}(OH)_2$[e]	2.4[b,f]	0.7[b,f]	48[b,f]	Use of a natural sample. See Ref. 30 for more recent results not agreeing with this work.	34
Talc $Mg_3Si_4O_{10}(OH)_2$				Use of STMAS.	30
Site 1	2.8	1.0	25(6)		
Site 2	2.1	0.3	16(6)		

Chrysotile $Mg_3Si_2O_5(OH)_4$	n.d.	n.d.	−59[h]	Use of a natural sample.	34
Diopside $CaMgSi_2O_6$	2.00(5)	0.95(5)	8(3)	Use of isotopic enrichment. See Refs. 30,150 for more recent results.	149
Diopside $CaMgSi_2O_6$	2.1(1)	0.75(10)	8.0(5)	Use of isotopic enrichment. Experimental data compared with first-principles calculations in Ref. 40.	150
Diopside $CaMgSi_2O_6$	2.1	0.7	10	Use of STMAS.	30
Akermanite $Ca_2MgSi_2O_7$	2.8(1)	0.25(10)	49(4)	Use of isotopic enrichment. See Ref. 150 for more recent results.	149
Akermanite $Ca_2MgSi_2O_7$	2.8(1)	0.2(1)	47(1)	Use of isotopic enrichment. Experimental data compared with first-principles calculations in Refs. 39,40.	150
Grandidierite $(Mg,Fe)Al_3SiBO_9$	3.8(1)	0.60(5)	55(2)	Use of a natural sample.	35
Hectorite $[Mg_{5.3}Li_{0.6}]Si_8O_{20}(OH)_4Na_{0.9}\cdot nH_2O$	2.2[f]	1.0[f]	43[f]		34
Antigorite $(Mg_{2.81}Fe_{0.05})[Si_{1.95}Al_{0.05}]O_5(OH)_{3.68}$	2.9[f]	0.7[f]	50[f]	Use of a natural sample.	34
Phlogopite $K_2(Mg_{5.1}Fe_{0.3})[Si_{5.1}Al_{2.1}Ti_{0.1}]O_{20}(OH)_4$	3.0[f]	0.65[f]	68[f]	Use of a natural sample.	34
Sepiolite $[Mg_{7.6}Al_{0.46}]Si_{12.4}O_{30}(OH)_{1.8}(OH_2)_4\cdot 8H_2O\cdot K_{0.2}$	2.7[f]	0.7[f]	51[f]	Use of a natural sample.	34
Palygorskite $[Mg_{2.2}Al_{1.7}Fe_{0.4}]Si_8O_{19.6}(OH)_{1.9}(OH_2)_{4.5}Ca_{0.4}$	3.2[f]	0.5[f]	80[f]	Use of a natural sample.	34

(*continued*)

TABLE 2 (*continued*)

Compound	C_q (MHz)	η_q	δ_{iso} (ppm)[a]	Comments	References
Saponite $Mg_6Si_{7.4}Al_{0.66}O_{20}(OH)_4(½Ca,Na)_{0.66}$	0	–	0	Use of a natural sample. The authors report δ_{cg}=−1ppm; a broader component at ca. −30ppm could also be observed, depending on the processing methods.	34
Montmorillonite $[Al_2MgFe](Si_{7.5}Al_{0.5})O_{20}(OH)_4(½Ca,K)_{0.7}$				Use of a natural sample.	34
Site 1	2.8	0	−4		
Site 2	1.5	0	11		
Pyrope $Mg_3Al_2(SiO_4)_3$	n.d.	n.d.	0(200)[g]		33
Spinel $MgAl_2O_4$	0	–	52(3)		33
Spinel $MgAl_2O_4$	0.4(1)[b]	n.d.	52(1)	Use of a natural sample. C_q estimated from spinning sidebands span range. Experimental data compared with first-principles calculations in Ref. 40. See Refs. 33,39 for other C_q results not agreeing with this work.	150
Spinel $MgAl_2O_4$	0.0	–	48.2(1.0)	Experimental data supported by first-principles calculations.	39
Magnesite[i]	2.5	0	4.8[b]	Natural samples of diverse geographical origins gave different results. See Refs. 39,129 for other results not agreeing with this work.	34
$MgCO_3$	2.6	0.3[b]	8.8[b]		
Magnesite $MgCO_3$	2.40(2)	0	26[b,d,j]	Experimental data supported by first-principles calculations of EFG components. See Ref. 39 for a more recent δ_{iso} result not agreeing with this work.	129

Magnesite $MgCO_3$	2.244(20)	0.04(2)	−3.8(2)	Experimental data supported by first-principles calculations.	39
Dolomite $MgCa(CO_3)_2$	0.9	0	−4.3	Use of a natural sample.	34
Artinite $Mg_2CO_3(OH)_2 \cdot 3H_2O$	2.05(5)	0.77(10)	5(1)	Use of FSG-RAPT. Experimental data supported by first-principles calculations.	40
Hydromagnesite $Mg_5(CO_3)_4(OH)_2 \cdot 4H_2O$				Spectral shape and quadrupolar features greatly affected by the processing methods.	34
Site 1	3.6	0	−4		
Site 2	3.1	0	16		
Hydrotalcite $Mg_5Al_3(OH)_{16} \cdot 1.5CO_3 \cdot 3.6H_2O$	4.4	0	10		34
$Mg(VO_3)_2$	8.88(20)	0.76(5)	−0.4(5.0)	Use of QCPMG. Experimental data compared with first-principles calculations in Ref. 40.	36
$Mg(VO_3)_2$	8.850(100)	0.97(2)	−8.7(4.0)	Use of QCPMG. Experimental data supported by first-principles calculations.	39
$Mg_3(VO_4)_2$				Use of QCPMG. Experimental data supported by first-principles calculations.	39
Site 1	2.937(20)	0.36(2)	7.1(3)		
Site 2	8.162(50)	0.20(3)	13.1(3.0)		
α-$Mg_2V_2O_7$				Use of QCPMG. Experimental data supported by first-principles calculations.	39
Site 1	2.129(20)	0.88(2)	2.8(2)		
Site 2	2.439(20)	0.74(1)	−4.4(3)		
$MgWO_4$	2.196(10)	1.00(2)	−1.7(1)	Experimental data supported by first-principles calculations.	39

(*continued*)

TABLE 2 (*continued*)

Compound	C_q (MHz)	η_q	δ_{iso} (ppm)[a]	Comments	References
$MgMoO_4$				Experimental data supported by first-principles calculations.	39
Site 1	2.359(40)	1.00(3)	−10.6(3)		
Site 2	4.287(20)	0.21(2)	−8.3(3)		
Geikielite $MgTiO_3$	1.88(3)	0.10(3)	11(1)[d]	Experimental data compared with first-principles calculations in Ref. 40.	148
Geikielite $MgTiO_3$	1.816(20)	0.10(4)	9.9(1)	Experimental data supported by first-principles calculations.	39
α-$MgSO_4$	7.405(50)	0.35(2)	−8.1(1.0)	Use of QCPMG. Experimental data supported by first-principles calculations. Detection of a small CSA contribution.	39
β-$MgSO_4$	10.4(1)	1.00(2)	0.2(3.0)	Use of QCPMG. Experimental data supported by first-principles calculations.	39
$MgSO_4 \cdot H_2O$	1.8(2)[k]	0.9	−7(1)	Use of FSG-RAPT. Experimental data supported by first-principles calculations. A Gaussian distribution of C_q was used to fit the spectra, with mean value of 1.8MHz and FWHM=1.4MHz.	40
$MgSO_4 \cdot 6H_2O$	1.6[b]	0[b]	0(15)[b]	See Refs. 39,40 for other results not agreeing with this work.	33
$MgSO_4 \cdot 6H_2O$				Use of FSG-RAPT. Experimental data supported by first-principles calculations. See Refs. 33,39 for other results not agreeing with this work.	40
Site 1	1.65(10)[b]	0.00(1)[b]	7(1)[b]		
Site 2	2.40(10)[b]	0.00(1)[b]	4(1)[b]		

$MgSO_4 \cdot 6H_2O$				Experimental data supported by first-principles calculations. See Refs. 33,40 for other results not agreeing with this work.	39
Site 1	0.0[b]	–	1.0(1)[b]		
Site 2	2.147(3)[b]	0.40(2)[b]	1.2(2)[b]		
$MgSO_4 \cdot 7H_2O$	1.95(10)	0.40(10)	2(1)	Use of FSG-RAPT. Experimental data supported by first-principles calculations.	40
$MgSO_4 \cdot 7H_2O$	1.80(1)	0.20(2)	1.6(1)	Experimental data supported by first-principles calculations.	39
$Mg(NH_4)_2(SO_4) \cdot 6H_2O$	2.613(20)	0.61(2)	4.0(5)	Experimental data supported by first-principles calculations.	39
$MgNO_3 \cdot 6H_2O$	1.448	0.74	n.d.	Data obtained at 77K using NQR with field cycling and double resonance. See Refs. 39,40 for more recent and apparently discrepant results, using high-field NMR at room temperature.	155
$MgNO_3 \cdot 6H_2O$	1.65(10)	0.18(10)	0.2(1.0)	Use of FSG-RAPT. Experimental data supported by first-principles calculations.	40
$MgNO_3 \cdot 6H_2O$	1.496(20)	0.00(5)	0.18(5)	Experimental data supported by first-principles calculations.	39
$Mg_3(PO_4)_2 \cdot 8H_2O$				Experimental data supported by first-principles calculations.	39
Site 1	1.409(10)	0.52(3)	1.5(2)		
Site 2	6.549(100)	0.00(10)	7.7(1.5)		
$MgHPO_4 \cdot 3H_2O$	2.493(100)	0.05(5)	−6.3(2)	Experimental data supported by first-principles calculations.	39

(*continued*)

TABLE 2 (*continued*)

Compound	C_q (MHz)	η_q	δ_{iso} (ppm)[a]	Comments	References
$MgCl_2$	1.619(20)	0.00(5)	2.32(10)	Experimental data supported by first-principles calculations.	39
$MgCl_2 \cdot 6H_2O$	1.477	0.20	n.d.	Data obtained at 77K using NQR with field cycling and double resonance. See Ref. 39 for more recent and apparently discrepant results, using high-field NMR at room temperature.	155
$MgCl_2 \cdot 6H_2O$	0.0	–	−0.16(3)	Experimental data supported by first-principles calculations.	39
$MgBr_2$	0.85(20)	0	−16.25(15)	Experimental data supported by first-principles calculations.	45
$MgBr_2 \cdot 6H_2O$	1.004	0.52	n.d.	Data obtained at 77K using NQR with field cycling and double resonance.	155
MgF_2	3.438	0.28	n.d.	Data obtained at 77K using NQR with field cycling and double resonance.	155
$BaMgF_4$	5.47	0.47	0	Experimental data supported by first-principles calculations. Static data collected at 14.1T at 292 and 150K, which showed significant deviation from the CASTEP calculations attributed to the limitations of the pseudopotentials used.	132
MgS	0	–	−3.0(5)[b]	See Ref. 39 for a more recent report, with a δ_{iso} value not agreeing with this work.	33
MgS	0.0	–	−1.11(2)	Experimental data supported by first-principles calculations.	39
Mg_2Si	0	–	61.0(5)		33
Mg_2Si	0.0	–	361.67(10)	Experimental data supported by first-principles calculations.	39

MgH_2	3.056(20)	0.89(5)	10.3(1.0)	Experimental data supported by first-principles calculations.	39
Mg_3N_2	n.d.	n.d.	10(100)[b,g]	See Ref. 39 for more recent results.	33
Mg_3N_2	9.300(50)	0.44(1)	101.0(2.0)	Use of QCPMG. Experimental data supported by first-principles calculations. Detection of the largest CSA contribution among the studied Mg compounds (although still small, $\Delta\delta\sim42$ppm). Largest deshielding ever reported for ^{25}Mg (correctly predicted by calculations).	39
$MgSiN_2$	n.d.	n.d.	79,[g] 45,[g] −57[g]		156
$MgAlSiN_3$	n.d.	n.d.	45,[g] −59[g]		156
MgAPO-20 $(Mg,Al)PO_4$, with Al/Mg=2.5	3.8(2)	0.85(5)	50(5)	Use of DFS and QCPMG. Experimental data supported by first-principles calculations. Detection of a small CSA.	38
Dittmarite $NH_4MgPO_4\cdot H_2O$	1.7(1)	0.5(1)	2(1)	Use of DFS and QCPMG. Experimental data supported by first-principles calculations.	108
$[NH_3(CH_2)_4NH_3]_{0.5}[MgPO_4\cdot H_2O]$	2.7(1)	0.4(1)	2(2)	Use of DFS and QCPMG. Experimental data supported by first-principles calculations.	108
$[NH_3(CH_2)_2NH_3]_{0.5}[MgPO_4\cdot H_2O]$	3.3(2)	0.5(1)	4(2)	Use of DFS and QCPMG. Experimental data supported by first-principles calculations.	108
$MgHPO_4\cdot 1.2H_2O$	3.5(2)	0.6(1)	−1(2)	Use of DFS and QCPMG. Experimental data supported by first-principles calculations.	108

(*continued*)

TABLE 2 (*continued*)

Compound	C_q (MHz)	η_q	δ_{iso} (ppm)[a]	Comments	References
MgAl-33 LDH $Mg_{1-x}Al_x(OH)_2(NO_3)_x \cdot yH_2O$, with Mg/Al=2.0	4.6(1)	0.025(25)	13(2)	Use of MQMAS and isotopic enrichment.	46
$(MgO)_x(SiO_2)_{100-x}$ glasses with x=33.3, 40 and 50	7.6[k]	0.35[k]	17	A Gaussian distribution of quadrupole parameters (with FWHM=3MHz for C_q and 0.1 for η_q) was used to fit the spectra.	47

[a] Isotropic chemical shift given with respect to Mg^{2+} in aqueous solution (e.g. of $MgCl_2$ or $MgSO_4$).
[b] Data not confirmed by other reports; see column "Comments".
[c] n.d., not determined.
[d] The authors reported δ_{iso} values with respect to MgO.
[e] Although the crystal structures of these compounds contain more than one Mg site, only one resonance was detected in the reported ^{25}Mg MAS NMR measurements.
[f] The reported results correspond to the maximum value of C_q required for fitting the spectra, giving maximum δ_{iso} as well; the authors state that other C_q values ranging down to 0 are possible, with large line broadening and with corresponding changes in δ_{iso}.
[g] This is the peak position, not the isotropic chemical shift.
[h] This is the centre of gravity of the spectrum, not the isotropic chemical shift.
[i] Different results were achieved for samples of diverse origins.
[j] Estimated.
[k] A Gaussian distribution of quadrupole parameters was used to fit the featureless and asymmetrically broadened spectra in these cases.

Grant et al. described an investigation of the ternary complex of Mg^{2+}, ATP and bis(2-pyridyl)amine (MgATP/BPA), using advanced solid-state NMR methods such as $^{1}H—^{25}Mg$ REDOR and ^{25}Mg MQMAS in ^{25}Mg-isotopically enriched samples.[48] In the 3QMAS spectrum, the authors detected the presence of two Mg sites with close ^{25}Mg quadrupole parameters. With help of a REDOR experiment, the assignment of these two sets of parameters to Mg^{2+} ions either coordinated to water molecules or to phosphate oxygen donors was then possible.

Wu and collaborators[50,51] reported a series of investigations on Mg-containing metalloporphyrins and related compounds, supported by first-principles calculations, as described in Section 3. The quadrupole parameters found for chlorophyll *a* and phthalocyanine[51] did not agree with previously published results by Lumpkin,[166] who determined ^{25}Mg quadrupole parameters for these substances at very low temperature (1.3K) using a completely different (and unusual, considering current state of art) approach: double-resonance experiments combined with field cycling and detection of ^{25}Mg NQR signal. The C_q values obtained in this way were more than three times smaller than the results reported by Wong et al. at room temperature using high-field NMR.[51] It is not clear if such a large discrepancy is due to the temperature difference of the measurements, inaccuracy in the identification of composition and/or structure of the analysed samples or to problems involved in the early methods of measurement.

As already mentioned in Section 2, Lipton et al.[57] used a special probe designed for low-temperature experiments (down to 10K) at strong magnetic fields up to 18.8T and employed $^{1}H—^{25}Mg$ CP combined with QCPMG to study the nature of Mg^{2+}-binding sites in a DNA repair protein. With such an approach, they showed the disordered nature of the single Mg^{2+}-binding site to the protein, both in the presence and in the absence of DNA.

Kakitani et al.[52] studied the stacking of bacteriochlorophyll (BChl) *c* molecules to form the structure of chlorosome (an antenna complex found in some bacteria). They recorded natural abundance solid-state ^{25}Mg NMR of the intact chlorosome and the solid aggregate formed from BChl *c* molecules, using single-pulse MAS experiments performed at strong magnetic field (21.8T). The results are shown in Figure 23. Two superimposed powder patterns with very different quadrupole coupling constants (identified as signals 1 and 2 in the figure) were identified in the intact chlorosome, attributed to sites with different coordination to water molecules in dimer-based stacking of BChl *c* molecules. However, only a single broader resonance (identified as 3 in the figure) was found in the solid aggregate, associated with penta-coordinated Mg. No fitting result was reported in that work, so that no quadrupole or chemical shift parameters are available for the described Mg sites.

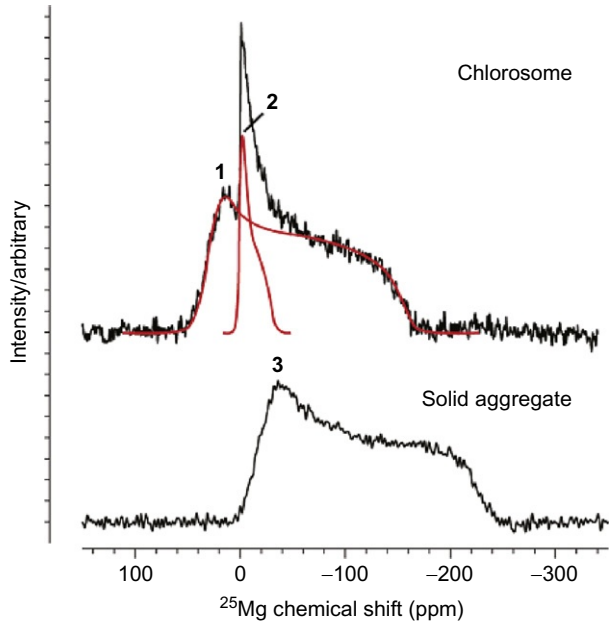

Figure 23 ^{25}Mg MAS NMR spectra of intact chlorosome and of solid aggregate of BChl *c* molecules. Reprinted with permission from Kakitani et al.,[52] Copyright 2009 American Chemical Society.

Cahill et al.[40] recorded ^{25}Mg NMR spectra at multiple magnetic fields for the Mg-containing amino acids L-aspartate and L-glutamate. In the case of Mg L-glutamate tetrahydrate, the spectrum showed the singularities expected for the quadrupole-affected CT resonance, allowing the determination of the NMR parameters with reasonable accuracy: $C_q = 1.75(5)$ MHz, $\eta_q = 0.68(1)$ and $\delta_{iso} = -1(1)$ ppm. The spectrum recorded at 11.7 T was achieved with use of FSG-RAPT for a 100 mg sample (with ^{25}Mg at natural abundance) in ca. 8 h, showing the benefit of the signal-enhancement method in this case. On the other hand, Mg L-aspartate dihydrate gave a featureless, asymmetrically broadened lineshape, reflecting a distribution of quadrupole coupling parameters associated with diverse Mg local environments.[6] The multiple-field spectra were fitted in this case assuming a Gaussian distribution of quadrupole parameters,[22] with mean $C_q = 2.6$ MHz, FWHM = 2.1 MHz, $\eta_q = 0$ and $\delta_{iso} = -2$ ppm.

Laurencin et al.[165] studied the substitution of Mg for Ca in hydroxyapatite, combining ^{1}H, ^{25}Mg, ^{31}P and ^{43}Ca solid-state NMR results (all nuclides at natural abundance) and DFT calculations of the NMR parameters associated with each nuclide. Despite the reported difficulties in achieving good-quality spectra (even at 19.6 T) from samples with small

Mg contents (such as the studied Mg-substituted hydroxyapatites, with up to 10 mol.% Mg with respect to the total cationic concentration), the authors reported a ^{25}Mg MAS NMR spectrum containing a complex lineshape. This was tentatively attributed to the existence of several local environments around Mg sites, leading to a distribution of quadrupole parameters. DFT calculations (supported by ^{1}H, ^{31}P and ^{43}Ca NMR and other experimental results) yielded ^{25}Mg NMR parameters (C_q, η_q and δ_{iso}) that differed depending on the type of Ca site substituted by Mg. The C_q values were particularly sensitive to the details of the local Mg environment in the substituted hydroxyapatites. Even with the observed preference for Mg substitution into Ca(II) sites, small deviations in Mg—O bond lengths could cause large C_q variations, which explains the complex and featureless lineshape observed in the ^{25}Mg NMR spectrum.

Table 3 gives a compilation of the experimentally derived solid-state ^{25}Mg NMR parameters (C_q, η_q and δ_{iso}) reported to date for various Mg-containing organic compounds. Similarly to what was done before for the inorganic compounds, the special methods used to improve sensitivity or resolution in the performed experiments are mentioned in the table, as well as the cases where there are inconsistencies between results achieved by different researchers.

From this dataset, it is apparent that isotropic chemical shift values cover a relatively small range, roughly from 14 to −9 ppm (see also Figure 14A in Section 3), for materials containing oxygen and/or nitrogen as Mg^{2+} first neighbours in similar coordination geometry (distorted octahedral in most cases). The case of the compound $MgCp_2$—with neither oxygen or nitrogen coordination—is noteworthy, since it presents the most shielded ^{25}Mg site (i.e. most negative δ_{iso} value) ever reported, probably due to the interaction with the aromatic Cp rings.[107]

Regarding the quadrupole coupling constants, the typical range corresponding to Mg^{2+} ions in distorted octahedral geometry is ca. 1.5–3.5 MHz (see also Figure 14B in Section 3). A number of compounds having Mg^{2+} coordinated to nitrogen present C_q values above this range. The largest C_q (15.32 MHz) is found for the compound bis(pyridine)-(5,10,15,20-tetraphenylporphyrinato)magnesium(II), with MgN_6 distorted octahedral bonding.[50]

Some tentative graphical correlations between NMR-derived results and structural parameters were given by Cahill et al.[40] For organic compounds with Mg—O bonds in an octahedral arrangement around the central Mg^{2+} ion, the best observed correlation was between C_q values and the longitudinal strain (Equation 16), which is a measure of the deviations of Mg—O bond lengths from ideal values. The accumulation of a larger number of reliable NMR data in Mg-containing organic materials—with accurately determined structures and supported by first-principles calculations—is

TABLE 3 Experimental ^{25}Mg NMR parameters for Mg-containing organic compounds

Compound	C_q (MHz)	η_q	δ_{iso} (ppm)[a]	Comments	References
Bis(cyclopentadienyl)Mg $MgCp_2$	5.80(5)	0.01(1)	−91(3)	Use of QCPMG. Experimental data supported by first-principles calculations. See Refs. 39,40 for comparisons of these experimental data with other results of first-principles calculations. Detection of a small CSA contribution. Largest shielding ever reported for ^{25}Mg.	107
Bis(pyridine)(5,10,15,20-tetraphenylporphyrinato) Mg(II) $Mg(TTP)\cdot Py_2$	15.32(2)	0.00(5)	n.d.[b]	Use of isotopic enrichment. Largest C_q ever reported for ^{25}Mg. Spectra (very broad) recorded with changing RF transmitter offset. Experimental data supported by first-principles calculations. See Ref. 40 for comparison of these experimental data with other results of first-principles calculations.	50
Chlorophyll *a*	3.73	0.2	n.d.	Use of double-resonance NQR. Measurements at low temperature (1.3K). See Ref. 51 for more recent results, at room temperature.	166
Chlorophyll *a*	12.9(1)	1.00(5)	n.d.	Experimental data supported by first-principles calculations.	51
Mg acetate tetrahydrate $Mg(OAc)\cdot 4H_2O$	1.90[c]	0.82[c]	27[c]	Use of isotopic enrichment. See Refs. 39,40 for more recent results not agreeing with this work.	49

Mg acetate tetrahydrate $Mg(OAc)\cdot 4H_2O$	2.8	0.67	n.d.	Measurements at low temperature (50 K), with $^{1}H—^{25}Mg$ CP and QCPMG. See Refs. 39,40 for more recent results at room temperature.	54
Mg acetate tetrahydrate $Mg(OAc)\cdot 4H_2O$	2.534(20)	0.75(3)	4.1(3)	Experimental data supported by first-principles calculations.	39
Mg acetate tetrahydrate $Mg(OAc)\cdot 4H_2O$	2.55(5)	0.73(2)	5(1)	Experimental data supported by first-principles calculations. Use of FSG-RAPT.	40
Mg acetylacetonate dihydrate $Mg(Acac)_2\cdot 2H_2O$	7.1(2)	1.00(1)	−1(1)	Use of FSG-RAPT. Experimental data supported by first-principles calculations.	40
Mg acetylacetonate dihydrate $Mg(Acac)_2\cdot 2H_2O$	7.2(1)	0.96(2)	2.7(4.0)	Use of QCPMG. Experimental data supported by first-principles calculations.	39
Mg adenosine-5′-triphosphate bis(2-pyridyl)amine				Use of isotopic enrichment. Use of MQMAS and $^{1}H—^{25}Mg$ REDOR.	48
Mg ATP/BPA					
Site 1	2.3	1.0	−9		
Site 2	1.6	1.0	−2		
Mg apurinic/apyrimidinic endonuclease 1				Use of isotopic enrichment. Measurements at low temperature (10K), with $^{1}H—^{25}Mg$ CP and QCPMG.	57
Mg APE1					
Site 1	2.4	0.95			
Site 2	1.3	0.79	−2.4[d]		

(*continued*)

TABLE 3 (*continued*)

Compound	C_q (MHz)	η_q	δ_{iso} (ppm)[a]	Comments	References
Mg apurinic/apyrimidinic endonuclease 1/DNA Mg APE1/DNA				Use of isotopic enrichment. Measurements at low temperature (10K), with $^{1}H—^{25}Mg$ CP and QCPMG.	57
Site 1	2.4	0.97			
Site 2	1.3	0.98	−25.8[d]		
Mg disodium EDTA tetrahydrate $Na_2MgEDTA{\cdot}4H_2O$	1.675(5)	0.15(1)	0.25(10)	Use of DFS, WURST and HS pulses (for testing methods). Sample with fast spin relaxation.	41
Mg formate dihydrate $Mg(HCOO)_2{\cdot}2H_2O$				Use of isotopic enrichment. See Refs. 39,40 for more recent results not agreeing with this work.	49
Site 1	1.70[c]	1.0[c]	10[c]		
Site 2	1.40[c]	0.80[c]	10[c]		
Mg formate dihydrate $Mg(HCOO)_2{\cdot}2H_2O$				Experimental data supported by first-principles calculations. Use of FSG-RAPT.	40
Site 1	2.40(10)	0.85(1)	−8(1)		
Site 2	3.75(10)	0.27(1)	−3(1)		
Mg formate dihydrate $Mg(HCOO)_2{\cdot}2H_2O$				Experimental data supported by first-principles calculations.	39
Site 1	2.336(50)	0.81(4)	−0.6(3)		
Site 2	3.521(30)	0.23(4)	−3.9(3)		
Mg L-aspartate dihydrate	2.6[e]	0	−2	Use of FSG-RAPT. A Gaussian distribution of C_q was used to fit the spectra.	40
Mg L-glutamate tetrahydrate	1.75(5)	0.68(1)	−1(1)	Use of FSG-RAPT. Experimental data supported by first-principles calculations.	40

Mg methylmalonate tetrahydrate	1.95[c]	0.80[c]	12[c]	Use of isotopic enrichment. See Ref. 40 for more recent results not agreeing with this work.	49
Mg methylmalonate tetrahydrate	2.55(5)	0.15(5)	14(1)	Experimental data supported by first-principles calculations. Use of FSG-RAPT.	40
Mg phthalocyanine MgPc	3.79	0.1	n.d.	Use of double-resonance NQR. Measurements at low temperature (1.3K). See Ref. 51 for more recent results on a related compound, at room temperature.	166
Monopyridinated aqua(Mg) phthalocyanine $MgPc \cdot H_2O \cdot Py$	13.0(1)	0.00(5)	n.d.	Use of isotopic enrichment and QCPMG. Experimental data supported by first-principles calculations.	51
Tetraaqua-(Orotato-*N*,*O*)-Mg-2.5 hydrate	2.56	0.15	6	Use of isotopic enrichment. See Ref. 40 for comparisons of these experimental data with results of first-principles calculations.	49

[a] Isotropic chemical shift given with respect to Mg^{2+} in aqueous solution (e.g. of $MgCl_2$ or $MgSO_4$).
[b] n.d., not determined.
[c] Data not confirmed by more recent results; see column ''Comments''.
[d] This is the chemical shift difference between the two sites.
[e] A Gaussian distribution of C_q (with mean C_q=2.6MHz and FWHM=2.1MHz) was used to fit the featureless and asymmetrically broadened spectra in this case.

certainly required for the establishment of meaningful and useful correlations between the ^{25}Mg NMR parameters and structural aspects of the bonding involving Mg^{2+} ions in organic systems.

5. SUMMARY AND OUTLOOK

The development of ^{25}Mg solid-state NMR over effectively the past 25 years has been explored. The initial studies were limited in the context of a nucleus with a small magnetic moment and a moderate electric quadrupole moment, but nevertheless there were hints of what could be possible by ^{25}Mg NMR as a probe of materials. The key developments in the past decade have been the availability of much higher magnetic fields along with new schemes for enhancing signal intensity from half-integer spin quadrupolar nuclei. ^{25}Mg provides a good case study of how such changes can drive new developments. This is also true of how the NMR methodology has been much enhanced by the availability of first-principles calculations of the NMR parameters. These factors have all been examined in detail here with ^{25}Mg as the exemplar nucleus. The methodology has opened up a whole range of applications to the local structural information provided by ^{25}Mg NMR. The importance of magnesium as an element in materials chemistry, biology and Earth sciences means that there should be an ever increasing number of applications of this approach and the next decade is likely to see a large increase in the number of ^{25}Mg NMR reports from solids and it is hoped this review is helpful in setting the scene for that development.

ACKNOWLEDGEMENTS

J. C. C. F. gratefully acknowledges the support of Brazilian agencies FAPES, CAPES, FINEP and CNPq. M. E. S. thanks a range of organisations—EPSRC, BBSRC, the University of Warwick, and Birmingham Science City Hydrogen Advanced Materials Projects supported by AWM and the European Regional Development Fund in the latter case. We thank those collaborators we have worked with on ^{25}Mg NMR projects and all the copyright owners who gave permission to use figures. Dr. S. Ashbrook (University of St Andrews) is thanked for providing information about ^{25}Mg of enstatite prior to publication.

REFERENCES

1. A. Hartwig, Role of magnesium in genomic stability. *Mutat. Res.*, 2001, **475,** 113–121.
2. M. E. Maguire and J. A. Cowan, Magnesium chemistry and biochemistry. *Biometals*, 2002, **15,** 203–210.
3. A. Sreedhara and J. A. Cowan, Structural and catalytic roles for divalent magnesium in nucleic acid biochemistry. *Biometals*, 2002, **15,** 211–223.
4. M. J. Arnaud, Update on the assessment of magnesium status. *Br. J. Nutr.*, 2008, **99,** S24–S36.

5. M. E. Smith, Recent progress in solid-state NMR of low-γ nuclei. *Annu. Rep. NMR Spectrosc.*, 2001, **43,** 121–175.
6. K. J. D. MacKenzie and M. E. Smith, Multinuclear Solid-State NMR of Inorganic Materials. Pergamon, Amsterdam, 2002.
7. R. K. Harris, E. D. Becker, S. M. C. De Menezes, R. Goodfellow and P. Granger, NMR nomenclature. Nuclear spin properties and conventions for chemical shifts (IUPAC recommendations 2001). *Pure Appl. Chem.*, 2001, **73,** 1795–1818.
8. I. P. Gerothanassis, Methods of avoiding the effects of acoustic ringing in pulsed Fourier transform nuclear magnetic resonance spectroscopy. *Prog. Nucl. Magn. Reson. Spectrosc.*, 1987, **19,** 267–329.
9. M. E. Smith and E. R. H. van Eck, Recent advances in experimental solid state NMR methodology for half-integer spin quadrupolar nuclei. *Prog. Nucl. Magn. Reson. Spectrosc.*, 1999, **34,** 159–201.
10. M. H. Levitt, Spin Dynamics. Basics of Nuclear Magnetic Resonance. John Wiley & Sons, Chichester, 2001.
11. U. Haeberlen, *in*: Advances in Magnetic Resonance, Suppl. 1, J. S. Waugh (ed.,) Academic Press, New York, 1976.
12. M. Mehring, Principles of High Resolution NMR in Solids. 2nd edn. Springer-Verlag, Berlin, 1983.
13. J. Mason, Conventions for the reporting of nuclear magnetic shielding (or shift) tensors suggested by participants in the NATO ARW on NMR shielding constants at the University of Maryland, College Park, July 1992. *Solid State Nucl. Magn. Reson.*, 1993, **2,** 285–288.
14. R. K. Harris, E. D. Becker, S. M. C. De Menezes, P. Granger, R. E. Hoffman and K. W. Zilm, Further conventions for NMR shielding and chemical shifts (IUPAC recommendations 2008). *Pure Appl. Chem.*, 2008, **80,** 59–84.
15. A. Abragam, Principles of Nuclear Magnetism. Oxford University Press, Oxford, 1961.
16. C. P. Slichter, Principles of Magnetic Resonance. 3rd edn., rev-Springer, Berlin, 1996.
17. R. K. Harris, J. Kowalewski and S. M. C. De Menezes, Parameters and symbols for use in nuclear magnetic resonance (IUPAC recommendations 1997). *Pure Appl. Chem.*, 1997, **69,** 2489–2495.
18. M. J. Duer, Introduction to Solid-State NMR Spectroscopy. Blackwell Science, Oxford, 2004.
19. D. Massiot, F. Fayon, M. Capron, I. King, S. Le Calvé, B. Alonso, J. O. Durand, B. Bujoli, Z. Gan and G. Hoatson, Modelling one- and two-dimensional solid state NMR spectra. *Magn. Reson. Chem.*, 2002, **40,** 70–76.
20. A. P. M. Kentgens, A practical guide to solid-state NMR of half-integer quadrupolar nuclei with some applications to disordered systems. *Geoderma*, 1997, **80,** 271–306.
21. M. Bak, J. T. Rasmussen and N. C. Nielsen, SIMPSON: a general simulation program for solid-state NMR spectroscopy. *J. Magn. Reson.*, 2000, **147,** 296–330.
22. T. F. Kemp and M. E. Smith, QuadFit—a new cross-platform computer program for simulation of NMR line shapes from solids with distributions of interaction parameters. *Solid State Nucl. Magn. Reson.*, 2009, **35,** 243–252.
23. K. Eichele and R. E. Wasylishen, WSolids1—Solid State NMR Simulations Version 1.20.15. Universität Tübingen, Germany, 2011.
24. L. Frydman and J. S. Harwood, Isotropic spectra of half-integer quadrupolar spins from bidimensional magic-angle spinning NMR. *J. Am. Chem. Soc.*, 1995, **117,** 5367–5368.
25. S. P. Brown and S. Wimperis, Two-dimensional multiple-quantum MAS NMR of quadrupolar nuclei: a comparison of methods. *J. Magn. Reson.*, 1997, **128,** 42–61.
26. A. Goldburt and P. K. Madhu, Multiple-quantum magic-angle spinning: high resolution solid-state NMR of half-integer spin quadrupolar nuclei. *Annu. Rep. NMR Spectrosc.*, 2004, **54,** 81–153.

27. J. Kanellopoulos, D. Freude and A. Kentgens, A practical comparison of MQMAS techniques. *Solid State Nucl. Magn. Reson.*, 2007, **32,** 99–108.
28. J. P. Amoureux, M. Pruski, D. P. Lang and C. Fernandez, The effect of RF power and spinning speed on MQMAS NMR. *J. Magn. Reson.*, 1998, **131,** 170–175.
29. Z. Gan, Isotropic NMR spectra of half-integer quadrupolar nuclei using satellite transitions and magic-angle spinning. *J. Am. Chem. Soc.*, 2000, **122,** 3242–3243.
30. N. G. Dowell, S. E. Ashbrook and S. Wimperis, Satellite-transition MAS NMR of low-γ nuclei at natural abundance: sensitivity, practical implementation, and application to ^{39}K ($I = 3/2$) and ^{25}Mg ($I = 5/2$). *J. Phys. Chem. B*, 2004, **108,** 13292–13299.
31. S. E. Ashbrook and S. Wimperis, High-resolution NMR of quadrupolar nuclei in solids: the satellite-transition magic angle spinning (STMAS) experiment. *Prog. Nucl. Magn. Reson. Spectrosc.*, 2004, **45,** 53–108.
32. J. Trebosc, J.-P. Amoureux and Z. Gan, Comparison of high-resolution solid-state NMR MQMAS and STMAS methods for half-integer quadrupolar nuclei. *Solid State Nucl. Magn. Reson.*, 2007, **31,** 1–9.
33. R. Dupree and M. E. Smith, Solid-state magnesium-25 n.m.r. spectroscopy. *J. Chem. Soc. Chem. Commun.*, 1988, 1483–1485.
34. K. J. D. MacKenzie and R. H. Meinhold, ^{25}Mg nuclear magnetic resonance spectroscopy of minerals and related inorganics: a survey study. *Am. Mineral.*, 1994, **79,** 250–260.
35. K. J. D. MacKenzie and R. H. Meinhold, MAS NMR study of pentacoordinated magnesium in grandidierite. *Am. Mineral.*, 1997, **82,** 479–482.
36. F. H. Larsen, J. Skibsted, H. J. Jakobsen and N. C. Nielsen, Solid-state QCPMG NMR of low-γ quadrupolar metal nuclei in natural abundance. *J. Am. Chem. Soc.*, 2000, **122,** 7080–7086.
37. M. Hatakeyama, T. Nemoto, K. Kanehashi and K. Saito, Natural abundance solid-state ^{25}Mg MQMAS NMR studies of inorganic solids at a high magnetic field of 16.4 T. *Chem. Lett.*, 2005, **34,** 864–865.
38. J. Zhu, Z. Lin and Y. Huang, ^{91}Zr and ^{25}Mg solid-state NMR characterization of the local environments of the metal centers in microporous materials. *Chem. Phys. Lett.*, 2008, **461,** 260–265.
39. P. J. Pallister, I. L. Moudrakovski and J. A. Ripmeester, Mg-25 ultra-high field solid state NMR spectroscopy and first principles calculations of magnesium compounds. *Phys. Chem. Chem. Phys.*, 2009, **11,** 11487–11500.
40. L. S. Cahill, J. V. Hanna, A. Wong, J. C. C. Freitas, J. R. Yates, R. K. Harris and M. E. Smith, Natural abundance ^{25}Mg solid-state NMR of Mg oxyanion systems: a combined experimental and computational study. *Chem. Eur. J.*, 2009, **15,** 9785–9798.
41. J. C. C. Freitas, A. Wong and M. E. Smith, Solid-state natural abundance ^{25}Mg NMR studies of $Na_2MgEDTA{\cdot}4H_2O$—a possible new reference compound for ^{25}Mg NMR spectroscopy. *Magn. Reson. Chem.*, 2008, **47,** 9–15.
42. K. Shimoda, T. Nemoto and K. Saito, Local structure of magnesium in silicate glasses: a ^{25}Mg 3QMAS NMR study. *J. Phys. Chem. B*, 2008, **112,** 6747–6752.
43. K. Shimoda, Y. Tobu, K. Kanehashi, T. Nemoto and K. Saito, Total understanding of the local structures of an amorphous slag: perspective from multi-nuclear (^{29}Si, ^{27}Al, ^{17}O, ^{25}Mg, and ^{43}Ca) solid-state NMR. *J. Non Cryst. Solids*, 2008, **354,** 1036–1043.
44. Z. Gan, P. L. GorKov, W. W. Brey, P. J. Sideris and C. P. Grey, Enhancing MQMAS of low-γ nuclei using a high B_1 field balanced probe circuit. *J. Magn. Reson.*, 2009, **200,** 2–5.
45. C. M. Widdifield and D. L. Bryce, Crystallographic structure refinement with quadrupolar nuclei: a combined solid-state NMR and GIPAW DFT example using $MgBr_2$. *Phys. Chem. Chem. Phys.*, 2009, **11,** 7120–7122.
46. P. J. Sideris, U. G. Nielsen, Z. Gan and C. P. Grey, Mg/Al ordering in layered double hydroxides revealed by multinuclear NMR spectroscopy. *Science*, 2008, **321,** 113–117.

47. S. Sen, H. Maekawa and G. N. Papatheodorou, Short-range structure of invert glasses along the pseudo-binary join $MgSiO_3$–Mg_2SiO_4: results from ^{29}Si and ^{25}Mg MAS NMR spectroscopy. *J. Phys. Chem. B*, 2009, **113,** 15243–15248.
48. C. V. Grant, V. Frydman and L. Frydman, Solid-state ^{25}Mg NMR of a magnesium(II) adenosine 5′-triphosphate complex. *J. Am. Chem. Soc.*, 2000, **122,** 11743–11744.
49. S. Sham and G. Wu, Solid-state ^{25}Mg NMR study of inner-sphere Mg^{2+} binding complexes. *Inorg. Chem.*, 2000, **39,** 4–5.
50. G. Wu, A. Wong and S. Wang, Solid-state ^{25}Mg NMR, X-ray crystallographic, and quantum mechanical study of bis(pyridine)-(5,10,15,20-tetraphenylporphyrinato)magnesium(II). *Can. J. Chem.*, 2003, **81,** 275–283.
51. A. Wong, R. Ida, X. Mo, Z. Gan, J. Poh and G. Wu, Solid-state ^{25}Mg NMR spectroscopic and computational studies of organic compounds. Square-pyramidal magnesium(II) ions in aqua(magnesium) phthalocyanine and chlorophyll *a*. *J. Phys. Chem. A*, 2006, **110,** 10084–10090.
52. Y. Kakitani, Y. Koyama, Y. Shimoikeda, T. Nakai, H. Utsumi, T. Shimizu and H. Nagae, Stacking of bacteriochlorophyll *c* macrocycles in chlorosome from *Chlorobium limicola* as revealed by intermolecular ^{13}C magnetic-dipole correlation, X-ray diffraction, and quadrupole coupling in ^{25}Mg NMR. *Biochemistry*, 2009, **48,** 74–86.
53. B. Derighetti, S. Hafner, H. Marxer and H. Rager, NMR of ^{29}Si and ^{25}Mg in Mg_2SiO_4 with dynamic polarization technique. *Phys. Lett. A*, 1978, **66,** 150–152.
54. A. S. Lipton, J. A. Sears and P. D. Ellis, A general strategy for the NMR observation of half-integer quadrupolar nuclei in dilute environments. *J. Magn. Reson.*, 2001, **151,** 48–59.
55. A. S. Lipton, R. W. Heck, J. A. Sears and P. D. Ellis, Low temperature solid-state NMR experiments of half-integer quadrupolar nuclides: caveats and data analysis. *J. Magn. Reson.*, 2004, **168,** 66–74.
56. P. D. Ellis and A. S. Lipton, Low-temperature solid-state NMR spectroscopy: a strategy for the direct observation of quadrupolar nuclides of biological interest. *Annu. Rep. NMR Spectrosc.*, 2006, **60,** 1–38.
57. A. S. Lipton, R. W. Heck, S. Primak, D. R. McNeill, D. M. Wilson, III and P. D. Ellis, Characterization of Mg^{2+} binding to the DNA repair protein apurinic/apyrimidic endonuclease 1 via solid-state ^{25}Mg NMR spectroscopy. *J. Am. Chem. Soc.*, 2008, **130,** 9332–9341.
58. E. M. Dickson and E. F. W. Seymour, Knight shift and electric quadrupole coupling in Mg metal. *J. Phys. C: Solid State Phys.*, 1970, **3,** 666–670.
59. M. A. Fedotov and G. F. Gerasimova, ^{25}Mg and ^{17}O NMR in MgO and $Ni_xMg_{1-x}O$ solid solutions. *React. Kinet. Catal. Lett.*, 1983, **22,** 113–117.
60. L. J. Azevedo, J. E. Schirber, A. C. Switendick, R. J. Baughman and B. Morosin, Nuclear magnetic resonance study of $Cu_{2-x}Zn_xMg$ in the cubic Laves phase. *J. Phys. F: Met. Phys.*, 1981, **11,** 1521–1530.
61. K. P. Such and G. Lehmann, Superposition of ^{29}Si and ^{25}Mg NMR data for forsterite Mg_2SiO_4. *Chem. Phys. Lett.*, 1988, **143,** 463–466.
62. K. J. D. MacKenzie and R. H. Meinhold, A ^{25}Mg magic-angle spinning nuclear magnetic resonance study of the thermal decomposition of magnesium carbonate. *J. Mater. Sci. Lett.*, 1993, **12,** 1696–1698.
63. K. J. D. MacKenzie and R. H. Meinhold, Thermal decomposition of dolomite (calcium magnesium carbonate) studied by ^{25}Mg solid-state nuclear magnetic resonance. *Thermochim. Acta*, 1993, **230,** 331–337.
64. K. J. D. MacKenzie and R. H. Meinhold, Thermal decomposition of brucite, $Mg(OH)_2$: a ^{25}Mg MAS NMR study. *Thermochim. Acta*, 1993, **230,** 339–343.
65. K. J. D. MacKenzie and R. H. Meinhold, ^{27}Al and ^{25}Mg solid-state magic-angle spinning nuclear magnetic resonance study of hydrotalcite and its thermal decomposition sequence. *J. Mater. Chem.*, 1993, **3,** 1263–1269.

66. K. J. D. MacKenzie and R. H. Meinhold, The thermal reactions of talc studied by ^{29}Si and ^{25}Mg MAS NMR. *Thermochim. Acta*, 1994, **244,** 195–203.
67. K. J. D. MacKenzie and R. H. Meinhold, The thermal reactions of synthetic hectorite studied by ^{29}Si, ^{25}Mg and ^{7}Li magic angle spinning nuclear magnetic resonance. *Thermochim. Acta*, 1994, **232,** 85–94.
68. K. J. D. MacKenzie and R. H. Meinhold, Thermal reactions of chrysotile revisited: a ^{29}Si and ^{25}Mg MAS NMR study. *Am. Mineral.*, 1994, **79,** 43–50.
69. T. J. Bastow, Temperature dependence of the nuclear quadrupole coupling and relaxation time of ^{25}Mg in Mg metal. *J. Phys. Condens. Matter*, 1991, **3,** 753–756.
70. T. J. Bastow and M. E. Smith, Observation of precipitation in Mg-Al alloys by ^{25}Mg and ^{27}Al NMR. *J. Phys. Condens. Matter*, 1995, **7,** 4929–4937.
71. T. J. Bastow and S. Celotto, Temperature variation of the Knight shift for ^{25}Mg in magnesium metal. *Solid State Commun.*, 1999, **110,** 271–273.
72. T. J. Bastow, ^{25}Mg NMR determination of Knight shift, spin-lattice relaxation and electric field gradient in MgB_2. *Solid State Commun.*, 2002, **124,** 269–273.
73. T. J. Bastow and S. Celotto, ^{25}Mg NMR site analysis in metals and intermetallics. *Solid State Nucl. Magn. Reson.*, 2009, **35,** 217–222.
74. F. H. Larsen, H. J. Jakobsen, P. D. Ellis and N. C. Nielsen, Sensitivity-enhanced quadrupolar-echo NMR of half-integer quadrupolar nuclei. Magnitudes and relative orientation of chemical shielding and quadrupolar coupling tensors. *J. Phys. Chem. A*, 1997, **101,** 8597–8606.
75. F. H. Larsen, H. J. Jakobsen, P. D. Ellis and N. C. Nielsen, QCPMG-MAS NMR of half-integer quadrupolar nuclei. *J. Magn. Reson.*, 1998, **131,** 144–147.
76. R. Lefort, J. W. Wiench, M. Pruski and J.-P. Amoureux, Optimization of data acquisition and processing in Carr-Purcell-Meiboom-Gill multiple quantum magic angle spinning nuclear magnetic resonance. *J. Chem. Phys.*, 2002, **116,** 2493–2501.
77. P. K. Madhu, A. Goldburt, L. Frydman and S. Vega, Sensitivity enhancement of the MQMAS NMR experiment by fast amplitude modulation of the pulses. *Chem. Phys. Lett.*, 1999, **307,** 41–47.
78. Z. Yao, H. T. Kwak, D. Sakellariou, L. Emsley and P. J. Grandinetti, Sensitivity enhancement of the central transition NMR signal of quadrupolar nuclei under magic-angle spinning. *Chem. Phys. Lett.*, 2000, **327,** 85–90.
79. H.-T. Kwak, S. Prasad, T. Clark and P. J. Grandinetti, Enhancing sensitivity of quadrupolar nuclei in solid-state NMR with multiple rotor assisted population transfers. *Solid State Nucl. Magn. Reson.*, 2003, **24,** 71–77.
80. P. K. Madhu, K. J. Pike, R. Dupree, M. H. Levitt and M. E. Smith, Modulation-aided signal enhancement in the magic angle spinning NMR of spin-5/2 nuclei. *Chem. Phys. Lett.*, 2003, **367,** 150–156.
81. A. P. M. Kentgens and R. Verhagen, Advantages of double frequency sweeps in static, MAS and MQMAS NMR of spin $I = 3/2$ nuclei. *Chem. Phys. Lett.*, 1999, **300,** 435–443.
82. D. Iuga, H. Schäfer, R. Verhagen and A. P. M. Kentgens, Population and coherence transfer induced by double frequency sweeps in half-integer quadrupolar spin systems. *J. Magn. Reson.*, 2000, **147,** 192–209.
83. R. Siegel, T. T. Nakashima and R. E. Wasylishen, Signal enhancement of NMR spectra of half-integer quadrupolar nuclei in solids using hyperbolic secant pulses. *Chem. Phys. Lett.*, 2004, **388,** 441–445.
84. R. Siegel, T. T. Nakashima and R. E. Wasylishen, Sensitivity enhancement of NMR spectra of half-integer quadrupolar nuclei in the solid state via population transfer. *Concepts Magn. Reson.*, 2005, **26A,** 47–61.
85. K. K. Dey, S. Prasad, J. T. Ash, M. Deschamps and P. J. Grandinetti, Spectral editing in solid-state MAS NMR of quadrupolar nuclei using selective satellite inversion. *J. Magn. Reson.*, 2007, **185,** 326–330.

86. N. M. Trease, K. K. Dey and P. J. Grandinetti, Optimum excitation of ''enhanced'' central transition populations. *J. Magn. Reson.*, 2009, **200,** 334–339.
87. T. T. Nakashima, K. J. Harris and R. E. Wasylishen, Pulse FT NMR of non-equilibrium states of half-integer spin quadrupolar nuclei in single crystals. *J. Magn. Reson.*, 2010, **202,** 162–172.
88. E. van Veenendaal, B. H. Meier and A. P. M. Kentgens, Frequency stepped adiabatic passage excitation of half-integer quadrupolar spin systems. *Mol. Phys.*, 1998, **93,** 195–213.
89. R. W. Schurko, I. Hung and C. M. Widdifield, Signal enhancement in NMR spectra of half-integer quadrupolar nuclei via DFS-QCPMG and RAPT-QCPMG pulse sequences. *Chem. Phys. Lett.*, 2003, **379,** 1–10.
90. R. Siegel, T. T. Nakashima and R. E. Wasylishen, Signal-to-noise enhancement of NMR spectra of solids using multiple-pulse spin-echo experiments. *Concepts Magn. Reson.*, 2005, **26A,** 62–77.
91. L. A. O'Dell, K. Klimm, J. C. C. Freitas, S. C. Kohn and M. E. Smith, ^{33}S MAS NMR of a disordered sulfur-doped silicate: signal enhancement via RAPT, QCPMG and adiabatic pulses. *Appl. Magn. Reson.*, 2008, **35,** 247–259.
92. K. K. Dey, J. T. Ash, N. M. Trease and P. J. Grandinetti, Trading sensitivity for information: Carr-Purcell-Meiboom-Gill acquisition in solid-state NMR. *J. Chem. Phys.*, 2010, **133,** 054501.
93. I. Hung and Z. Gan, On the practical aspects of recording wideline QCPMG NMR spectra. *J. Magn. Reson.*, 2010, **204,** 256–265.
94. L. A. O'Dell and C. I. Ratcliffe, Crystal structure based design of signal enhancement schemes for solid-state NMR of insensitive half-integer quadrupolar nuclei. *J. Phys. Chem. A*, 2011, **115,** 747–752.
95. A. J. Pell, G. Kervern, L. Emsley, M. Deschamps, D. Massiot, P. J. Grandinetti and G. Pintacuda, Broadband inversion for MAS NMR with single-sideband-selective adiabatic pulses. *J. Chem. Phys.*, 2011, **134,** 024117.
96. S. Prasad, H.-T. Kwak, T. Clark and P. J. Grandinetti, A simple technique for determining nuclear quadrupole coupling constants with RAPT solid-state NMR spectroscopy. *J. Am. Chem. Soc.*, 2002, **18,** 4964–4965.
97. E. Kupče and J. Freeman, Adiabatic pulses for wideband inversion and broadband decoupling. *J. Magn. Reson. A*, 1995, **115,** 273–276.
98. A. Tannús and M. Garwood, Adiabatic pulses. *NMR Biomed.*, 1997, **10,** 423–434.
99. R. R. Ernst, G. Bodenhausen and A. Wokaun, Principles of Nuclear Magnetic Resonance in One and Two Dimensions. Oxford University Press, Oxford, 1987.
100. R. Siegel, T. T. Nakashima and R. E. Wasylishen, Sensitivity enhancement of NMR spectra of half-integer spin quadrupolar nuclei in solids using hyperbolic secant pulses. *J. Magn. Reson.*, 2007, **184,** 85–100.
101. D. Possa, A. C. Gaudio and J. C. C. Freitas, Numerical simulation of NMR/NQR: applications in quantum computing. *J. Magn. Reson.*, 2011, **209,** 250–260.
102. H. Y. Carr and E. M. Purcell, Effects of diffusion on free precession in nuclear magnetic resonance experiments. *Phys. Rev.*, 1954, **94,** 630–638.
103. S. Meiboom and D. Gill, Modified spin-echo method for measuring nuclear relaxation times. *Rev. Sci. Instrum.*, 1958, **29,** 688–691.
104. A. N. Garroway, Homogeneous and inhomogeneous nuclear spin echoes in organic solids: adamantane. *J. Magn. Reson.*, 1977, **28,** 365–371.
105. B. A. Cowans and J. B. Grutzner, Examination of homogeneous broadening in solids via rotationally synchronized spin-echo NMR spectroscopy. *J. Magn. Reson.*, 1993, **105,** 10–18.
106. M. M. Maricq and J. S. Waugh, NMR in rotating solids. *J. Chem. Phys.*, 1979, **70,** 3300–3316.
107. I. Hung and R. W. Schurko, Solid-state ^{25}Mg QCPMG NMR of bis(cyclopentadienyl) magnesium. *Solid State Nucl. Magn. Reson.*, 2003, **24,** 78–93.

108. J. Zhu and Y. Huang, A natural abundance solid-state ^{25}Mg NMR study of layered magnesium phosphates. *Can. J. Chem.*, 2011, **89,** 803–813.
109. M. C. Davis, W. J. Brouwer, A. S. Lipton, Z. Gan and K. T. Mueller, Characterization of cation environments in polycrystalline forsterite by ^{25}Mg MAS, MQMAS, and QCPMG NMR. *Am. Mineral.*, 2010, **95,** 1601–1607.
110. M. C. Davis, W. J. Brouwer, D. J. Wesolowski, L. M. Anovitz, A. S. Lipton and K. T. Mueller, Magnesium silicate dissolution investigated by ^{29}Si MAS, ^{1}H–^{29}Si CPMAS, ^{25}Mg QCPMG, and ^{1}H–^{25}Mg CP QCPMG NMR. *Phys. Chem. Chem. Phys.*, 2009, **11,** 7013–7021.
111. C. J. Pickard and F. Mauri, Calculations of magnetic resonance parameters in solids and liquids using periodic boundary conditions. *in*: Calculation of NMR and EPR Parameters. Theory and Applications, M. Kaupp, M. Bühl, and V. G. Malkin (eds.), Wiley, Weinheim, 2004, pp. 265–278. Chapter 16.
112. J. R. Yates and C. J. Pickard, Computations of magnetic resonance parameters for crystalline systems: principles. *in*: Encyclopedia of Magnetic Resonance, R. K. Harris, R. E. Wasylishen, and M. J. Duer (eds.), Wiley, New York, 2008.
113. T. Charpentier, The PAW/GIPAW approach for computing NMR parameters: a new dimension added to NMR study of solids. *Solid State Nucl. Magn. Reson.*, 2011, **40,** 1–20.
114. T. Helgaker, M. Jaszunski and K. Ruud, Ab initio methods for the calculation of NMR shielding and indirect spin-spin coupling constants. *Chem. Rev.*, 1999, **99,** 293–352.
115. J. C. Facelli, Shielding calculations. *in*: Encyclopedia of Magnetic Resonance, D. M. Grant and R. K. Harris (eds.), Wiley, New York, 2007.
116. M. J. Frisch, G. W. Trucks, H. B. Schlegel, G. E. Scuseria, M. A. Robb, J. R. Cheeseman, G. Scalmani, V. Barone, B. Mennucci, G. A. Petersson, H. Nakatsuji M. Caricato, *et al.*, Gaussian 09, Revision A.1. Gaussian, Inc., Wallingford, CT, 2009.
117. B. Winkler, P. Blaha and K. Schwarz, Ab initio calculation of electric-field-gradient tensors of forsterite. *Am. Miner.*, 1996, **81,** 545–549.
118. P. Blaha, K. Schwarz and P. Herzig, First-principles calculation of electric field gradient of Li_3N. *Phys. Rev. Lett.*, 1985, **54,** 1192–1195.
119. K. Schwarz, C. Ambrosch-Draxl and P. Blaha, Charge distribution and electric-field gradients in $YBa_2Cu_3O_{7-x}$. *Phys. Rev. B*, 1990, **42,** 2051–2061.
120. H. M. Petrilli, P. E. Blöchl, P. Blaha and K. Schwarz, Electric-field-gradient calculations using the projector augmented wave method. *Phys. Rev. B*, 1998, **57,** 14690–14697.
121. J. Cuny, S. Messaoudi, V. Alonzo, E. Furet, J.-F. Halet, E. Le Fur, S. E. Ashbrook, C. J. Pickard, R. Gautier and L. Le Polles, DFT calculations of quadrupolar solid-state NMR properties: some examples in solid-state inorganic chemistry. *J. Comput. Chem.*, 2008, **29,** 2279–2287.
122. K. Schwarz, P. Blaha and G. K. H. Madsen, Electronic structure calculations of solids using the WIEN2k package for materials sciences. *Comput. Phys. Commun.*, 2002, **147,** 71–76.
123. P. Blaha, K. Schwarz, G. K. H. Madsen, D. Kvasnicka and J. Luitz, Wien2k, Version 10.1. 2010, Inst. f. Materials Chemistry, TU Vienna.
124. K. Wolinski, J. F. Hinton and P. Pulay, Efficient implementation of the gauge-independent atomic orbital method for NMR chemical-shift calculations. *J. Am. Chem. Soc.*, 1990, **112,** 8251–8260.
125. M. D. Segall, P. J. D. Lindan, M. J. Probert, C. J. Pickard, P. J. Hasnip, S. J. Clark and M. C. Payne, First-principles simulations: ideas, illustrations and the CASTEP code. *J. Phys. Condens. Matter*, 2002, **14,** 2717–2744.
126. M. D. Segall, , M. J. Probert, , P. J. D. Lindan, , S. J. Clark, , C. J. Pickard, , P. J. Hasnip, , K. Refson, , J. R. Yates , and M. C. Payne, CASTEP Developers Group, CASTEP, Version 5.0. 2010.
127. C. J. Pickard and F. Mauri, All-electron magnetic response with pseudopotentials: NMR chemical shifts. *Phys. Rev. B*, 2001, **63,** 245101.

128. S. E. Ashbrook, Recent advances in solid-state NMR spectroscopy of quadrupolar nuclei. *Phys. Chem. Chem. Phys.*, 2009, **11,** 6892–6905.
129. T. J. Bastow, Electric field gradients at the M-site in MCO_3: M = Mg, Ca, Sr and Ba. *Chem. Phys. Lett.*, 2002, **354,** 156–159.
130. A. V. Tsvyashchenko, L. N. Fomicheva, M. V. Magnitskaya, E. N. Shirani, V. B. Brudanin, D. V. Filossofov, O. I. Kochetov, N. A. Lebedev, A. F. Novgorodov, A. V. Salamatin, N. A. Korolev A. I. Velichkov, *et al*., Electric field gradients in MgB_2 synthesized at high pressure: ^{111}Cd TDPAC study and ab initio calculation. *Solid State Commun.*, 2001, **119,** 153–158.
131. S. Rossano, F. Mauri, C. J. Pickard and I. Farnan, First-principles calculation of ^{17}O and ^{25}Mg NMR shieldings in MgO at finite temperature: rovibrational effect in solids. *J. Phys. Chem. B*, 2005, **109,** 7245–7250.
132. R. M. Kowalczyk, T. F. Kemp, D. Walker, K. J. Pike, P. A. Thomas, J. Kreisel, R. Dupree, M. E. Newton, J. V. Hanna and M. E. Smith, A variable temperature solid-state nuclear magnetic resonance, electron paramagnetic resonance and Raman scattering study of molecular dynamics in ferroelectric fluorides. *J. Phys. Condens. Matter*, 2011, **23,** 315402.
133. J. F. Griffin, A. J. Berry and S. E. Ashbrook, Observation of ''hidden'' magnesium: first-principles calculations and ^{25}Mg solid-state NMR of enstatite. *Solid State Nucl. Magn. Reson.*, 2011, **40,** 91–99.
134. P. S. Fiske, J. F. Stebbins and I. Farnan, Bonding and dynamical phenomena in MgO: a high temperature ^{17}O and ^{25}Mg NMR study. *Phys. Chem. Miner.*, 1994, **20,** 587–593.
135. R. K. Harris, P. Hodgkinson, C. J. Pickard, J. R. Yates and V. Zorin, Chemical shift computations on a crystallographic basis: some reflections and comments. *Magn. Reson. Chem.*, 2007, **45,** S174–S186.
136. D. H. Brower, A structure refinement strategy for NMR crystallography: an improved crystal structure of silica-ZSM-12 zeolite from ^{29}Si chemical shift tensors. *J. Magn. Reson.*, 2008, **194,** 136–146.
137. C. J. Pickard and R. J. Needs, *Ab initio* random structure searching. *J. Phys. Condens. Matter*, 2011, **23,** 053201.
138. N. Bloemberger, On the magnetic resonance absorption in conductors. *J. Appl. Phys.*, 1952, **23,** 1383–1389.
139. J. Nagamatsu, N. Nakagawa, T. Muranaka, Y. Zenitani and J. Akimitsu, Superconductivity at 39 K in magnesium diboride. *Nature (London)*, 2001, **410,** 63–64.
140. M. Mali, J. Roos, A. Shengelaya and H. Keller, ^{25}Mg NMR study of the MgB_2 superconductor. *Phys. Rev. B*, 2002, **65,** 100518.
141. E. Pavarini and I. I. Mazin, NMR relaxation rates and Knight shifts in MgB_2. *Phys. Rev. B*, 2001, **64,** 140504.
142. A. V. Chadwick, I. J. F. Poplett, D. T. S. Maitland and M. E. Smith, Oxygen speciation in nanophase MgO from solid state ^{17}O NMR. *Chem. Mater.*, 1998, **10,** 864–870.
143. L. A. O'Dell, S. L. P. Savin, A. V. Chadwick and M. E. Smith, A ^{27}Al, ^{29}Si, ^{25}Mg and ^{17}O NMR investigation of alumina and silica Zener pinned, sol-gel prepared nanocrystalline ZrO_2 and MgO. *Faraday Discuss.*, 2007, **134,** 83–102.
144. Y. I. Kim, S. Cadars, R. Shayib, T. Proffen, C. S. Feigerle, B. F. Chmelka and R. Seshadri, Local structures of polar wurtzites $Zn_{1-x}Mg_xO$ studied by Raman and ^{67}Zn/^{25}Mg NMR spectroscopies and by total neutron scattering. *Phys. Rev. B*, 2008, **78,** 195205.
145. K. Murakami, K. Yamada, K. Deguchi, T. Shimizu and S. Ando, Preparation of soluble polyimide/MgO nanohybrid films by *in situ* hybridization method and evaluation of their thermal conductivity. *J. Photopolym. Sci. Technol.*, 2010, **23,** 501–506.
146. T. J. Bastow, ^{25}Mg nuclear quadrupole coupling in $Mg(OH)_2$. *Solid State Commun.*, 1991, **77,** 547–548.
147. N. Pecoul, S. Bourbigot and B. Revel, ^{13}C, ^{25}Mg and ^{11}B solid-state NMR study of a fire retarded ethylene-vinyl acetate copolymer. *Macromol. Symp.*, 1997, **119,** 309–315.

148. D. Padro, A. P. Howes, M. E. Smith and R. Dupree, Determination of titanium NMR parameters of $ATiO_3$ compounds: correlations with structural distortion. *Solid State Nucl. Magn. Reson.*, 2000, **15,** 231–236.
149. P. S. Fiske and J. F. Stebbins, The structural role of Mg in silicate liquids: a high-temperature ^{25}Mg, ^{23}Na and ^{29}Si NMR study. *Am. Mineral.*, 1994, **79,** 848–861.
150. S. Kroeker and J. F. Stebbins, Magnesium coordination environments in glasses and minerals: new insight from high-field magnesium-25 MAS NMR. *Am. Mineral.*, 2000, **85,** 1459–1464.
151. J. F. Stebbins, Magnesium site exchange in forsterite: a direct measurement by high-temperature ^{25}Mg NMR spectroscopy. *Am. Mineral.*, 1996, **81,** 1315–1320.
152. A. M. George and J. F. Stebbins, Structure and dynamics of magnesium in silicate melts: a high-temperature ^{25}Mg NMR study. *Am. Mineral.*, 1998, **83,** 1022–1029.
153. S. Ghose and T. Tsang, Structural dependence of quadrupole coupling constant e^2qQ/h for ^{27}Al and crystal field parameter D for Fe^{3+} in aluminosilicates. *Am. Mineral.*, 1973, **58,** 748–755.
154. A. Buzlukov, A. Trokiner, V. Kozhevnikov, S. Verkhovskii, A. Yakubovsky, I. Leonidov, A. Gerashenko, A. Stepanov, I. Baklanova and A. Tankeyev, Vacancy ordering and oxygen dynamics in oxide ion conducting $La_{1-x}Sr_xGa_{1-x}Mg_xO_{3-x}$ ceramics: ^{71}Ga, ^{25}Mg and ^{17}O NMR. *J. Solid State Chem.*, 2011, **184,** 36–43.
155. Y. Hiyama, P. M. Woyciesjes, T. L. Brown and D. A. Torchia, Magnesium-25 nuclear quadrupole resonance. *J. Magn. Reson.*, 1987, **72,** 1–12.
156. K. J. D. MacKenzie and R. H. Meinhold, Role of additives in the sintering of silicon nitride: a ^{29}Si, ^{27}Al, ^{25}Mg and ^{89}Y MAS NMR and X-ray diffraction study. *J. Mater. Chem.*, 1994, **4,** 1595–1602.
157. M. E. Smith, Application of ^{27}Al NMR techniques to structure determination in solids. *Appl. Magn. Reson.*, 1993, **4,** 1–64.
158. S. Kroeker, P. S. Neuhoff and J. F. Stebbins, Enhanced resolution and quantitation from 'ultrahigh' field NMR spectroscopy of glasses. *J. Non Cryst. Solids*, 2001, **293,** 440–445.
159. S. C. Kohn, R. Dupree and M. E. Smith, A multinuclear magnetic resonance study of the structure of hydrous albite glasses. *Geochim. Cosmochim. Acta*, 1989, **53,** 2925–2935.
160. S. C. Kohn, M. E. Smith, P. J. Dirken, E. R. H. van Eck, A. P. M. Kentgens and R. Dupree, Sodium environments in dry and hydrous albite glasses: improved ^{23}Na solid state NMR data and their implications for water dissolution mechanisms. *Geochim. Cosmochim. Acta*, 1998, **62,** 79–87.
161. K. Shimoda, Y. Tobu, M. Hatakeyama, T. Nemoto and K. Saito, Structural investigation of Mg local environments in silicate glasses by ultra-high field ^{25}Mg 3QMAS NMR spectroscopy. *Am. Mineral.*, 2007, **92,** 695–698.
162. J. R. Allwardt and J. F. Stebbins, Ca-Mg and K-Mg mixing around non-bridging O atoms in silicate glasses: an investigation using ^{17}O MAS and 3QMAS NMR. *Am. Mineral.*, 2004, **89,** 777–784.
163. K. J. D. MacKenzie and R. H. Meinhold, Additive-assisted pressureless sintering of carbothermal β′-sialon: an X-ray and solid-state MAS NMR study. *J. Mater. Chem.*, 1996, **6,** 821–831.
164. K. J. D. MacKenzie, C. M. Sheppard and C. McCammon, Effect of MgO, Y_2O_3, and Fe_2O_3 on silicothermal synthesis and sintering of X-sialon. An XRD, multinuclear MAS NMR and ^{57}Fe Mössbauer study. *J. Eur. Ceram. Soc.*, 2000, **20,** 1975–1985.
165. D. Laurencin, N. Almora-Barrios, N. H. de Leeuw, C. Gervais, C. Bonhomme, F. Mauri, W. Chrzanowski, J. C. Knowles, R. J. Newport, A. Wong, Z. Gan and M. E. Smith, Magnesium incorporation into hydroxyapatite. *Biomatererials*, 2011, **32,** 1826–1837.
166. O. Lumpkin, ^{25}Mg and ^{14}N nuclear quadrupole resonances in chlorophyll-a and magnesium phthalocyanine. *J. Chem. Phys.*, 1975, **62,** 3281–3283.

CHAPTER 3

Methods and Applications of Phosphorus NMR Spectroscopy *In Vivo*

Jing-Huei Lee,[*,†,‡] **Richard A. Komoroski,**[†,‡] **Wen-Jang Chu,**[†,‡] and **Jonathan A. Dudley**[*,‡]

Contents

Abstract

Phosphorus-31 MRS is one of the earliest *in vivo* MRS methods. It was widely employed by the MR community even before the advent of clinical MRI and is an excellent technique to study *in vivo*

* School of Energy, Environmental, Biological, and Medical Engineering, University of Cincinnati, Cincinnati, Ohio, USA
† Department of Psychiatry and Behavioral Neuroscience, University of Cincinnati, Cincinnati, Ohio, USA
‡ Center for Imaging Research, University of Cincinnati, Cincinnati, Ohio, USA

Annual Reports on NMR Spectroscopy, Volume 75
ISSN 0066-4103, DOI: 10.1016/B978-0-12-397018-3.00003-X

metabolism associated with bioenergy and cell membranes. During its almost 40 years practice in *in vivo* research, there have been many reviews. In this review, we focus on the past 5 years of research applications and development, based on a PUBMED search using the keywords "phosphorus-31 OR 31P" and "MRS". In addition to reporting the current trend of ^{31}P MRS technical development, we also emphasize its application in biomedical research, particularly in disease diagnosis and biomarkers. We also give brief comments on the future direction of *in vivo* ^{31}P MRS.

Key Words: ^{31}P MRS, ^{31}P MRSI, High fields, Human MRS, MRS animal models

1. INTRODUCTION

NMR spectroscopy, commonly called magnetic resonance spectroscopy (MRS) in its *in vivo* application, is continuing to expand its reach in both biomedical research and clinical medicine.[1] Currently, most *in vivo* MRS utilizes ^{1}H as a straightforward addition to ^{1}H MRI on a clinical scanner. The high sensitivity of ^{1}H permits relatively small tissue volumes, on the order of 1–8ml, to be probed *in vivo* in humans. With water suppression, ^{1}H MRS of brain detects several compounds that are markers of important metabolic processes.

Phosphorus-31 MRS, which has been widely applied since the early days of *in vivo* MRS, is also an excellent technique to study *in vivo* metabolism. The ^{31}P isotope (I=1/2) is 100% naturally abundant with a sensitivity of 6.63% that of ^{1}H. An early review provided an excellent introduction to many aspects of *in vivo* ^{31}P MRS.[2] A more recent update focused on several areas of particular interest to those authors.[3] Here, we first provide a brief introduction and update to key characteristics and methodological developments of *in vivo* ^{31}P MRS. We then review major trends for *in vivo* applications appearing in English in both humans and animals over approximately the past 5 years. Finally, we speculate concerning the future direction and impact of ^{31}P MRS in biomedicine.

2. METHODS

2.1. Chemical shifts and information content

The chemical-shift range of ^{31}P MRS for biologically relevant compounds is about 30ppm, which is substantially larger than for the proton, which spans about 5ppm. Also, because fewer compounds are typically

observed, ^{31}P MR spectra are relatively uncrowded compared to ^{1}H MR spectra. Phosphorus-31 MRS provides information on a very different group of compounds than does ^{1}H MRS. In *In vivo,* it monitors essentially two classes of compounds—high-energy-phosphorus metabolites and phospholipid metabolites. The key high-energy-phosphorus metabolites adenosine triphosphate (ATP) and phosphocreatine (PCr) are readily measured. Inorganic phosphate (Pi), a degradation product of all biological phosphorus compounds, is also observed. The phosphomonoesters (PMEs), phosphocholine (PC) and phosphoethanolamine (PE), which are synthetic precursors to the corresponding phospholipids, are observable either separately or in combination, as are the phosphodiester (PDE) degradation products of phospholipid metabolism, glycerophosphocholine (GPC), and glycerophosphoethanolamine (GPE). Depending on signal-to-noise ratio (SNR), spectral resolution, and the system being studied, several other P-containing compounds may be detected.[2] Estimates of intracellular pH (pHi) and intracellular Mg^{2+} concentration can be made from the chemical-shift separations of Pi and PCr, and β-ATP and PCr, respectively.[4,5] A typical *in vivo* spectrum of brain is shown in Figure 1.[6] Additionally, adenosine diphosphate (ADP), which plays an important role in mitochondrial function and cell maintenance, can also be determined indirectly from [ATP], [PCr], [Cr] (measured from ^{1}H MRS) with some assumptions.[7,8]

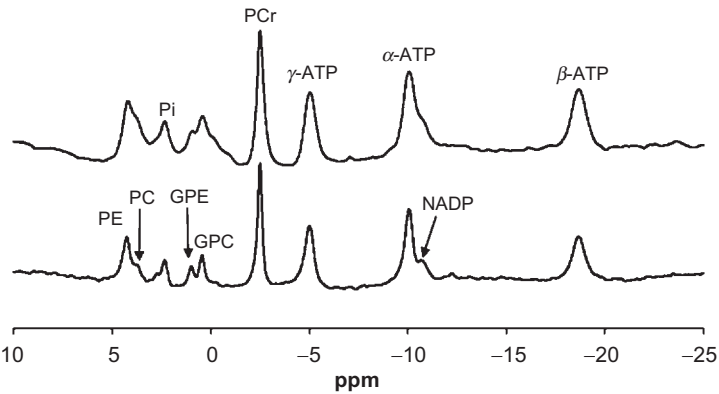

Figure 1 *In vivo* ^{31}P spectra acquired from the human occipital lobe at 4 T (top)and 7 T (bottom) using the same experimental setup and NMR acquisition parameters (TR=3 s and 128 signal averages). PE, phosphoethanolamine; PC, phosphocholine; Pi, inorganic phosphate; GPE, glycerophosphoethanolamine; GPC, glycerophosphocholine; PCr, phosphocreatine; ATP, adenosine triphosphate; NADP, nicotinamide adenine dinucleotide phosphate. Reprinted from reference 6.

2.2. High magnetic fields

Most ^{31}P MRS studies of human subjects have been performed at 1.5T, whereas studies of small animals are usually at higher fields on dedicated, narrow-bore scanners from 4.7 to 16.45T. Magnetic fields from 3 to 9.4T are now becoming more widely available for human studies. The sensitivity and spectral resolution of ^{31}P MRS undoubtedly benefit from higher magnetic field.[6,9,10] Figure 1 demonstrates the effects of increasing the magnetic field from 4 to 7T for ^{31}P MRS of human occipital lobe.[6] Whereas at 4T the individual PMEs and PDEs are marginally resolved, they are well resolved without spin decoupling at 7T.

2.3. Spin decoupling

Given the line broadening due to the heterogeneity of magnetic susceptibility of tissue, which depends approximately linearly on magnetic field, spin couplings are usually not observed for *in vivo* ^{31}P MRS of most organs. The unresolved three-bond ^{31}P—^{1}H couplings of about 6–7Hz for the phospholipid metabolites are never resolved and contribute to significant line broadening at lower fields (e.g. 1.5T). This broadening contributes to PE and PC (PMEs) remaining unresolved *in vivo* and similarly for GPE and GPC (PDEs). The two-bond ^{31}P—^{31}P couplings of about 16Hz in ATP and similar compounds are sometimes resolved at lower fields but usually result in further broadening of those ^{31}P resonances at high fields. Proton decoupling collapses the coupled ^{31}P multiplets of the phospholipid metabolites, permitting resolution of PC from PE and GPC from GPE *in vivo* at magnetic fields less than 4T.[11] Of course, care must be taken to not exceed specific-absorption-rate (SAR) limits from the substantial additional RF power from decoupling and possibly the nuclear Overhauser enhancement (see below). Proton spin decoupling typically is of little use for *in vivo* ^{31}P MRS at higher fields, because magnetic susceptibility effects dominate the line broadening and the individual PMEs and PDEs are often resolved in any event.[2]

2.4. Spin-relaxation times

Phosphorus-31 spin relaxation times have been measured over a range of magnetic fields. While there is some disagreement on the precise values, T_1s are typically in the range of 0.6–6s in brain and muscle, with values in liver being somewhat shorter.[6,10,12,13] As expected, T_2 values are substantially shorter than the corresponding T_1 values, with T_2 values for most metabolites in the range of several hundred milliseconds. The exception is ATP, which has significantly shorter T_2s, with reported values ranging from about 8 to 90ms.[9,10,13] The magnitude of T_2 is particularly important

as it strongly influences the choice of localization method for *in vivo* MRS (see below). In contrast to the typical behaviour of ^{1}H with magnetic field, in brain and muscle, T_1 decreases with increasing field;[6,12] in muscle, T_2 also has been shown to decrease with increasing field.[10] The decreases in spin relaxation times with field strength are consistent with the increased contribution of the chemical-shift-anisotropy (CSA) relaxation mechanism, relative to the dipolar mechanism, at higher field.[14] However, this may not be the case for liver, where paramagnetic ions may contribute significantly to ^{31}P spin relaxation.[15] Tables 1 and 2 provide compilations of reported T_1s and T_2s in humans and rats, respectively.

2.5. Sensitivity enhancement by pulse technique

Given the low sensitivity of ^{31}P relative to ^{1}H, methods to enhance sensitivity are highly valuable. Unlike for ^{13}C, isotopic enrichment is not possible. Beyond the use of higher magnetic field (see above) or instrumental technique improvements (see below), it is generally necessary to rely on double-resonance methods to improve sensitivity. Perhaps the most straightforward method relies on the Nuclear Overhauser Effect (NOE),[1] whereby the ^{31}P signal is increased by irradiation of the protons which are dipolar coupled. The NOE can yield a maximum enhancement factor of 224% for ^{31}P totally relaxed by a dipolar mechanism to irradiated protons. Observed enhancements are usually reduced from the maximum,[2,9,14] depending on metabolite, and are further reduced or eliminated at higher magnetic fields, where the dipolar mechanism is less favoured relative to the CSA mechanism. For example, Lei et al. found NOEs of 10–44% depending on metabolite for human brain at 7T.[9] The advantage of the NOE relative to polarization-transfer methods (see below) is that the entire spectrum is still observed. The major disadvantage is power deposition and the potential for exceeding SAR limits.

Polarization-transfer techniques have long been applied in high-resolution NMR.[34,35] In these techniques, the higher nuclear spin polarization of a nucleus such as ^{1}H is transferred to a J-coupled, lower-sensitivity nucleus (X). The transfer is accomplished by applying synchronized radiofrequency (RF) pulses at the two frequencies such that the two spin species share common energy levels. This results in a theoretical enhancement of γ_H/γ_X (for ^{31}P, a factor of 2.5). Moreover, additional sensitivity gains are realized because pulse repetition rates are governed by the ^{1}H T_1s, which are typically much shorter than for ^{31}P. These techniques are now being applied to ^{31}P *in vivo*.[36–39] Klomp et al. have implemented a technique dubbed *s*elective *r*efocused *i*nsensitive *n*uclei *e*nhanced by *p*olarization transfer (sRINEPT) on a 3-T clinical MRI scanner.[36] This 3D magnetic resonance spectroscopic imaging (MRSI) pulse sequence is shown in Fig. 2 of Ref. 36. The sequence can be implemented on a

TABLE 1 Relaxation times of ^{31}P metabolites for human *in vivo* studies

B_0 (T)	Tissue type	Method	PME	Pi	PDE	PCr	γ-ATP	α-ATP	β-ATP
		T_1 relaxation time (s)							
1.5	Brain [16]	IR	1.42	1.45	1.32	3.14	0.65	0.85	0.8
	Brain [17]	Fast IR	1.4	1.4	1.3	3.1	0.6	0.8	0.8
	Brain [18]	IR	2.74	1.47	1.64	3.29	1.36	0.97	1.03
	Calf muscle [19]	IR		4.0		5.5	4.7	3.6	4.3
	Calf muscle [20]	SR		4.7		6.5	4.2	3.9	4.1
	Calf muscle [21]	SR		3.5		5.0	4.1	2.9	3.6
	Calf muscle [22]	IR		4.2		6.1	4.6	3.2	3.7
	Calf muscle [22]	PS		4.0		5.6	4.5	3.4	3.8
1.9	Brain [23]	SR	2.8	2.5	2.4	4.8	1.0		
2.0	Brain [17]	Fast IR	1.7	1.4	1.3	2.7	0.6	1.0	0.7
	Brain [24]	STEAM	4	2.5	2	3	0.7	0.7	1
	Calf muscle [25]	2-angle		5.4		6.0	3.5	3.9	3.9
	Calf muscle [25]	IR		4.6		6.5	4.8	3.5	3.6
3.0	Calf muscle [8]	IR	8.1	6.9	8.6	6.7	5.5	3.4	3.9
	Calf muscle [26]	STEAM		5.2		6.4	4.5	2.6	3.5
4.0	Occipital lobe [6]	IR				4.27			
4.1	White matter [27]	PS	1.573	1.591	2.208	2.385	0.786	0.849	0.771
7.0	Occipital lobe [6]	IR				3.37			
	Visual cortex [7]	IR		3.19		3.37	1.27	1.26	1.02
	Calf muscle [6]	IR	3.1	6.3	6.0	4.0	3.3	1.8	1.8

		T_2 relaxation time (ms)							
1.5	Calf muscle [28]	SE		205		424	16	22	8
	Calf muscle [29]	sel. SE/SE		240		425	93	74	75
2.0	Brain [24]	STEAM	70	80	20	150	30	30	20
3.0	Calf muscle [8]	sel. SE		153	414	354	62	47	
	Calf muscle [26]	STEAM		148		334	78	55	55
7.0	Visual cortex [7]	SE				132	26	26	
	Calf muscle [6]	sel. SE		109	314	217	29		

IR, inversion recovery; SR, saturation recovery; PS, progressive saturation; STEAM, progressive saturation with stimulated echo acquisition mode; SE, Hahn spin-echo; sel. SE, frequency selective spin-echo.

TABLE 2 Relaxation times of ^{31}P metabolites for rat *in vivo* studies

B_0 (T)	Tissue type	Method	PME	Pi	PCr	γ-ATP	α-ATP	β-ATP
				T_1 relaxation time (s)				
1.9	Leg muscle[10]	SR			5.6			2.4
	Leg muscle[30]	ss ST			6.0	2.5	2.7	2.3
	Brain[10]	SR			3.9			
4.7	Leg muscle[10]	SR			4.5	2.8	2.0	2.0
	Leg muscle[11]	SE			5.1	3.7	2.7	2.7
	Brain[10]	SR		5.6	4.4	2.0	1.5	1.6
	Brain[31]	SE	3.8	2.6	3.5	1.4	1.3	1.1
	Brain, 5–6 months[32]	SR		2.01	3.02	1.68	1.85	1.00
	Brain, 11–12 months[32]	SR		3.22	3.04	1.72	1.10	1.06
	Brain, 24–25 months[32]	SR		3.00	2.71	1.51	0.97	1.45
	Brain, newborn pup[33]	SR	4.66		3.52			1.45
	Brain glioma[11]	SE	5.4	4.9	4.7	2.1	2.2	2.1
	Liver[10]	SR	1.3	1.0		0.3	0.4	0.2
8.5	Leg muscle[10]	SR			2.7	1.7	1.1	1.2
	Brain[10]	SR		3.2	2.8	1.1	0.9	0.7
	Liver[10]	SR	1.3	1.0		0.4	0.4	0.3
				T_2 relaxation time (ms)				
4.7	Leg muscle[11]	SE			234	11.5	12	9
	Brain[31]	SE	84	62	169	40.5	32.7	22.2
	Brain glioma[31]	SE	136	120	171	53.6	40.5	24.8

SR, saturation recovery; ss ST, steady state saturation transfer; SE, Hahn spin-echo.

single-channel broadband system, as the polarization-transfer pulses need not be rigorously synchronized.[36,38] Because anti-phase magnetization components are refocused, ^{31}P spectra can be acquired with ^{1}H-decoupling. The competing effects of homonuclear ^{1}H—^{1}H spin coupling on polarization-transfer efficiency are eliminated by selective polarization of ^{31}P-coupled protons only. Essentially full enhancement of the ^{1}H-coupled ^{31}P signals was realized. The major limitation of the technique is that only the PMEs and PDEs of phospholipid metabolism are suitable for enhancement; P-atoms of high-energy metabolites have no significant spin coupling to ^{1}H and are eliminated from the spectrum.

The technique of J-cross-polarization (JCP), which is based on cross-relaxation between heteronuclear J-coupled spins,[40] is an alternative

double-resonance technique for sensitivity enhancement of ^{31}P *in vivo*.[41] Currently, it does not deliver enhancements comparable to the more highly developed sRINEPT.[36,39] As for INEPT-based polarization transfer, it is necessary to have significant heteronuclear J-coupling between ^{1}H and ^{31}P to realize signal enhancement with JCP, and again only PMEs and PDEs are observed for ^{31}P MRS.

Several methods are available to produce non-Boltzmann (hyperpolarized) spin states with the accompanying very large increases (>10,000) in sensitivity.[42] The most common are dynamic nuclear polarization (DNP) and *para*-hydrogen-induced polarization (PHIP), which have seen considerable development for ^{13}C and other low-abundance isotopes *in vivo*. Application to ^{31}P is at the earliest stage, perhaps because *in vivo* ^{31}P MRS is already a well-developed technique. The deoxynucleotide triphosphate ^{31}P signals were substantially enhanced by DNP *in vitro*,[43] while the γ-P of ATP was enhanced via the PHIP technique in the production of ^{13}C-enhanced pyruvate from the precursor phosphoenolpyruvate.[24] The ultimate utility of hyperpolarization techniques for ^{31}P MRS must await further technique development.

2.6. Spatial localization and data acquisition

In most cases, precise spatial localization to the tissue of interest is critical for informative *in vivo* MRS. For ^{1}H MRS, a wide variety of methods have been employed to achieve either single-voxel or multi-voxel localization.[1] Because of the short T_2s and large spectral width relative to ^{1}H MRS, the choices are fewer for ^{31}P MRS in practice. Image-selected *in vivo* spectroscopy (ISIS),[44] often combined with outer-volume suppression, remains the single-voxel technique of choice for ^{31}P MRS, particularly for human studies. Its advantages and limitations are well known.[1] Many refinements have rendered ISIS an advantageous technique, even at high field.[45] Other single-voxel sequences, such as STEAM and PRESS at very low TEs around 2–3 ms, can be used for ^{31}P in some cases, although pulse bandwidth limitations preclude full excitation of the entire ^{31}P chemical-shift range.[46] Some variation of MRSI is the preferred approach for multi-voxel acquisition of ^{31}P spectra *in vivo*.[3] Pulse-acquired 3D MRSI is well suited for acquisition of short-T_2 components of ^{31}P MR spectra of brain. Although time-consuming, 3D MRSI has become clinically feasible with the introduction of sparse-sampling methods.[47] High magnetic fields have allowed substantially reduced voxel sizes relative to early, low-field studies. Actual voxel sizes of about 15 cc can be expected at 4 T,[47] whereas 6–8 cc can be achieved at 7 T.[48] The feasibility of ^{31}P—{^{1}H} echo-planar spectroscopic imaging has been demonstrated for human brain.[49]

2.7. Magnetization transfer

A good summary of magnetization or saturation transfer techniques to measure biochemical reaction rates in ^{31}P MRS appears in Ref. 1. With the increasing availability of high fields, quality *in vivo* applications in humans are becoming more common. Lei et al. used single-site ^{31}P saturation transfer at 7T with surface-coil localization to measure the rate of conversion of Pi to ATP (catalyzed by the enzyme ATP synthase) *in vivo* in human visual cortex.[50] Their value of $12.1 \pm 2.8\,\mu\text{mol ATP/g/min}$ agreed with the cerebral metabolic rate of glucose consumption. Schmid et al. measured the Pi to ATP conversion in liver at 3T with ISIS localization.[51] Chen and co-workers extended the single-site technique to saturation transfer among multiple ^{31}P sites so as to include the flux between PCr and ATP [catalyzed by the enzyme creatine kinase (CK)] and determine the forward and reverse pseudo-first order rate constants for the coupled PCr–ATP–Pi exchange network.[52] Bottomley and co-workers modified their previously developed ^{31}P approach for measuring localized CK reaction rates in muscle and heart for efficient operation using a surface coil at 3T.[53,54] The ^{31}P magnetization-transfer experiment for brain has also been extended to 3T using a dual-tuned, ^{1}H/^{31}P volume coil and ISIS localization.[55] Although magnetization and saturation transfer clearly are powerful methods for probing enzymatic reaction rates *in vivo*, proper interpretation must recognize that in different tissues a variety of enzymatic pathways beyond the above may contribute to the simple, measured rates.[56,57]

2.8. Quantitation and post-processing

The several approaches to quantitation of *in vivo* MR spectra, including ^{31}P, have been described in Ref. 1. Typically, the spectrum is initially fitted using an appropriate computer programme. For ^{31}P, the jMRUI package has generally become the programme of choice.[58] This Java-based, graphical-user-interface software contains a variety of quantitation modules, in particular, the nonlinear least-squares AMARES algorithm, which enables the user to input prior knowledge of expected chemical shifts, spin-coupling constants, and line widths.[58] Resonance intensities can then be normalized to a within-spectrum standard or to a suitable external (phantom) standard as appropriate.[1]

Automated analysis of many ^{31}P spectra of low SNR, as might be obtained from a typical 3D-MRSI acquisition, is challenging. Wang and Lee have developed an iterative-reduction-of-interference-signal, Hankel-singular-value-decomposition (IRIS-HSVD) algorithm which uses so-called interference signals to iteratively optimize prior knowledge for

parameter estimation.[59] The major advantage of the technique is its ability to handle raw data suffering from baseline distortion, as is often the case for ^{31}P 3D-MRSI. The method compares favourably to the AMARES algorithm in jMRUI.

Because of the relatively long T_1s of most ^{31}P resonances (see above), *in vivo* spectra are usually acquired with relatively short TRs and reduced flip angle, resulting in variable saturation of resonances. Accurate quantitation requires determination of the saturation factor, which depends on T_1, for each resonance by comparison to a spectrum with very long TR or at a widely different flip angle. Such correction is problematic for dynamic studies where chemical exchange or T_1 changes are occurring, such as are often encountered for muscle and heart. Tyler et al. have developed a correction method for such studies based on an ongoing dual-flip-angle acquisition during the dynamic experiment.[60] The method is generally superior to single-point corrections; its major limitation is the loss of temporal resolution arising from the need to acquire two spectra for each concentration measurement.

2.9. Radiofrequency coils and hardware

A wide range of multinuclear and special-application RF coils for both human and small-animal studies are now available from a variety of small manufacturers. With the proper hardware and software tools, specialized, double-tuned ^{1}H/^{31}P coils can be built in-house.[61] With the advent of the MR phased array and parallel imaging, MRI RF-coil development has further blossomed.[62,63] Phased-array receive coils can provide substantial increases in SNR for spectroscopic applications. Although most phase-array technology has been developed for ^{1}H studies and parallel imaging, a few multinuclear applications of the technology have been developed. For example, Avdievich and Hetherington have built a double-tuned ^{1}H/^{31}P volume coil for the human head that combines a ^{1}H/^{31}P TEM transmit/receive coil with a 4-channel ^{31}P-receive phased array. Two-to-threefold improvement was obtained at the periphery of the brain for ^{31}P.[64] It is expected that phased-array coils will become standard issue for multinuclear applications in the future.

Specialty coils closely tailored to the specific application can often be quite useful.[65–67] Howe et al. have developed a needle microcoil for insertion into tissue to obtain ^{1}H MR images or ^{31}P spectra of small, adjacent regions.[67] Coil performance was demonstrated for rat thigh muscle at 4.7T. Such a coil, which could be batch-fabricated and intended for a single use, might be useful for obtaining localized spectra during interventional surgery or of the walls of large blood vessels.

3. RECENT APPLICATIONS

3.1. Brain

3.1.1. Bipolar disorder

Phosphorus-31 MRS studies have provided numerous evidences implicating mitochondrial dysfunction in the pathophysiology of bipolar disorder (BD). The most commonly reported result of such studies is that of decreased pHi. In the case of mitochondrial impairment, demands for energy in the form of ATP are not met by oxidative phosphorylation and a shift towards glycolytic energy production occurs. The resulting increase in production of reactive oxygen species leads to oxidative stress, which causes pHi to drop. The first report of decreased pHi in BD was published by Kato et al. in 1992.[68] They reported decreased pHi in the frontal lobe of euthymic BD subjects on lithium (Li^+) treatment relative to controls. Further studies reproduced these findings in the frontal lobe[69,70] and basal ganglia (BG)[71] of medicated euthymic BD subjects as well as the frontal lobe of medication-free euthymic BD subjects,[72] suggesting that decreased pHi is not a result of lithium treatment. Table 3 summarizes these results.

TABLE 3 Summary of ^{31}P MRS studies of pHi in bipolar disorder

Brain region	Results	Subjects	Medication	References
Frontal lobe	↓ pHi in euthymic BD relative to depressed BD and control	Euthymic, n=10 Depressed, n=10 Control, n=10	All BD subjects on Li^+	68
Frontal lobe	↓ pHi in euthymic BD relative to manic BD and control	Euthymic, n=17 Manic, n=17 Control, n=17	All BD subjects on Li^+	69
Frontal lobe	↓ pHi in euthymic BD relative to control	Euthymic, n=12 Control, n=59	Uncontrolled	70
Basal ganglia/ whole brain	↓ pHi in euthymic BD relative to control	Euthymic, n=12/11 Control, n=8/10	Uncontrolled	71
Frontal lobe	↓ pHi in euthymic BD relative to control	Euthymic, n=7 Control, n=60	Medication free	72

The investigation of metabolite levels has been another useful tool afforded by ^{31}P MRS for the study of mitochondrial dysfunction in BD, as illustrated by the results summarized in Table 4. A 1994 study by Kato et al. reported significantly decreased PCr peak area percentages in the frontal lobe of hypomanic, euthymic, and depressed BD patients relative to controls.[70] A later study by the same group found decreased PCr peak area percentages in the left frontal lobe of depressed BD subjects and the right frontal lobe of manic and euthymic BD subjects.[73] These decreases of PCr may be explained by an imbalance of the CK equilibrium which would strongly implicate mitochondrial dysfunction. However, these results may be confounded as subjects were not medication free in either study, and both lithium and sodium valproate are known to decrease total creatine signal in ^{1}H MRS.[79]

Perhaps the most interesting metabolic finding from ^{31}P MRS studies is the apparent dependency of PME levels on mood state. Numerous studies have found PME levels to be decreased in euthymic BD subjects relative to healthy controls regardless of medication status.[68,69,74–77] However, significant increases in PME levels have been reported in both depressed-state and manic-state BD subjects relative to euthymic BD subjects.[68,69,77,78] The PME signal is predominantly composed of the membrane precursors PE and PC, so alterations in PME levels typically indicate changes in membrane synthesis. The observed decreased levels of PME in euthymic BD subjects may be evidence of mitochondrial impairment as an environment of energy shortage may inhibit membrane synthesis, causing a reduction in PE and PC concentrations and thus a drop in PME signal. However, the increased PME levels in manic and depressed BD subjects relative to euthymic BD subjects are more difficult to explain. The apparent state dependency of PME levels may be the result of a compensatory mechanism of the brain attempting to normalize the bioenergetic environment. However, these findings could be attributed to the effect of lithium treatment, although several studies reproduced these findings in unmedicated or equally medicated groups.[74,75,78]

The substantial number of ^{31}P MRS studies of BD in the 1990s and early 2000s provided considerable evidence for the role of mitochondrial dysfunction in the disease, as summarized in Tables 3 and 4. However, recently the focus has shifted from investigating the pathophysiology of BD to examining the effects of treatment and identifying potential biomarkers. In a 2008 study, Jensen et al. investigated the effect of Triacetyluridine (TAU) treatment on 11 depressed-state BD patients.[80] Taken orally, TAU is converted to free uridine, which in turn allows less expenditure of ATP during the production of high-energy metabolic intermediates. After 2, 3, and 4 weeks of TAU treatment, Montgomery-Asberg Depression Rating Scale (MADRS) scores were significantly decreased compared to baseline. Additionally, ^{31}P MRS scans revealed significantly

TABLE 4 Summary of ^{31}P MRS studies of metabolite levels in bipolar disorder

Brain region	Results	Subjects	Medication	References
Frontal Lobe	↓ PCr BDII relative to control	BDII, *n*=15 Control, 59	Uncontrolled	70
Frontal lobe, bilateral	↓ PCr in depressed, euthymic, and manic BD relative to control	Depressed, *n*=11 Euthymic, *n*=21 Manic, *n*=12 Control, *n*=21	Uncontrolled	73
Temporal lobes, bilateral/ Frontal lobe	↓ PME in euthymic BD relative to control	Euthymic, *n*=12 Control, *n*=14/16	Medication free, 1 week	74,75
Frontal lobe	↓ PME in euthymic BD relative to control	Euthymic, *n*=10 Control, *n*=10	Uncontrolled	68
Frontal lobe	↓ PME in euthymic BD relative to control	Euthymic, *n*=17 Control, *n*=17	Uncontrolled	69
Frontal lobe	↓ PME in euthymic BD relative to control	Euthymic, *n*=40 Control, *n*=60	2 weeks Li^+ treatment	76
Various	↓ PME in euthymic BD relative to control	*Meta analysis*	Uncontrolled	77
Frontal lobe	↑ PME in depressed BD relative to euthymic	Depressed, *n*=10 Euthymic, *n*=10	Uncontrolled	68
Frontal lobe	↑ PME in manic BD relative to euthymic	Manic, *n*=17 Euthymic, *n*=17	Uncontrolled	69
Various	↑ PME in depressed BD relative to euthymic	*Meta analysis*	Uncontrolled	77

TABLE 4 (*continued*)

Brain region	Results	Subjects	Medication	References
Frontal lobe	↑ PME in manic BD relative to euthymic and control	Manic, n=9 Euthymic, n=9	Manic, euthymic BD on Li^+ treatment	78

increased brain pH among BD subjects who responded to TAU treatment, potentially indicating improved mitochondrial function. Other ongoing studies continue to investigate the relationship between biochemical information and clinical manifestations and treatment efficacy. For example, in a ^{31}P study of unmedicated adolescent BD subjects, Dudley et al. found pHi and ADP concentration in the anterior cingulate to be negatively correlated with Young Mania Rating Scale (YMRS) scores.[8]

In summary, ^{31}P MRS has provided considerable support for mitochondrial dysfunction in BD. Findings of decreased pHi are strong indicators of oxidative stress brought on by mitochondrial impairment. Observations of metabolic differences, namely PCr and PME, also strongly implicate mitochondrial dysfunction in the pathogenesis of BD, although many of these studies are confounded to some degree by the effect of pharmacological treatment. Phosphorus-31 MRS studies of BD could be of further value by examining the effect of various medications as well as determining if changes in the metabolic environment are widespread throughout the brain or localized to specific regions or brain structures that are implicated in the manifestation of symptoms.

3.1.2. Attention-deficit/hyperactivity disorder

Attention-deficit/hyperactivity disorder (ADHD) has only very recently become the target of ^{31}P MRS studies. As a result, only two reports have been published to date; however, these studies offer novel findings that are in agreement with much of what is known about the disorder from investigations using other modalities. ADHD is characterized by a wide range of cognitive deficits such as impairments in executive function, inhibitory regulation, perception, motor control, and motivational processes.[81–84] Neuronal networks formed between the prefrontal cortex (PFC) and BG are known to be associated with many of these cognitive functions, and these regions have been implicated in ADHD by numerous structural and functional neuroimaging studies.[85–89]

Stanley et al. published the first ^{31}P MRS study of ADHD which examined the PFC, BG, and superior temporal (ST) region of children

with the disorder compared to healthy controls.[90] Decreased levels of PME were found bilaterally in both the PFC and BG of children with ADHD compared to the control group. The ratio of PME to PDE was also found to be decreased in the BG of children with ADHD. A second study by Stanley et al. found bilateral decreases of PME levels in the BG as well as increases of PME in the right hemispheric inferior parietal region of unmedicated children with ADHD.[91] Interestingly, correlations of PME levels with age differed between ADHD and control groups in the PFC and inferior parietal region. A significant positive correlation was found between PME and age in the PFC for the control group compared to a non-significant negative correlation among children with ADHD. In the inferior parietal region, negative correlation between PME and age was found to be much stronger in the control group than in the ADHD group.

These findings of alterations in PME levels are consistent with previous neuroimaging studies of ADHD. The findings by Stanley et al. are consistent with the findings of structural abnormalities and functional deficits reported in other MRI studies. Collectively, these results suggest regionally specific impairment of dendritic branching and of formation of new synapses in children with ADHD. Continued ^{31}P MRS studies of ADHD may provide a sensitive means of examining biochemical alterations in the brain as they relate to the progression of this disorder throughout childhood and into adolescence. Table 5 summarizes the results of ^{31}P MRS studies of ADHD.

3.1.3. Schizophrenia

A major hypothesis concerning the pathophysiology of schizophrenia is centred on the membrane composition and functional perturbations associated with the disease.[92] Therefore, ^{31}P MRS has been utilized extensively

TABLE 5 Summary of ^{31}P MRS studies of attention-deficit/hyperactivity disorder

Brain region	Results	Subjects	Medication	References
PCF, BG	↓ PME, bilaterally in ADHD versus controls	ADHD, n=10 Control, n=15	Two ADHD subjects on psychostimulants	90
BG, inferior parietal	↓ PME, bilaterally in BG of ADHD ↑ PME, right inferior parietal of ADHD	ADHD, n=31 Control, n=36	All ADHD subjects unmedicated	91

in investigations of schizophrenia because it affords a sensitive method of detecting the membrane precursors PC and PE as well as the membrane breakdown products GPC and GPE. However, the variation in MRS methodologies, patient groups, and medication regimens across these studies has resulted in conflicting findings.

At lower magnetic field strengths, as noted above, the MRS signals from PC and PE and from GPC and GPE cannot be resolved and the pairs are collectively observed, along with other components, as the PME and phosphodiester PDE peaks, respectively. Many earlier ^{31}P MRS studies have reported decreased PME levels[93–99] and increased PDE levels[93–96] in neuroleptic-treatment-naive schizophrenics. Using the assumption that observed PME and PDE levels are reflective of membrane precursor and breakdown product concentrations, respectively, these results indicate an environment of accelerated phospholipid degradation in schizophrenia. A recent longitudinal study by Miller et al. conducted at 4.0T was able to quantify PC, PE, GPC, and GPE.[100] At baseline, the group reported increased GPC in the anterior cingulate of first-episode schizophrenics. After 30 months, GPC levels from that region had normalized and a decrease in GPE was observed in the left thalamus of the schizophrenic group relative to the baseline as well as controls. Based on these findings, Miller et al. hypothesized that the early stages of schizophrenia are accompanied by accelerated phospholipid degradation and that this membrane turnover decreases with the progression of the illness.

However, contrary to the membrane hypothesis, other early ^{31}P MRS studies have reported no change[101–104] or decreases[105] in PDE levels among neuroleptic-treatment-naive schizophrenics. There is some evidence that much of the findings of increased PDE levels may be confounded as GPC and GPE signals are contaminated by broad signals from molecules with short T_2* such as micelles and synaptic vesicles.[99,106] Smesny et al. attempted to reduce the contributions from these molecules by applying a convolution difference filter during preprocessing such that measured levels of PDE more accurately reflect GPC and GPE concentrations.[107] Interestingly, they found decreased PDE levels in the medial and lateral PFC of unmedicated and neuroleptic-naive schizophrenics compared to controls, indicating disturbed phospholipid generation rather than accelerated phospholipid degradation.

Recent postmortem studies by Komoroski et al. utilized high-resolution ^{31}P NMR spectroscopy such that GPC, GPE, PC, and PE signals could be quantified individually without contamination from the short T_2* phospholipids.[108,109] They found no significant differences in the membrane precursors PC and PE in schizophrenics compared to controls. GPC was found to be significantly increased among male schizophrenics relative to controls in extracts from the frontal, temporal, and occipital regions. While this finding is possibly attributable to schizophrenia, it is likely that

neurotoxic effects from the long-term use of antipsychotics could be responsible. Given that membrane precursor levels were unchanged and that GPC levels were altered in regions not otherwise associated with the disease, these postmortem studies do not support the hypothesis that accelerated phospholipid degradation plays a substantial role in schizophrenia.

Outside of membrane synthesis findings, recent ^{31}P MRS studies of schizophrenia have identified abnormalities in high-energy phosphate (HEP) levels in various brain regions. Jensen et al. found the frontotemporal–striatal region of first-episode schizophrenics to possess increased levels of β-ATP in white matter and decreased levels of β-ATP in grey matter, yet no corresponding alterations in PCr levels were observed.[110] Despite the mixed medication status among patients and the small sample size, these results would seem to indicate a widespread shift in brain bioenergetics at the onset of symptoms. Complementary to this finding, Jayakumar et al. found significantly decreased PCr to ATP ratios in the BG of antipsychotic-naive schizophrenics relative to age-, sex-, and handedness-matched controls.[111] A follow-up study of these cohorts after 30 months of antipsychotic treatment found PCr/ATP to be normalized and that the change in the ratio was significantly positively correlated with change in positive and negative syndrome scale (PANSS) score.[112]

From the early findings of altered phospholipid concentrations that supported the membrane hypothesis to more recent results of HEP differences that implicate alterations in brain bioenergetics, ^{31}P MRS has proven to be a useful method for the *in vivo* investigations of schizophrenia. The most problematic confounding factors present in much of the research to date are the effects of antipsychotic treatment and changes brought about by the progression of the illness itself. Controlling for these factors and including larger patient groups would enable further ^{31}P MRS investigations to better elucidate the pathophysiology of schizophrenia. Table 6 summarizes the results of ^{31}P MRS studies of schizophrenia.

3.1.4. Parkinson's disease

Much like for BD, mitochondrial dysfunction is implicated in the pathogenesis of Parkinson's disease (PD). The use of ^{31}P MRS, however, has remained somewhat limited in the study of this neurodegenerative condition. Early studies reported abnormalities of the mitochondrial respiratory chain in the substantia nigra[113–115] and skeletal muscle[116–118] of PD patients. In order to investigate these findings *in vivo*, ^{31}P MRS studies of PD measured the ratio of Pi to PCr to characterize the rate of intracellular energy metabolism. Penn et al. compared ^{31}P data from resting forearms of 28 PD patients and 28 control subjects.[119] The results suggested mitochondrial dysfunction with Pi/PCr of PD patients significantly higher than controls (p=0.004). Their results contradicted an earlier study by

TABLE 6 Summary of recent ^{31}P MRS studies of schizophrenia

Brain region	Results	Subjects (M/F, age)	Medication	References
Anterior cingulate, left thalamus	↑ GPC in ACC at baseline ↓ GPE in left thalamus at 30 months	S: 13 FE (12/1, 24.3) C: 13 (12/1, 28.8)	6 on AP at baseline 10 on AP at 30 months	100
Medial and lateral prefrontal cortex	↓ PME ↓ PDE	S: 31, 12 FE 19 ME (15/16, 37.1) C: 31 (sex, age matched)	F.E.: AP naive ME: off AP for 2 weeks	107
Frontal, temporal, occipital regions (extractions)	↑ GPC in males, all regions ↑ GPE in males, occipital region	S: 20 ME (15/5, 71) C: 20 (20/0, 71)	11 on AP at time of death 9 unknown	108,109
Fronto-temporal–striatal region	↑ β-ATP in WM ↓ β-ATP in GM	S: 12 FE (11/1, 23.2) C: 11 (9/2, 22.2)	3 on AP 6 on anxiolytics/ antidepressants	110
Basal Ganglia	↓ PCr/ATP at baseline Δ PCr/ATP correlates with Δ PANSS	S: 14 ME (8/6, 29) C: 14 (11/3, 29)	AP naive at baseline On AP at 30 months	111,112

Note: S, schizophrenic; C, control; FE, first episode; ME, multiple episode; AP, antipsychotics.

Taylor et al.,[120] which found no significant difference in Pi/PCr between resting finger flexor muscles of 7 PD subjects and 11 age-matched controls. Methodological differences, unknown pharmacological effects of medication, and the low statistical power of the Taylor et al. study could attribute to the discrepancies between the findings of these studies.

More recently, Rango et al. examined mitochondrial dysfunction in the visual cortex of PD patients at rest, during, and after visual activation.[121]

While the visual cortex does not hold any clinical relevance to PD, this technique was employed by the same group to demonstrate mitochondrial impairment in patients with known mitochondrial diseases without central nervous system involvement.[122] The results for the PD study were that HEPs did not differ between PD and control groups at rest or during visual activation. However, during recovery from activation, HEPs increased in controls by 16% yet declined in PD by 36%. The slower return to normal levels of HEPs after visual activation indicates mitochondrial impairment in PD patients. This deficiency of HEP production is potentially obscured during visual activation as the increased demand of HEPs may be met by a shift towards anaerobic glycolysis, which does not rely on mitochondrial function. Further investigation is required to determine why evidence of mitochondrial dysfunction exists in the visual cortex of PD patients, although this suggests widespread impairment of mitochondria in this disease.

In 2000, Hu et al. used ^{31}P MRS in conjunction with fluorodeoxyglucose PET (FDG-PET) imaging to investigate cortical dysfunction in non-demented PD patients.[123] Results from the ^{31}P data showed increased Pi/β-ATP levels bilaterally in the temporo-parietal cortex of PD patients relative to controls (p=0.002 and 0.014 for right and left cortex, respectively). Complementing these results, analysis of FDG-PET data revealed bilateral reductions in glucose metabolism in PD patients relative to controls. Hu posits that mitochondrial impairment in PD negatively impacts oxidative phosphorylation, causing a shift towards glycolytic energy production to replenish ATP levels. This anaerobic glycolysis draws MR invisible Pi from the mitochondria to the cytoplasm where it becomes detectable by ^{31}P MRS.

In summary, ^{31}P MRS has provided evidence to support the role of mitochondrial dysfunction in PD. Findings of altered energy metabolism in brain regions not linked to clinical symptoms of the disease indicate that widespread mitochondrial impairment is very likely associated with the underlying pathology. Due to the relatively small number of studies, it is difficult to ascertain the extent to which effects of medication, age, severity, and other parameters have had on the results of the studies. Phosphorus-31 MRS studies of PD could be of further value by examining these variables and also by investigating indirectly measurable values such as pHi, ADP, and free Mg^{2+} concentration as these may provide further characterization of the tissue bioenergetics. Table 7 summarizes the results of ^{31}P MRS studies of PD.

3.1.5. Stroke and ischemic insult

Alterations in energy metabolism are known to occur during ischemic conditions which have been associated with pathologies such as stroke, migraine, and perinatal hypoxia–ischemia (HI). Phosphorus-31 MRS

TABLE 7 Summary of ^{31}P MRS studies of Parkinson's disease

Tissue	Results	Number	Age	Medication	References
Forearm muscle	↑ Pi/PCr	PD: 28 Controls: 28	58.6 56.3	L-Dopa	119
Forearm muscle	No significant results	PD: 7 Controls: 11	56–73 Age matched	Selegiline and L-dopa	120
Visual cortex	36% ↓ HEPs in PD versus 16% ↑ in controls during recovery	PD: 20 Controls: 20	63±9 62±13	L-Dopa taken 1h before scan No dopamine agonists 1 week before scan	121
Temporo-parietal cortex	↑ Pi/β-ATP bilaterally	PD: 10 Controls: 9	62.2±7.0 56.8±7.7	L-Dopa, 4 on dopamine agonists, all medication stopped previous evening	123

studies of these conditions have been quite fruitful as information on the local energy metabolism has in some situations informed treatments and predicted outcomes.

Among all ischemic events, perinatal HI—and the resulting neonatal encephalopathy—has perhaps been the most extensively studied by ^{31}P MRS. Numerous studies have found this pathology to be characterized by a biphasic pattern of energy failure: an initial bioenergetic impairment occurs during HI and is followed by an apparent recovery of energy generation before a period of secondary energy failure (SEF).[124–127] Investigations of ^{1}H and ^{31}P MRS have identified low cerebral PCr/Pi and NTP/total exchangeable high-energy phosphate pool (EPP) as well as increased pHi and brain lactate as specific metabolic markers of SEF.[128–132] Recent studies have demonstrated the ability of ^{31}P MRS to predict the severity of SEF, indicating this modality may provide useful insight to the pathophysiology of HI and neonatal encephalopathy. Cady et al. observed SEF severity to be linearly correlated with [Pi]/[EPP], [PCr]/[Pi], and [NTP]/[EPP] measured approximately 2h after induced HI in newborn piglets.[133] Using ^{31}P MRS in conjunction with near infrared spectroscopy (NIRS), Kusaka et al. found greater neuropathologic damage when [PCr]/[Pi] was positively correlated with cerebral haemoglobin oxygen saturation after HI.[134] In a different ^{31}P and NIRS study, Winter et al. suggested mitochondrial dysfunction may occur after HI based on their findings of incomplete recovery of NTP.[135] However, as the cerebral metabolic rate of oxygen did not correlate with any metabolic changes, they concluded impaired mitochondrial function could not be the only factor.

Various types of stroke with ischemic events have been the subject of ^{31}P MRS investigations. Knowledge of how the metabolic environment changes during and after these periods of ischemia could have a substantial impact on the efficacy of treatment. Both ischemic and hemorrhagic strokes can lead to ischemic damage and infarction of brain tissue, potentially causing impairments to speech, movement, and memory. In a review of ^{31}P MRS investigations of stroke,[136] Yang et al. found consistent reports among animal studies that cortical free Mg^{2+} and energy metabolism were significantly decreased following stroke.[137–142] Further, several of these studies reported that the degree of decrease in these measures was strongly correlated with the severity of the ischemic event[137–139] and that alterations in energy metabolism lag decrease in free Mg^{2+}.[140] Unfortunately, there is a relative scarcity of ^{31}P MRS studies of stroke in human patients; however, it has been demonstrated that the modality is sensitive to alterations of free Mg^{2+} and cortical energy metabolism in limited *in vivo* studies of stroke.[142–144]

For reasons not well understood, migraine is closely associated with ischemic stroke.[145–147] A review of the literature by Sparaco et al.

highlights evidence for a hypothesis of mitochondrial dysfunction as the molecular basis for the pathology.[148] In addition to morphological and genetic studies, ^{31}P MRS has provided significant support for impaired mitochondrial oxidative metabolism in migraine. Specifically, studies have found decreased PCr, increased Pi, increased ADP, and an increased V/V_{max} of ATP biosynthesis across different forms of migraine.[149–152] A study by Schulz et al. 2009 investigated whether migrainous stroke and severe aura were connected by the same pathologic mechanism.[153] They reported that patients with persistent aura without infarction had lower PCr/Pi ratios compared to controls and patients with migrainous stroke in cortical tissue. Metabolite ratios did not differ significantly for patients with migrainous stroke relative to controls. These results indicate migrainous infarction has a different pathologic mechanism than migraine with persistent aura and that the former is not simply a severe form of the latter. Table 8 summarizes the results of ^{31}P MRS studies of migraine.

3.2. Muscle

Non-invasive ^{31}P MRS has become one of the most useful tools to investigate *in vivo* muscle metabolism since the first muscle ^{31}P MRS study reported by Hoult et al. in 1974.[154] Many muscle ^{31}P MRS studies in human or animal models have been reported and reviewed. For example, recently Kemp and his co-workers reported a quantitative review of phosphorus metabolite concentrations in human muscle.[155] Here, we

TABLE 8 Summary of ^{31}P MRS studies of migraine

Brain region	Result	Condition	References
Whole brain	↓ PCr, ↑ ADP, ↑ V/V_{max}	Migraine w/o aura	149
Whole brain	↓ PCr, ↑ Pi, ↑ ADP, ↑ V/V_{max}	Migraine with aura	150
Whole brain	↓ PCr, ↑ ADP, ↑ V/V_{max}	Migraine with prolonged aura	151
Cerebral grey matter	↓ PCr/Pi	Migraine, during interictal period	152
Cortical tissue	↓ PCr/Pi versus controls and migrainous stroke	Migraine and migrainous stroke, during interictal period	153

briefly reviewed some muscle ^{31}P MRS studies particularly associated with certain diseases published during 2005–2010.

3.2.1. Diabetes, injury, and other diseases

When glucose is oversupplied, our body stores the excess in the liver and muscle by making glycogen to maintain constant blood glucose level. One of the important functions of insulin is to decrease whole body glucose mainly by stimulating glycogen synthesis. The glycogen in muscle cells serves as an immediate reserve source of available glucose for muscle action. Insulin resistance (insulin becomes less effective in lowering blood glucose level) is an early event in the pathogenesis of type 2 diabetics. The exact processes leading to insulin resistance remain unresolved, but mitochondrial dysfunction has been found in the muscle of diabetes patients and a cause-and-effect relationship between the impairment of oxidative capacity and pathogenesis of type 2 diabetes has been proposed.[156–158] This proposed relationship was not supported by several studies published in 2008.[159–161] Trenell et al. found that resting and maximal ATP turnover are not impaired in well-controlled diabetes type 2 patients, when compared with healthy controls.[159] De Feyter et al. investigated mitochondrial function via PCr and ADP recovery in early, advanced stages of type 2 diabetes and healthy controls and found no difference between groups.[160] Lim et al. studied the ATP turnover rate in a group of young healthy subjects using ^{31}P MRS saturation transfer and found glycogen synthesis was not limited by ATP availability in this population.[162] In counterpoint to those studies, Befroy et al. demonstrated that there is a deficit in muscle TCA cycle flux in the subjects that occurred before impaired glucose tolerance and concluded that defective muscle mitochondrial function is an early factor in the pathogenesis of type 2 diabetes.[163,164] Befroy et al. believe that there are muscle-group specific differences in mitochondrial function and capacity in healthy subjects and in the modulation of energy production by disease. The disparities between these studies have been influenced by the precise characteristics of the populations studied and the muscle chosen for analysis.[165]

Peterson et al. found an increase in intramyocellular lipid content and reduction in mitochondria phosphorylation (mitochondrial rates of ATP production) in insulin-resistant subjects versus insulin-sensitive subjects.[166] They concluded that their results supported the hypothesis that insulin resistance is due to dysregulation of intramyocellular fatty acid metabolism, which may be caused by an inherited defect in mitochondrial oxidative phosphorylation.

Muscular pain and discomfort in wrist resulting from repetitive strain injury are referred to as work-related myalgia (WRM). A ^{31}P MRS study in a group of 18 women with WRM showed earlier onset of the rapid phase of pHi decline and log([Pi]/[PCr]) in the WRM group.[167] The data

suggested that WRM may have contributed to an increased reliance on nonoxidative metabolism with rising power output/ATP demands.

Peripheral artery disease (PAD) patients usually feel leg pain when walking, which is caused by insufficient blood flow to keep up with energy demand. The ^{31}P MRS data collected in a PAD patient group showed prolonged PCr recovery rate (or time constants) in the calf muscle after exhaustive exercise, suggesting the transition from anaerobic to aerobic energy metabolism is delayed due to impaired oxygen supply or mitochondria function caused by atherosclerosis.[168]

Phosphorus-31 MRS has been used widely to investigate mitochondria diseases in muscle. Trenell et al. measured an elevated ADP concentration and pHi in a group of mitochondrial myopathy (MM) patients, which is evidence of impaired oxidative ATP production in their skeletal muscle.[169] This study also showed that increased inspired oxygen concentration improves oxidative function in MM patients. In a separate study, Jeppesen et al. could not differentiate healthy subjects and MM patients using ^{31}P MRS.[170] They concluded the ^{31}P MRS should not be a routine test in the diagnosis for MM patients.

After 2 years of poliomyelitis onset, patients still suffering from the paralysis, fatigue, or weakness of muscle are referred to as having post-polio residual paralysis (PPRP). Sharma et al. studied the calf muscle of the affected leg in a group of 19 PPRP patients with ^{31}P MRS.[171] They found that PCr/Pi ratio was lower in patients than in controls. They also found significant increases in both PME/PCr and PDE/PCr ratios in patients, a point which needs further investigation.

When combined with the measurement of NIRS, *in vivo* ^{31}P MRS provides a way to investigate the effects of pulmonary diseases on muscle metabolism. Kutsuzawa et al. measured the oxygenation state and energy metabolism in muscle for patients with chronic obstructive pulmonary disease (COPD) using NIRS and ^{31}P MRS simultaneously.[172] Their result showed that the time delay of deoxygenation kinetics during on-transition of forearm exercise may suggest a slower increase in O_2 delivery in COPD patients with a low pHi, which might partly account for altered muscle energy metabolism (i.e. the reduced PCr levels in muscle). Another study using ^{31}P MRS and NIRS simultaneously in muscle was also reported by Okuma et al. in 2007. The ^{31}P MRS data (PCr and pHi) and NIRS data (intramuscular oxygenated, deoxygenated, and total haemoglobin) allowed them to monitor the steroid therapy in polymyositis patients.[173]

3.2.2. Medication and supplementation on muscle metabolism

Creatine (Cr) is one of the most widely used supplements for muscle performance enhancement. Creatine supplementation may result in an increase in muscle total Cr relative to PCr. Brault et al. investigated the ratio of PCr to total Cr (TCr=PCr+Cr) in a group of adult men using ^{31}P

and ^{1}H MRS.[174] The Cr concentration in plasma and red-blood cell did increase 10- and 2-fold, respectively, after the 3rd day of supplementation. However, the MRS data showed that Cr supplementation does not alter the PCr/TCr ratio, and hence the cytoplasmic Gibbs free energy of ATP hydrolysis in skeletal muscle at rest.

Some studies also investigated the effects of Cr supplementation on pathological muscle metabolism. In a study of steroid-naive, ambulatory boys with Duchenne muscular dystrophy (DMD), Banerjee et al. reported that oral Cr supplement significantly improved the muscle PCr/Pi ratio and preserved the muscle strength in the short term (8 weeks). But they found no evidence to show that Cr supplementation provides a benefit after long-term treatment or has any positive effect on patient lifespan. This study also revealed that the PCr stores in DMD boys are depleted at baseline.[175] In a study of 6-week Cr supplementation, Kornblum et al. reported PCr/ATP at rest did not increase and there were no changes in PCr consumption under Cr supplementation in patients with chronic progressive external ophthalmoplegia (CPEO) or Kearns–Sayre syndrome (KSS). They also found no facilitation in post-exercise oxidative PCr re-synthesis in this study. They concluded that Cr supplementation did not improve skeletal muscle oxidative phosphorylation in the CPEO patient population.[176]

Capsiate has been reported to increase body temperature and oxygenation in humans. It has been considered a potential dietetic therapy for obesity, which results from an imbalance between energy intake and expenditure thereby leading to a significant weight gain and excessive intra-abdominal adipose tissue accumulation.[177,178] Uncoupling protein-3 (UCP3) is a mitochondrial inner membrane protein that plays important roles in energy expenditure, the maintenance of body weight, and thermoregulation. In 2007, Faraut et al. reported that a single oral administration of capsiate significantly downregulated UCP3 gene expression in rat skeletal muscle while the rate of mitochondrial ATP production was increased both at rest and during a stimulation protocol.[179] In 2009, they further published the results from a rat study of 14-day administration with capsiate. They found that capsiate reduced UCP3 gene expression and increased PCr level at baseline and during stimulation period in muscle. The pHi data showed a larger alkalosis in the capsiate group during stimulation suggesting lower glycolysis and a compensatory higher aerobic contribution to ATP production. The capsiate group also showed a lower weight gain coupled to a decreased abdominal fat content. Based on the ^{31}P MRS and ^{1}H MRI data, they hypothesize that change in UCP3 expression is a causative factor of weight loss.[178]

Phosphorus-31 MRS provides a valuable research tool to investigate the correlation between metabolic turnover and pathological fatigue in muscle such as asthenia and chronic fatigue syndrome (CFS). Jones et al.

reported that exercise-induced intramuscular pH recovery is altered in CFS patients and is related to autonomic dysfunction.[180] In a separate rat study, Giannesini et al. used citrulline malate (CM) to treat asthenia and found that the supplementation prevented the basal PCr/ATP ratio reduction and normalized the pHi time-course during muscular activity.[181] They conclude that CM supplementation corrects the impaired control of oxidative function and has protective effect on basal energy metabolism. The data from either human or animal studies provide a potential approach to therapy.

3.2.3. Miscellaneous applications

Magnetization transfer is a useful tool to study phosphoryl exchange reactions, which play a major role of bioenergetics in living organs. A small reduction of the β-ATP signal upon the saturation of the γ-ATP signal has been observed but generated few further, in-depth studies.[182,183] Nabuurs et al. reported a well-designed skeletal muscle study in mouse model to address this issue.[184] The study results indicate the cross-relaxation between free cellular ATP and ATP bound to slowly rotating macromolecules, observed as NOEs, is responsible for reduction of the β-ATP signal upon the saturation of the γ-ATP signal. This relaxation process provides the information on the association state of ATP in cell.

Similar to pHi as measured by the chemical shift between PCr and other phosphates, intracellular magnesium concentration $[Mg^{2+}]_i$ can be measured by the chemical shift between the PCr and β-ATP resonances. However, the accuracy of measurement has been limited by the relatively small changes in the chemical-shift difference, which eventually gives large variation in $[Mg^{2+}]_i$. McCully et al. found the prior exercise does not affect resting $[Mg^{2+}]_i$ measurement.[185] They also reported the reproducibility of measurement of $[Mg^{2+}]_i$ and muscle oxidative capacity. They concluded that the measurements of $[Mg^{2+}]_i$ and PCr recovery kinetics to be reproducible, but in different ways. The PCr recovery kinetics has better ability than $[Mg^{2+}]_i$ to detect the differences among healthy subjects, as shown by higher intraclass correlation coefficients. As pointed out in the study of Nabuurs,[184] the association state of ATP in the cell may affect the β-ATP signal. In future studies, it will be interesting to address how this may affect the measurement of $[Mg^{2+}]_i$ in muscle.

3.3. Other organs and systems

3.3.1. Heart

Since 2006, four reviews of ^{31}P MRS of the heart have appeared,[186–189] with one as recently as 2010.[189] These works give a good introduction to many technique details specific to cardiac ^{31}P MRS, as well as topical

reviews of applications addressing specific clinical issues. Hence, here our treatment of cardiac ^{31}P MRS is brief and covers only the most recent work.

As expected, increased magnetic field substantially improves ^{31}P MRS of the heart, as demonstrated in two recent reports.[190,191] Bottomley and co-workers extended their previous quantitative cardiac ^{31}P MRS methods to 3T by incorporating adiabatic pulses of increased bandwidth to reduce SAR and a dual TR method to measure T_1.[192] They report ^{31}P T_1s at 3T for PCr and ATP in both heart muscle and skeletal muscle.

A recent ^{31}P MRS study at 1.5T found that the myocardial PCr/ATP ratio was reduced relative to controls in hypertensive patients with diastolic but not systolic dysfunction.[193] In a retrospective study, Zhang et al. showed that the PCr/β-ATP ratio after coronary artery bypass grafting was significantly higher than prior to grafting (1.71±0.29 after, 1.43±0.24 before), although both ratios were significantly lower than controls (2.13±0.21).[194]

Although ^{31}P MRS can be used to measure pH in isolated, perfused hearts, it is not suitable *in vivo* because 2,3-diphosphoglycerate in ventricular blood interferes with the myocardial Pi resonance.[195] Schroeder et al. have developed a possible alternative method for *in vivo* use based on the carbonic-anhydrase-catalyzed, pH-dependent equilibrium of CO_2 and HCO_3^-.[195] Infusion of hyperpolarized 1-^{13}C-pyruvate generates strong signals of metabolically produced $^{13}CO_2$ and $H^{13}CO_3^-$ to yield pH by the Henderson–Hasselbalch equation. Applicability of the method in humans remains to be demonstrated.

Little cardiac ^{31}P MRS has been reported in animal models. Lee et al. describe methods for measuring myocardial energetics using surface-coil ^{31}P MRS of the open-chested mouse at 4.7T.[196] In a ^{31}P MRSI study performed on a 9.4-T vertical-bore spectrometer, Flögel et al. were able to map localized energetics in several regions of the heart in a transgenic murine cardiomyopathy model.[197] They found that cardiac dysfunction in the mutant was associated with impaired energy state.

3.3.2. Liver and kidney

Two reviews, one a comprehensive account of ^{31}P MRS of liver[198] and the other a survey of liver and bile MRS,[199] cover the literature through 2003. As for MRS in other organs, ^{31}P MRS of liver has benefitted from increased magnetic field. Wylezinska et al. compared ISIS-localized ^{31}P MRS of liver at 1.5 versus 3.0T in controls and patients with chronic liver disease.[15] Spectral resolution improved somewhat at 3.0 relative to 1.5T with or without decoupling. An effective SNR increase of 21% was found for the PME resonance upon going to 3.0T. A quantitative ^{31}P 3D-MRSI protocol has been developed for liver at 3.0T.[200] The protocol provides good spectral quality at a spatial resolution of about 18cc in 34min.

Except for one case,[201] recent clinically oriented ^{31}P MRS studies of human liver have been at 1.5T. Several studies applied *in vivo* ^{31}P MRS to diffuse liver disease.[202–204] The PDE intensity was lower in cirrhosis than in controls[203] and served to distinguish the alcoholic, viral, and cholestatic etiologies of diffuse liver disease.[202] However, there was no difference between patients with non-alcoholic fatty liver disease (NAFLD) and controls.[203] Sharma et al.,[204] using the relative PME intensity as a measure of altered gluconeogenesis (this peak can contain glucose-6-P and 3-phosphoglycerate in addition to PC and PE), found that hepatic gluconeogenesis was altered in both obese and non-obese Asian Indians with NAFLD, relative to non-obese subjects without NAFLD.

An earlier cross sectional study had found that the PME/PDE ratio was a measure of disease severity in chronic hepatitis-C.[205] More recently, it was found that this ratio may also serve as a biomarker of response to treatment with antiviral therapy.[206] Whereas non-responders had similar or even elevated PME/PDE initially, that ratio declined from 0.27 ± 0.02 (standard error) to 0.16 ± 0.01 after treatment ($p<0.001$) in responders. Liver resection is a common therapy for liver metastases. Prior portal vein embolization (PVE) of the resected lobe results in hypertrophy of the remaining contralateral lobe. Phosphorus-31 MRSI has been used to monitor metabolism of the regenerating lobe after PVE.[207]

Working at 3.0T with proton decoupling, Sevastianova et al. partially resolved the resonance of nicotinamide adenine dinucleotide phosphate (NADPH) from that of α-NTP.[201] NADPH was higher in subjects with non-alcoholic steatohepatitis and cirrhosis than in healthy controls and correlated with disease severity. Solga et al. investigated the reliability of both ^{1}H and ^{31}P MRS at 1.5T in cohorts of obese diabetic subjects and healthy controls.[208] Whereas hepatic fat could be reliably measured with relative ease, hepatic ATP proved difficult with obese subjects due to reduced ^{31}P SNR.

Graft rejection is a major problem with liver transplantation, the primary treatment for end-stage liver disease. The ability of ^{31}P MRS to probe liver energy and PL metabolic status non-invasively in humans may make it a viable diagnostic alternative to repeated biopsy after transplantation. A study in adults found lower PDE/β-ATP ratios for well-functioning versus chronically rejected grafts at 101–351 days after transplantation.[209] In a paediatric study,[210] patients with good graft function displayed ^{31}P MR spectral profiles similar to those of healthy subjects, whereas patients with abnormal liver function and hepatic complications showed elevated PME/total phosphate ratios.

Hepatocyte transplantation is being explored as an alternative to whole-organ transplantation.[211] In addition, gene transfer therapy is being developed for familial hypercholesterolemia.[212] A non-invasive method to serially assess the metabolic status and proliferation of hepatocytes transferred as treatment for end-stage liver disease or genetic

disease would be valuable. A possible method is to label transplanted cells genetically for later detection. Two studies have appeared that demonstrate the use of a CK marker gene.[211,212] Because CK is not normally expressed in the liver, transplanted cells labelled with the CK gene will produce PCr, which is absent from liver ^{31}P MR spectra. *In vivo* ^{31}P MRS readily detected the PCr expressed by hepatocytes transplanted from transgenic mice and carrying the CK marker.[211,212] The ATP level was found to correlate with the degree of hepatic injury as measured by the biochemically based liver damage score (LDS) in experimental rabbits.[213]

Relatively little ^{31}P MRS has been performed recently in kidney. As a model of the role of sepsis in acute renal failure, May et al. have studied the effect of septic shock on kidney energy metabolism in a sheep model.[214] Using an implanted ^{31}P surface coil on a clinical 3-T scanner, they found that despite marked, sepsis-induced hypotension, renal ATP and pH changed little prior to circulatory arrest. *In vivo* ^{31}P MRS has been proposed as a method for following the viability of kidney grafts. Using a surface coil and ISIS volume selection at 1.5T, Fiorina et al. found that simultaneous kidney–pancreas transplantation displayed a higher β-ATP/Pi ratio than kidney-alone transplantation in diabetic patients, suggesting that restoration of β-cell function positively affects kidney graft metabolism.[215]

3.3.3. Cancer—Human studies

Perhaps surprisingly, beyond the brain, there are relatively few *in* vivo ^{31}P MRS studies of tumours directly in humans in the past 5 years. Chawla et al. report a multinuclear MRS study of squamous-cell cancer of the head and neck.[216] They conclude that the biochemical pathways determining the tCho peak in ^{1}H MRS may differ from those of the PME peak in ^{31}P MRS, rendering their information content complementary.

The Cooperative Group on MRS Applications in Cancer conducted a multi-institutional trial to demonstrate the utility and reproducibility of *in vivo* ^{31}P MRS in several human cancers, including non-Hodgkin's lymphoma (NHL), sarcomas of soft tissue and bone, breast cancer, and head and neck cancer.[217,218] Initially, they showed basic technique reproducibility *in vitro* and for quadriceps muscle in volunteers across participating institutions.[217] Spectral quality and reproducibility varied among the different cancers.[218] Later, they demonstrated that a reproducible measure of PME normalized to nucleoside–triphosphate resonances could be obtained for a select group of matched patients with NHL.[218]

3.3.4. Cancer—*In vivo* models

Phosphorus-31 MRS continues to be a powerful tool to study cancer models in rodent xenografts. Because such studies are conducted at high magnetic fields with dedicated surface or volume coils, SNR and

spectral resolution are usually considerably better than from human *in vivo* studies. Such studies are well suited for evaluating therapeutic interventions, and *in vivo* results can readily be confirmed by *ex vivo* NMR analysis. Recent studies have been reported on breast cancer,[219–222] colon cancer,[220,223–225] and large B-cell lymphoma.[226,227] Bansal and co-workers developed an in-magnet set-up for delivering controlled hyperthermia to implanted mouse tumours and used it to measure therapy response by MRS of ^{31}P, ^{1}H, and ^{23}Na.[228]

Because woodchuck hepatitis virus is similar to human hepatitis B, that rodent is a good animal model for the infection. McKenzie et al. followed the development in woodchucks of hepatocellular carcinoma arising from the infection over 6 months using ^{31}P 2D MRSI.[229] They attributed the increased ratio of PME/β-NTP to increased cellular proliferation of the liver tumour.

3.3.5. Miscellaneous applications

Disease modelling using genetically altered mice has become a major tool in biomedical studies. Renema et al. review the use of transgenic mice to study the enzymatic processes of HEP metabolism by multinuclear MRS, including ^{31}P.[230]

In a relatively unusual application, Pörtner and co-workers have used *in vivo* ^{31}P MRS to study water-breathing animals, primarily fish.[231,232] Earlier work involved restrained or resting fish, but recent techniques have been developed to study fish while swimming.[231] They have also recently examined *in vivo* muscle energy metabolism in the cuttlefish, a marine invertebrate.[232]

4. SUMMARY AND FUTURE DIRECTIONS

Phosphorus-31 MRS is continuing to advance and see wider application. The capability to perform ^{31}P MRS on both clinical and high-field animal scanners is steadily becoming more widespread. Advances such as high magnetic fields and improved RF hardware, data-acquisition approaches, spectrum analysis automation, and pulse sequences promise a technique of increased speed and spectral and spatial resolution, with a widening range of potential applications.

An area where we see increasing application is in cancer diagnosis and treatment. Currently, there is much effort on characterizing breast and prostate cancer using either single- or multi-voxel ^{1}H MRS.[233,234] This effort focuses primarily on phosphatidylcholine metabolism, as represented by the resonance assigned to ''total choline'', which arises from unresolved PC, GPC, and choline.[235] If sufficient spatial resolution and speed can be realized from high fields and instrumental advances,

^{31}P MRS should be useful in breast and prostate cancer, as it can provide resolved resonances for PC, PE, GPC, and GPE. Initial efforts appear promising.[47,236]

We also see increasing use for ^{31}P MRS in studying mental illnesses. The ability to characterize tissue energetics (via PCr and ATP) and phospholipid metabolism (via PMEs and PDEs) in sufficiently localized brain regions should help clarify the roles of mitochondrial dysfunction and phospholipid metabolism in schizophrenia and BD, as suggested by earlier efforts.[237,238]

REFERENCES

1. R. A. de Graaf, In vivo NMR Spectroscopy. Principles and Techniques. 2nd edn. Wiley, Chichester, 2007.
2. M. Rudin and A. Sauter, In vivo phosphorus-31 NMR: potential and limitations. *in*: In-Vivo Magnetic Resonance Spectroscopy III: In-Vivo MR Spectroscopy: Potential and Limitations, M. Rudin (ed.), Springer-Verlag, Berlin, 1992, 161–188.
3. F. Arias-Mendoza and T. R. Brown, *In vivo* measurement of phosphorus markers of disease. *Dis. Markers*, 2004, **19,** 49–68.
4. O. A. C. Petroff, J. W. Prichard, K. L. Behar, J. R. Alger, J. A. den Hollander and R. G. Shulman, Cerebral intracellular pH by ^{31}P nuclear magnetic resonance spectroscopy. *Neurology*, 1985, **35,** 781–788.
5. H. R. Halvorson, A. M. Q. Vande Linde, J. A. Helpern and K. M. A. Welch, Assessment of magnesium concentrations by ^{31}P NMR *in vivo*. *NMR Biomed.*, 1992, **5,** 53–58.
6. H. Qiao, X. Zhang, X.-H. Zhu, F. Du and W. Chen, In vivo ^{31}P MRS of human brain at high/ultrahigh fields: a quantitative comparison of NMR detection sensitivity and spectral resolution between 4 T and 7 T. *Magn. Reson. Imaging*, 2006, **24,** 1281–1286.
7. J. W. Pan and K. Takahashi, Interdependence of N-acetyl aspartate and high-energy phosphates in healthy human brain. *Ann. Neurol.*, 2005, **57**(1), 92–97.
8. J. Dudley, W. Weber, W.-J. Chu, M. Norris, M. DelBello, S. Strakowski and J.-H. Lee, Decreased pHi and [ADP] in anterior cingulate cortex of bipolar disorder: further evidence of mitochondrial dysfunction. *Proc. Int. Soc. Magn. Reson. Med.*, 2010, **18,** 594.
9. H. Lei, X.-H. Zhu, X.-L. Zhang, K. Ugurbil and W. Chen, In vivo ^{31}P magnetic resonance spectroscopy of human brain at 7 T: an initial experience. *Magn. Reson. Med.*, 2003, **49,** 199–205.
10. W. Bogner, M. Chmelik, A. I. Schmid, E. Moser, S. Trattnig and S. Gruber, Assessment of ^{31}P relaxation times in the human calf muscle: a comparison between 3 T and 7 T in vivo. *Magn. Reson. Med.*, 2009, **62,** 574–582.
11. P. R. Luyten, G. Bruntink, F. M. Sloff, J. W. A. H. Vermeulen, J. I. van der Heijden, J. A. den Hollander and A. Heerschap, Broadband proton decoupling in human ^{31}P NMR spectroscopy. *NMR Biomed.*, 1989, **4,** 177–183.
12. J. L. Evelhoch, C. S. Ewy, B. A. Siegfried, J. J. H. Ackerman, D. W. Rice and R. W. Briggs, ^{31}P spin–lattice relaxation times and resonance linewidths of rat tissue *in vivo*: dependence upon the static magnetic field strength. *Magn. Reson. Med.*, 1985, **2,** 410–417.
13. W. M. Brooks, J. Field, M. G. Irving and D. M. Doddrell, *In vivo* determination of ^{31}P spin relaxation times (T_1, T_2, $T_{1\rho}$) in rat leg muscle. Use of an off-axis solenoid coil. *Magn. Reson. Imaging*, 1986, **4,** 245–250.
14. R. Mathur-De Vre, C. Maerschalk and C. Delporte, Spin–lattice relaxation times and nuclear Overhauser enhancement effect for ^{31}P metabolites in model solutions at two

frequencies: implications for in vivo spectroscopy. *Magn. Reson. Imaging*, 1990, **8,** 691–698.
15. M. Wylezinska, J. F. L. Cobbold, J. Fitzpatrick, M. J. W. McPhail, M. M. E. Crossey, H. C. Thomas, J. V. Hajnal, W. Vennart, I. J. Cox and S. D. Taylor-Robinson, A comparison of single-voxel clinical *in vivo* hepatic ^{31}P MR spectra acquired at 1.5 and 3.0 Tesla in health and diseased states. *NMR Biomed.*, 2011, **24,** 231–237.
16. K. Roth, B. Hubesch, D. J. Meyerhoff, J. Nause, J. R. Gober, T. J. Lawry, M. D. Boska, G. B. Matson and M. W. Weiner, Non-invasive quantitation of phosphorous metabolites in human brain tissue by NMR spectroscopy. *J. Magn. Reson.*, 1989, **81,** 299–311.
17. B. Hubesch, D. Sappey-Marinier, K. Roth, D. J. Meyerhoff, G. B. Matson and M. W. Weiner, P-31 MR spectroscopy of normal human brain and brain tumors. *Radiology*, 1990, **174,** 401–409.
18. P. R. Luyten, J. P. Groen, J. W. Vermeulen and J. A. den Hollander, Experimental approaches to image localized human 31P NMR spectroscopy. *Magn. Reson. Med.*, 1989, **11,** 1–21.
19. C. Thomsen, K. E. Jensen and O. Henriksen, In vivo measurements of T1 relaxation times of 31P-metabolites in human skeletal muscle. *Magn. Reson. Imaging*, 1989, **7,** 231–234.
20. S. D. Buchthal, W. J. Thoma, J. S. Taylor, S. J. Nelson and T. R. Brown, In vivo T1 values of phosphorus metabolites in human liver and muscle determined at 1.5 T by chemical shift imaging. *NMR Biomed.*, 1989, **2,** 298–304.
21. T. R. Brown, R. Stoyanova, T. Greenberg, R. Srinivasan and J. Murphy-Boesch, NOE enhancements and T1 relaxation times of phosphorylated metabolites in human calf muscle at 1.5 Telsa. *Magn. Reson. Med.*, 1995, **33,** 417–421.
22. B. R. Newcomer and M. D. Boska, T1 measurements of 31P metabolites in resting and exercising human gastrocnemius/soleus muscle at 1.5 Tesla. *Magn. Reson. Med.*, 1999, **41,** 486–494.
23. R. D. Oberhaensli, G. J. Galloway, D. Hilton-Jones, P. J. Bore, P. Styles, B. Rajagopalan, D. J. Taylor and G. K. Radda, The study of human organs by phosphorus-31 topical magnetic resonance spectroscopy. *Br. J. Radiol.*, 1987, **60,** 367–373.
24. J. Bargon and R. R. Rizi, ^{13}C- & ^{31}P-hyperpolarized intermediates of glucolysis and gluconeogenesis: phosphoenolpyruvate. *Proc. Int. Soc. Magn. Reson. Med.*, 2009, **17,** 2439.
25. P. A. Bottomley and R. Ouwerkerk, The dual-angle method for fast, sensitive T-1 measurement in-vivo with low-angle adiabatic pulses. *J. Magn. Reson. B*, 1994, **104,** 159–167.
26. M. Meyerspeer, M. Krssak and E. Moser, Relaxation times of ^{31}P-metabolites in human calf muscle at 3 T. *Magn. Reson. Med.*, 2003, **49,** 620–625.
27. W. J. Chu, G. F. Mason and H. P. Hetherington, Phosphorous metabolic differences in gray and white matter: ^{31}P NMR spectroscopic imaging studies of human brain at 4.1T. *Proc. Int. Soc. Magn. Reson. Med.*, 1997, **5,** 1407.
28. C. Thomsen, K. E. Jensen and O. Henriksen, ^{31}P NMR measurements of T_2 relaxation times of metabolites in human skeletal muscle in vivo. *Magn. Reson. Imaging*, 1989, **7,** 557–559.
29. W. I. Jung, K. Straubinger, M. Bunse, F. Schick, K. Kuper, G. Dietze and O. Lutz, ^{31}P transverse relaxation times of the ATP NMR signals of human skeletal muscle in vivo. *Magn. Reson. Med.*, 1995, **28,** 305–310.
30. A. Horska and R. G. Spencer, Measurement of spin–lattice relaxation times and kinetic rate constants in rat muscle using progressive partial saturation and steady-state saturation transfer. *Magn. Reson. Med.*, 1996, **36,** 233–240.
31. C. Remy, J. P. Albrand, A. L. Benabid, M. Decorps, M. Jacrot, J. Riondel and M. F. Foray, In vivo ^{31}P nuclear magnetic resonance studies of T_1 and T_2 relaxation times in rat brain and in rat brain tumors implanted to nude mice. *Magn. Reson. Med.*, 1987, **4,** 144–152.

32. J. A. Stolk, J. I. Olsen, D. W. Alderman and M. P. Schweizer, Effects of age on apparent ^{31}P spin–lattice relaxation times of rat brain phosphates. *Magn. Reson. Med.*, 1987, **5,** 78–82.
33. K. Hida, I. L. Kwee and T. Nakada, T_1 values of phosphomonoester and phosphocreatine of brain show no significant change during development. *Magn. Reson. Med.*, 1992, **27,** 179–182.
34. G. A. Morris and R. Freeman, Enhancement of nuclear magnetic resonance signals by polarization transfer. *J. Am. Chem. Soc.*, 1979, **101,** 760–762.
35. D. P. Burum and R. R. Ernst, Net polarization transfer via a J-ordered state for signal enhancement of low-sensitivity nuclei. *J. Magn. Reson.*, 1980, **39,** 163–168.
36. D. W. J. Klomp, J. P. Wijnen, T. W. J. Scheenen and A. Heerschap, Efficient ^{1}H to ^{31}P polarization transfer on a clinical 3T MR system. *Magn. Reson. Med.*, 2008, **60,** 1298–1305.
37. T. Wokrina, M. Ulrich, W. Weber-Fahr and G. Ende, 3D RINEPT {1H}–31P CSI: a feasible approach for the study of membrane turnover in the human brain. *Magn. Reson. Med.*, 2008, **59,** 999–1004.
38. D. W. J. Klomp, A. P. M. Kentgens and A. Heerschap, Polarization transfer for sensitivity-enhanced MRS using a single radio frequency transmit channel. *NMR Biomed.*, 2008, **21,** 444–452.
39. J. P. Wijnen, T. W. J. Scheenen, D. W. J. Klomp and A. Heerschap, ^{31}P magnetic resonance spectroscopic imaging with polarization transfer of phosphomono- and diesters at 3 T in the human brain: relation with age and spatial differences. *NMR Biomed.*, 2010, **23,** 968–976.
40. R. D. Bertrand, W. B. Moniz, A. N. Garroway and G. C. Chingas, ^{13}C-^{1}H cross polarization in liquids. *J. Am. Chem. Soc.*, 1978, **100,** 5227–5229.
41. L. Mancini, G. S. Payne and M. O. Leach, Implementation and evaluation of CSI-localized J cross-polarization for detection of ^{31}P magnetic resonance spectra in vivo. *Magn. Reson. Med.*, 2005, **54,** 1065–1071.
42. B. D. Ross, P. Bhattacharya, S. Wagner, T. Tran and N. Sailasuta, Hyperpolarized MR Imaging: neurologic applications of hyperpolarized metabolism. *AJNR Am. J. Neuroradiol.*, 2010, **31,** 24–33.
43. D. Bhattacharyya, D. B. Nama and S. Reynolds, Deoxynucleotide triphosphates and oligonucleotides by ^{31}P DNP NMR. 2008. Oxford Instruments Application Note, HypAppNote/31P/0108.
44. R. J. Ordidge, A. Connelly and J. A. B. Lohman, Image-selected *in vivo* spectroscopy (ISIS). A new technique for spatially selective NMR spectroscopy. *J. Magn. Reson.*, 1986, **66,** 283–294.
45. W. Bogner, M. Chmelik, O. C. Andronesi, A. G. Sorensen, S. Trattnig and S. Gruber, In vivo ^{31}P spectroscopy by fully adiabatic extended image selected in vivo spectroscopy: a comparison between 3 T and 7 T. *Magn. Reson. Med.*, 2011, **66,** 923–930.
46. K. D. Merboldt, D. Chien, W. Hanicke, M. L. Gyngell, H. Bruhn and J. Frahm, Localized ^{31}P NMR spectroscopy of the adult human brain *in vivo* using stimulate-echo (STEAM) sequences. *J. Magn. Reson.*, 1990, **89,** 343–361.
47. J. E. Jensen, D. J. Drost, R. S. Menon and P. C. Williamson, *In vivo* brain ^{31}P-MRS: measuring the phospholipid resonances at 4 Tesla from small voxels. *NMR Biomed.*, 2002, **15,** 338–347.
48. M. Lagemaat, T. Kobus, S. Orzada, A. Bitz, A. Heerschap and T. Scheenen, Characterization of the human prostate by *in vivo* ^{31}P MR spectroscopic imaging at 7 Tesla. *Proc. Int. Soc. Magn. Reson. Med.*, 2011, **19,** 1055.
49. M. Ulrich, T. Wokrina, G. Ende, M. Lang and P. Bachert, ^{31}P-{^{1}H} Echo-planar spectroscopic imaging of the human brain in vivo. *Magn. Reson. Med.*, 2007, **57,** 784–790.
50. H. Lei, K. Ugurbil and W. Chen, Measurement of unidirectional Pi to ATP flux in human visual cortex at 7 T by using *in vivo* ^{31}P magnetic resonance spectroscopy. *Proc. Natl. Acad. Sci. USA*, 2003, **100,** 14409–14414.

51. A. I. Schmid, M. Chmelik, J. Szendroedi, M. Krssak, A. Brehm, E. Moser and M. Roden, Quantitative ATP synthesis in human liver measured by localized ^{31}P spectroscopy using the magnetization transfer experiment. *NMR Biomed.*, 2008, **21,** 437–443.
52. F. Du, X.-H. Zhu, H. Qiao, X. Zhang and W. Chen, Efficient in vivo ^{31}P magnetization transfer approach for noninvasively determining multiple kinetic parameters and metabolic fluxes of ATP metabolism in the human brain. *Magn. Reson. Med.*, 2007, **57,** 103–114.
53. M. Schär, A.-M. M. El-Sharkawy, R. G. Weiss and P. A. Bottomley, Triple repetition time saturation transfer (TRiST) ^{31}P spectroscopy for measuring human creatine kinase reaction kinetics. *Magn. Reson. Med.*, 2010, **63,** 1493–1501.
54. P. A. Bottomley, R. Ouwerkerk, R. F. Lee and R. G. Weiss, Four-angle saturation transfer (FAST) method for measuring creatine kinase reaction rates in vivo. *Magn. Reson. Med.*, 2002, **47,** 850–863.
55. E.-K. Jeong, Y.-H. Sung, S.-E. Kim, C. Zuo, X. S. Shi, E. A. Mellon and P. F. Renshaw, Measurement of creatine kinase reaction rate in human brain using magnetization transfer image-selected *in vivo* spectroscopy (MT-ISIS) and a volume ^{31}P/^{1}H radiofrequency coil in a clinical 3-T MRI system. *NMR Biomed.*, 2011, **24,** 765–770.
56. A. H. From and K. Ugurbil, Standard magnetic resonance based measurements of the Pi-ATP rate do not index the rate of oxidative phosphorylation in cardiac and skeletal muscles. *Am. J. Physiol. Cell Physiol.*, 2011, **301,** C1–C11.
57. R. S. Balaban and A. P. Koretsky, Interpretation of ^{31}P NMR saturation transfer experiments: what you can't see might confuse you. *Am. J. Physiol. Cell Physiol.*, 2011, **301,** C12–C15.
58. D. Stefan, F. Di Cesare, A. Andrasescu, E. Popa, A. Lazariev, E. Vescovo, O. Strbak, S. Williams, Z. Starcuk, M. Cabanas, D. van Ormondt and D. Graveron-Demilly, Quantitation of magnetic resonance spectroscopy signals: the jMRUI software package. *Meas Sci. Technol.*, 2009, **20,** 104035.
59. X. Wang and J.-H. Lee, IRIS-HSVD algorithm for automatic quantitation of *in vivo* ^{31}P MRS. *J. Magn. Reson.*, 2009, **196,** 23–32.
60. D. J. Tyler, O. Lopez, M. A. Cole, C. A. Carr, D. J. Stuckey, E. Lakatta, K. Clarke and R. G. Spencer, Ongoing dual-angle measurements for the correction of partial saturation in ^{31}P MR spectroscopy. *Magn. Reson. Med.*, 2010, **64,** 957–966.
61. Y. Duan, B. S. Peterson, F. Liu, T. R. Brown, T. S. Ibrahim and A. Kangarlu, Computational and experimental optimization of a double-tuned ^{1}H/^{31}P four-ring birdcage head coil for MRS at 3T. *J. Magn. Reson. Imaging*, 2009, **29,** 13–22.
62. P. B. Roemer, W. A. Edelstein, C. E. Hayes, S. P. Souza and O. M. Mueller, The NMR phased array. *Magn. Reson. Med.*, 1990, **16,** 192–225.
63. R. M. Heidemann, O. Ozsarlak, P. M. Parizel, J. Michiels, B. Kiefer, V. Jellus, M. Muller, F. Breuer, M. Blaimer, M. A. Griswold and P. M. Jakob, A brief review of parallel magnetic resonance imaging. *Eur. Radiol.*, 2003, **13,** 2323–2337.
64. N. I. Avdievich and H. P. Hetherington, 4 T Actively detuneable double-tuned ^{1}H/^{31}P head volume coil and four-channel ^{31}P phased array for human brain spectroscopy. *J. Magn. Reson.*, 2007, **186,** 341–346.
65. T. Morimoto, T. Obata, T. Ohno, Y. Suzuki, H. Ikehira, T. Suhara, S. Furukawa, H. Tsujii and T. Nakano, Phosphorous-31 magnetic resonance spectroscopy of cervical cancer using a transvaginal surface coil. *Magn. Reson. Med. Sci.*, 2005, **4,** 197–201.
66. R. L. Greenman and R. Rakow-Penner, Evaluation of the RF field uniformity of a double-tuned ^{31}P/^{1}H birdcage RF coil for spin-echo MRI/MRS of the diabetic foot. *J. Magn. Reson. Imaging*, 2005, **22,** 427–432.
67. F. A. Howe, R. R. A. Syms, M. M. Ahmad, L. M. Rodrigues, J. R. Griffiths and I. R. Young, In vivo ^{31}P magnetic resonance spectroscopy using a needle microcoil. *Magn. Reson. Med.*, 2009, **61,** 1238–1241.

68. T. Kato, S. Takahashi, T. Shioiri and T. Inubushi, Brain phosphorous metabolism in depressive disorders detected by phosphorus-31 magnetic resonance spectroscopy. *J. Affect. Disord.*, 1992, **26,** 223–230.
69. T. Kato, S. Takahashi, T. Shioiri and T. Inubushi, Alterations in brain phosphorous metabolism in bipolar disorder detected by in vivo ^{31}P and ^{7}Li magnetic resonance spectroscopy. *J. Affect. Disord.*, 1993, **27,** 53–59.
70. T. Kato, S. Takahashi, T. Shioiri, J. Murashita, H. Hamakawa and T. Inubushi, Reduction of brain phosphocreatine in bipolar II disorder detected by phosphorus-31 magnetic resonance spectroscopy. *J. Affect. Disord.*, 1994, **31,** 125–133.
71. H. Hamakawa, J. Murashita, N. Yamada, T. Inubushi, N. Kato and T. Kato, Reduced intracellular pH in the basal ganglia and whole brain measured by ^{31}P-MRS in bipolar disorder. *Psychiatry Clin. Neurosci.*, 2004, **58,** 82–88.
72. T. Kato, J. Murashita, A. Kamiya, T. Shioiri, N. Kato and T. Inubushi, Decreased brain intracellular pH measured by ^{31}P-MRS in bipolar disorder: a confirmation in drug-free patients and correlation with white matter hyperintensity. *Eur. Arch. Psychiatry Clin. Neurosci.*, 1998, **248,** 301–306.
73. T. Kato, T. Shioiri J. Murashita, *et al.*, Lateralized abnormality of high energy phosphate metabolism in the frontal lobes of patients with bipolar disorder detected by phase-encoded ^{31}P-MRS. *Psychol. Med.*, 1995, **25,** 557–566.
74. R. F. Deicken, M. W. Weiner and G. Fein, Decreased temporal lobe phosphomonoesters in bipolar disorder. *J. Affect. Disord.*, 1995, **33,** 195–199.
75. R. F. Deicken, G. Fein and M. W. Weiner, Abnormal frontal lobe phosphorous metabolism in bipolar disorder. *Am. J. Psychiatry*, 1995, **152,** 915–918.
76. T. Kato, T. Shioiri, J. Murashita, H. Hamakawa, T. Inubushi and S. Takahashi, Phosphorus-31 magnetic resonance spectroscopy and ventricular enlargement in bipolar disorder. *Psychiatry Res.*, 1994, **55,** 41–50.
77. A. Yildiz, G. S. Sachs, D. J. Dorer and P. F. Renshaw, ^{31}P nuclear magnetic resonance spectroscopy findings in bipolar illness: a metaanalysis. *Psychiatry Res.*, 2001, **106,** 181–191.
78. T. Kato, T. Shioiri, S. Takahashi and T. Inubushi, Measurement of brain phosphoinositide metabolism in bipolar patients using in vivo ^{31}P-MRS. *J. Affect. Disord.*, 1991, **22,** 185–190.
79. T. O'Donnell, S. Rotzinger, T. T. Nakashima, C. C. Hanstock, M. Ulrich and P. H. Silverstone, Chronic lithium and sodium valproate both decrease the concentration of myo-inositol and increase the concentration of inositol monophosphates in rat brain. *Brain Res.*, 2000, **880,** 84–91.
80. J. E. Jensen, M. Daniels, C. Haws, N. R. Bolo, I. K. Lyoo, S. J. Yoon, B. M. Cohen, A. L. Stoll, J. R. Rusche and P. F. Renshaw, Triacetyluridine (TAU) decreases depressive symptoms and increases brain pH in bipolar patients. *Exp. Clin. Psychopharmacol.*, 2008, **16,** 199–206.
81. R. A. Barkley, Behavioral inhibition, sustained attention, and executive functions: constructing a unifying theory of ADHD. *Psychol. Bull.*, 1997, **121,** 65–94.
82. F. X. Castellanos and R. Tannock, Neuroscience of attention-deficit/hyperactivity disorder: the search for endophenotypes. *Nat. Rev. Neurosci.*, 2002, **3,** 617–628.
83. E. J. Sonuga-Barke, Causal models of attention-deficit/hyperactivity disorder: from common simple deficits to multiple developmental pathways. *Biol. Psychiatry*, 2005, **57,** 1231–1238.
84. J. T. Nigg and B. J. Casey, An integrative theory of attention-deficit/hyperactivity disorder based on the cognitive and affective neurosciences. *Dev. Psychopathol.*, 2005, **17,** 785–806.
85. E. M. Valera, S. V. Faraone, K. E. Murray and L. J. Seidman, Meta-analysis of structural imaging findings in attention-deficit/hyperactivity disorder. *Biol. Psychiatry*, 2007, **61**(12), 1361–1369.

86. J. N. Giedd, J. Blumenthal, E. Molloy and F. X. Castellanos, Brain imaging of attention-deficit/hyperactivity disorder. *Ann. N. Y. Acad. Sci.*, 2001, **931,** 33–49.
87. B. J. Casey, J. T. Nigg and S. Durston, New potential leads in the biology and treatment of attention-deficit/hyperactivity disorder. *Curr. Opin. Neurol.*, 2007, **20,** 119–124.
88. F. X. Castellanos, P. P. Lee, W. Sharp, N. O. Jeffries, D. K. Greenstein, L. S. Clasen, J. D. Blumenthal, R. S. James, C. L. Ebens, J. M. Walter, A. Zijdenbos A. C. Evans, *et al.*, Developmental trajectories of brain volume abnormalities in children and adolescents with attention-deficit/hyperactivity disorder. *JAMA*, 2002, **288,** 1740–1748.
89. L. J. Seidman, E. M. Valera and N. Makris, Structural brain imaging of attention-deficit/hyperactivity disorder. *Biol. Psychiatry*, 2005, **57,** 1263–1272.
90. J. A. Stanley, H. Kipp, E. Greisenegger, F. P. MacMaster, K. Panchalingam, J. W. Pettegrew, M. S. Keshavan and O. G. Bukstein, Regionally specific alterations in membrane phospholipids in children with ADHD: an in vivo ^{31}P spectroscopy study. *Psychiatry Res.*, 2006, **148,** 217–221.
91. J. A. Stanley, H. Kipp, E. Greisenegger, F. P. MacMaster, K. Panchalingam, M. S. Keshavan, O. G. Bukstein and J. W. Pettegrew, Evidence of developmental alterations in cortical and subcortical regions of children with attention-deficit/hyperactivity disorder. *Arch. Gen. Psychiatry*, 2008, **65,** 1419–1428.
92. R. Reddy and M. S. Keshavan, Phosphorus magnetic resonance spectroscopy: its utility in examining the membrane hypothesis of schizophrenia. *Prostaglandins Leukot. Essent. Fatty Acids*, 2003, **69,** 401–405.
93. J. W. Pettegrew, M. S. Keshavan, K. Panchalingam, S. Strychor, D. B. Kaplan, M. G. Tretta and M. Allen, Alterations in brain high-energy phosphate and membrane phospholipid metabolism in first episode, drug-naïve schizophrenics. A pilot study of the dorsal prefrontal cortex by in vivo phosphorus 31 nuclear magnetic resonance spectroscopy. *Arch. Gen. Psychiatry*, 1991, **48,** 563–568.
94. H. Fukuzako, T. Fukuzako, T. Hashiguchi, S. Kodama, M. Takigawa and T. Fujimoto, Changes in levels of phosphorus metabolites in temporal lobes of drug-naïve schizophrenic patients. *Am. J. Psychiatry*, 1999, **156,** 1205–1208.
95. H. Fukuzako, T. Fukuzako, S. Kodama, T. Hashiguchi, M. Takigawa and T. Fujimoto, Haloperidol improves membrane phospholipid abnormalities in temporal lobes of schizophrenic patients. *Neuropsychopharmacology*, 1999, **21,** 542–549.
96. J. A. Stanley, P. C. Williamson, D. J. Drost, T. J. Carr, R. J. Rylett, A. Malla and R. T. Thompson, An in vivo study of the prefrontal cortex of schizophrenic patients at different stages of illness via phosphorus magnetic resonance spectroscopy. *Arch. Gen. Psychiatry*, 1995, **52,** 399–406.
97. T. Kato, T. Shioiri, J. Murashita, H. Hamakawa, T. Inubushi and S. Takahashi, Lateralized abnormality of high-energy phosphate and bilateral reduction of phosphomonoester measured by phosphorus-31 magnetic resonance spectroscopy of the frontal lobes in schizophrenia. *Psychiatry Res.*, 1995, **61,** 151–160.
98. M. S. Keshavan, J. W. Pettegrew, C. F. Reynolds, III, K. S. Panchalingam, D. Montrose, J. Miewald and D. J. Kupfer, Biological correlates of slow wave sleep deficits in functional psychoses: ^{31}P-magnetic resonance spectroscopy. *Psychiatry Res.*, 1995, **57,** 91–100.
99. J. J. Potwarka, D. J. Drost, P. C. Williamson, T. Carr, G. Canaran, W. J. Rylett and R. W. A. Neufeld, ^{1}H-decoupled ^{31}P chemical shift imaging study of medicated schizophrenic patients and healthy controls. *Biol. Psychiatry*, 1999, **45,** 687–693.
100. J. Miller, P. Williamson J. E. Jensen, *et al.*, Longitudinal 4.0 Tesla ^{31}P magnetic resonance spectroscopy changes in the anterior cingulate and left thalamus in first episode schizophrenia. *Psychiatry Res.*, 2009, **173,** 155–157.
101. T. Fujimoto, T. Nakano, T. Takano, Y. Hokazono, T. Asakura and T. Tsuji, Study of chronic schizophrenics using ^{31}P magnetic resonance chemical shift imaging. *Acta Psychiatr. Scand.*, 1992, **86,** 455–462.

102. G. Calabrese, R. F. Deicken, G. Fein, E. L. Merrin, F. Schoenfeld and M. W. Weiner, 31-Phosphorus magnetic resonance spectroscopy of the temporal lobes in schizophrenia. *Biol. Psychiatry*, 1992, **32,** 26–32.
103. E. O'Callaghan, O. Redmond, R. Ennis, J. Stack, A. Kinsella, J. T. Ennis, C. Larkin and J. L. Waddington, Initial investigation of the left temporoparietal region in schizophrenia by ^{31}P magnetic resonance spectroscopy. *Biol. Psychiatry*, 1991, **29,** 1149–1152.
104. T. Shioiri, T. Kato, T. Inubushi, J. Murashita and S. Takahashi, Correlations of phosphomonoesters measured by phosphorus-31 magnetic resonance spectroscopy in the frontal lobes and negative symptoms in schizophrenia. *Psychiatry Res.*, 1994, **55,** 223–235.
105. H. P. Volz, S. Riehemann I. Maurer, *et al.*, Reduced phosphodiesters and high-energy phosphates in the frontal lobe of schizophrenic patients: a (31)P chemical shift spectroscopic-imaging study. *Biol. Psychiatry*, 2000, **47,** 954–961.
106. J. A. Stanley, In vivo magnetic resonance spectroscopy and its application to neuropsychiatric disorders. *Can. J. Psychiatry*, 2002, **47,** 315–326.
107. S. Smesny, T. Rosburg I. Nenadic, *et al.*, Metabolic mapping using 2D ^{31}P-MR spectroscopy reveals frontal and thalamic metabolic abnormalities in schizophrenia. *Neuroimage*, 2007, **35,** 729–737.
108. R. A. Komoroski, J. M. Pearce and R. E. Mrak, ^{31}P NMR spectroscopy of phospholipid metabolites in postmortem schizophrenic brain. *Magn. Reson. Med.*, 2008, **59,** 469–474.
109. J. M. Pearce, R. A. Komoroski and R. E. Mrak, Phospholipid composition of postmortem schizophrenic brain by ^{31}P NMR spectroscopy. *Magn. Reson. Med.*, 2009, **61,** 28–34.
110. J. E. Jensen, J. Miller, P. C. Williamson, R. W. Neufeld, R. S. Menon, A. Malla, R. Manchanda, B. Schaefer, M. Densmore and D. J. Drost, Grey and white matter differences in brain energy metabolism in first episode schizophrenia: 31P-MRS chemical shift imaging at 4 Tesla. *Psychiatry Res.*, 2006, **146,** 127–135.
111. P. N. Jayakumar, G. Venkatasubramanian, M. S. Keshavan, J. S. Srinivas and B. N. Gangadhar, MRI volumetric and ^{31}P MRS metabolic correlates of caudate nucleus in antipsychotic-naïve schizophrenia. *Acta Psychiatr. Scand.*, 2006, **114,** 346–351.
112. P. N. Jayakumar, B. N. Gangadhar, G. Venkatasubramanian, S. Desai, L. Velayudhan, D. Subbakrishna and M. S. Keshavan, High energy phosphate abnormalities normalize after antipsychotic treatment in schizophrenia: a longitudinal ^{31}P MRS study of basal ganglia. *Psychiatry Res.*, 2010, **181,** 237–240.
113. A. H. V. Schapira, J. M. Cooper, D. Dexter, P. Jenner, J. B. Clark and C. D. Marsden, Mitochondrial complex I deficiency in Parkinson's disease. *Lancet*, 1989, **1,** 1269.
114. A. H. V. Schapira, J. M. Cooper, D. Dexter, J. B. Clark, P. Jenner and C. D. Marsden, Mitochondrial complex I deficiency in Parkinson's disease. *J. Neurochem.*, 1990, **54,** 823–827.
115. A. H. V. Schapira, V. M. Mann, J. M. Cooper, D. Dexter, S. E. Daniel, P. Jenner, J. B. Clark and C. D. Marsden, Anatomic and disease specificity of NADH CoQ1 reductase (complex I) deficiency in Parkinson's disease. *J. Neurochem.*, 1990, **55,** 2142–2145.
116. L. A. Bindoff, M. Birch-Machin, N. E. Cartlidge, W. D. Parker, Jr. and W. D. Turnbull, Mitochondrial function in Parkinson's disease. *Lancet*, 1989, **1,** 49.
117. J. M. Schoffner, R. L. Watts, J. L. Juncos, A. Torroni and D. C. Wallace, Mitochondrial oxidative phosphorylation defects in Parkinson's disease. *Ann. Neurol.*, 1991, **30,** 332–339.
118. C. Cardellach, M. J. Marti, J. Fernandez-Sola, C. Marin, J. B. Hoeck, E. Tolosa and A. Urbano-Marquez, Mitochondrial respiratory chain activity in skeletal muscle from patients with Parkinson's disease. *Neurology*, 1993, **43,** 2258–2262.
119. A. M. W. Penn, T. Roberts, J. Hodder, P. S. Allen, G. Zhu and W. R. W. Martin, Generalized mitochondrial dysfunction in Parkinson's disease detected by magnetic resonance spectroscopy of muscle. *Neurology*, 1995, **45,** 2097–2099.

120. D. J. Taylor, D. Krige, P. R. J. Barnes, G. J. Kemp, M. T. Carroll, V. M. Mann, J. M. Cooper, C. D. Marsden and A. H. V. Schapira, A ^{31}P magnetic resonance spectroscopy study of mitochondrial function in skeletal muscle of patients with Parkinson's disease. *J. Neurol. Sci.*, 1994, **125,** 77–81.
121. M. Rango, C. Bonifati and N. Bresolin, Parkinson's disease and brain mitochondrial dysfunction: a functional phosphorus magnetic resonance spectroscopy study. *J. Cereb. Blood Flow Metab.*, 2006, **26,** 283–290.
122. M. Rango, M. Bozzali, A. Prelle, G. Scarlato and N. Bresolin, Brain activation in normal subjects and in patients affected by mitochondrial disease without clinical central nervous system involvement—a phosphorus magnetic resonance spectroscopy study. *J. Cereb. Blood Flow Metab.*, 2001, **21,** 85–91.
123. M. T. M. Hu, S. D. Taylor-Robinson, K. Ray Chaudhuri, J. D. Bell, C. Labbe, V. J. Cunningham, M. J. Koepp, A. Hammers, R. G. Morris, N. Turjanski and D. J. Brooks, Cortical dysfunction in non-demented Parkinson's disease patients. *Brain*, 2000, **123,** 340–352.
124. P. L. Hope, A. M. Costello, E. B. Cady, D. T. Delpy, P. S. Tofts, A. Chu, P. A. Hamilton, E. O. Reynolds and D. R. Wilkie, Cerebral energy metabolism studied with phosphorus NMR spectroscopy in normal and birth-asphyxiated infants. *Lancet*, 1984, **2,** 366–370.
125. A. Lorek, Y. Takei, E. B. Cady, J. S. Wyatt, J. Penrice, A. D. Edwards, D. Peebles, M. Wylezinska, H. Owen-Reece V. Kirkbride, *et al.*, Delayed (secondary) cerebral energy failure after acute hypoxia-ischemia in the newborn piglet: continuous 48-hour studies by phosphorus magnetic resonance spectroscopy. *Pediatr. Res.*, 1994, **36,** 699–706.
126. R. M. Blumberg, E. B. Cady, J. S. Wigglesworth, J. E. McKenzie and A. D. Edwards, Relation between delayed impairment of cerebral energy metabolism and infarction following transient focal hypoxia-ischaemia in the developing brain. *Exp. Brain Res.*, 1997, **113,** 130–137.
127. R. C. Vannucci, J. Towfighi and S. J. Vannucci, Secondary energy failure after cerebral hypoxia-ischemia in the immature rat. *J. Cereb. Blood Flow Metab.*, 2004, **24,** 1090–1097.
128. N. J. Robertson and O. Iwata, Bench to bedside strategies for optimizing neuroprotection following perinatal hypoxia-ischaemia in high and low resource settings. *Early Hum. Dev.*, 2007, **83,** 801–811.
129. D. Azzopardi, J. S. Wyatt, E. B. Cady, D. T. Delpy, J. Baudin, A. L. Stewart, P. L. Hope, P. A. Hamilton and E. O. Reynolds, Prognosis of newborn infants with hypoxic–ischemic brain injury assessed by phosphorus magnetic resonance spectroscopy. *Pediatr. Res.*, 1989, **25,** 445–451.
130. E. Martin, R. Buchli, S. Ritter, R. Schmid, R. Largo, E. Boltshauser, S. Fanconi, G. Duc and H. Rumpel, Diagnostic and prognostic value of cerebral ^{31}P magnetic resonance spectroscopy in neonates with perinatal asphyxia. *Pediatr. Res.*, 1996, **40,** 749–758.
131. N. Robertson, I. Cox, F. Cowan, S. Counsell, D. Azzopardi and A. Edwards, Cerebral intracellular lactic alkalosis persisting months after neonatal encephalopathy measured by magnetic resonance spectroscopy. *Pediatr. Res.*, 1999, **46,** 287–296.
132. N. Robertson, F. Cowan, I. Cox and A. Edwards, Brain alkaline intracellular pH after neonatal encephalopathy. *Ann. Neurol.*, 2002, **52**(6), 732–742.
133. E. B. Cady, O. Iwata, A. Bainbridge, J. S. Wyatt and N. J. Robertson, Phosphorus magnetic resonance spectroscopy 2 h after perinatal cerebral hypoxia-ischemia prognosticates outcome in the newborn piglet. *J. Neurochem.*, 2008, **107,** 1027–1035.
134. T. Kusaka, M. Ueno, T. Kuboi, S. Nakamura, K. Koyano, S. Ijichi, S. Yasuda, K. Okubo, K. Kawada, M. Namba, T. Nishida T. Imai, *et al.*, Relationship between cerebral oxygenation and phosphorylation potential during secondary energy failure in hypoxic-ischemic newborn piglets. *Pediatr. Res.*, 2009, **65,** 317–322.

135. J. D. Winter, K. M. Tichauer, N. Gelman, R. T. Thompson, T. Y. Lee and K. St. Lawrence, Changes in cerebral oxygen consumption and high-energy phosphates during early recovery in hypoxic-ischemic piglets: a combined near-infrared and magnetic resonance spectroscopy study. *Pediatr. Res.*, 2009, **65,** 181–187.
136. H. Yang, X. Tang, L. Tan, L. Zeng and Z. Hu, Use of ^{31}P magnetic resonance spectroscopy to study the effect of cortical magnesium and energy metabolism after subarachnoid hemorrhage. *Cerebrovasc. Dis.*, 2008, **26,** 223–230.
137. R. Vink, T. K. McIntosh, P. Demediuk, M. W. Weiner and A. I. Faden, Decline in intracellular free Mg^{2+} is associated with irreversible tissue injury after brain trauma. *J. Biol. Chem.*, 1988, **263,** 757–761.
138. Y. Handa, T. Kubota, A. Tsuchida, M. Kaneko, H. Caner, H. Kobayashi and T. Kubota, Effect of systemic hypotension on cerebral energy metabolism during chronic cerebral vasospasm in primates. *J. Neurosurg.*, 1993, **78,** 112–119.
139. Z. Domingo, J. K. Bradley, K. Blamire, A. M. Brindle, P. Styles and B. Rajagopalan, Diffusion weighted imaging and magnetic resonance spectroscopy in a low flow ischaemia model due to endothelin induced vasospasm. *NMR Biomed.*, 2000, **13,** 154–162.
140. L. Nowak, P. Bregestovski, P. Ascher, A. Herbet and A. Prochiantz, Magnesium gates glutamate-activated channels in mouse central neurones. *Nature*, 1984, **307,** 462–465.
141. B. M. Altura, A. Gebrewold, B. T. Altura and R. K. Gupta, Role of brain $[Mg^{2+}]_i$ in alcohol-induced hemorrhagic stroke in a rat model: a ^{31}P-NMR in vivo study. *Alcohol*, 1995, **12,** 131–136.
142. B. M. Altura and B. T. Altura, Role of magnesium and calcium in alcohol-induced hypertension and strokes as probed by in-vivo television microscopy, digital image microscopy, optical spectroscopy, ^{31}P-NMR spectroscopy and a unique magnesium ion-selective electrode. *Alcohol. Clin. Exp. Res.*, 1994, **18,** 1057–1068.
143. N. S. R. Brooke, R. Ouwerkerk, C. B. T. Adams, G. K. Radda, J. G. G. Ledingham and B. R. Ajagopalan, Phosphorus-31 magnetic resonance spectra reveal prolonged intracellular acidosis in the brain following subarachnoid hemorrhage. *Proc. Natl. Acad. Sci. USA*, 1994, **91,** 1903–1907.
144. K. Yoshida, M. Furuse, A. Izawa, N. Iizima, H. Kuchiwaki and S. Inao, Dynamics of cerebral blood flow and metabolism in patients with cranioplasty as evaluated by ^{133}Xe CT and ^{31}P magnetic resonance spectroscopy. *J. Neurol. Neurosurg. Psychiatry*, 1996, **61,** 166–171.
145. M. Etminan, B. Takkouche, F. C. Isorna and A. Samii, Risk of ischemic stroke in people with migraine: systematic review and meta-analysis of observational studies. *BMJ*, 2005, **330,** 63–66.
146. J. Olesen, L. Friberg, T. S. Olsen, A. R. Andersen, N. A. Lassen, P. E. Hansen and A. Karle, Ischemia-induced (symptomatic) migraine attacks may be more frequent than migraine-induced ischemic insults. *Brain*, 1993, **116,** 187–202.
147. M. G. Bousser and K. M. Welch, Relationship between migraine and stroke. *Lancet Neurol.*, 2005, **4,** 533–542.
148. M. Sparaco, M. Feleppa, R. B. Lipton, A. M. Rapoport and M. E. Bigal, Mitochondrial dysfunction and migraine: evidence and hypotheses. *Cephalalgia*, 2005, **26,** 361–372.
149. P. Montagna, P. Cortelli, L. Monari, G. Pierangeli, P. Parchi, R. Lodi, S. Iotti, C. Frassineti, P. Zaniol E. Lugaresi, *et al.*, ^{31}P-Magnetic resonance spectroscopy in migraine without aura. *Neurology*, 1994, **44,** 666–669.
150. B. Barbiroli, P. Montagna, P. Cortelli, R. Funicello, S. Iotti, L. Monari, G. Pierangeli, P. Zaniol and E. Lugaresi, Abnormal brain and muscle energy metabolism shown by ^{31}P magnetic resonance spectroscopy in patients affected by migraine with aura. *Neurology*, 1992, **42,** 1209–1214.

151. T. Sacquegna, R. Lodi, P. De Carolis, P. Tinuper, P. Cortelli, P. Zaniol, R. Funicello, P. Montagna and B. Barbiroli, Brain energy metabolism studied by ^{31}P-MR spectroscopy in a case of migraine with prolonged aura. *Acta Neurol. Scand.*, 1992, **86,** 376–380.
152. U. G. Schulz, A. M. Blamire, R. G. Corkill, P. Davies, P. Styles and P. M. Rothwell, Association between cortical metabolite levels and clinical manifestations of migrainous aura: an MR-spectroscopy study. *Brain*, 2007, **130,** 3102–3110.
153. U. G. Schulz, A. M. Blamire, P. Davies, P. Styles and P. M. Rothwell, Normal cortical energy metabolism in migrainous stroke: a 31P-MR spectroscopy study. *Stroke*, 2009, **40,** 3740–3744.
154. D. I. Hoult, S. J. W. Busby, D. G. Gadian, G. K. Radda, R. E. Richards and R. J. Seeley, Observation of tissue metabolites using ^{31}P nuclear magnetic resonance. *Nature*, 1974, **252,** 285–287.
155. G. J. Kemp, M. Meyerspeer and E. Moser, Absolute quantification of phosphorus metabolite concentrations in human muscle in vivo by ^{31}P MRS: a quantitative review. *NMR Biomed.*, 2007, **20,** 555–565.
156. D. E. Kelley, J. He, E. V. Menshikova and V. B. Ritov, Dysfunction of mitochondria in human skeletal muscle in type 2 diabetes. *Diabetes*, 2002, **51,** 2944–2950.
157. K. Morino, K. F. Petersen, S. Dufour, D. Befroy, J. Frattini, N. Shatzkes, S. Neschen, M. F. White, S. Bilz, S. Sono, M. Pypaert and G. I. Shulman, Reduced mitochondrial density and increased IRS-1 serine phosphorylation in muscle of insulin-resistant offspring of type 2 diabetic parents. *J. Clin. Invest.*, 2005, **115,** 3587–3593.
158. E. Phielix and M. Mensink, Type 2 diabetes mellitus and skeletal muscle metabolic function. *Physiol. Behav.*, 2008, **94,** 252–258.
159. M. I. Trenell, K. G. Hollingsworth, E. L. Lim and R. Taylor, Increased daily walking improves lipid oxidation without changes in mitochondrial function in type 2 diabetes. *Diabetes Care*, 2008, **31,** 1644–1649.
160. H. M. De Feyter, N. M. van den Broek, S. F. Praet, K. Nicolay, L. J. van Loon and J. J. Prompers, Early or advanced stage type 2 diabetes is not accompanied by in vivo skeletal muscle mitochondrial dysfunction. *Eur. J. Endocrinol.*, 2008, **158,** 643–653.
161. N. Turner and L. K. Heilbronn, Is mitochondrial dysfunction a cause of insulin resistance? *Trends Endocrinol. Metab.*, 2008, **19,** 324–330.
162. E. L. Lim, K. G. Hollingsworth, P. E. Thelwall and R. Taylor, Measuring the acute effect of insulin infusion on ATP turnover rate in human skeletal muscle using phosphorus-31 magnetic resonance saturation transfer spectroscopy. *NMR Biomed.*, 2010, **23,** 952–957.
163. D. E. Befroy, K. F. Petersen, S. Dufour, G. F. Mason, R. A. de Graaf, D. L. Rothman and G. I. Shulman, Impaired mitochondrial substrate oxidation in muscle of insulin-resistant offspring of type 2 diabetic patients. *Diabetes*, 2007, **56,** 1376–1381.
164. D. E. Befroy, K. F. Petersen, G. I. Shulman and D. L. Rothman, Localized ^{31}P saturation transfer reveals differences in gastrocnemius and soleus rates of ATP synthesis in-vivo. *Proc. Int. Soc. Magn. Reson. Med.*, 2008, **16,** 2565.
165. D. E. Befroy, K. Petersen, D. L. Rothman and G. I. Shulman, Assessment of in vivo mitochondrial metabolism by magnetic resonance spectroscopy. *Methods Enzymol.*, 2009, **457,** 373–393.
166. K. F. Petersen, S. Dufour, D. Befroy, R. Garcia and G. I. Shulman, Impaired mitochondrial activity in the insulin-resistant offspring of patients with type 2 diabetes. *N. Engl. J. Med.*, 2004, **350,** 664–671.
167. G. H. Raymer, H. J. Green, D. A. Ranney, G. D. Marsh and R. T. Thompson, Muscle metabolism and acid–base status during exercise in forearm work-related myalgia measured with 31P-MRS. *J. Appl. Physiol.*, 2009, **106,** 1198–1206.
168. R. Esterhammer, M. Schocke, O. Gorny, L. Posch, H. Messner, W. Haschke, G. Fraedrich and A. Greiner, Phosphocreatine kinetics in the calf muscle of patients with bilateral symptomatic peripheral arterial disease during exhaustive incremental exercise. *Mol. Imaging Biol.*, 2008, **10,** 30–39.

169. M. I. Trenell, C. M. Sue, C. H. Thompson and G. J. Kemp, Supplemental oxygen and muscle metabolism in mitochondrial myopathy patients. *Eur. J. Appl. Physiol.*, 2007, **99,** 541–547.
170. T. D. Jeppesen, B. Quistorff, F. Wibrand and J. Vissing, ^{31}P-MRS of skeletal muscle is not a sensitive diagnostic test for mitochondrial myopathy. *J. Neurol.*, 2007, **254,** 29–37.
171. U. Sharma, V. Kumar, S. Wadhwa and N. R. Jagannathan, In vivo ^{31}P MRS study of skeletal muscle metabolism in patients with postpolio residual paralysis. *Magn. Reson. Imaging*, 2007, **25,** 244–249.
172. T. Kutsuzawa, S. Shioya, D. Kurita and M. Haida, Deoxygenated hemoglobin/myoglobin kinetics of forearm muscle from rest to exercise in patients with chronic obstructive pulmonary disease. *Tohoku J. Exp. Med.*, 2009, **217,** 9–15.
173. H. Okuma, D. Kurita, T. Ohnuki, M. Haida and Y. Shinohara, Muscle metabolism in patients with polymyositis simultaneously evaluated by using ^{31}P-magnetic resonance spectroscopy and near-infrared spectroscopy. *Int. J. Clin. Pract.*, 2007, **61,** 684–689.
174. J. J. Brault, T. F. Towse, J. M. Slade and R. A. Meyer, Parallel increases in phosphocreatine and total creatine in human vastus lateralis muscle during creatine supplementation. *Int. J. Sport Nutr. Exerc. Metab.*, 2007, **17,** 624–634.
175. B. Banerjee, U. Sharma, K. Balasubramanian, M. Kalaivani, V. Kalra and N. R. Jagannathan, Effect of creatine monohydrate in improving cellular energetics and muscle strength in ambulatory Duchenne muscular dystrophy patients: a randomized, placebo-controlled 31P MRS study. *Magn. Reson. Imaging*, 2010, **28,** 698–707.
176. C. Kornblum, R. Schröder, K. Müller, M. Vorgerd, J. Eggers, M. Bogdanow, A. Papassotiropoulos, K. Fabian, T. Klockgether and J. Zange, Creatine has no beneficial effect on skeletal muscle energy metabolism in patients with single mitochondrial DNA deletions: a placebo-controlled, double-blind 31P-MRS crossover study. *Eur. J. Neurol.*, 2005, **12,** 300–309.
177. Y. Masuda, S. Haramizu, K. Oki, K. Ohnuki, T. Watanabe, S. Yazawa, T. Kawada, S. Hashzume and T. Fushiki, Upregulation of uncoupling proteins by oral administration of capsiate, a nonpungent capsaicin analog. *J. Appl. Physiol.*, 2003, **95,** 2408–2415.
178. B. Faraut, B. Giannesini, V. Matarazzo, Y. Le Fur, G. Rougon, P. J. Cozzone and D. Behdahan, Capsiate administration results in an uncoupling protein-3 downregulation, an enhanced muscle oxidative capacity and a decreased abdominal fat content in vivo. *Int. J. Obes. (Lond)*, 2009, **339,** 1348–1355.
179. B. Faraut, B. Giannesini, V. Matarazzo, T. Marqueste, C. Dalamasso G. Rougon, *et al.*, Downregulation of uncoupling protein-3 is linked to changes in muscle mitochondrial energy metabolism in vivo as a result of capsiate administration. *Am. J. Physiol. Endocrinol. Metab.*, 2007, **292,** E1474–E1482.
180. D. E. Jones, K. G. Hollingsworth, R. Taylor, A. M. Blamire and J. L. Newton, Abnormalities in pH handling by peripheral muscle and potential regulation by the autonomic nervous system in chronic fatigue syndrome. *J. Intern. Med.*, 2010, **267,** 394–401.
181. B. Giannesini, M. Izquierdo, Y. Le Fur, P. J. Cozzone, M. Verleye, M. E. Le Guern, J. M. Gillardin and D. Bendahan, Beneficial effects of citrulline malate on skeletal muscle function in endotoxemic rat. *Eur. J. Pharmacol.*, 2009, **602,** 143–147.
182. E. Le Rummeur, N. Le Tallec, F. Kernec and J. D. de Certaines, Kinetics of ATP to ADP β-phosphoryl conversion in contracting skeletal muscle by in vivo ^{31}P NMR magnetization transfer. *NMR Biomed.*, 1997, **10,** 67–72.
183. X. Ravalec, N. Le Tallec, F. Carré, J. D. de Certaines and E. Le Rumeur, Kinetics of PCr to ATP and beta-ATP to beta-ATP phosphoryl conversion are modified in working rat skeletal muscle after training. *MAGMA*, 1999, **9,** 52–58.
184. C. Nabuurs, B. Huijbregts, B. Wieringa, C. W. Hibers and A. Heerschap, ^{31}P saturation transfer spectroscopy predicts differential intracellular macromolecular association of ATP and ADP in skeletal muscle. *J. Biol. Chem.*, 2010, **285,** 39588–39596.

185. K. K. McCully, T. N. Turner, J. Langley and Q. Zhao, The reproducibility of measurements of intramuscular magnesium concentrations and muscle oxidative capacity using ^{31}P MRS. *Dyn. Med.*, 2009, **8,** 5–12.
186. F. Sardanelli and M. Quarenghi, MR spectroscopy of the heart. *Radiol. Med.*, 2006, **111,** 1025–1034.
187. L. E. Hudsmith and S. Neubauer, Detection of myocardial disorders by magnetic resonance spectroscopy. *Nat. Clin. Pract. Cardiovasc. Med.*, 2008, **5,** S49–S56.
188. L. E. Hudsmith and S. Neubauer, Magnetic resonance spectroscopy in myocardial disease. *J. Am. Coll. Cardiol. Imaging*, 2009, **2,** 87–96.
189. R. Beadle and M. Frenneaux, Magnetic resonance spectroscopy in myocardial disease. *Expert Rev. Cardiovasc. Ther.*, 2010, **8,** 269–277.
190. D. J. Tyler, L. E. Hudsmith, K. Clarke, S. Neubauer and M. D. Robson, A comparison of cardiac ^{31}P MRS at 1.5 and 3 T. *NMR Biomed.*, 2008, **21,** 793–798.
191. G. N. Shivu, K. Abozguia, T. T. Phan, I. Ahmed, A. Henning and M. Frenneaux, ^{31}P magnetic resonance spectroscopy to measure *in vivo* cardiac energetics in normal myocardium and hypertrophic cardiomyopathy: experiences at 3 T. *Eur. J. Radiol.*, 2010, **73,** 255–259.
192. A.-M. El-Sharkawy, M. Schär, R. Ouwerkerk, R. G. Weiss and P. A. Bottomley, Quantitative cardiac ^{31}P spectroscopy at 3 Tesla using adiabatic pulses. *Magn. Reson. Med.*, 2009, **61,** 785–795.
193. T. Burkhard, C. Herzog, S. Linzbach, I. Spyridopoulos, F. Huebner and T. J. Vogl, Cardiac ^{31}P-MRS compared to echocardiographic findings in patients with hypertensive heart disease without overt systolic dysfunction—preliminary results. *Eur. J. Radiol.*, 2009, **71,** 69–74.
194. Z. Zhang, J. Li, S. Wu, Y. Liu, Z. Fan, X. Zhou, H. Zhao, D. Li and Y. Huan, Cine-MRI and ^{31}P-MRS for evaluation of myocardial energy metabolism and function following coronary artery bypass graft. *Magn. Reson. Imaging*, 2010, **28,** 936–942.
195. M. A. Schroeder, P. Swietach, H. J. Atherton, F. A. Gallagher, P. Lee, G. K. Radda, K. Clarke and D. J. Tyler, Measuring intracellular pH in the heart using hyperpolarized carbon dioxide and bicarbonate: a ^{13}C and ^{31}P magnetic resonance spectroscopy study. *Cardiovasc. Res.*, 2010, **86,** 82–91.
196. J. Lee, Q. Hu, Y. Nakamura, X. Wang, X. Zhang, X. Zhu, W. Chen, Q. Yang and J. Zhang, Open-chest ^{31}P magnetic resonance spectroscopy of mouse heart at 4.7 Tesla. *J. Magn. Reson. Imaging*, 2006, **24,** 1269–1276.
197. U. Flögel, C. Jacoby, A. Gödecke and J. Schrader, In vivo 2D mapping of impaired murine cardiac energetics in NO-induced heart failure. *Magn. Reson. Med.*, 2007, **57,** 50–58.
198. S. F. Solga, A. Horska, J. M. Clark and A. M. Diehl, Hepatic ^{31}P magnetic resonance spectroscopy: a hepatologist's user guide. *Liver Int.*, 2005, **25,** 490–500.
199. S. A. Khan, I. J. Cox, G. Hamilton, H. C. Thomas and S. D. Taylor-Robinson, *In vivo* and *in vitro* nuclear magnetic resonance spectroscopy as a tool for investigating hepatobiliary disease: a review of ^{1}H and ^{31}P MRS applications. *Liver Int.*, 2005, **25,** 273–281.
200. M. Chmelik, A. I. Schmid, S. Gruber, J. Szendroedi, M. Krssak, S. Trattnig, E. Moser and M. Roden, Three-dimensional high-resolution magnetic resonance spectroscopic imaging for absolute quantification of ^{31}P metabolites in human liver. *Magn. Reson. Med.*, 2008, **60,** 796–802.
201. K. Sevastianova, A. Hakkarainen, A. Kotronen, A. Corner, P. Arkkila, J. Arola, J. Westerbacka, R. Bergholm, J. Lundbom, N. Lundbom and H. Yki-Järvinen, Nonalcoholic fatty liver disease: detection of elevated nicotinamide adenine dinucleotide phosphate with in vivo 3.0-T ^{31}P MR spectroscopy with proton decoupling. *Radiology*, 2010, **256,** 466–473.

202. M. Dezortova, P. Taimr, A. Skoch, J. Spicak and M. Hajek, Etiology and functional status of liver cirrhosis by ^{31}P MR spectroscopy. *World J. Gastroenterol.*, 2005, **11,** 6926–6931.
203. B. Noren, O. Dahlqvist, P. Lundberg, S. Almer, S. Kechagias, M. Ekstedt, L. Franzen, S. Wirell and Ö. Smedby, Separation of advanced from mild fibrosis in diffuse liver disease using ^{31}P magnetic resonance spectroscopy. *Eur. J. Radiol.*, 2008, **66,** 313–320.
204. R. Sharma, S. Sinha, K. A. Danishad, N. K. Vikram, A. Gupta, V. Ahuja, N. R. Jagannathan, R. M. Pandey and A. Misra, Investigation of hepatic gluconeogenesis in non-diabetic Asian Indians with non-alcoholic fatty liver disease using *in vivo* (^{31}P) phosphorus magnetic resonance spectroscopy. *Atherosclerosis*, 2009, **203,** 291–297.
205. A. K. P. Lim, N. Patel, G. Hamilton, R. D. Goldin, J. V. Hajnal and S. D. Taylor-Robinson, Findings at ^{31}P MR spectroscopy correlate with histology in chronic hepatitis C. *Hepatology*, 2003, **37,** 788–794.
206. A. K. P. Lim, N. Patel, G. Hamilton, K. Mylvahan, Y.-T. Kuo, R. D. Goldin and S. D. Taylor-Robinson, ^{31}P MR spectroscopy in assessment of response to antiviral therapy for hepatitis-C virus-related liver disease. *AJR Am. J. Roentgenol.*, 2007, **189,** 819–823.
207. J. Qi, A. Shukla-Dave, Y. Fong, M. Gönen, L. H. Schwartz, W. M. Jarnigan, J. A. Koutcher and K. L. Zakian, ^{31}P MR spectroscopic imaging detects regenerative changes in human liver stimulated by portal vein embolization. *J. Magn. Reson. Imaging*, 2011, **34,** 336–344.
208. S. F. Solga, A. Horska, S. Hemker, S. Crawford, C. Diggs, A. M. Diehl, F. L. Brancati and J. M. Clark, Hepatic fat and adenosine triphosphate measurement in overweight and obese adults using ^{1}H and ^{31}P magnetic resonance spectroscopy. *Liver Int.*, 2008, **28,** 675–681.
209. T. Jiang, S. Liu, X. S. Xiao, X. F. Tao, G. H. Liu and J. L. Wang, Diagnosis of rejection after liver transplantation: use of phosphorus-31 magnetic resonance spectroscopy (^{31}P-MRS). *Abdom. Imaging*, doi: 10.1007/s00261-008-9451-1.
210. W. C. Chu, W. W. Lam, K. H. Lee, D. K. Yeung, J. Sihoe and C.-K. Yeung, Phosphorus-31 MR spectroscopy in pediatric liver transplant recipients: a noninvasive assessment of graft status with correlation with liver function tests and liver biopsy. *AJR Am. J. Roentgenol.*, 2005, **184,** 1624–1629.
211. C. S. Landis, K. Yamanouchi, H. Zhou, S. Mohan, N. Roy-Chowdhury, D. A. Shafritz, A. Koretsky, J. Roy-Chowdhury, H. P. Hetherington and C. Guha, Noninvasive evaluation of liver repopulation by transplanted hepatocytes using ^{31}P MRS imaging in mice. *Hepatology*, 2006, **44,** 1250–1258.
212. Z. Li, H. Qiao, C. Lebherz, S. R. Choi, X. Zhou, G. Gao, H. F. Kung, D. J. Rader, J. M. Wilson, J. D. Glickson and R. Zhou, Creatine kinase, a magnetic resonance-detectable marker gene for quantification of liver-directed gene transfer. *Hum. Gene Ther.*, 2005, **16,** 1429–1438.
213. R.-S. Yu, L. Hao, F. Dong, J.-S. Mao, J.-Z. Sun, Y. Chen, M. Lin, Z.-K. Wang and W.-H. Ding, Biochemical metabolic changes assessed by ^{31}P magnetic resonance spectroscopy after radiation-induced hepatic injury in rabbits. *World J. Gastroenterol.*, 2009, **15,** 2723–2730.
214. C. May, L. Wan, J. Williams, M. R. Wellard, G. Pell, C. Langenverg, G. Jackson and R. Bellomo, A technique for the simultaneous measurement of renal ATP, blood flow and pH in a large animal model of septic shock. *Crit. Care Resusc.*, 2007, **9,** 30–33.
215. P. Fiorina, G. Perseghin, F. de Cobelli, C. Gremizzi, A. Petrelli, L. Monti, P. Maffi, L. Luzi, A. Secchi and A. del Maschio, Altered kidney graft high-energy phosphate metabolism in kidney-transplanted end-stage renal disease Type 1 diabetic patients. *Diabetes Care*, 2007, **30,** 597–603.
216. S. Chawla, S. Kim, L. A. Loevner, H. Quon, S. Wang, F. Mutale, G. Weinstein, E. J. Delikatny and H. Poptani, Proton and phosphorous MR spectroscopy in squamous cell carcinomas of the head and neck. *Acad. Radiol.*, 2009, **16,** 1366–1372.

217. F. Arias-Mendoza, K. Zakian, A. Schwartz, F. A. Howe, J. A. Koutcher, M. O. Leach, J. R. Griffiths, A. Heerschap, J. D. Glickson, S. J. Nelson, J. L. Evelhoch H. C. Charles, *et al*., Methodological standardization for a multi-institutional *in vivo* trial of localized (31)P MR spectroscopy in human cancer research. *NMR Biomed.*, 2004, **17,** 382–391.
218. F. Arias-Mendoza, G. S. Payne, K. Zakian, A. J. Schwartz, M. Stubbs, R. Stoyanova, D. Ballon, F. A. Howe, J. A. Koutcher, M. O. Leach, J. R. Griffiths A. Heerschap, *et al*., *In vivo* ^{31}P MR spectral patterns and reproducibility in cancer patients studied in a multi-institutional trial. *NMR Biomed.*, 2006, **19,** 504–512.
219. D. L. Morse, N. Raghunand, P. Sadarangani, S. Murthi, C. Job, S. Day, C. Howison and R. J. Gillies, Response of choline metabolites to docetaxel therapy is quantified in vivo by localized ^{31}P MRS of human breast cancer xenografts and in vitro by high-resolution ^{31}P NMR spectroscopy of cell extracts. *Magn. Reson. Med.*, 2007, **58,** 270–280.
220. N. M. S. Al-Saffar, H. Troy, A. Ramirez de Molina, L. E. Jackson, B. Madhu, J. R. Griffiths, M. O. Leach, P. Workman, J. C. Lacal, I. R. Judson and Y.-L. Chung, Noninvasive magnetic resonance spectroscopic pharmacodynamic markers of the choline kinase inhibitor MN58b in human carcinoma models. *Cancer Res.*, 2006, **66,** 427–434.
221. M. Muruganandham, A. A. Alfieri, C. Matei, Y. Chen, G. Sukenik, I. Schemainda, M. Hasmann, L. B. Saltz and J. A. Koutcher, Metabolic signatures associated with a NAD synthesis inhibitor-induced tumor apoptosis identified by ^{1}H-decoupled-^{31}P magnetic resonance spectroscopy. *Clin. Cancer Res.*, 2005, **11,** 3503–3513.
222. D. L. Morse, D. Carroll, S. Day, H. Gray, P. Sadarangani, S. Murthi, C. Job, B. Baggett, N. Raghunand and R. J. Gillies, Characterization of breast cancers and therapy response by MRS and quantitative gene expression profiling in the choline pathway. *NMR Biomed.*, 2009, **22,** 114–127.
223. H. W. M. van Laarhoven, G. Gambarota, J. Lok, M. Lammens, Y. L. M. Kamm, T. Wagener, C. J. A. Punt, A. J. van der Kogel and A. Heerschap, Carbogen breathing differentially enhances blood plasma volume and 5-fluorouracil uptake in two murine colon tumor models with a distinct vascular structure. *Neoplasia*, 2006, **8,** 477–487.
224. G. R. Silberhumer, K. Zakian, S. Malhotra, P. Brader, M. Göne, J. Koutcher and Y. Fong, Relationship between ^{31}P metabolites and oncolytic viral therapy sensitivity in human colorectal cancer xenografts. *Br. J. Surg.*, 2009, **96,** 809–816.
225. T. P. F. Gade, I. M. Buchanan, M. W. Motley, Y. Mazaheri, W. M. Spees and J. A. Koutcher, Imaging intratumoral convection: pressure-dependent enhancement in chemotherapeutic delivery to solid tumors. *Clin. Cancer Res.*, 2009, **15,** 247–255.
226. M. Q. Huang, D. S. Nelson, S. Pickup, H. Qiao, E. J. Delikatny, H. Poptani and J. D. Glickson, In vivo monitoring response to chemotherapy of human diffuse large B-cell lymphoma xenografts in SCID mice by ^{1}H and ^{31}P MRS. *Acad. Radiol.*, 2007, **14,** 1531–1539.
227. S.-C. Lee, M. Q. Huang, D. S. Nelson, S. Pickup, S. Wehrli, O. Adegbola, H. Poptani, E. J. Delikatny and J. D. Glickson, *In vivo* MRS markers of response to CHOP chemotherapy in the WSU-DLCL2 human diffuse large B-cell lymphoma xenograft. *NMR Biomed.*, 2008, **21,** 723–733.
228. J. R. James, Y. Gao, V. C. Soon, S. M. Topper, A. Babsky and N. Bansal, Controlled radiofrequency hyperthermia using an MR scanner and simultaneous monitoring of temperature and therapy response by ^{1}H, ^{23}Na and ^{31}P magnetic resonance spectroscopy in subcutaneously implanted 9L-gliosarcoma. *Int. J. Hyperthermia*, 2010, **26,** 79–90.
229. E. J. McKenzie, M. Jackson, J. Sun, V. Volotovskyy and M. L. H. Gruwel, Monitoring the development of hepatocellular carcinoma in woodchucks using ^{31}P-MRS. *MAGMA*, 2005, **18,** 201–205.
230. W. K. J. Renema, H. E. Kan, B. Wieringa and A. Heerschap, *In vivo* magnetic resonance spectroscopy of transgenic mouse models with altered high-energy phosphoryl transfer metabolism. *NMR Biomed.*, 2007, **20,** 448–467.

231. G. J. Lurman, C. H. Bock and H.-O. Pörtner, An examination of the metabolic processes underpinning critical swimming in Atlantic cod (*Gadus morhua* L.) using *in vivo* ^{31}P-NMR spectroscopy. *J. Exp. Biol.*, 2007, **210,** 3749–3756.
232. F. Melzner, C. Bock and H.-O. Pörtner, Critical temperatures in the cephalopod *Sepia officinalis* investigated using *in vivo* ^{31}P NMR spectroscopy. *J. Exp. Biol.*, 2006, **209,** 891–906.
233. I. S. Haddadin, A. McIntosh, S. Meisamy, C. Corum, A. L. Styczynski Snyder, N. J. Powell, M. T. Nelson, D. Yee, M. Garwood and P. J. Bolan, Metabolite quantification and high-field MRS in breast cancer. *NMR Biomed.*, 2009, **22,** 65–76.
234. J. Kurhanewicz and D. B. Vigneron, Advances in MR spectroscopy of the prostate. *Magn. Reson. Imaging Clin. N. Am.*, 2008, **16,** 697–710.
235. K. Glunde, C. Jie and Z. M. Bhujwalla, Molecular causes of the aberrant choline phospholipid metabolism in breast cancer. *Cancer Res.*, 2004, **64,** 4270–4276.
236. D. W. Klomp, B. L. van de Bank, A. Raaijmakers, M. A. Korteweg, C. Possanzini, V. O. Boer, C. A. van de Berg, M. A. van de Bosch and P. R. Luijten, ^{31}P MRSI and ^{1}H MRS at 7 T: initial results in human breast cancer. *NMR Biomed.*, doi: 10.1002/nbm.1696.
237. C. Stork and P. F. Renshaw, Mitochondrial dysfunction in bipolar disorder: evidence from magnetic resonance spectroscopy research. *Mol. Psychiatry*, 2005, **10,** 900–919.
238. J. W. Pettegrew, M. S. Keshavan, J. A. Stanley, R. J. McClure, C. R. Johnson and K. Panchalingam, Magnetic resonance spectroscopy in the assessment of phospholipid metabolism in schizophrenia and other psychiatric disorders. *in*: Phospholipid Spectrum Disorder in Psychiatry, 2nd edn. M. Peet, I. Glen, and D. F. Horrobin (eds.), Marius, Carnforth, UK, 2003, pp. 239–255.

CHAPTER 4

Compact Superconducting Magnet Design for Nuclear Magnetic Resonance: The Minimum Stored Energy Approach

Quang M. Tieng and **Viktor Vegh**

Contents

Centre for Advanced Imaging, University of Queensland, Brisbane, Australia

Annual Reports on NMR Spectroscopy, Volume 75
ISSN 0066-4103, DOI: 10.1016/B978-0-12-397018-3.00004-1

Abstract Superconducting magnet coil arrangements applicable in nuclear magnetic resonance across a range of magnetic field strengths are described in the context of the minimum stored energy (MSE) design. The approach is based on first calculating an optimal current density map, which is then used to allocate coils for the second stage of the optimization process. Having stated the coil domain, required magnetic field strength and constraint of current density, a set of superconducting magnet coil arrangements can be computed. Low- and high-field magnet coils achieving field strengths of 1, 3, 7 and 11.75 T are provided for the cylindrical compact designs, 1T for the asymmetric coil arrangement and 1T for the open double-doughnut configuration magnet. Irrespective of the magnet type, our findings show that individual magnet coils should be arranged at the local positive maxima and negative minima of the current density map and around the perimeter of the domain used to specify possible coil locations. Moreover, at high-field, which we assume to be larger than 3T, the maximum fields are located on coils with the smallest radii, whereas at low-field, this is not the case. This becomes a critical observation for high-field applications, as the superconducting magnet design freedom is restricted by inherent peak field limits on superconductors. To reduce the peak field experienced by any coil, the domain has to be made longer, resulting in physically large magnets. Our findings also suggest that at low-field, reverse current coils can be employed to shorten the length of the magnet. When the field strengths is greater than 3T, large peak fields produced between adjacent coils with alternating currents limit the ability to incorporate reverse current coils without a breach of the peak field limit.

Key Words: Nuclear magnetic resonance, Superconducting magnet, Minimum stored energy, Magnetic resonance imaging

1. INTRODUCTION

Nuclear magnetic resonance (NMR) and Magnetic resonance imaging (MRI) superconducting magnets are present in both low- and high-field applications, as resistive magnets are limited to field strengths of less than a Tesla (T).[1] The superconducting magnet field strength inside the field-of-view (FOV) is used to classify scanners and it is proportional to the signal-to-noise ratio (SNR), allowing image resolutions to be increased. For this reason, low-field has often been associated with low-resolution imaging, and high-field magnets are needed to improve image resolution. The gained SNR at high-field can be traded for a reduction in data

acquisition times, which is particularly helpful in the clinic, where patient throughput is important. Our work aims to improve the quality of NMR/MRI superconducting magnets for use within the clinical and research settings, as measured by FOV static magnetic field strength, its homogeneity and size, and the extent of the stray or fringe field. Our intention here is to outline magnet designs across a range on field strengths and configurations and discuss differences between coil arrangements of different field strength magnets. The magnets considered achieve static field strengths from as low as 1T and up to 11.75T, with substantially large (1m) inner diameters necessary to image a person.

Previously, we have outlined the MSE magnet design strategy and applied it to compact clinical magnets,[2,3] open magnets for use in interventional systems,[4] MRI and positron emission tomography (PET) multimodal imaging of animals[5] and ultra high-field systems.[6] We have also compared 1 to 3 to 7T and highlighted specific differences.[7] Previously, we have not published asymmetric magnet coil arrangements, details of which we provide here on top of existing symmetric designs. In all configurations, the primary objective of the problem formulation was to reduce superconducting magnet cost[8] and to improve performance as measured by magnetic field attributes.[1] This work brings together all of our low- to high-field designs and summarizes our findings from before by considering compact symmetric magnets (1, 3, 7 and 11.75T), an asymmetric magnet design (1T) and a double-doughnut open magnet design (1T).

1.1. Design parameters

The methodology of designing magnets has broadly been investigated by researchers. In view of superconducting magnet designs alone, different optimization strategies have been utilized to obtain coil layouts, coil arrangements that achieve predefined magnetic field homogeneities within a specified imaging region or the FOV. Across the various magnet design stages, the stray field of the coil layout is also considered, since the fringe field determines the magnet footprint, and therefore, the ability to safely house the NMR/MRI scanner. The technique to obtain a specific collection of coils that together deliver an appropriate homogeneity and strong magnetic field to the FOV, and at the same time minimizing magnet footprint, requires consideration to not only these factors but also to the ability of the superconductor to carry a sufficiently large transport current with minimum superconducting material. Moreover, the magnet at field implies that the superconductor is exposed to a self-generated static field, which if large enough can cause the magnet to quench, or the inability to bring the magnet to the field achieved in the simulation. For this reason, superconductors are limited by the transport

current, or current density, and the peak field on the conductor.[9] Essentially, the combination of the transport current and the magnetic field around the superconductor creates stresses on the assembly through the generation of Lorentz forces. The magnitude of the created forces should be sufficiently small, such that the stresses produced are not large enough to quench the magnet.

NMR/MRI magnets are generally actively shielded, meaning that the final coil arrangements utilize reverse current direction coils to help reduce the magnetic field footprint of the system. In the past, the reverse current coils were placed furthest from the FOV, to minimize their impact on the imaging field strength and to maximize stray field reductions. Recent advances have shown that this arrangement of coils can be the case but does generalize to all magnet designs across all field strengths. On top of active shielding, the magnet should be designed and built in a way that restricts the peak magnetic field produced inside the superconductors themselves, whilst minimizing magnetic fields external to the assembly.[10]

The final designs should require less energy and therefore incur lower manufacturing costs,[8] which ultimately translate to more affordable systems with reduced scan costs. The amount of stored energy present defines superconducting magnet quality, because training time reduces, as well as providing the ability to release energy quickly in case of a quench. Attempts have been made to address the concerns of weight, size and magnetic field nonlinearity in magnet systems, with the intention of lowering manufacturing cost of systems.[11,12] Notably, a number of specific advancements have seen improved and cheaper technologies emerge in magnet construction and performance,[11–17] which benefit the community through better, more insightful diagnostic and preventative medical imaging.

1.2. Optimization approaches and cost functions

Having noted the common factors influencing superconducting magnet design, previously employed optimization methods can be grouped into two categories: approaches that search a large parameter space from which an optimal superconducting coil configuration is obtained,[18–21] or where a predefined set of constraints is used as part of the optimization strategy to speed up computation whilst stabilizing convergence towards the optimal solution.[22–24] In the prior, large computational resources are needed to obtain coil arrangements, and the latter employs existing knowledge as part of the optimization to improve convergence to a solution. It has been shown that the various methods have a tendency to achieve a similar result, irrespective of the approach adopted.[25] Further, it was also shown that superconducting magnet coil layout can be

improved through the use of subdomains for coil arrangements.[10] The use of subdomains can be restrictive, as coils cannot move outside of them during the iterations of the optimization process.

Our work uses the concept of a single magnet domain and an MSE current density map, from which we seed individual magnet coils.[2] The seed coils are used in the second stage of the optimization process to yield an optimal coil configuration.[3] Our approach minimizes the superconductor volume and the current density experienced by individual conductors by minimizing the magnet stored energy. We achieve an MSE coil arrangement, because the stored energy is a function of inductance and current density, and the self-inductance is proportional to the superconductor volume, which are components of the energy cost function.

In contrast to our MSE technique, Kakugawa et al.[26] formulated the cost function to be minimized as a product of coil cross sectional area and its current density. The result is an optimal coil configuration for the coil cross sectional area and coil current density. However, it is not clear that the superconducting volume is also minimized when cross sectional area is reduced, as individual coil volumes are a function of the coil radius, which was not considered.

Xu[27] and Jensen[28] independently developed methods of designing magnets by minimizing the dissipated power. The approach is only suitable for designing resistive magnets, as dissipated power in superconductors is negligible, and to achieve a smaller resistance, a larger wire cross sectional area is required. Therefore, conductor volume and manufacturing cost increase, since dissipated power is proportional to conductor resistance. Jensen[28] also described a technique based on minimizing coil volumes, which required fixing the value for the coil current density prior to optimization. Another contrasting technique to our MSE approach is by Park et al.,[29] where the stored energy is maximized, which is only useful as an energy storage device.

1.3. MSE magnet coil arrangement and implementation

Coil arrangement layers in the MSE design are not referred to as primary and shield, as is the case in the literature for other design methods,[30,31] since all coils act in unison to achieve optimal design parameters. Therefore, action of individual coils is not considered. In the MSE design, positive and negative transport current coils are not restricted to a particular layer of the domain used in the optimization, and alternating current coils are only employed to achieve FOV magnetic field homogeneity and to constrain the size of the stray field. Therefore, we make no reference to primary and shield layers, and all designs depicted are classified as actively shielded magnets.

In our method, the implementation of the magnet domain requires a discretization strategy involving a number of small cells, which is often adopted in the other magnet design approaches. Others approximate cells by the filament coils, from which magnetic fields are calculated. However, in the MSE approach, the actual cell dimensions in relation to conductor cross section are used in the computations. As a consequence, and as an outcome of the first step of the optimization, the current density map gives exactly the desired magnet field. In the second stage of the optimization process, we go onto obtaining coil configurations with minimal conductor volumes and optimal current densities, such that collectively the stored energy is minimized.

2. METHOD OUTLINE

The MSE method of designing superconducting magnets consists of two independent steps, which are to determine:

(1) MSE current density map over a predefined magnet domain, where superconducting coils will be laid out, subject to constraints, such as the homogeneity of the FOV and footprint of the magnet stray field.
(2) Magnet arrangement with the initial coil layout based on the MSE current density map. The coil locations and sizes are refined to enhance the field homogeneity and to decrease the footprint of the magnet, without changing the original constraints defined for the MSE current density map.

The second step of the optimization process is repeated a few times, as a breach of superconductor peak field values have to be carefully and manually considered given different types of superconductor.

2.1. Magnetic field computation

In both steps, the magnetic field generated by electronic current carrying conductor needs to be quickly and repeatedly calculated as part of the optimization processes. Thus, an efficient method of magnetic field computation must be employed. In this work, the magnetic field produced by an arbitrarily shaped electric current carrying conductor cell is expressed as the sum of an infinite series of spherical harmonics. The amplitude and sign of each spherical harmonic expansion term depend on the cell geometry, current strength, winding direction and relative positions of cells in a particular domain configuration. Hence, a collective set of cells expressed in terms of spherical harmonics can be arranged in space to satisfy design specific constraints, through appropriate choice of size, current

magnitude/direction and spacing. In addition, we have found that only the first few spherical harmonic terms are needed. Therefore, spherical harmonic expansions are used to define individual current carrying cells to reduce the computational cost and overall optimization complexity.

Figure 1 shows how we defined the geometry and reference frame for a conductor in space, where the inherent symmetry is assumed to be characterized by the cylindrical nature of the system. This also allowed us to simplify the problem to two coordinate directions. We assume the z-axis to be along the longitudinal direction of the system aligned with the magnet field (B_0), and to be the direction in which samples are inserted into the scanner.

The axial component of the magnetic field at a point ($r<r_0,\theta$) in an axisymmetric configuration comprising current carrying circular conductors coaxial with the z-axis is given by:[32]

$$B_z(r < r_0, \theta) = J \sum_{n=1}^{\infty} a_n P_{n-1}(\cos\theta) r^{n-1}, \tag{1}$$

where

$$a_n = -\frac{\mu_0}{2} \sin\theta_0 \frac{P_n^1(\cos\theta_0)}{r_0^n}.$$

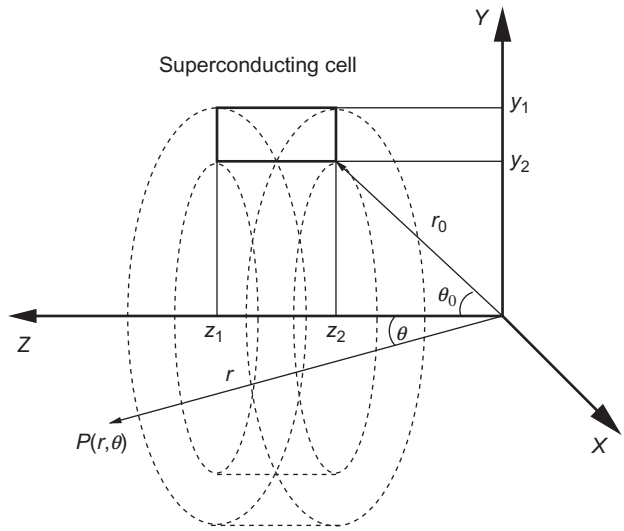

Figure 1 Illustration of how a magnetic field is defined at a point $P(r,\theta)$ produced by a cylindrical superconductor cross-sectioned in the yz-plane.

In Equation (1), $\mu_0$is the permeability of free space, J is the element current density, (r_0,θ_0) defines the element geometry with respect to an arbitrary origin, (r,θ) is the field point with respect to the origin and $P_n^m(\cos\theta)$ is the associated Legendre polynomial evaluated at the appropriate location in space.The corresponding field expansion for points lying in the external region defined for $r>r_0$ is given by:[32]

$$B_z(r > r_0, \theta) = J \sum_{n=1}^{\infty} b_n \frac{P_{n+1}(\cos\theta)}{r^{n+2}}, \tag{2}$$

where

$$b_n = -\frac{\mu_0}{2} \sin\theta_0 P_n^1(\cos\theta)_0 r_0^{n+1}.$$

For more appropriate element definitions, Equations (1) and (2) are extended to allow for the calculation of the magnetic field generated by a rectangular cross section element as:

$$\begin{aligned} B_z\left(r < \sqrt{y_2^2 + z_2^2}, \theta\right) &= J \sum_{n=1}^{\infty} \alpha_n P_{n-1}(\cos\theta) r^{n-1}, \\ B_z\left(r > \sqrt{y_1^2 + z_1^2}, \theta\right) &= J \sum_{n=1}^{\infty} \beta_n \frac{P_{n+1}(\cos\theta)}{r^{n+2}}, \end{aligned} \tag{3}$$

where

$$\alpha_n = -\frac{\mu_0}{2} \int_{z_2}^{z_1} \int_{y_2}^{y_1} \frac{y}{\sqrt{y^2 + z^2}} \frac{P_n^1\left(\frac{z}{\sqrt{y^2 + z^2}}\right)}{(y^2 + z^2)^{n/2}} \mathrm{d}y\mathrm{d}z,$$

$$\beta_n = -\frac{\mu_0}{2} \int_{z_2}^{z_1} \int_{y_2}^{y_1} \frac{y}{\sqrt{y^2 + z^2}} P_n^1\left(\frac{z}{\sqrt{y^2 + z^2}}\right) \left(y^2 + z^2\right)^{(n+1)/2} \mathrm{d}y\mathrm{d}z.$$

In Equation (3), coordinates (y_1,z_1) and (y_2,z_2) define the rectangular conductor cross section in the yz-plane, as shown in Figure 1. The harmonic coefficients (α_n and β_n) can be computed analytically or numerically. The analytic expressions for the coefficients can be obtained by solving the integral for α_n and β_n, but in our implementation, we used Gaussian quadrature[33] to compute α_n and β_n individually. The procedure of using Gaussian quadrature was found to be both accurate and efficient, when compared to the analytic expressions. For reference, the first two harmonic coefficients in analytic form for the inner region are:

$$\alpha_1 = -\frac{\mu_0}{2}\left[z_1 \ln\left(\frac{y_2+\sqrt{y_2^2+z_1^2}}{y_1+\sqrt{y_1^2+z_1^2}}\right) + z_2 \ln\left(\frac{y_1+\sqrt{y_1^2+z_2^2}}{y_2+\sqrt{y_1^2+z_2^2}}\right)\right],$$

$$\alpha_2 = -\frac{\mu_0}{2}\left[y_1\left(\frac{1}{\sqrt{y_1^2+z_2^2}} - \frac{1}{\sqrt{y_1^2+z_1^2}}\right) - y_2\left(\frac{1}{\sqrt{y_2^2+z_2^2}} - \frac{1}{\sqrt{y_2^2+z_1^2}}\right)\right]$$
$$-\frac{\mu_0}{2}\ln\left(\frac{\left(y_1+\sqrt{y_1^2+z_1^2}\right)\left(y_2+\sqrt{y_2^2+z_2^2}\right)}{\left(y_1+\sqrt{y_1^2+z_2^2}\right)\left(y_2+\sqrt{y_2^2+z_1^2}\right)}\right),$$

and for the outer region:

$$\beta_1 = -\frac{\mu_0}{2}\left[\frac{1}{3}\left(y_1^3 - y_2^3\right)\left(z_2 - z_1\right)\right],$$

$$\beta_2 = -\frac{\mu_0}{2}\left[\frac{1}{2}\left(y_1^3 - y_2^3\right)\left(z_2^2 - z_1^2\right)\right].$$

2.2. MSE current density map

As the spherical harmonic expression only defines the magnetic field outside its current source, we divide magnetic fields in two disjointed regions, referred to as the inner and outer regions with respect to the magnet domain; illustrated in Figure 2. The inner region encases the FOV and the outer region is used to define the stray field of the magnet, from which we later calculate the magnet footprint. To achieve a desirable magnetic field inside the FOV and to limit the extent of the stray field, inner and outer spherical harmonics are made to vanish through successive iterations of the optimization process. The number of zeroed inner and outer harmonics, respectively, defines the order and degree of the MSE magnet. To generate the MSE current density map, the magnet domain is divided into K elements, for each of which the internal and external spherical harmonic coefficients are computed using the approach from above. The current density associated with each small conductor, or element k, is calculated by minimizing the stored energy sum given in terms of self-inductance (L) and current density (J):

$$\min_{J_k} F = \frac{1}{2}\sum_{k=0}^{K-1} L_k J_k^2 A_k^2, \tag{4}$$

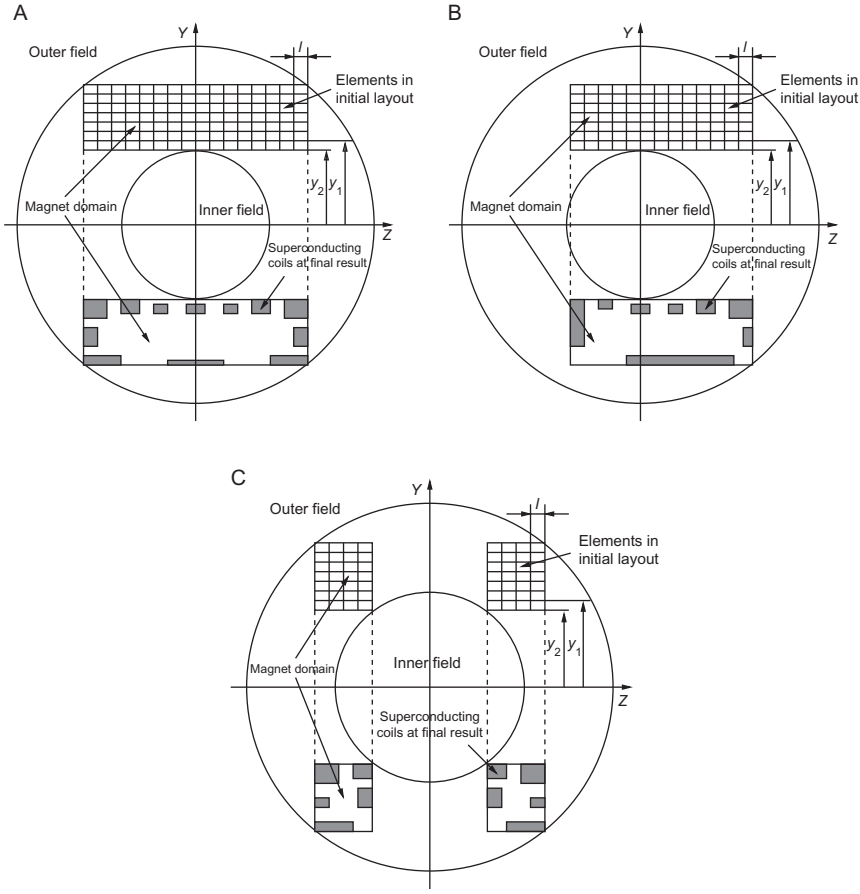

Figure 2 Illustration of the magnet domain, inner and outer fields, elements or conductors within the domain and specific dimensions used throughout the optimization process for (A) symmetric magnet, (B) asymmetric magnet and (C) symmetric open magnet.

where A_k is the element cross sectional area corresponding to location k and L_k is the self-inductance.[34] We assume that the element cross sectional area corresponds to the superconductor cross section, although this does not have to be the case. To obtain the MSE current density map, Equation (4) is solved subject to linear constraints on the magnet field strength (B_0), the vanished $N-1$ internal (α) and M external (β) spherical harmonics:

$$\begin{aligned}
&\sum_{k=0}^{K-1}\alpha_{k,1}J_k = B_0,\\
&\sum_{k=0}^{K-1}\alpha_{k,n}J_k = 0, \quad n = 2\ldots N,\\
&\sum_{k=0}^{K-1}\beta_{k,m}J_k = 0, \quad m = 1\ldots M,\\
&J_{\min} \le J_k \le J_{\max},
\end{aligned} \tag{5}$$

where ($J_{\min}$,$J_{\max}$) provides a bound on the individual current densities; $\alpha_{k,\,n}$ and $\beta_{k,m}$ are the inner α_n and outer β_m harmonics of the kth element. The problem relating to the MSE current density map cost function given in Equation (4) is solved using the general quadratic program (QP),[35] subject to constraints stated in Equation (5). The mutual inductance is not incorporated into the current density map cost function in Equation (4), because we intended to state the problem as strictly convex, which enables a global solution to be attained.

For magnet configurations in which coils are coaxial and symmetric about the illustrated *xy*-plane, such as the magnet configurations in Figure 2A and C, the spherical harmonic expansion results in the elimination of all even order terms within the expansion. To further reduce computational complexity, the strategy employed here considers only one quarter of the magnet domain, and thus, the constraints in Equation (5) simplify to:

$$\begin{aligned}
&\sum_{k=0}^{K^*-1}\alpha_{k,1}J_k = \frac{B_0}{2},\\
&\sum_{k=0}^{K^*-1}\alpha_{k,2n+1}J_k = 0, \quad n = 1\ldots\frac{N-1}{2},\\
&\sum_{k=0}^{K^*-1}\beta_{k,2m+1}J_k = 0, \quad m = 0\ldots\frac{M-1}{2},\\
&J_{\min} \le J_k \le J_{\max},
\end{aligned}$$

where $K^*$is the number of elements in one quarter of the magnet domain.

Figure 3 provides illustration of MSE current density maps with different order and degree for 3 and 1m length magnet domains. The figure shows that the current density map has several local maxima and minima within the magnet domain, referred to as extremities. The number of extremities is proportional to the number of eliminated spherical harmonics. The extremities lie around the perimeter of the magnet region.

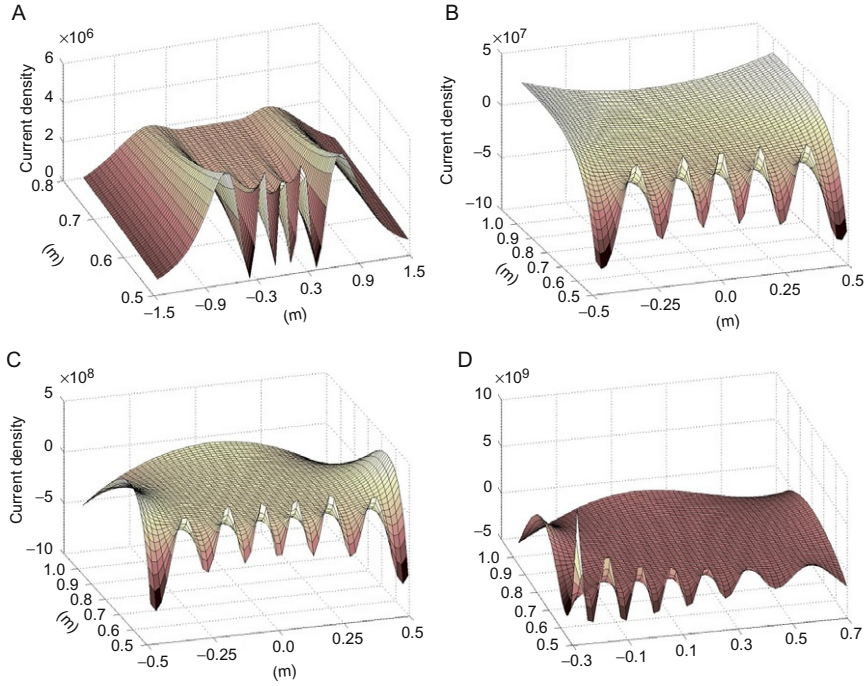

Figure 3 Illustration of different MSE current density maps. Given are MSE current density maps of (A) order 10 degree 0 for a 3-m length symmetric magnet domain, (B) order 14 degree 0 for a 1-m length symmetric magnet domain, (C) order 16 degree 4 for a 1-m length symmetric magnet domain and (D) order 16 degree 4 for a 1-m length asymmetric magnet domain.

For long magnet domains, the current density map may have a relatively large number of successive maxima and minima of a common polarity, such that positive maxima are adjacent to positive minima, and vice versa, as shown in Figure 3A. As the length of the magnet region is reduced, the number of such extremities becomes smaller, with a further reduction in the size of the magnet domain resulting in the adjacent extremities having opposite polarities, as shown in Figure 3B–D. This means that in compact designs, positive maxima are located adjacent to negative minima.

2.3. MSE coil configuration

The coil structures are initially positioned coincident with the positive maxima and negative minima of the MSE current density map with their initial cross sectional areas being proportional to the value of the associated current densities. The coil locations and dimensions are then

refined to generate desired internal and external magnetic fields through a non-linear optimization method that minimizes the following cost function:[3]

$$\min_{J,M_{kh}} \quad F = \frac{1}{2}\sum_{k=0}^{H-1}\sum_{h=0}^{H-1} M_{kh}(A_k J_k)(A_h J_h), \tag{6}$$

where $|J_k|=|J_h|=J$ is the current density in all H coils. It is possible to have different cross sectional superconductors amongst different coils, yielding different current densities, but here we simplify the problem to constant current density to enforce standard definitions and allow comparisons between designs. In Equation (6), M_{kh} is either self ($h=k$) or mutual inductance ($h\neq k$). Specifically, self-inductances are calculated using the equation given by Edminister,[34] and mutual inductances are computed using the Lyle method of equivalent filaments.[36] To solve Equation (6), sequential quadratic programming (SQP)[37] was used subject to constraints:

$$\begin{aligned}
&\sum_{h=0}^{H-1}\alpha_{h,1}J_h = B_0,\\
&\sum_{h=0}^{H-1}\alpha_{h,n}J_h = 0, \quad n = 2\ldots N,\\
&\sum_{h=0}^{H-1}\beta_{h,m}J_h = 0, \quad m = 1\ldots M,\\
&0 < J_h \leq J_{\max},
\end{aligned} \tag{7}$$

where spherical harmonics are defined as outlined above. Similarly to the process employed to calculate the MSE current density map, if the magnets are cylindrical and symmetric, then the constraints (7) can be simplified as follows:

$$\begin{aligned}
&\sum_{h=0}^{H^*-1}\alpha_{h,1}J_h = \frac{B_0}{2},\\
&\sum_{h=0}^{H^*-1}\alpha_{h,2n+1}J_h = 0, \quad n = 1\ldots\frac{N-1}{2},\\
&\sum_{h=0}^{H^*-1}\beta_{h,2m+1}J_h = 0, \quad m = 0\ldots\frac{M-1}{2},\\
&0 < J_h \leq J_{\max},
\end{aligned}$$

where H^* is the number of superconducting coils in one quarter of the magnet domain.

2.4. MSE magnet design procedure

In the MSE approach, the size and field homogeneity of the FOV are proportional to number of zeroed inner spherical harmonics, and number of vanished outer harmonics defines the size of the system footprint. We recall that the number of inner and outer spherical harmonics made to vanish refers to the order and degree of the design. Once the order and degree are specified based on the requirements of the FOV and the stray field, and the magnet domain has been established, then the MSE current density map is calculated.

At the second step, the seed coils have been selected based on the MSE current density map, they are optimized for location and size without changing the total number of coils. The total number of coils proportionally increases with the sum of the order and degree of the design. This means that the order and degree of the design remains fixed throughout the design process. Due to the relationship between the total number of coils and the order and degree of the design, we cannot continue to increase the FOV and decrease the coil layout footprint by increasing the order and degree without altering the magnet domain dimensions. This is because the number of coils will increase and the distance between adjacent coils will decrease, in turn increasing the peak magnetic field on the superconductors. Essentially, the continual increase in both order and degree of the design creates magnetic fields above superconductivity limits or results in overlapping coils.

After convergence has been achieved at the second stage of the optimization, the magnetic field experienced by the superconducting coils is calculated using the method outlined by Forbes et al.[38] If within the coils the peak field is greater than the allowable limit,[9] then before the second stage of the optimization is repeated, the spacing between problematic adjacent coils is adjusted and geometrical constraints can be applied if required to reduce the peak field.[3]

3. MSE MAGNET CONFIGURATIONS AND DISCUSSION

The MSE magnet design method was used to obtain coil configurations for compact superconducting magnets, with the aim of having an inner bore diameter of 1m. The outer diameter and length was manipulated to meet the criteria of superconductivity, as limited by the current density and the peak field on the superconductors at a given operating temperature.

The combination of the transport current and magnetic field surrounding superconductors creates stresses on the assembly through the generation of Lorentz forces. Calculation of coil stresses for final coil

arrangements is included, since sufficient stress conditions are needed to be able to build the proposed magnet designs. The hoop stresses along the radial direction at the middle plane of each coil are calculated using Appleton's method.[39] An alternative method based on the *BJr* relationship[40] is also used to compare stresses against Appleton's method. The hoop stresses obtained using the *BJr* approach are reported for all magnet coil configurations.

We only report coil configurations for active shielded magnets. For uncommon unshielded magnets, readers could refer to our recent works.[3,4] The design steps for actively shielded and unshielded magnets are similar to what we have already described. To design an active shielded magnet, both inner and outer spherical harmonics are considered. However, as only the outer harmonics affect the stray field, the outer harmonic constraints are ignored in both steps of unshielded magnet design.

3.1. Layout of compact symmetric superconducting magnets

Four different magnetic field strength compact magnets (1, 3, 7 and 11.75 T) are depicted to compare the salient features of the designs. The magnets all have different field distributions that allow a certain coil arrangement to be obtained, and these are highlighted within this section. We also point out the important considerations that should be made towards low-field and high-field magnets, and how these change as the FOV field strengths are increased, or for that matter decreased.

Figures 4–7 respectively provide illustrations associated with the design and features of the 1, 3, 7 and 11.75T magnets. These magnets have been designed using the magnet domain shown in Figure 2A. The domain divides the magnetic field into two disjointed regions. The origin of the spherical harmonic expression (provided in Figure 1) or the FOV centre is placed at the centroid of the domain. The designs of the 1, 3 and 7 T magnets assume the use of NbTi superconducting wire, with detailed characteristics provided in Sciver and Marken.[9] Hence, in our designs, the peak field on any coil was restricted to be less than 9T, and the conductor at this field strength is capable of carrying a transport current of no more than 250A/mm^2 at 4.2K. The 11.75T design uses a composite of NbTi–Cu Rutherford wire with a critical current density of 165A/mm^2 at 12T and 2.8K, which is a target for all coils and has been used previously.[41]

Figures 4A, 5A, 6A and 7A depict current density map contour plots along with the placement of the seed coils used for the second stage optimization. The seed coils are placed at local positive maxima and negative minima of the MSE current density map. The current direction of each coil is defined by the polarity of these local extremities. It is also important to mention that the local extremities in the MSE current density

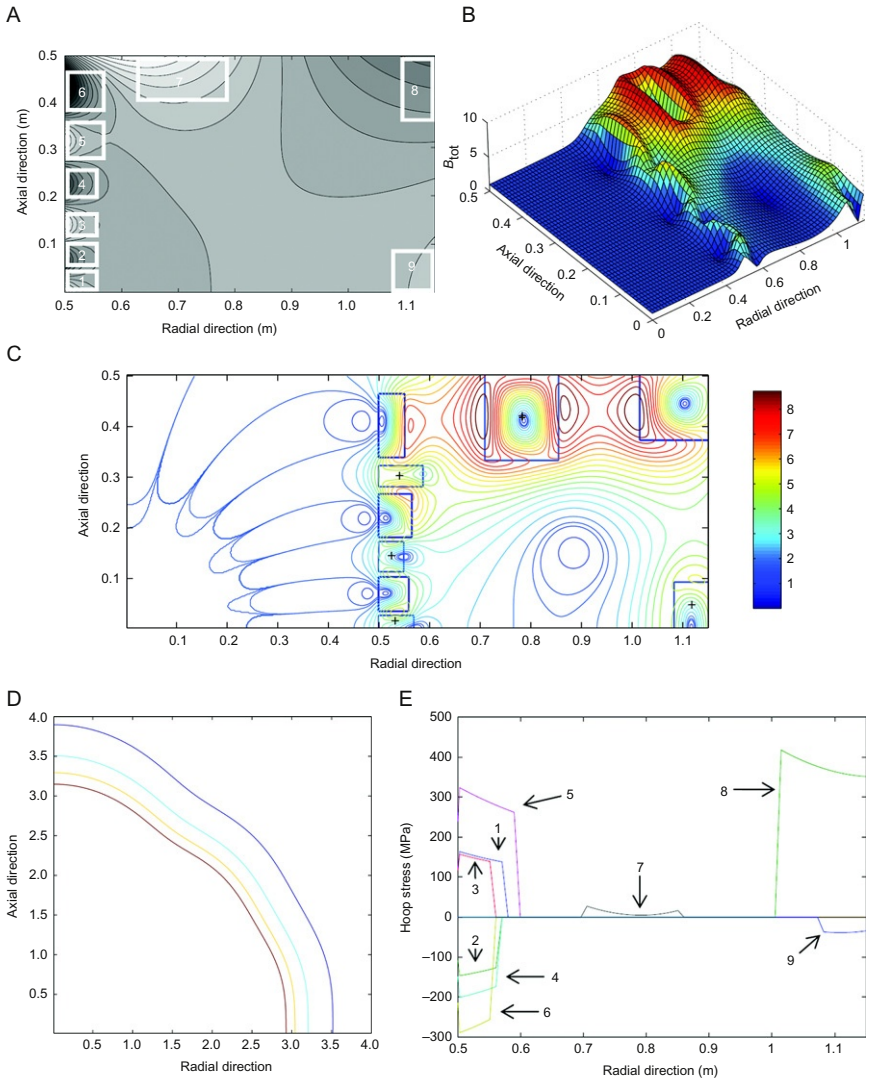

Figure 4 The 1T order 14 degree 4 magnet design. Illustrations of (A) the MSE current density map distribution with locations for initial seed coils, (B) the total magnet field distribution, (C) the final coil layout and associated inner field, (D) the outer field cut-off with 20, 15, 10, and 5G contours from inside out and (E) the stress with respect to the radial direction inside each of the coils. The '+' signs in (C) indicate positive transport current, otherwise the transport current is negative and the contours correspond to the field in (B).

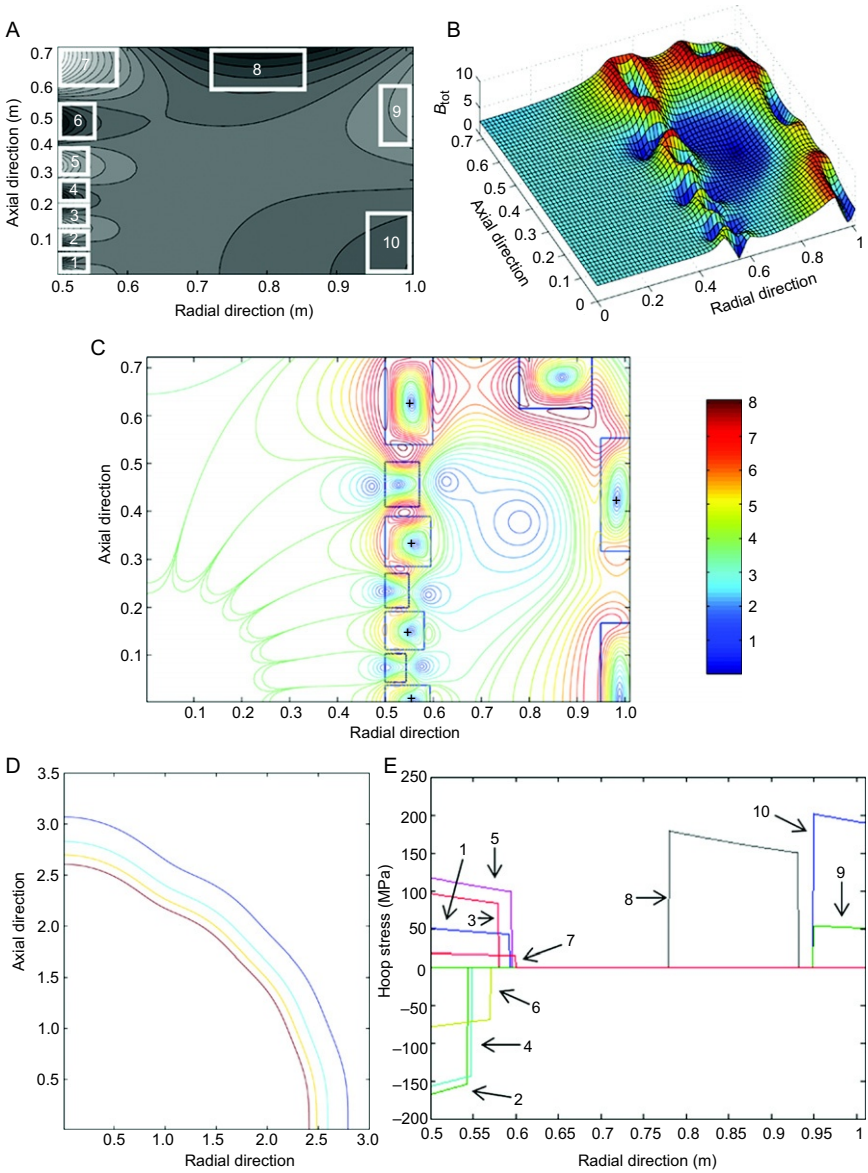

Figure 5 The 3T order 14 degree 6 magnet design. Illustrations of (A) the MSE current density map distribution with locations for initial seed coils, (B) the total magnet field distribution, (C) the final coil layout and associated inner field, (D) the outer field cut-off with 20, 15, 10 and 5G contours from inside out and (E) the stress with respect to the radial direction inside each of the coils. The '+' signs in (C) indicate positive transport current, otherwise the transport current is negative and the contours correspond to the field in (B).

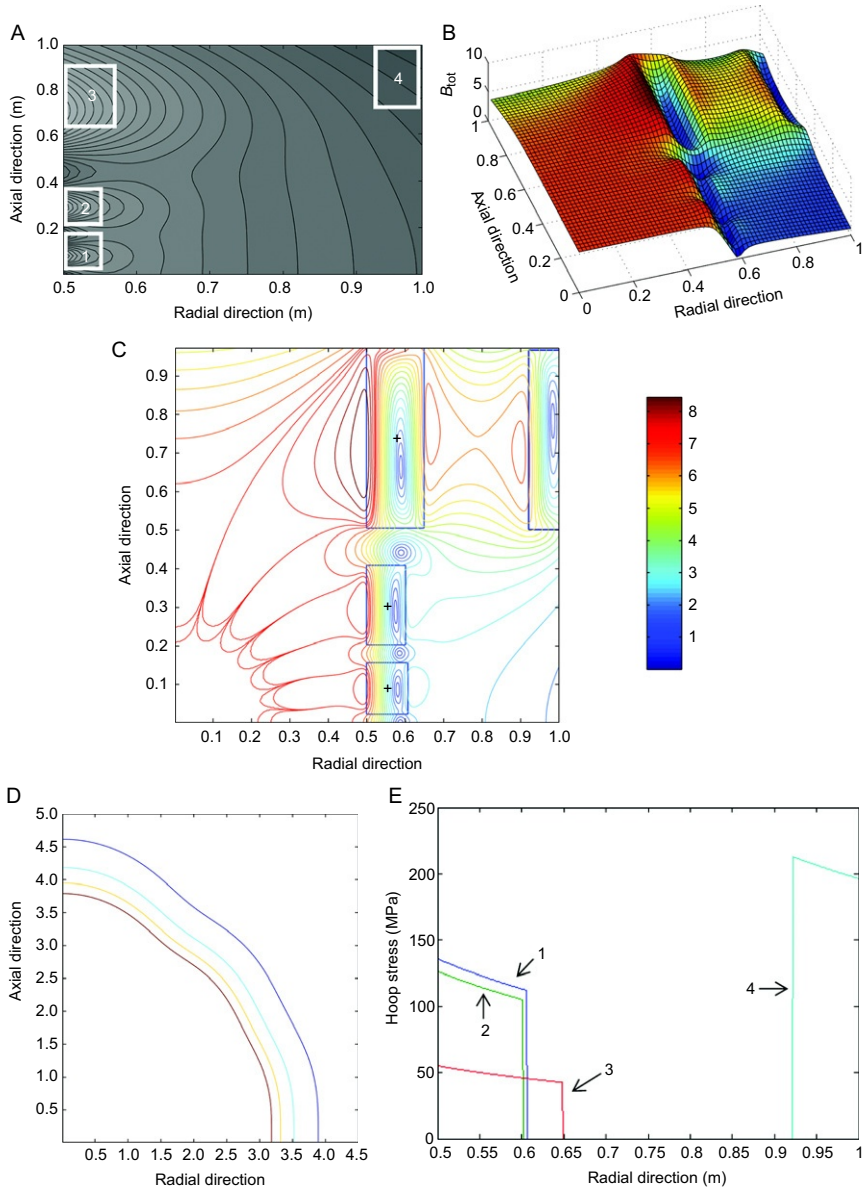

Figure 6 The 7T order 12 degree 4 magnet design. Illustrations of (A) the MSE current density map distribution with locations for initial seed coils, (B) the total magnet field distribution, (C) the final coil layout and associated inner field, (D) the outer field cut-off with 20, 15, 10 and 5G contours from inside out and (E) the stress with respect to the radial direction inside each of the coils. The '+' signs in (C) indicate positive transport current, otherwise the transport current is negative and the contours correspond to the field in (B).

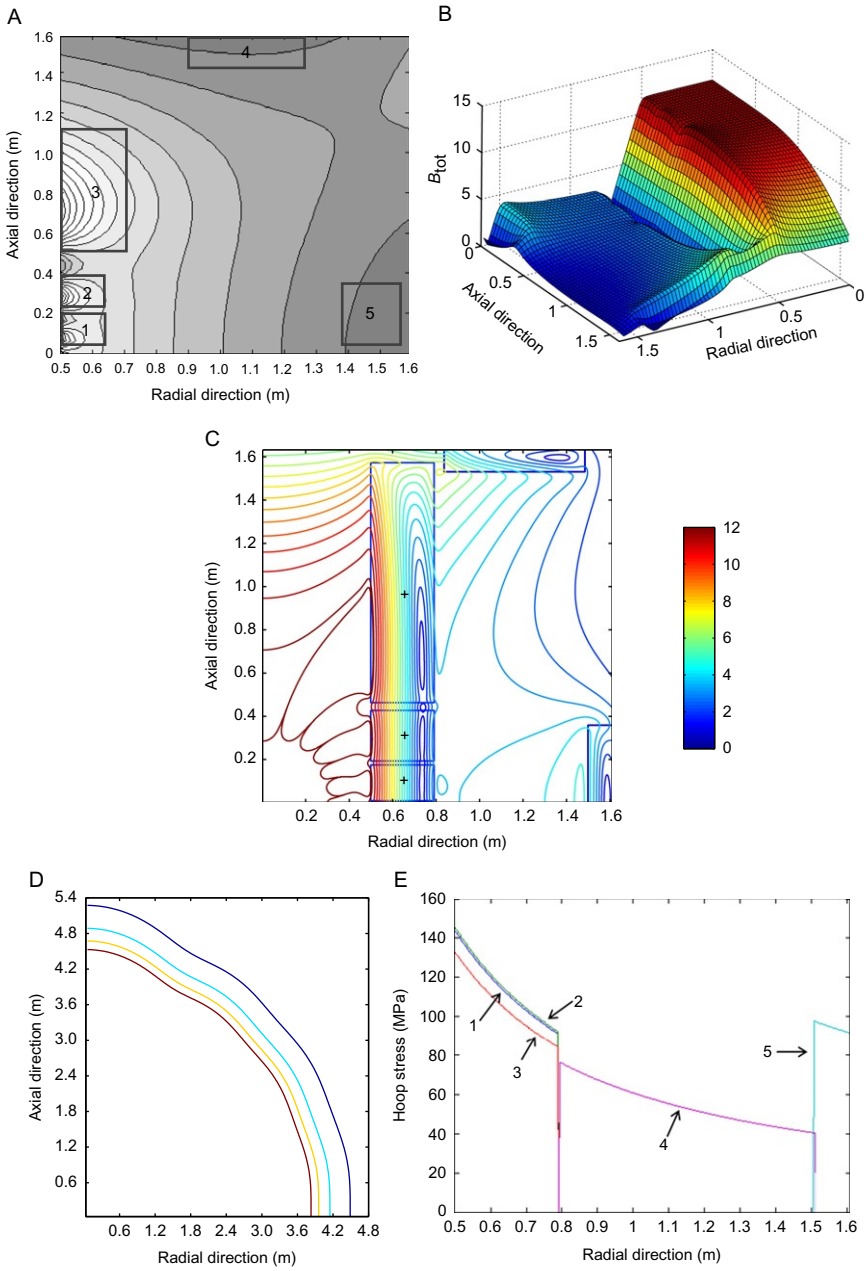

Figure 7 The 11.75T order 12 degree 6 open magnet design. Illustrations of (A) the MSE current density map distribution with locations for initial seed coils, (B) the total magnet field distribution, (C) the final coil layout and associated inner field, (D) the outer field cut-off with 20, 15, 10 and 5G contours from inside out and (E) the stress with respect to the radial direction inside each of the coils. The '+' signs in (C) indicate positive transport current, otherwise the transport current is negative and the contours correspond to the field in (B).

map appear around the magnet domain perimeter, and seed coils for the second stage of the optimization are defined accordingly.

The magnetic field distribution of the final configurations is depicted in Figures 4B, 5B, 6B and 7B. Its contours are plotted as part of the final coil configuration of Figures 4C, 5C, 6C and 7C, wherein the positive transport current coils are identified by the '+' sign and other coils have negative transport current. From the plots, it can be seen that, for the 1T magnet coil arrangement, the total magnetic field tends to be largest between the middle and outer layer coils (i.e. coils 7 and 8 in Figure 4B). From the field strength of the 3T magnet in Figure 5B, it can be seen that the maximum fields are now between the inner and middle layer coils (i.e. coils 7 and 8). In the case of 7 and 11.75T configurations given as Figures 6B and 7B, the maximum total fields have moved to the inner diameter of the magnet. This is an important observation, since peak field problems for high-field magnets appear to be associated with the inner coils, whereas in low-field designs, it may be that the inner coils experience less problems associated with high-magnetic field strengths. Therefore, to reduce the peak field on superconducting coils for- low and medium-field magnets, the relative distance between coils at the middle layer, and coils at the inner or outer layer, should be adjusted. However, for high-field magnets, the peak field can only be reduced by increasing the length of the magnet domain and by reducing the current density on the superconducting coils.

Figures 4D, 5D, 6D and 7D are the stray field contour plots, where the contours represent the 5, 10, 15 and 20G lines, from outside in. In all designs, the 5G line extends approximately 5m in all directions from the FOV centre, which is better than clinical magnets provided by the major manufactures with 45–50cm FOVs.

Figures 4E, 5E, 6E and 7E depict the individual coil hoop stresses along the radial direction at the middle plane of each coil. Particularly for the high-field 11.75T magnet, the stress calculation indicates that the most inner coils are the ones that are most crucial in the design, because they are exposed to the greatest magnetic fields and stresses. It is possible to use different superconductors (i.e. cheaper) to build the outer superconducting coils, since these are well within the superconductivity limit.

The MSE 1T design can be compared to the primary 1T magnet reported in Cheng et al.[25] using 110A transport current. Cheng's magnet has the same inner diameter and a larger outer diameter (1.35m compared to our 1.15m), smaller FOV (30cm compared to 40cm at 1ppm peak-to-peak variation) and larger stray field (11.9 by 9.8m compared to 7.8 by 7m at the 5G line).

Table 1 provides the specifications of interest obtained for the various designs. In Table 2, further information is provided with respect to the coil arrangements. The central location of the coils with respective radial

TABLE 1 Specifications of interest obtained from the six different designs

Specification	1T	3T	7T	11.75T	$1T^{A}$	$1T^{O}$
Order (inner harmonics vanished)	14	14	12	12	11	14
Degree (outer harmonics vanished)	4	6	4	6	2	4
Length (m)	1.00	1.44	1.94	3.26	1.00	1.40
Inner diameter (m)	1.00	1.00	1.00	1.00	1.00	1.00
Outer diameter (m)	2.30	2.02	2.00	3.22	2.20	2.20
Radial FOV at 1ppm (m)	0.40	0.46	0.43	0.58	0.34	0.56
Axial FOV at 1ppm (m)	0.40	0.46	0.41	0.56	0.35	0.66
Radial footprint at 5G (m)	7.00	5.60	7.80	9.20	9.00	6.80
Axial footprint at 5G (m)	7.8	6.15	9.15	10.60	10.40	7.80
Stored energy (MJ)	33	36	58	155	7	16
Peak hoop stress (MPa)	369	188	182	129	276	286
Peak magnetic field (T)	8.73	8.16	8.76	12.11	8.47	6.79
Current density (A/mm^2)	160	175	94	47	155	175

The critical current density of the NbTi/Cu Rutherford wire used in the 11.75T design is $165 A/mm^2$ at the magnetic field strength of 12T operating at 2.8K. The critical current density of the NbTi wire used in other designs is $250 A/mm^2$ at the magnetic field strength of 9T at 4.2K. (^{A}asymmetric, ^{O}open).

and axial coordinates is given as (r_c,z_c), and the corresponding coil has dimensions (D_r,D_z). The peak field (B_{peak}) for each coil is reported along with the calculated hoop stress (σ_θ) using the BJr relationship, where B is the average axial magnetic field, J is the current density and r is the average radius.[40]

3.2. Layout of asymmetric superconducting magnet

Figure 8 provides the MSE asymmetric magnet design. Its domain is given in Figure 2B. The FOV centre is moved near to one end of the domain along the z-axis to create an asymmetric magnetic field with respect to the domain. The design is order 11 and degree 2. These values were selected to ensure that the peak field on each superconductor is within an acceptable range. However, as this design has the smallest achievable order and degree, it also has the smallest FOV but a large footprint, as given in Table 1. A 1-mm^2 cross section NbTi wire was used and the maximum peak field for the conductor has to be less than 9T at 175A and 4.2K.[9] The current density map and seed coils are provided in Figure 8A. Figure 8B shows the magnetic field distribution for the inner region of the magnet domain. Figure 8C illustrates the field contours and the final coil configuration. Plots show that the magnetic field has been shifted to one end of the coil arrangement, and the larger coils appear at this end. As adjacent coils have opposite current polarity and are close to

TABLE 2 The coil configurations for the six designs are provided

Magnet	Coil	Polarity	I (A/mm^2)	Volume (m^3)	B_{peak} (T)	r_c (m)	z_c (m)	D_r (m)	D_z (m)	σ_θ (MPa)
1T	1	+	160	0.0056	4.2145	0.5344	0.0122	0.0689	0.0243	155.171
	2	−	160	0.0128	4.4176	0.5289	0.0676	0.0579	0.0663	146.690
	3	+	160	0.0088	4.0903	0.5236	0.1410	0.0472	0.0566	132.594
	4	−	160	0.0179	6.1822	0.5316	0.2217	0.0632	0.0850	191.774
	5	+	160	0.0122	5.5941	0.5433	0.3003	0.0866	0.0411	307.353
	6	−	160	0.0204	6.3448	0.5251	0.4003	0.0501	0.1233	278.592
	7	+	160	0.1181	8.7248	0.7819	0.4165	0.1438	0.1671	68.9890
	8	−	160	0.1161	8.7223	1.0832	0.4362	0.1336	0.1277	369.317
	9	+	160	0.0413	4.6549	1.1171	0.0446	0.0659	0.0893	34.9437
3T	1	+	175	0.0110	5.1712	0.5462	0.0173	0.0925	0.0347	83.0100
	2	−	175	0.0082	5.0338	0.5212	0.0714	0.0424	0.0592	188.144
	3	+	175	0.0213	5.4672	0.5401	0.1492	0.0801	0.0783	124.006
	4	−	175	0.0111	5.9871	0.5240	0.2335	0.0480	0.0703	179.269
	5	+	175	0.0334	7.2336	0.5473	0.3353	0.0947	0.1025	126.146
	6	−	175	0.0216	6.8989	0.5348	0.4538	0.0697	0.0924	88.2740
	7	+	175	0.0623	7.7368	0.5495	0.6288	0.0990	0.1824	10.4410
	8	−	175	0.0858	8.0787	0.8553	0.6670	0.1506	0.1060	123.763
	9	+	175	0.0862	7.3361	0.9800	0.4333	0.0600	0.2334	58.1230
	10	−	175	0.0607	6.5604	0.9800	0.0821	0.0600	0.1642	182.224
7T	1	+	93.734	0.0477	7.0221	0.5526	0.0881	0.1052	0.1305	119.113
	2	+	93.734	0.0715	7.0704	0.5504	0.3042	0.1008	0.2050	120.887
	3	+	93.734	0.2484	8.4426	0.5740	0.7373	0.1480	0.4654	54.0865
	4	−	93.734	0.2175	5.8079	0.9611	0.7318	0.0777	0.4636	181.819

11.75T	1	+	44.400	0.1912	11.757	0.6455	0.0913	0.2910	0.1645	127.645
	2	+	44.400	0.2735	11.812	0.6455	0.3116	0.2910	0.2333	128.652
	3	+	44.400	1.3016	12.108	0.6455	1.0152	0.2910	1.0947	104.760
	4	−	44.400	0.4732	6.4423	1.1607	1.5810	0.6616	0.0970	73.9070
	5	−	44.400	0.3826	3.5121	1.5599	0.1953	0.1001	0.3907	93.8790
$1T^{A}$	1	−	155	0.0202	7.3588	0.5000	−0.3367	0.0510	0.1260	275.915
	2	+	155	0.0087	4.1991	0.5258	−0.2235	0.0517	0.0511	175.085
	3	−	155	0.0114	4.3260	0.5234	−0.1425	0.0467	0.0741	94.1320
	4	+	155	0.0098	3.2526	0.5241	−0.0526	0.0481	0.0617	83.1000
	5	−	155	0.0063	2.9329	0.5171	0.0271	0.0342	0.0567	52.2210
	6	+	155	0.0085	2.6471	0.5185	0.1149	0.0371	0.0706	51.5930
	7	−	155	0.0054	2.3240	0.5153	0.2038	0.0307	0.0542	29.6750
	8	+	155	0.0086	2.6748	0.5188	0.3073	0.0377	0.0698	66.5320
	9	−	155	0.0089	3.4772	0.5147	0.4434	0.0293	0.0943	82.0880
	10	+	155	0.0338	4.4609	0.6525	0.5774	0.1823	0.0452	80.1380
	11	−	155	0.0697	2.2910	1.0904	−0.0973	0.0192	0.5298	127.184
	12	+	155	0.5657	8.4084	0.7269	−0.3597	0.2338	0.5298	146.078
$1T^{O}$	1	+	175	0.0068	2.8406	0.5496	0.3630	0.0760	0.0260	26.1530
	2	−	175	0.0061	3.3164	0.5170	0.4035	0.0340	0.0550	108.254
	3	+	175	0.0080	3.5979	0.5236	0.4744	0.0470	0.0520	123.876
	4	−	175	0.0142	5.7564	0.5243	0.5810	0.0490	0.0880	165.020
	5	+	175	0.0206	5.3065	0.6553	0.3754	0.0980	0.0510	182.115
	6	−	175	0.0404	6.1251	0.6731	0.6765	0.2030	0.0470	125.311
	7	+	175	0.0737	5.9765	1.0777	0.5788	0.0450	0.2420	285.821
	8	−	175	0.0753	6.7900	0.8922	0.3866	0.1840	0.0730	6.13800

For each coil, the peak magnetic field along with the average hoop stress has been calculated. In the table, (D_r, D_z) provides the coil dimension at centre (r_o, z_c) along to the radial (r) and axial (z) coordinate directions. The hoop stress (σ_θ) for each coil is reported in the last column. All 12 coils of the asymmetric magnet are provided. For symmetric magnets, only a half of number of coils is provided. (^{A}asymmetric, ^{O}open).

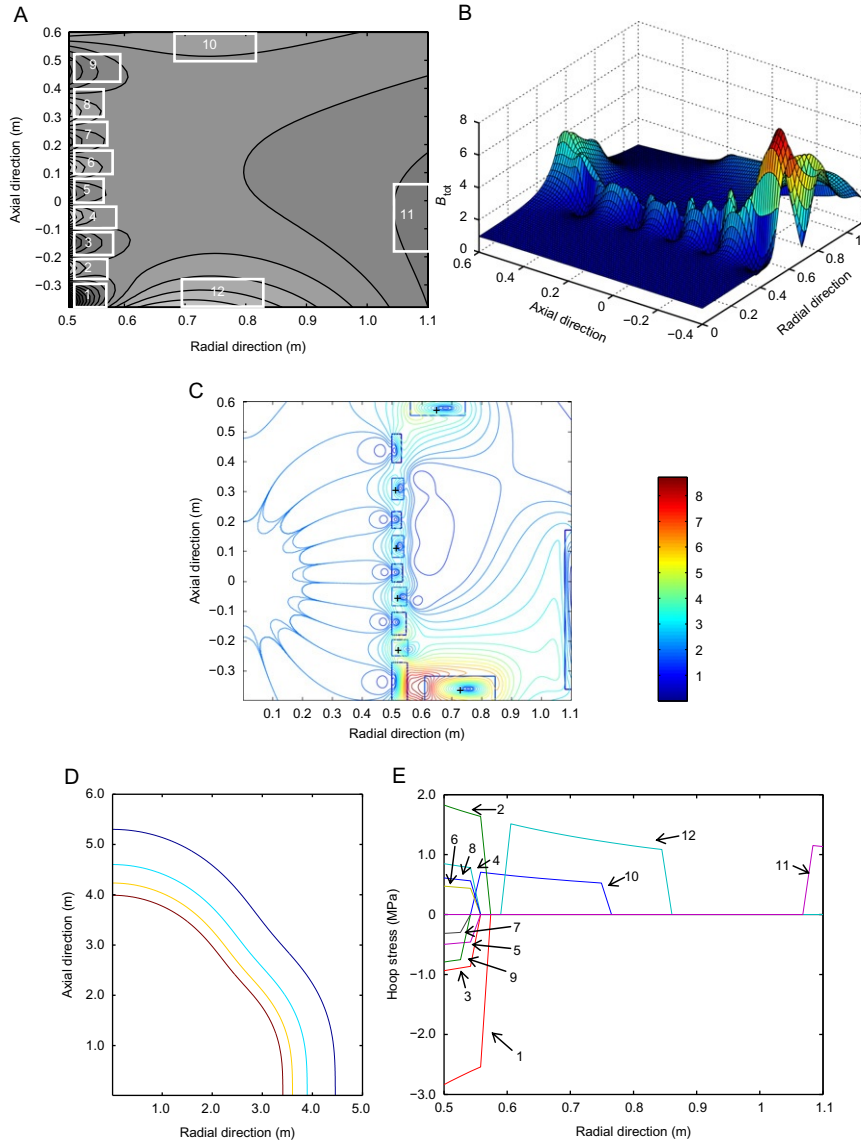

Figure 8 The 1T order 11 degree 2 asymmetric magnet design. Illustrations of (A) the MSE current density map distribution with locations for initial seed coils, (B) the total magnet field distribution, (C) the final coil layout and associated inner field, (D) the outer field cut-off with 20, 15, 10 and 5G contours from inside out, and (E) the stress with respect to the radial direction inside each of the coils. The '+' signs in (C) indicate positive transport current, otherwise the transport current is negative and the contours correspond to the field in (B).

each other at one end, higher peak field on these superconducting coils is created than that of symmetric magnet configurations. Figure 8D provides the stray field of the design. Since the design has a small degree, the footprint is large in comparison to the 1T symmetric design, but the 5G line is still only 5m in all directions from the FOV centre. The hoop stress of each coil at the middle plane along the radial direction is given in Figure 8E. It shows that the coil with the largest hoop stress is the one at the end of the domain close to the FOV centre. The specification of the design is given in Table 1 and individual coils details are provided in Table 2.

3.3. Layout of symmetric open superconducting magnet

Figure 9 illustrates the MSE actively shielded order 14 degree 4 open magnet design. The magnet domain of the symmetric open magnet configuration is shown in Figure 2C. Similar to the compact symmetric system, the FOV centre was placed at the centre of the domain. The domain is split along *xy*-plane to create an open space. In this design, a 1-mm^2 cross section NbTi wire was used and the maximum peak field must be less than 9T at 175A and 4.2K.[9] The choice of order 14 was found to be sufficient to obtain a FOV of at least 50cm in diameter with better than 1ppm field homogeneity. The elimination of four external harmonics provided adequate shielding, as measured by the magnet stray field. In Figure 9A, the current density map with seed coils is provided. The magnetic field strength distribution in the inner field and on the final configuration is shown in Figure 9B. Figure 9C depicts the field contours and final coil configuration. Figure 9D is the illustration of the stray field of the design. It shows that using degree 4 for the design, the 5G line extends less than 4m in all directions from the FOV centre. Figure 9E gives the hoop stresses along the radial direction at the middle plane of individual coils. Table 1 provides the specification of the whole design, and the details of each coil can be found in Table 2.

This symmetric open design can directly be compared to the double-doughnut system in Schirmer et al.[42] Their system has an FOV of 30cm, inner bore diameter of 60cm (including shims, gradient and radiofrequency coils), 0.5T field strength with a 0.58m gap between doughnuts and stray field of 6 by 4m at the 5G field level. In comparison, our design has a 60-cm magnet FOV, inner bore of 1m (clear bore, not including shims, gradient and radiofrequency coils), 1T field strength with 0.7m gap (not including coil support and cooling) and stray field of 3.8 by 3.4m measured at the 5G line.

It should be noted that here we only illustrated theoretical coil layouts using the MSE approach without considering particular manufacturing aspects and other possible limitations. In some cases, the designs may not

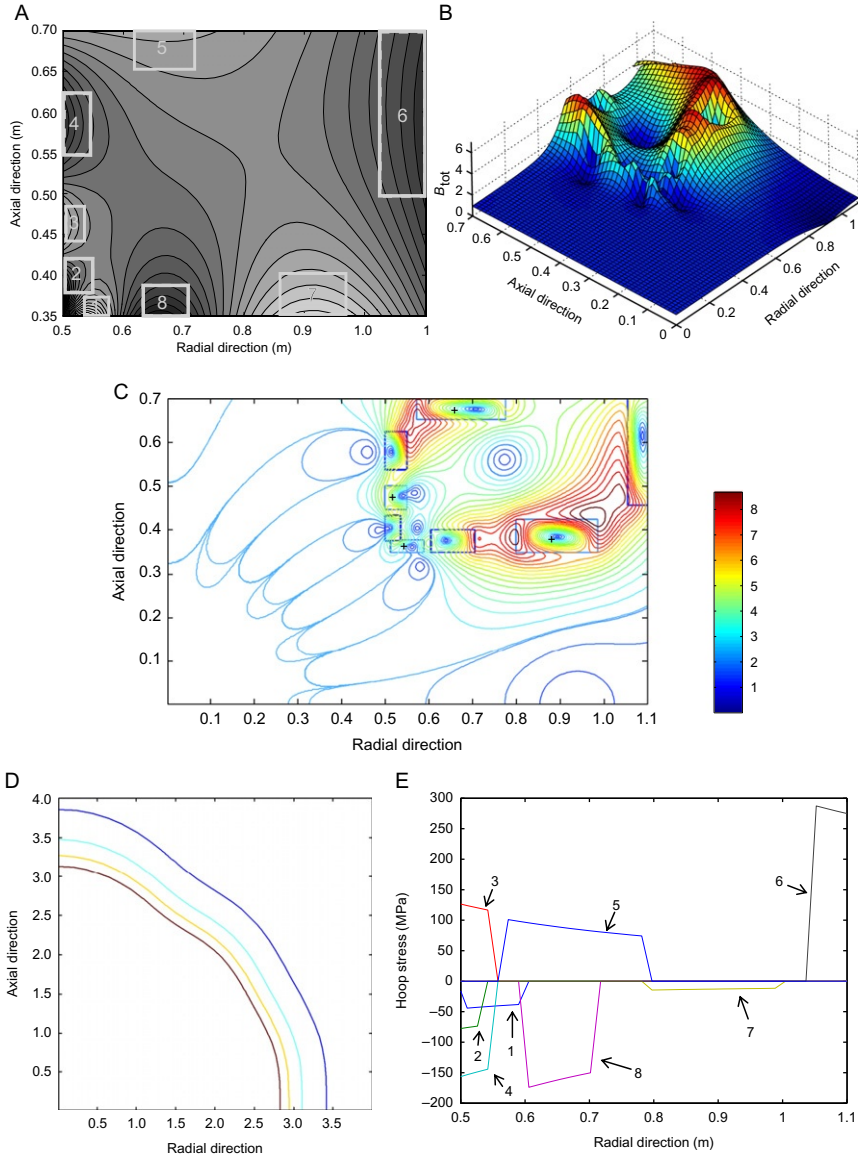

Figure 9 The 1T order 14 degree 4 open magnet design. Illustrations of (A) the MSE current density map distribution with locations for initial seed coils, (B) the total magnet field distribution, (C) the final coil layout and associated inner field, (D) the outer field cut-off with 20, 15, 10 and 5G contours from inside out, and (E) the stress with respect to the radial direction inside each of the coils. The '+' signs in (C) indicate positive transport current, otherwise the transport current is negative and the contours correspond to the field in (B).

be best practice from a manufacturing point of view. It is possible that some coils will experience a bucking effect that requires special mechanical support, or coils are too large for practical manufacturing purposes. These unwanted effects can be avoided by including additional individual coil constraints, such as coil aspect ratio (i.e. radial to axial dimension) and maximum cross sectional area in the optimization. The additional constraints utilized in the designs may be different for each manufacturer. Further, the above effects could possibly be reduced by subdividing large problematic coils into several small coils carrying the same current and polarity. The order and degree of the design could also be varied to meet manufacturer specifications. However, this will affect the size of the FOV and footprint of the final magnet coil layout. Additionally, NbTi superconducting wire was used in the designs elucidated here, and Nb_3Sn type superconductor with higher current carrying capacity and peak magnetic field support could also be considered to reduce coil block sizes. Generally, this type of superconductor is more expensive, harder to work with and can further complicate manufacturing processes.

4. CONCLUSIONS

The MSE method of designing superconducting magnets for MRI whole body imaging was outlined. The method was then used to design four compact magnets with 1, 3, 7 and 11.75T static magnetic field strengths measured at the FOV. The method was then extended to design other magnet configurations. We provided a 1T magnet design for an asymmetric and an open magnet coil configuration. All designs had an inner diameter of 1m. Comparisons between the different coil arrangements were made and we performed qualitative and quantitative analyses of our results. The discussions were based on FOV size, footprint, peak magnetic field and coil stress.

We found that using the MSE approach, superconducting magnet coils are allocated on the perimeter of the magnet domain. The manner in which these coils are distributed depends on the field strength, size of the FOV and extent of the stray field. To increase the size of the FOV and to decrease the stray field, it is necessary to increase the number of zeroed inner and outer harmonics, or the order and degree of the harmonics defining the magnetic field produced by the magnet. An increase in the order and degree also increases the number of coils, potentially causing problems with the peak field/current criteria on individual superconductors. Therefore, there is an appropriate choice of order and degree, for which the most compact designs can be obtained.

Given a suitable choice of order and degree, adjacent coils in low-field strength compact magnets (i.e. to 3T) tend to have polarities that alternate

in current directions. This is not observed in high-field strength magnets (i.e. 7T and above), because the peak fields are now in close proximity to the magnet bore. The magnet domain needs to be increased to reduce them to an acceptable range specified for the superconductor. A reduction in the magnet domain can introduce reverse current coils in the design, increase the peak magnetic field and essentially breach the ability of the superconductor to carry an electric current.

REFERENCES

1. G. Morrow, Progress in MRI magnets. *IEEE Trans. Appl. Supercond.*, 2000, **10**(1), 744–751.
2. Q. M. Tieng, V. Vegh and I. M. Brereton, Globally optimal superconducting magnets Part I: minimum stored energy (MSE) current density map. *J. Magn. Reson.*, 2009, **196**(1), 1–6.
3. Q. M. Tieng, V. Vegh and I. M. Brereton, Globally optimal superconducting magnets. Part II: symmetric MSE coil arrangement. *J. Magn. Reson.*, 2009, **196**(1), 7–11.
4. Q. M. Tieng, V. Vegh and I. M. Brereton, Globally optimal, minimum stored energy, double-doughnut superconducting magnets. *Magn. Reson. Med.*, 2010, **63**(1), 262–267.
5. Q. Tieng and V. Vegh, Minimum stored energy split superconducting magnet for 3T MRI-PET animal imaging system. International Society of Magnetic Resonance in Medicine, 2010.
6. Q. M. Tieng, V. Vegh and I. M. Brereton, Minimum stored energy high-field MRI superconducting magnets. *IEEE Trans. Appl. Supercond.*, 2009, **19,** 3645–3652.
7. V. Vegh, Q. M. Tieng and I. M. Brereton, Minimum stored energy MRI superconducting magnets: from low to high field. *Concepts Magn. Reson. Part A*, 2009, **35**(3), 180–189.
8. M. A. Green and B. P. Strauss, The cost of superconducting magnets as a function of stored energy and design magnetic induction times the field volume. *IEEE Trans. Appl. Supercond.*, 2008, **18**(2), 248–251.
9. S. W. V. Sciver and K. R. Marken, Superconducting magnets above 20 Tesla. *Phys. Today*, 2002, **55**(8), 37–42.
10. B. Zhang, C. Gazdzinski, B. A. Chronik, H. Xu, S. M. Conolly and B. K. Rutt, Simple design guidelines for short MRI systems. *Concepts Magn. Reson. Part B*, 2005, **25B**(1), 53–59.
11. H. Zhao and S. Crozier, A design method for superconducting MRI magnets with ferromagnetic material. *Meas. Sci. Technol.*, 2002, **13,** 2047–2052.
12. V. Cavaliere, A. Formisano, R. Martone and M. Primizia, A genetic algorithm approach to the design of split coil magnets for MRI. *IEEE Trans. Appl. Supercond.*, 2000, **10**(1), 1376–1379.
13. J. Caldwell, Magnetostatic field calculcations associated with superconducting coils in the presence of magnetic material. *IEEE Trans. Magn.*, 1982, **18**(2), 397–400.
14. A. K. Kalafala, Optimized configurations for actively shielded magnetic resonance imaging magnets. *IEEE Trans. Magn.*, 1991, **27**(2), 1696–1699.
15. A. Zisserman, R. Saunders and J. Caldwell, Analytic solutions for axisymmetric magnetostatic systems involving iron. *IEEE Trans. Magn.*, 1987, **23**(6), 3895–3902.
16. A. Ishiyama, M. Hondoh, N. Ishida and T. Onuki, Optimal design of MRI magnets with magnetic shielding. *IEEE Trans. Magn.*, 1989, **25**(2), 1885–1888.
17. A. Ishiyama and H. Hirooka, Magnetic shielding for MRI superconducting magnets. *IEEE Trans. Magn.*, 1991, **27**(2), 1692–1695.
18. N. R. Shaw and R. E. Ansorge, Genetic algorithms for MRI magnet design. *IEEE Trans. Appl. Supercond.*, 2002, **12,** 733–736.

19. H. Zhao, S. Crozier and D. M. Doddrell, A hybrid, inverse approach to the design of magnetic resonance imaging magnets. *Med. Phys.*, 2000, **27**(3), 599–607.
20. M. R. Thompson, R. W. Brown and V. C. Srivastava, An inverse approach to the design of MRI main magnets. *IEEE Trans. Magn.*, 1994, **30,** 108–112.
21. A. K. Kalafala, A design approach for actively shielded magnetic resonance imaging magnets. *IEEE Trans. Magn.*, 1990, **26,** 1181–1188.
22. Y. C. N. Cheng, T. P. Eagan, R. W. Brown, S. M. Shvartsman and M. R. Thompson, Design of actively shielded main magnets: an improved functional method. *Magn. Reson. Mater. Phys. Biol. Med.*, 2003, **16**(2), 57–67.
23. S. Crozier and D. M. Doddrell, Compact MRI magnet design by stochastic optimization. *J. Magn. Reson.*, 1997, **127**(2), 233–237.
24. H. Zhao, S. Crozier and D. M. Doddrell, Compact clinical MRI magnet design using multi-layer current density approach. *Magn. Reson. Med.*, 2001, **45,** 331–340.
25. Y. C. N. Cheng, R. W. Brown, M. R. Thompson, T. P. Eagan and S. M. Shvartsman, A comparison of two design methods for MRI magnets. *IEEE Trans. Appl. Supercond.*, 2004, **14**(3), 2008–2014.
26. S. Kakugawa, N. Hino, A. Komura, M. Kitamura, H. Takeshima and T. Honmei, A study on optimal coil configurations in a split-typesuperconducting MRI magnet. *IEEE Trans. Appl. Supercond.*, 1999, **2 Part 1,** 366–369.
27. H. Xu, S. M. Conolly, G. C. Scott and A. Macovski, Homogeneous magnet design using linear programming. *IEEE Trans. Magn.*, 2000, **36**(2), 476–483.
28. J. H. Jensen, Minimum-volume coil arrangements for generation of uniform magnetic fields. *IEEE Trans. Magn.*, 2002, **38**(6), 3579–3588.
29. I.-H. Park, J.-K. Byun, J. S. Kang and W. S. Nah, Topology optimization method for superconducting system with critical current condition. *IEEE Trans. Appl. Supercond.*, 2003, **13**(2), 1836–1839.
30. C. Wang, Q. Wang and Q. Zhang, Multiple layer superconducting magnet design for magnetic resonance imaging. *IEEE Trans. Appl. Supercond.*, 2010, **20**(3), 706–709.
31. C. Wang, T. Chang, M. Rong, Y. Dai, Z. Ni, L. Li and Q. Wang, Optimal design for high-field MRI superconducting magnet. *IEEE Trans. Appl. Supercond.*, 2011, **21**(3), 2245–2249.
32. W. R. Smythe, Static and Dynamic Electricity. McGraw-Hill Book Company Inc., New York, 1950.
33. W. H. Press, S. A. Teukolsky, W. T. Vetterling and B. P. Flannery, Numerical Recipes in C: The Art of Scientific Computing. Cambridge University Press, 2002.
34. J. A. Edminister, Theory and Problems of Electromagnetics. McGraw-Hill Book Company, New York, 1979.
35. J. Nocedal and S. J. Wright, Numerical Optimization. Springer, New York, 2006.
36. F. W. Grover, Inductance Calculations. Dover Publications, Mineola, 2004.
37. C. Lawrence, J. L. Zhou and A. L. Tits, User's Guide for CFSQP Version 2.5: A C Code for Solving (Large Scale) Constrained Nonlinear (Minimax) Optimization Problems, Generating Iterates Satisfying All Inequality Constraints. University of Maryland, College Park, MD, 1997.
38. L. K. Forbes, S. Crozier and D. M. Doddrell, Rapid computation of static fields produced by thick circular solenoids. *IEEE Trans. Magn.*, 1997, **33**(5), 4405–4410.
39. J. Caldwell, Stress in the windings of a coil carrying an electric current. *J. Phys. D Appl. Phys.*, 1980, **13**(8), 1379–1382.
40. S. Wolf (ed.) *In* Case Studies in Superconducting Magnets, Plenum Press, New York, 1994, 98–105.
41. P. Vedrine, G. Aubert, F. Beaudet, J. Belorgey, J. Beltramelli, C. Berriaud, P. Bredy, P. Chesny, A. Donati and G. Gilgrass, The whole body 11.7 T MRI magnet for Iseult/INUMAC Project. *IEEE Trans. Appl. Supercond.*, 2008, **18**(2), 868–873.
42. T. Schirmer, Y. Geoffroy, S. J. Koran and F. Ulrich, Signa SP/2–A MRI system for image guided surgery. *Med. Laser Appl.*, 2002, **17**(2), 105–116.

INDEX

Note: Page numbers followed by ''*f*'' indicate figures, and ''*t*'' indicate tables.